Doctoral theses at NTNU, 2021:125

Klas Solberg

Fatigue design for metallic components produced by additive manufacturing

Doctoral thesis

NTNU
Norwegian University of Science and Technology
Thesis for the Degree of
Philosophiae Doctor
Faculty of Engineering
Department of Mechanical and
Industrial Engineering

NTNU
Norwegian University of
Science and Technology

Klas Solberg

Fatigue design for metallic components produced by additive manufacturing

Thesis for the Degree of Philosophiae Doctor

Trondheim, April 2021

Norwegian University of Science and Technology

Faculty of Engineering

Department of Mechanical and Industrial Engineering

NTNU

Norwegian University of
Science and Technology

NTNU
Norwegian University of Science and Technology
Thesis for the Degree of Philosophiae Doctor
Faculty of Engineering
Department of Mechanical and Industrial Engineering

ISBN 978-82-326-6746-8 (printed ver.)
ISBN 978-82-326-6333-0 (electronic ver.)
ISSN 1503-8181 (printed ver.)
ISSN 2703-8084 (online ver.)

Doctoral theses at NTNU, 2021:125

Printed by NTNU Grafisk senter

Preface

This thesis was written as the final work of my doctoral studies which have spanned from January 2018 until December 2020. The project was started as an integrated PhD project, meaning that it was a continuation of my master thesis which was written spring 2018. The master project dealt with the notched fatigue behaviour of Inconel 718 specimens produced by laser powder bed fusion. In this project the Inconel specimens were further studied, along with specimens of 316L stainless steel and maragin steel grade 300. The experimental results were analysed by different means and finally some perspectives were given on the fatigue design of components produced by additive manufacturing. This thesis consists of two main parts; Part I: a chapter summarizing and discussing the main findings in the project and Part II: a collection of the articles published during the project.

During the work with the PhD, I have been a part of several collaborations. In the materials advisory group at DNVGL Høvik, I have been a part of AM related activities, such as organizing courses on additive manufacturing. This has given the PhD project a more industry focused direction. In October/November 2018 I had a research period at the Department of Industrial and Systems Engineering at The Hong Kong Polytechnic University (PolyU). Fall 2019 I was supposed to go back for a longer research period, this had to be cancelled due to the political situation in HK and in particular the demonstrators at PolyU. Based on this collaboration, four articles have been published, one of them is included in this thesis. As the research period in HK fall 2019 was cancelled, another research period was planned at Auburn University. I was supposed to leave for the US 13^{th} of March 2020, however, due to the Covid-19 situation the country borders were closed 12^{th} March.

Finalizing a PhD during a pandemic has been an interesting journey. All of the sudden our working routines and lives had to change, communication that once were done face-to-face has been changed to video calls and e-mails. It has now been nine months since the Covid-19 outbreak and the vaccination programmes have just started. It will be interesting to see how long time it takes before the virus becomes history and if we will ever go back to our old habits again.

Klas Solberg
Oslo, December 2020

Abstract

Additive manufacturing is a fast-rising manufacturing that brings new possibilities in terms of what has previously been possible in manufacturing. Additive manufacturing is a computer-controlled process where the material is added rather than forming or subtracting, which is common in most conventional manufacturing methods. The method allows for manufacturing on-demand, few geometric constraints and tailored designs. However, the characteristics of the materials are not fully understood and defects deriving from the manufacturing process are often found to reduce the performance of the materials. For metals produced by additive manufacturing, the fatigue behaviour is in particular sensitive to the defects.

This thesis aims to increase the understanding of how the defects deriving from the manufacturing process influence the fatigue behaviour and how to take them into account when designing components. The thesis is divided into two main parts; one part giving a brief review of the main results and findings and one part where the articles published in the project are appended. The first part is divided into several sections; first, the main topics of the thesis are introduced along with a description of the structure of the thesis and the main methods used. Then follows a part with the experimental results and discussions around the factors influencing the fatigue behaviour. After this, different fatigue assessment models used for correlating or predicting results are presented followed by some recommendations on fatigue design. Finally, a conclusion and a summary are given.

In the experimental work, three materials were investigated; the superalloy Inconel 718, the stainless steel 316L and the maraging steel 18Ni300. Different notch geometries of Inconel 718 was investigated in the as-built and heat-treated state. The 316L specimens were also investigated in the as-built state. The 18Ni300 specimens were heat-treated, partly machined and tested at different build orientations.

The experimental results showed that the fatigue behaviour of the materials is strongly influenced by defects deriving from the manufacturing process. By analysing the fatigue behaviour at different load levels it was found that different defects and geometric features are critical at different load levels. In the fatigue assessment part, concepts such as the $\sqrt{area}$-method, the theory of critical distance and strain energy density are used to correlate the defects and geometrical aspects to the fatigue behaviour. In the design part, three main design approaches of AM components for structural applications are proposed along with a framework for fatigue design of AM metallic components.

Acknowledgement

I would like to thank my supervisor Filippo Berto and my co-supervisor Jan Torgersen for the guidance and support I have been given during the project. You have given me the freedom to shape the direction of the research and the possibility to travel for conferences and collaborations where I have met many interesting people and experiences new cultures. I would also like to express my gratitude for the fact that I was encouraged to publish and finalize projects early. When the Covid-19 situation arose, I was lucky enough to already have finalized projects and due to this, I was able to finalize the project within the initial time frame.

I would like to thank all my co-authors, Shuai Guan, Even Hovig, Javad Razavi, Knut Sørby, Keith Chan, Torgeir Welo and other colleges assisting my work. I would like to thank other PhD students and former PhD students in the department; Steffen Sunde, Lise Sandnes, Håkon Dugstad, Abedin Gagani, Andrey Krauklis, Gaute Stenerud, Wei Song. I would like to thank Cecilie Haskins for encouraging me to take a step back and view the project from a new perspective, you have truly influenced the structure of this thesis. I would like to thank you former supervisor, Truls-Arne Frednes, for all the long discussions and the guidance. I would also like to thank all the staff in the administration at MTP for assisting and supporting me. I would like to thank all the master students that I have been fortunate enough to supervise during the last couple of years; Marius Hornnes, Tarjei Hamre, Gard Jonas Moen Gabrielsen, Vetle Kjærstad, Matija Cuzovic, Emanuelle Solfiti and Boris Baldin. Your input and perspectives have been valuable input to the research project.

I would also like to thank my current colleges in DNV, in particular, Ole-Bjørn Moe and Stian Gurrik, for interesting discussions on AM materials and their applications in the industry. I would like to thank Polyteknisk Forening for granting me the "Dr.ing Haakon Styris Studiefond" in the beginning of my PhD studies.

Finally, I would like to thank my friends and family who have followed and supported me during the process. I can not mention all of you, but I would like to mention a few of you that have supported me and contributed in discussions on my project: My family; Lise Dammann, Tor Solberg, Tellef Solberg, Åse Dammann, friends from my previous studies; Markus Eie, Stian Birkeland, Oddvin Østmoe, Oscar Flo, Haakon Hokstad, Mari Skarstein, Tuva Østby, Ruben Kolås, Fredrik Stokvik, friends form Oslo and Asker; Benjamin Isachsen, Håkon Tennøe, Kaja Ringerike, Aike Lindhagen, Aleksander Bachke, Andreas Offenberg, Carl Orrall, Eirik Liberg, Friends in Trondheim; Adeleide Bergsaker, Mathias Nyheim, Sven-Are Bjerke, Kristoffer Amundsen, Sofie Møller, Emil Dæhlin, Ivar Gravdal, Øystein Eldholm, Silje Ellefsen, the people living in Nedre Bakklandet 6; Laura Ann Morrison, Mia Fasting, Mari Neira and Felix Neira, new friends in Oslo in Lille Frøen buldreklub; Frikk Nesse, Tellef Storebakken, Brage Storebakken, Erik Grandelius, Olaf Mundal.

List of scientific contributions

List of appended articles

I **What is going on with fatigue of additively manufactured metals?**
K. Solberg, F. Berto
Material Design & Processing Communications 1 (2), 2019, e84
https://doi.org/10.1002/mdp2.84

II **Notch-defect interaction in additively manufactured Inconel 718**
K. Solberg, F. Berto
International Journal of Fatigue 122, 2019, pp. 35-45
https://doi.org/10.1016/j.ijfatigue.2018.12.021

III **A diagram for capturing and predicting failure locations in notch geometries produced by additive manufacturing**
K. Solberg, F. Berto
International Journal of Fatigue 134, 2020, pp.105428
https://doi.org/10.1016/j.ijfatigue.2019.105428

IV **The effect of defects and notches in quasi-static and fatigue loading of Inconel 718 specimens produced by selective laser melting**
K. Solberg, F. Berto
International Journal of Fatigue 137, 2020, pp.105637
https://doi.org/10.1016/j.ijfatigue.2020.105637

V **Fatigue assessment of as-built and heat-treated Inconel 718 specimens produced by additive manufacturing including notch effects**
K. Solberg, D. Wan, F. Berto
Fatigue & Fracture of Engineering Materials & Structures 43(10), 2020, pp. 2326-2336
https://doi.org/10.1111/ffe.13300

VI **Fatigue of additively manufactured 316L stainless steel: The influence of porosity and surface roughness**
K. Solberg, S. Guan, S.M.J. Razavi, T. Welo, K.C. Chan, F. Berto
Fatigue and Fracture of Engineering Materials and Structures, 42(9), 2019, pp. 2043-2052
https://doi.org/10.1111/ffe.13077

VII **Directional fatigue behaviour of maraging steel grade 300 produced by laser powder bed fusion**
K. Solberg, E.W. Hovig, K. Sørby, F. Berto
International Journal of Fatigue
https://doi.org/10.1016/j.ijfatigue.2021.106229

Statement of author contributions

The main idea of the project was designed and devolved together by **F. Berto** and **K. Solberg**. **K. Solberg** performed most of the experimental works in the project, with some exceptions. In Article V, **D. Wan** performed the BSE and EBSD imaging. Article VI was done in collaboration with a research group at PolyU where **S. Guan** printed the specimens and provided the XCT analysis. In Article VII the study was designed together by **E. Hovig** and **K. Solberg**. **E. Hovig** produced the specimens, **K. Solberg** performed the mechanical testing and investigations. **K. Solberg** was the first and corresponding author of all the appended articles, all co-authors reviewed, edited and joined discussions of the manuscripts and their results.

List of other related articles

An Investigation of the Elasto-plastic Anisotropy of Heat-Treated Maraging Steel Grade 300 Processed by Laser Powder Bed Fusion
E.W. Hovig, A.S. Azar, K. Solberg, K. Sørby
The International Journal of Advanced Manufacturing Technology
Accepted for publication

Additively manufactured CrMnFeCoNi/AlCoCrFeNiTi0.5 laminated high-entropy alloy with enhanced strength-plasticity synergy
S. Guan, D. Wan, K. Solberg, F. Berto, T. Welo, T.M. Yue, K.C. Chan
Scripta Materialia 183, 2020, 133-138
`https://doi.org/10.1016/j.scriptamat.2020.03.032`

Additive manufacturing of fine-grained and dislocation-populated CrMnFeCoNi high entropy alloy by laser engineered net shaping
S. Guan, D. Wan, K. Solberg, F. Berto, T. Welo, T.M. Yue, K.C. Chan
Materials Science and Engineering: A 761, 2019, 138056
`https://doi.org/10.1016/j.msea.2019.138056`

Formation of fully equiaxed grain microstructure in additively manufactured AlCoCrFeNiTi0.5 high entropy alloy
S. Guan, K. Solberg, D. Wan, F. Berto, T. Welo, T.M. Yue, K.C. Chan
Materials & Design 184, 2019, 108202
`https://doi.org/10.1016/j.matdes.2019.108202`

Fatigue Behaviour of Additively Manufactured Inconel 718 Produced by Selective Laser Melting
K. Solberg, J. Torgersen, F. Berto
Procedia Structural Integrity 13, 2018, 1762-1767
`https://doi.org/10.1016/j.prostr.2018.12.371`

List of oral presentations and posters

Some perspectives on design philosophies and fatigue assessment of metallic components produced by additive manufacturing
K. Solberg, F. Berto
Nasjonal konferanse for materialteknologi, 2020

The effect of defects from the manufacturing process on the static and fatigue behaviour of AM Inconel 718
K. Solberg, F. Berto
1st Virtual conference of structural integrity (VCSI1), 2019

Notched Fatigue Behavior of Additively Manufactured Inconel 718
K. Solberg, F. Berto
1st European Conference on the Structural Integrity of Additively Manufactured Materials (ESIAM), 2019

Fatigue does not initiate from the notch root
K. Solberg, F. Berto
1st European Conference on the Structural Integrity of Additively Manufactured Materials (ESIAM), 2019

Notched fatigue behaviour of Inconel 718 analysed by critical strain energy density
K. Solberg, J. Torgersen, F. Berto
2nd International Conference on Structural Integrity and Durability (ICSID 22), 2018

Fatigue Behaviour of Additively Manufactured Inconel 718 Produced by Selective Laser Melting
K. Solberg, J. Torgersen, F. Berto
22nd European Conference of Fracture (ECF 22), 2018

Fatigue strength of semi-circular notched Inconel 718 samples produced by selective laser melting
K. Solberg, J. Torgersen, F. Berto
Nasjonal konferanse for materialteknologi, 2018

List of abbreviations

AB	As-Built
AM	Additive Manufacturing
BD	Build Direction
BSE	BackScattered Electron
CAD	Computer Assisted Design
CT	Computed Tomography
EB	Electron Beam
EBSD	Electron BackScattered Diffraction
FEA	Finite Element Analysis
HB	Brinell Harness
HCF	High Cycle Fatigue
HIP	Hot Isostatic Pressing
HT	Heat Treated
HV	Vickers hardness
LB	Laser Beam
LCF	Low Cycle Fatigue
LEFM	Linear Elastic Fracture Mechanics
LoF	Lack of Fusion
OM	Optical microscope
PBF	Powder Bed Fusion
PP	Post-processed
QS	Quasi-Static
SED	Strain Energy Density
SEM	Scanning Electron Microscopy
SIF	Stress Intensity factor
SLM	Selective Laser Melting
SN	Stress - Number of cycles, Wohler diagram
TCD	Theory of Critical Distance

List of symbols

A	Vertical shift of Basquin curve / Fitting parameter
A_d	Defect size
a	Crack or defect size
$\sqrt{area}$	Defect size
$\sqrt{area}_0$	Critical defect size in the modified El-Haddad solution
B	Slope of Basquin curve / Fitting parameter
C	Fraction of fatigue life in Palmgren-Miner rule / vertical shift of stable crack growth regime / Fitting parameter
D	Fitting parameter
d	Hatch distance / Notch depth
E	Young's modulus / Energy density / Fitting parameter
H_a	Average failure locations
H_l	Lower limit of failure locations
H_u	Upper limit of failure locations
H_0	Notch root location
h	Layer height or distance within notch
h_0	Length of notch
K	SIF
k	Inverse slope of fatigue life curves
L	Critical distance
l	Defect size in El Haddad solution
l_0	Critical defect size in El Haddad solution
m	Slope of stable crack growth regime
N	Number of cycles
N_i	Number of cycles
N_w	Number of cycles at run out limit
N_f	Number of cycles to failure
n_i	Number of cycles deviating from trend line
n_{max}	Maximum value of number of cycles deviating from trend line
P	Laser power
R	Fatigue loading ratio
R_0	Critical radius for SED
Ra	Surface roughens - arithmetic mean deviation
Rz	Surface roughens - maximum height of profile
r	Distance from notch root
T	Scatter parameter
$T_{\Delta W}$	Scatter parameter for fatigue life given as SED
$T_{\Delta\sigma}$	Scatter parameter for fatigue life given as stress range

u, v	Coordinate system used for boundary conditions in Abaqus
u_0	Unit displacement
v	laser scanning speed
W	Strain Energy Density
W_c	Critical SED
$\bar{W}$	Average SED
x, y, z	Principal components of the coordinate system
Y	Shape factor
α	Notch opening angle
ΔK	SIF range
ΔK_{th}	Threshold SIF range
$\Delta\sigma$	Stress range
$\Delta\sigma_0$	Fatigue limit (TCD)
$\Delta\sigma_I$	Principal stress range (TCD)
$\Delta\sigma_{peak}$	Peak stress range (TCD)
$\Delta\sigma_{eff}$	Range of effective stress calculated by TCD
ρ	Notch radius
λ	Notch opening angle parameter
ξ	Notch acuity parameter
σ	Stress
σ_a	Stress amplitude
σ_{ar}	Equivalent stress amplitude for R=-1
σ_e	Fatigue limit with no defect
σ_m	Mean stress
σ_{nom}	Nominal stress
σ_{UTS}	Ultimate tensile strength
σ_w	Fatigue limit (Murakami and El-Haddad method)
τ	Shear stress
θ	Build angle / Angular deviation from the notch bi-sector line

List of Figures

List of Tables

Contents

Part I

Summary and perspectives

Chapter 1

Introduction

In this chapter the main concepts of the thesis are introduced and the structure and objectives of the thesis are explained.

1.1 Motivation

Additive Manufacturing (AM) is a fast-rising production method where parts are produced by adding material layer-by-layer in a computer-controlled process. In AM, parts can be manufactured on demand, each part can be tailored, few geometric constraints exist, parts can be produced close to the final shape and feedstock material can be reused. One of the main challenges of implementing AM parts in the industry is that the behaviour of the materials is not fully understood. In particular, metals produced by AM tend to have defects deriving from the manufacturing process which can strongly influence the fatigue performance of the materials. By moving production to AM, the cost can be reduced by reducing material usage. The required amount of spare parts to be stored can be reduced by manufacturing on demand. Further, obsolete or damaged parts can be replaced or fixed. However, for the industries to start taking advantage of this new production method for critical applications, a higher confidence level in the materials and the components needs to be achieved.

To have a secure transfer to AM in the industry, it is important to understand how the materials behave over time, i.e. to understand the fatigue behaviour of the materials. There are many methods for testing the mechanical performance of materials, the fatigue behaviour can be evaluated in laboratory experiments. To design durable parts some perspectives on fatigue design should be considered.

1.2 Additive manufacturing

1.2.1 General

This section gives a brief introduction to AM. AM is a manufacturing method where materials are added for creating a component [1, 2]. This is different from many conventional manufacturing processes where materials are usually subtracted or formed into components [1, 2]. The idea of creating objects by adding constituents together is not new; Pyramids are stone blocks added on top of each other, houses are bricks added onto each other, welding is metal deposited onto one-other and ceramic bowls can be created by adding toruses on top of each other. Although all of these "manufacturing methods" resembles additive manufacturing, we do not classify them as additive manufacturing. What we today categorize as additive manufacturing can be defined as an industrial production method where objects are manufactured by depositing materials, usually in layers, controlled by a computer system.

AM allows for building components automatically and many advantages can be listed, such as low

material use, tailored geometries, high geometric complexity, digital solutions and combination of materials and components. A wide variety of materials can be produced by additive manufacturing using different physical principles [3]. AM is an emerging field, and new production methods and principles are continuously being developed. ASTM has defined seven main categories of AM [4, 5], these are shown in Fig. 1.1, a short description of the categories follows below.

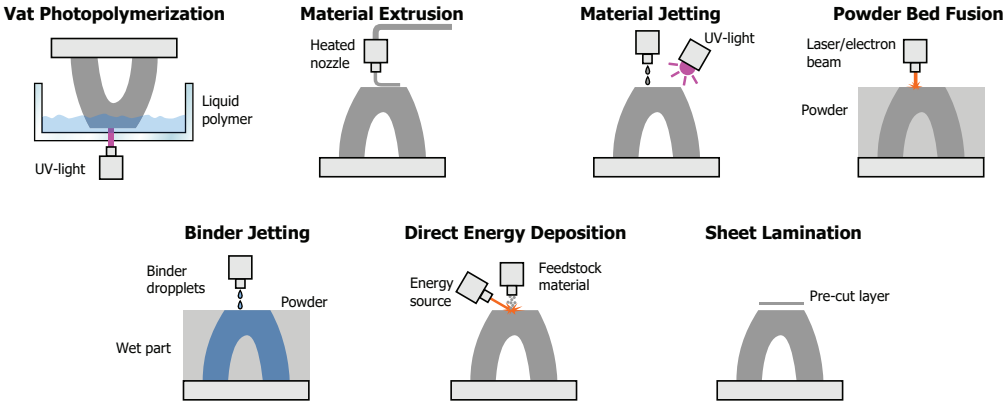

Figure 1.1: The seven main categories of AM according to ASTM

Vat Photopolymersization is based on curing liquid polymers by the use of a UV light. Usually, a platform is immersed into liquid polymer, then a UV-light selectivity cures the polymer from below. This process is repeated layer by layer until a solid part is formed, afterwards, additional curing may be required for archiving desired properties of the part. [6]

Material Extrusion is based on extruding material though a heated nozzle. The material is extruded and deposited in a selective manner layer by layer for forming the final component. Typical materials are thermoplastics, but the method can by used for other materials such as concrete. [7]

Material Jetting is based on jetting material to form a solid. The process is similar to material extrusion, but rather than continuously extruding material, it is jetted onto the part in droplets. After the droplets are jetted onto the part they are cured by a UV-lamp. [8]

Powder Bed Fusion is based on directly fusing together powder particles. Powder is spread in an even layer, and the powder particles are fused together layer by layer by a energy source. For metals a laser or electron beam is usually used. [9]

Binder Jetting is similar to powder bed fusion, but rather than directly fusing together the powder particles, a binder is used to bind the particles together creating a wet "green part". The green part is cured afterwards for removing the binder and fusing together the powder particles. [10]

Direct Energy Deposition is based on directly fusing a feedstock material (either a wire or powder) which is supplied from a nozzle. Powder or wire is deposited and melted by an energetic source to form a melted/sintered layer on a substrate. This process is repeated in a layer by layer manner. The method has the flexibility to be used for e.g. repair of existing components. [11]

Sheet Lamination is based on adding layer of pre-cut shapes together. Thin layers of materials are added on top of each other either by adhesive bonding between the layers in case of composites and paper, or by ultrasonic welding in the case of metals. [12]

In metal AM, powder bed fusion (PBF), metal binder jetting and direct energy deposition is the most common AM processes.

There are many advantages with AM. Because the material is fused together selectively by a laser, virtually any shape can be manufactured. It is possible to manufacture structures that are topology optimized [18, 19] or having internal channels and structures [19]. Another, advantage with AM is that the amount of material and machining usage can be substantially reduced if a part is built near-to-net shape [20]. Parts can be manufactured on demand and even tailored for each special case. This means that it could be possible to replace physical warehouses with digital warehouses, by storing parts digitally rather than physically. The AM industry has experienced rapid growth the last from 2010 to 2015, as shown in Fig. 1.2.

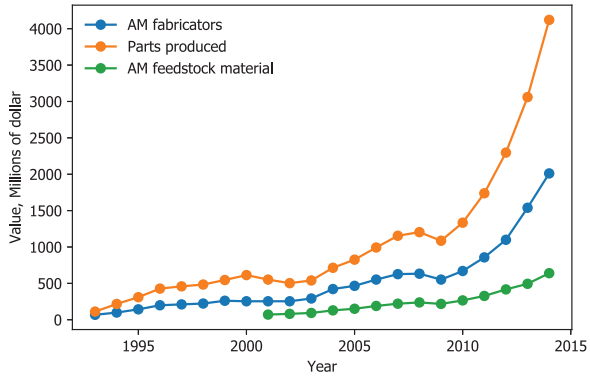

Figure 1.2: Worldwide growth of AM. Value of AM fabricators, parts produced and feedstock material sales [2].

1.2.2 Powder bed fusion

In this project, the manufacturing method in focus is PBF. Dealing with metals, two main PBF methods are used; Laser Beam (PBF-LB) and Electron Beam (PBF-EB). In both methods, powder particles are fused together by an energetic source. The main difference between the two is that PBF-EB uses an electron beam while PBF-LB uses a laser beam for fusing the powder. The PBF-LB process is illustrated in Fig. 1.3a. Thin layers of powder are selectively fused by a laser, then the powder is fed on top of the previous layer and the process is repeated until a final part is formed.

In the PBF-LB process, many parameters are affecting the quality and performance of the final part. In Fig. 1.3b a detailed view of the PBF-LB process is shown. The layer height, h [mm], is the height of each layer in the process and hatch distance, d [mm], is the distance between each hatch line. The laser beam is scanned with a scanning speed, v [mm/s], and a laser powder, P [W]. Based on these four simple parameters the energy density, E [J/mm^3], can be estimated. The energy density is then given by [13]:

$$E = \frac{P}{v \cdot h \cdot d}. \tag{1.1}$$

Fig. 1.3c and d show examples of scanning strategies. A wide variety of scanning strategies can be used, both in terms of outlines and internal hatching, but also variations between the different layers. Researches are working on finding the optimal scan strategies [14, 15, 16, 17]. PBF is a process where a high amount of energy/heat is applied selectively in local regions, this means that the heat is transferred away after melting and parts undergo thermal fluctuations. In many cases the parts can be oriented in a favourable orientation or support structures can be added during printing (both to support the part and to transfer heat).

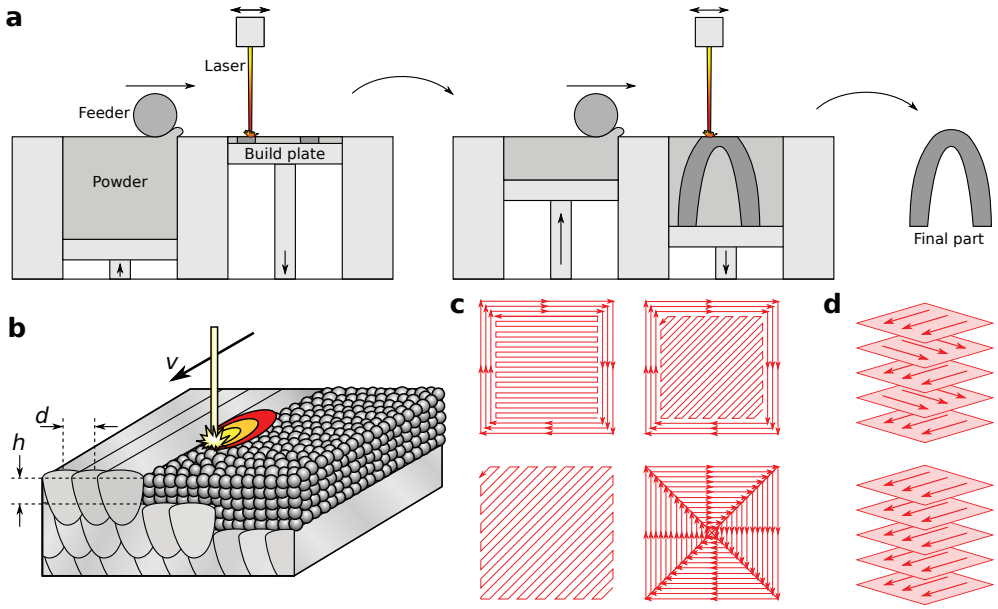

Figure 1.3: Schematic illustration of the PBF process. (a) Process (b) definition of layer height h, hatch spacing, and scaning speed, (c,d) scanning strategies.

1.3 Fatigue

1.3.1 General

This section gives a brief introduction and overview of the field of material fatigue. In material science, fatigue is the process of weakening a material over time due to applied cyclic stress. The cyclic stress results in localized material damage and the formation and growth of cracks. Fatigue cracks can initiate from geometrical defects or microstructural features within the material. After initiation, the fatigue crack grows for each load cycle applied. When the crack reaches a critical size, the crack propagates rapidly resulting in a sudden failure.

There are two main concerns when dealing with fatigue failure:

- Failure can occur suddenly without any warning such as visible deformations.
- Failure can occur at a lower load level than what corresponds to the strength of the material.

Because of these two aspects, design against fatigue is crucial for designing safe and cost-efficient components and structures. In the U.S., the cost of fatigue-related failure was estimated to be $119 billion in 1982 [21]. The gross domestic product the same year in the U.S. was $3 343 billion [22], this means that the fatigue-related failure had a cost corresponding to almost 4% of the gross domestic product!

1.3.2 Fatigue failure

Fatigue happens all around us, however as it is a process that does not involve large visible deformations, it can be difficult to detect. Here follow two examples of fatigue, one example without any consequences that will be familiar to the reader and one that had fatal consequences.

The first example is something many people will be familiar with; the cyclic loading of the handle on a beverage can, illustrated in Fig. 1.4. When opening the beverage can, the handle does not break, however,

when moving the handle back and forth a few times it will suddenly break and come off. Although we may not be able to observe the damage with the naked eye, the damage is accumulating in the deformed part of the handle due to the applied cyclic deformation. Fortunately, no serious consequences are related to this fatigue failure.

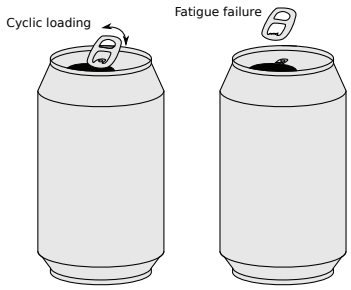

Figure 1.4: A familiar example of fatigue failure: Cyclic loading of the opener handle on a beverage can.

The second example of fatigue is one with far more serious consequences. Fig. 1.5 shows the Norwegian semi-submersible drilling rig Alexander L. Kielland platform which capsized in the Ekofisk oil field in March 1980, killing 123 people. The investigation report after the failure concluded that the rig collapsed due to the growth of a fatigue crack in a welded flange in one of the non-load bearing legs of the structure. The poor profile of the weld, in combination with several factors such as the cyclic loads from the weather conditions in the north sea finally caused the platform to capsize.

Figure 1.5: The Norwegian semi-submersible drilling rig Alexander L. Kielland platform which capsized in March 1980. [23]

The history of investigations of fatigue starts in 1837 with W.A.J. Albert who published the first know fatigue tests on conveyer chains [24]. The systematic investigations of fatigue failure started in the 1860s by A. Wöhler who investigated railway axles [24]. Since then the effort put into investigations and research of fatigue has increased, however, structures still fail unexpectedly from fatigue and the fatigue problem is yet not solved.

A fracture surface of a member failing from fatigue is shown in Fig. 1.6. The full fracture surface is shown in Fig. 1.6a, with the initiation site, crack growth region and the final rupture zone indicated. Fatigue initiated from a defect (shown in Fig. 1.6b), acting as a localized stress riser. After initiation the crack propagates for each cycle, resulting in striations on the fracture surface (Fig. 1.6c). Finally, when the crack reaches the critical length final rupture occurs (Fig. 1.6d). In the final rupture zone, dimples are observed, indicating that the rupture occurred in a ductile manner.

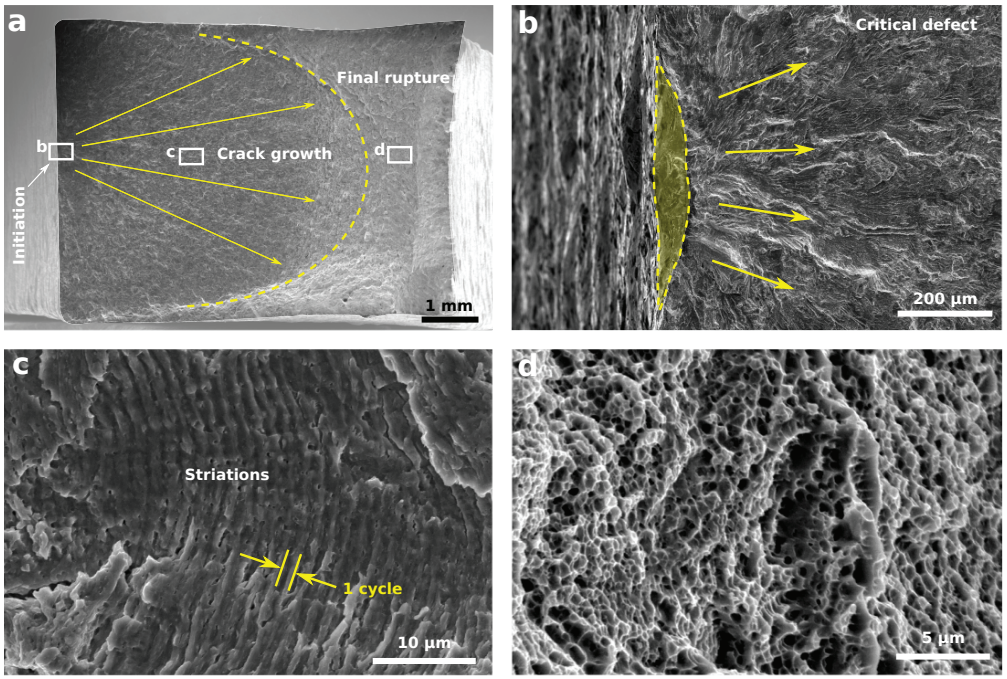

Figure 1.6: Fracture surface viewed in scanning electron microscope after failure due to fatigue loading. (a) Full fracture surface with initiation, crack growth and final rupture zone indicated, (b) Fatigue initiation site and the critical defect, (c) crack growth zone and striations for each loading cycle and (d) final rupture size with dimples indicating ductility.

1.3.3 Fatigue assessment

Fatigue in structures are often connected to simple manufacturing and design principles and can be avoided by taking precautions in the designs. The fatigue behaviour is dependent on factors such as the geometry of the part i.e. transitions or notches acting as stress risers, local geometric defects from the manufacturing process, the microstructure of the part, the environment the part is used in e.g. corrosive environments and other factors. The industry is driven by cost when designing parts, and it is not always possible or economically desirable to achieve "perfect" material quality for parts. Because of this, engineers need to take into account and design against fatigue failure. There are several approaches to fatigue design and assessment, I will not go into detail about the different methods, however, I will give a brief introduction to a few concepts and strategies which is used later in this thesis.

If a material is subjected to a load e.g. a force, F, the force is distributed within the material as stress, σ, which can be defined as force per area. This load can be applied in many different ways; if a cyclic load is applied, the cycles can be counted to see the effect of the load level and the number of cycles. An illustration of the cyclic stress and definitions are shown in Fig. 1.7b. σ_a is the stress amplitude, σ_m is the mean stress of the cycles and $\Delta\sigma$ is the stress range i.e. $2 \times \sigma_a$. Further, the cycles are counted for each oscillation, if the mean stress and amplitude are not constant, dedicated counting schemes can be used [25]. When comparing the applied stress and the number of cycles to failure, a linear trend is observed when taking the logarithm of the stress and the cycles, this is shown in Fig. 1.7c and is often referred to as an SN- or Wöhler-diagram. For some materials, this linear trend is followed by the endurance/fatigue limit under which fatigue failure does not occur. The linear trend of the fatigue data was proposed by Basquin who used the Wöhler data for obtaining the trend. The Basquin equation

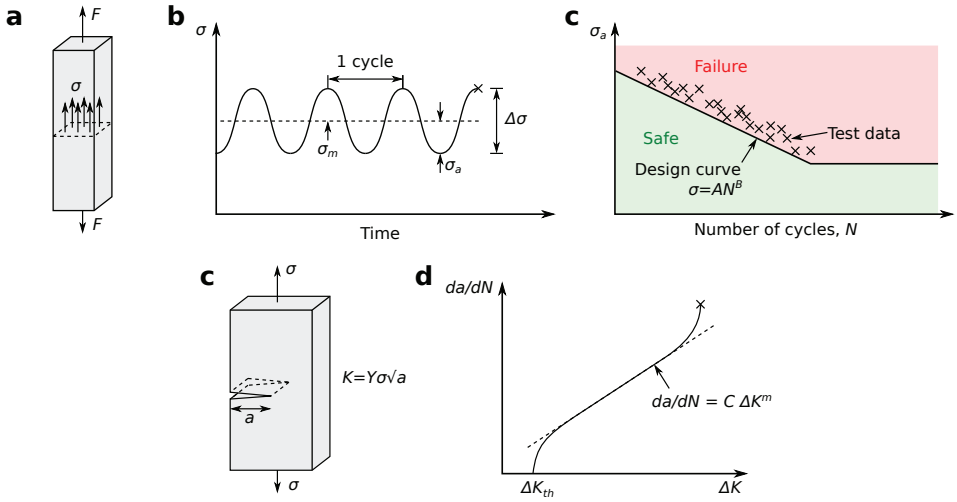

Figure 1.7: Methodology for fatigue assessment: (a) A material under the external load F resulting in the internal stress σ, (b) The definition of parameters describing fatigue loading, (c) S-N diagram for fatigue design (d) A material containing a crack under fatigue loading and (e) the crack growth rate during fatigue loading.

is given by

$$\sigma = AN^B, \tag{1.2}$$

where A is the vertical shift of the curve and B is the slope. Below the design curve and the endurance limit failure does not occur, and the design can be considered safe from fatigue failure. If the material is subjected to several load levels, Miner's rule can be used to estimate the fatigue life. The Miner's rule is given by

$$C = \sum_{i=1}^{k} \frac{n_i}{N_i} \tag{1.3}$$

where C is the fraction of the "used" fatigue life, n_i is the applied number of cycles for a given load level and N_i is the number of cycles resulting in failure for the same load level.

The fatigue life can also be estimated by taking into account the crack length. To do this, a concept from linear elastic fracture mechanics (LEFM) can be used; The Stress Intensity Factor (SIF). SIF is defined as

$$K = Y\sigma\sqrt{\pi a}, \tag{1.4}$$

where Y is a geometry factor and a is the crack size/length (defined in Fig. 1.7). In LEFM, a linear elastic material is assumed, i.e. a mathematical simplified model for a material that is not dependent on the load level but can be linearly scaled. In a real material, yielding/failure would occur when the stress reach a certain level, while in the simplified material model, stresses can tend to infinite. When introducing a sharp crack within such a material, the stress field ahead of the crack tip has an asymptotic trend, SIF is a parameter used to describe this stress singularity. The concept of SIF can also be applied to the propagation of cracks. Fig.1.7d shows the speed of a crack, da/dN, versus the SIF range, ΔK. The crack starts propagating above a threshold SIF ΔK_{th}. After initiation, it reaches a stable crack growth region described by

$$\frac{da}{dN} = C\Delta K^m, \tag{1.5}$$

as proposed by Paris and Erdogan [26]. Where C and m is the elevation and slope of the trend line, respectively. After the stable crack growth region, a rapid crack growth region follows, ending in final failure, where the crack reaches its critical length.

1.4 Objectives and scope

The objective of this thesis is to develop knowledge of the fatigue performance of metals produced by AM and to understand how the properties of these materials can be predicted when designing components. To achieve this, specimens produced by AM where mechanically tested and investigated. The following objectives were pursued:

- Developing experimental results for AM metals related to the mechanical and fatigue performance of the materials.
- Understanding which of the features that are deriving from the manufacturing process that are influencing the performance of the materials.
- Investigating and developing models for correlating the features influencing the performance of the materials to the fatigue behaviour.
- Understanding which factors and considerations that should be taken into account when designing AM parts for fatigue applications.
- The research aims to be a guide for designing components; a top-down approach is used in the investigations, i.e. first it is determined where the specimens fail from and reasons for this is examined, then the fracture surfaces are examined, taken small steps moving towards the microstructure in the end. Therefore a large emphasis is not set on the specific of the microstructure like is done in many other works dealing with the same topic.

Fatigue design for metallic components produced AM is a broad topic, and the scope of the project is limited to:

- Investigating three selected alloys produced by PBF-LB; the superalloy Inconel 718, the stainless steel 316L and the maraging steel 18Ni300. Many of the principles and features of these materials are also applicable to other alloys produced by AM.
- Investigating the main factors influencing the fatigue behaviour from a mechanical point of view. However, some aspects related to microstructural effects are also taken into account.
- Giving guidance on fatigue design based on experimental and analytical approaches. The design of real components is not included in the project.

1.5 Thesis overview and structure

The thesis consists of two main parts. Part I is a summary chapter with the main results and findings from the project. Part II is a collection of articles written during the PhD project, which part I is based on. Part I is divided into three main topics:

- Experimental results and descriptions of the main factors influencing the fatigue behaviour of AM metals
- Fatigue assessment of AM metallic components
- Different approaches to the design of AM components

These three topics make up Secs. 2 - 4. After these topics a summary and conclusion follows.

The articles written during the project does not follow the same structure as this thesis. The articles have a technical approach to the problems; e.g. an experimental part followed by some analysis reasoning for the results. The papers are therefore appended in Part II as a reference for further reading. For specifics about methods and technical details, the reader is referred to the articles. Part I is intended to describe and summarize the three above-mentioned topics, while the articles are intended to complement and give a more thorough description of the topics.

It should be noted that the articles mainly deals with experimental results and fatigue assessment. The part related to design does not have a role in the articles. The main idea behind this chapter derived from the course work in the course "PK8210 Systems Engineering Methods", and is based on the final project work in the course.

The following articles are appended in Part II of the thesis:

I **What is going on with fatigue of additively manufactured metals?**
K Solberg, F Berto
Material Design & Processing Communications 1 (2), e84
https://doi.org/10.1002/mdp2.84

II **Notch-defect interaction in additively manufactured Inconel 718**
K Solberg, F Berto
International Journal of Fatigue 122, 2019, pp. 35-45
https://doi.org/10.1016/j.ijfatigue.2018.12.021

III **A diagram for capturing and predicting failure locations in notch geometries produced by additive manufacturing**
K Solberg, F Berto
International Journal of Fatigue 134, 2020, pp.105428
https://doi.org/10.1016/j.ijfatigue.2019.105428

IV **The effect of defects and notches in quasi-static and fatigue loading of Inconel 718 specimens produced by selective laser melting**
K Solberg, F Berto
International Journal of Fatigue 137, 2020, pp.105637
https://doi.org/10.1016/j.ijfatigue.2020.105637

V **Fatigue assessment of as-built and heat-treated Inconel 718 specimens produced by additive manufacturing including notch effects**
K Solberg, D Wan, F Berto
Fatigue & Fracture of Engineering Materials & Structures 43(10), 2020, pp. 2326-2336
https://doi.org/10.1111/ffe.13300

VI **Fatigue of additively manufactured 316L stainless steel: The influence of porosity and surface roughness**
K Solberg, S Guan, SMJ Razavi, T Welo, KC Chan, F Berto
Fatigue and Fracture of Engineering Materials and Structures, 42(9), 2019, pp. 2043-2052
https://doi.org/10.1111/ffe.13077

VII **Directional fatigue behaviour of maraging steel grade 300 produced by laser powder bed fusion**
K Solberg, E Hovig, K Sørby, F Berto
https://doi.org/10.1016/j.ijfatigue.2021.106229

Article I gives an introduction to the main challenges when dealing with the fatigue of AM metals. The article gives a comparison of the fatigue behaviour of AM and wrought for some common engineering alloys. Article II-V deals with the fatigue behaviour of AM Inconel 718 and is connected as they deal with the same set of specimens. Article II deals with the fatigue behaviour of as-built Inconel 718 in the HCF regime. In this article, four different notch geometries were considered in the AB state, all fracture surfaces were investigated and the defect sizes were correlated to the fatigue life. Further, it was shown that fatigue did not initiate from the notch roots, but from defects adjacent. Strain energy density was used for generating unified fatigue life curves including all the notch geometries. Article III is a technical note to Article II, where an analytical model was proposed, correlating the notch acuities and failure locations in AM metals. Article IV investigates the transition from quasi-static loading to high cycle fatigue, and in particular how the failure locations shift for different load levels. In this work, a finite element analysis was carried out using a "real" notch geometry obtained from micrographs. The effect of heat treatment on the as-built Inconel 718 specimens was investigated in Article V. Here, the microstructure was studied in more detail and fatigue assessment was done based on the defect size, hardness and geometric effects. Article VI and VII are dealing with steels. Article VI deals with the fatigue behaviour of 316L steel. Here, the influence of the porosity and surface roughness was studied. The fatigue data showed a transition from failure from internal defects to surface defects when loading at lower stress amplitudes. Finally, the directional fatigue behaviour of PBF/LM maraging steel 18Ni300 was studied in Article VI. Here, a new test methodology is proposed, allowing the study of fatigue initiation from different surfaces with different orientations and properties.

1.6 Methods overview

Here, a brief overview of the methods used in the project is given. For the appended articles, the method sections describe in detail the different methods used. When discussing the results in the thesis, a short description might be given if relevant, for further reading the reader is referred to the method sections in the corresponding appended article.

In the research project, test specimens were produced, tested and analysed. The specimens were printed on commercially available AM systems using recommended processing parameters. In some cases, the specimens were tested in their as-built state while in other cases the specimens were post-processed before testing. The post-processing used was machining and/or heat treatment. Fig 1.8 shows a collection of the specimen geometries used in the project. The tensile and fatigue loading of the specimens was done in the fatigue lab at the department of mechanical and industrial engineering, NTNU. In the fatigue lab, several testing systems are available, the majority of the tests done in this project were done on an MTS servohydraulic uniaxial testing system with a load cell of 50kN. Most of the fatigue tests were done using loading ratios and frequencies at R=0 and 10Hz, respectively.

After mechanical testing of the specimens, the specimens were analysed by different approaches. First visual inspections were done mapping the failure locations and abnormalities of the specimens. Fractograpic analyses were done using Scanning Electron Microscopy (SEM). The microstructure of the materials was investigated by first cutting specimens at certain sections followed by polishing, then for the final stages two different approaches were done; either chemical etching and optical microscopy or oxide suspension polishing and electron backscatter analysis in the SEM.

For structural analyses, two main approaches were done, analytical modelling and finite element analysis (FEA). Abaqus CAE was used for the FEA, both planar (2D) and volumetric (3D) models were used. For analytical modelling, Python was used. Python was also used for processing all data generated during experimental testing, and the matplotlib library was used for the visualization.

Regarding the design-part of the thesis the discussions and perspectives derived from studies of the literature and discussions with industries working in AM. In addition to this, the spade systems design

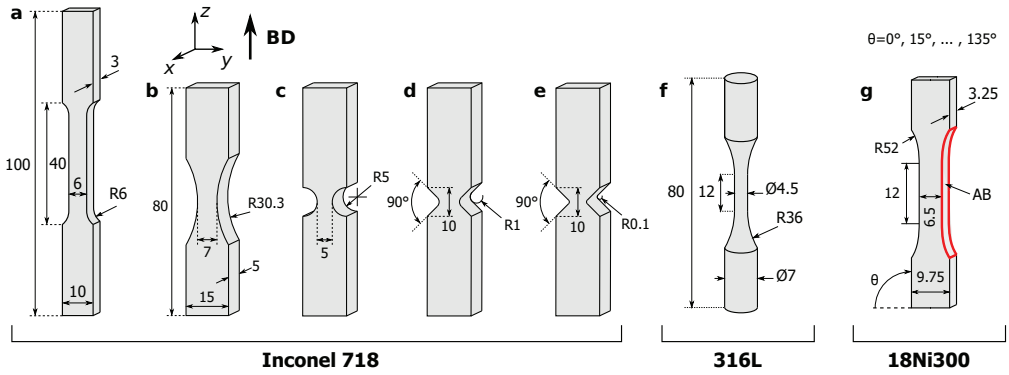

Figure 1.8: Specimen geometries: Inconel 718: tensile specimen, and four specimens for fatigue, 316L: specimen round dogbone specimen, 18Ni300 flat specimen built in 10 different angles, θ, ranging from 0 to 135 with a step size of 15. 18Ni300 specimens were machined except surface indicated by AB (as-built). BD indicates build direction.

Article	Material	Specimen	Build orientation [°]	Post-processing
I	-	-	-	-
II	Inconel 718	b, c, d, e	90	AB
III	Inconel 718	b, c, d, e	90	AB
IV	Inconel 718	a, b, d	90	AB
V	Inconel 718	a, b, d	90	AB, HT
VI	316L	f	90	AB
VII	18Ni300	g	0, 15, 30, 45, 60, 75, 90, 105, 120, 135	HT, Machined/AB

Table 1.1: Overview of material, specimen geometry, Build orientation (90 - vertical, 0/180 horizontal) and post-processing method used in the different articles.

framework proposed by Haskins was used [27].

Chapter 2

Experimental results

In this chapter, the fatigue behaviour of AM metals is discussed along with the main influencing factors deriving from the manufacturing process. First, an overview is given over the main defects deriving from the manufacturing process, then an overview of tensile and fatigue properties are given, followed by some more specific results and correlations based on the experimental work done during this project.

2.1 Defects and post processing

By reading the literature on AM in fatigue and fracture journals it is clear that the mechanical performance of AM metals is strongly influenced by the defects deriving from the manufacturing process. The main dominating features can be identified as:

- Surface roughness and surface defects
- Internal defects (porosity and lack-of-fusion)
- Residual stresses and distortions
- Microstructural anisotropy

Sec. 2.1.1 - 2.1.5 describes the different defect types, their origin and post-processing methods that can be used to remove them.

2.1.1 Surface roughness

The surface roughness and inherent resolution of AM parts are often one of the limiting factors when designing parts. The poor resolution will limit the designer's freedom and the surface roughness have been reported to strongly decrease the lifetime of AM metals [28]. The valleys in a surface profile can act as local stress risers where crack initiation may occur.

Fig. 2.1 shows the surface conditions for different build orientations of maraging steel grade 300 (18Ni300). Fig. 2.1a shows the cross-section of surfaces built with different orientations ranging from 0° to 135°. Based on these profiles, the surface roughness parameters Ra and Rz were calculated. Ra is the arithmetic mean deviation of the assessed profile and Rz is the maximum peak to valley height of the profile. The results are shown in Fig. 2.1b. The surface roughness increase when building surfaces facing downwards. Fig. 2.1c shows an illustration of different surfaces, the vertical (90°) and down-skin surface (135°) shows a general roughness, while the up-skin surface (15°) shows an effect that is called *stair-casing*. Stair-casing is surface roughness caused by the layer height and resolution of the build [29]. The surface roughness is higher in the down-skin regions because these are printed without support and the gravitation pulls the material down-ward onto the un-melted powder below [29].

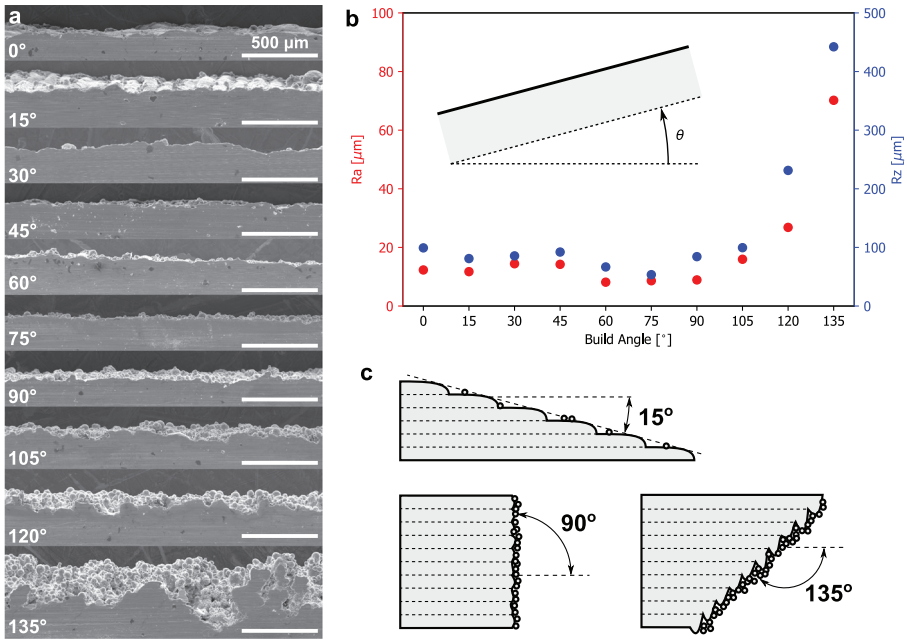

Figure 2.1: Correlation between build angle and surface roughness of PBF-LB/18Ni300.

2.1.2 Internal defects

Internal defects are a common problem in AM. The defect size and distribution are connected to the process parameters used during printing [30]. Fig. 2.2 shows three illustrations of the fusing process. In Fig. 2.2a an efficient process is shown. Fig. 2.2b shows insufficient penetration, the powder is not fused properly onto the previous layer, causing LoF defects. This can happen due to low energy density [31]. Fig. 2.2c shows the keyhole effect. The keyhole effect occurs due to the high recoil pressure as the metal evaporates. Under high laser power and low scanning speed, a deep and narrow keyhole is formed in the melt pool, and the laser is reflected multiple times within this keyhole. Instabilities in the keyhole cavity cause the formation of pores [32].

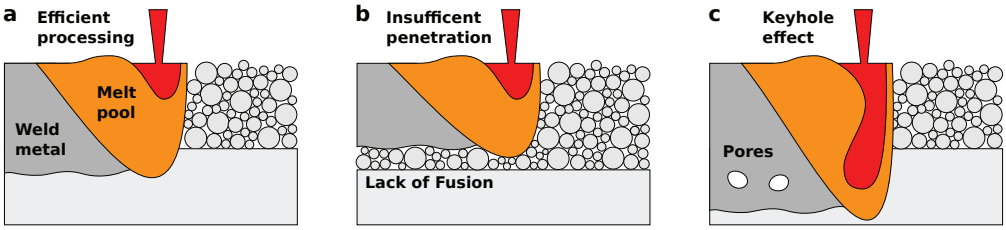

Figure 2.2: Illustration of different melt pools (a) Efficient process, (b) Insuficient penetration resulting in LoF and (c) Keyhole effect resulting in trapped pores. (Adapted from Ref. [33])

Fig. 2.3 shows an example of internal porosity in a PBF-LB/316L-specimen. Fig. 2.3a shows the data from a CT-scan from the centre of a specimen, the scan volume is shown in Fig. 2.3b. A micrograph from a polished cross-section is shown in Fig. 2.3c, where both a pore-defect and a LoF-defects are highlighted. From the CT-scan high amounts of pores were found with 1-2μm size (these had high sphericity), LoFs were found in the size range of 100-700μm (these had low sphericity), the porosities in the intermediate

size range had a medium value of sphericity.

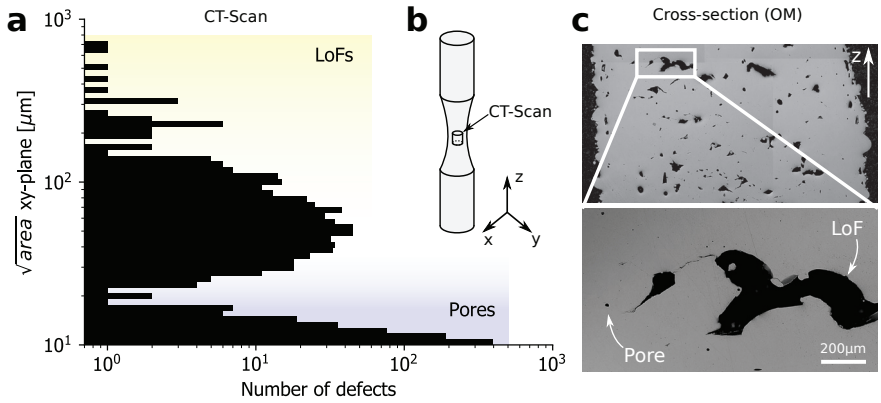

Figure 2.3: Internal defects in a 316L specimen. (a) Distribution of defects obtained from CT-scan (b) Specimen and coordinate system (c) Polished cross-section with detail showing the difference between LoF and pore defects.

2.1.3 Residual stresses

During both the PBF-LB and PBF-EB processes, high temperature gradients are achieved due to the energy input. A thin layer of powder is melted on top of a proceeding layer resulting in thermal fluctuations. When heat is applied, the material experience thermal expansion, and when the material solidifies and no heat is applied, thermal shrinkage occurs, this is illustrated in Fig. 2.4. These two repeating processes are likely to cause residual stresses and/or distortions in parts. It should be noted that PBF-LB and PBF-EB are somehow different, as the powder is preheated to a higher level in PBF-EB than PBF-LB lower amounts of residual stresses are achieved [34].

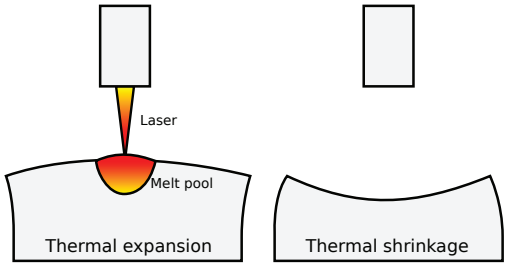

Figure 2.4: Thermal history during the manufacturing process. Adapted from Hamre [35]

It should also be noted that these thermal fluctuations can manifest either as residual stresses or as distortions. If a component is connected to the build platform by a supporting structure, the residual stresses might partially be relived upon removal of the supports, the component will then experience distortions. Based on this principle several researchers have proposed methods for estimating the residual stresses achieved in a print [34].

2.1.4 Microstructure

The microstructures achieved in AM are closely connected to the thermal history of the solidification process. In PBF, the powderparticles are fused by high energy in localized areas, the heat applied in

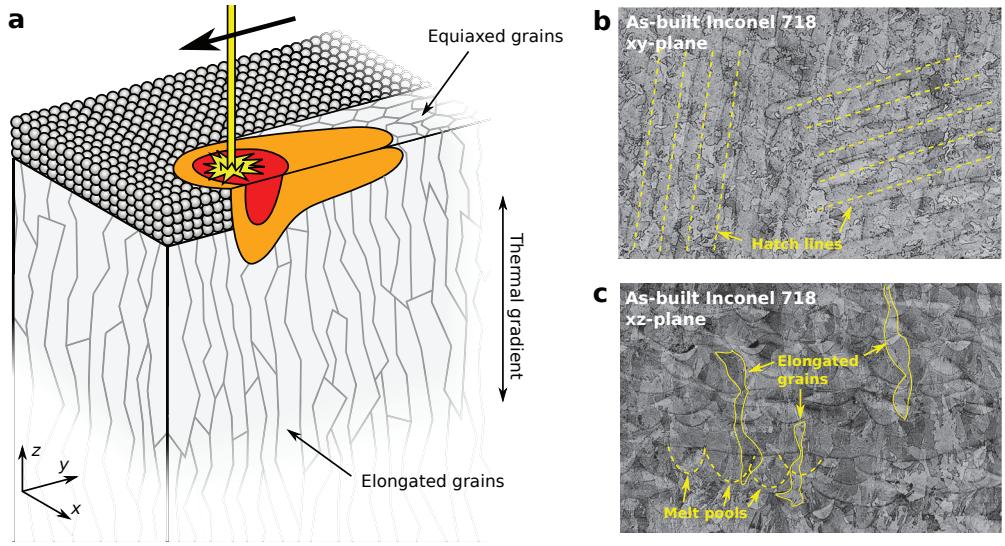

Figure 2.5: Microstructure deriving from the PBF process. (a) Illustration of the process, (b) microstructure in the xy-plane and (c) microstructure in the xz-plane.

these local areas are conducted away, usually towards the build platform. This produces steep thermal gradients in the z-direction of the build, which in many cases cause columnar grain growth i.e. the grains are oriented along the build direction [34]. The grains are usually equiaxed in the scanning plane (xy-plane). The columnar grain growth is shown in Fig. 2.5a.

Fig. 2.5b and c shows a polished and etched cross-section of AB Inconel 718. The xy-plane, shown in Fig. 2.5b, shows equiaxed grains and the hatch strategy from the build process is visible. The xz-plane, shown in Fig. 2.5c, shows the cross-sections of the melt pools and elongated grains spanning across several build layers.

2.1.5 Post-processing

In order to improve the mechanical behaviour from the AB state, it is common to do post-processing of the AM materials. The post-processing schemes are dependent on the alloy used and the intended use of the components. A collection of some common post-processing methods altering the geometric defects are shown in Fig. 2.6.

Sandblasting usually reduced the surface roughness, however, it might not remove subsurface defects. Machining is more likely to remove both the surface roughness and the sub-surface defects. Hot Isostatic Pressing (HIP) is a method where the part is heat and pressure treated. The high pressure can close and sometimes fully remove internal defects. It should be noted that defects open to the surface can not be closed by HIPing. If the goal is to remove all geometric defects, a combination of HIPing and machining can be employed. In addition to these post-processing methods dealing with the geometric aspects, it is also common to do heat treatment of the alloys. The heat treatment is usually specific for the specific alloy, and it can include e.g. stress relieving, ageing and solution treatment.

Although it is usually desired to remove all defects, this is not always possible or economically desirable. E.g. if designing a part with complex geometry and internal structures in low resolution, machining can not be done. In these cases, the designers are forced to deal with the defects deriving from the manufacturing process in the designs.

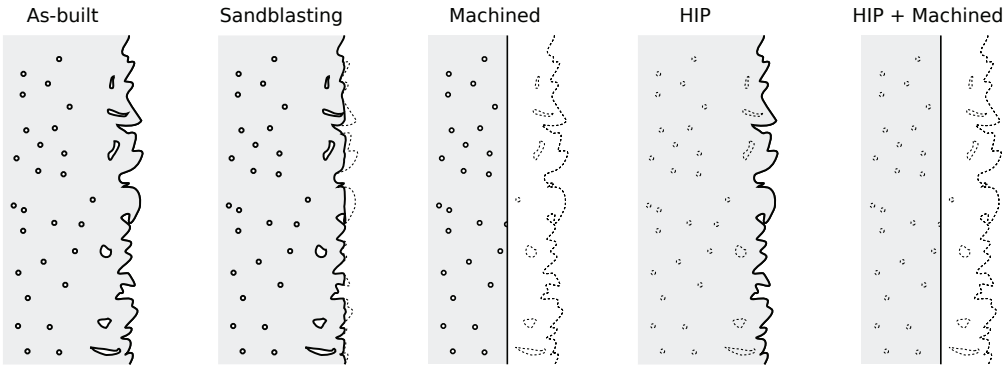

Figure 2.6: Various post processing schemes altering the geometric defects

2.2 Tensile properties

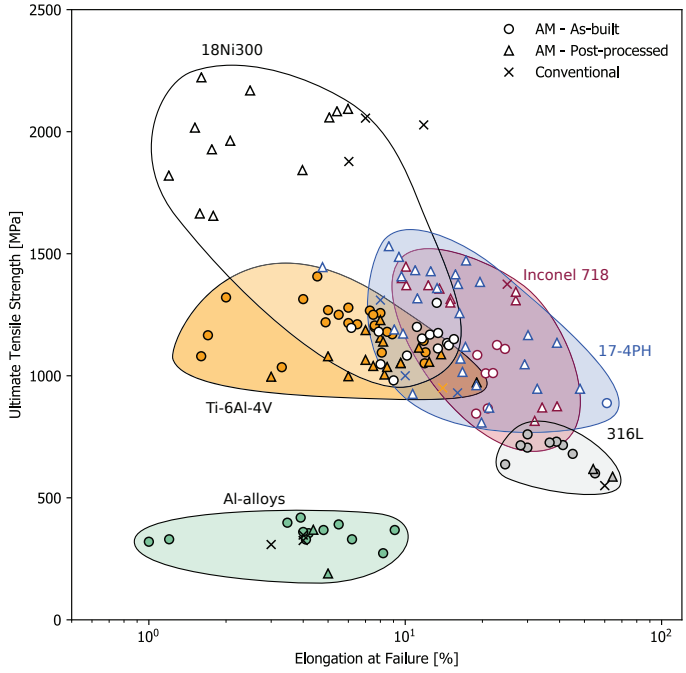

Figure 2.7: Material space comparison of ultimate tensile strength and elongation of some common engineering alloys. All materials are produced by PBF and both AB and PP are included [36, 37, 38, 39, 40, 41, 42, 43, 44, 45, 46]

In this section tensile properties of some engineering alloys are presented. The materials considered are the superalloy Inconel 718, the Ti-alloy Ti-6Al-4V, steel-alloys 316L, 17-4PH and 18Ni300 and Al-alloy (AlSi10Mg). The Ultimate Tensile Strength (UTS) and elongation at failure are presented in a material space shown in Fig. 2.7. In order to give a comparison also within each material, each material is presented in three different states; AB, PP and conventional. One general result for AM is that the presence of porosity typically decreases the elongation at failure. Materials are heat-treated for different reasons, in some cases to increase the strength at the expense of reduced elongation while in other cases to increase the ductility at the expense of reduced strength. In general, it is difficult to increase both the strength and the ductility of a material [47].

From the material space in Fig. 2.7 it is evident that high strength alloys are popular in AM. The material of highest strength (of the considered materials) is 18Ni300 in the annealed state. Here, the annealing increases the strength while also reducing the elongation at failure. In the wrought state, 18Ni300 shows comparable strength as the AM state, while the elongation at failure is higher. In the case of Inconel 718, there are also some heat treatments that decrease the strength and enhance the elongation, this is the case when HIPing the material and not doing solution treating or ageing. In the case of 316L, high strength is achieved in the AB state, while HT decreases the strength and enhance the elongation. The high strength in the AB state is often attributed to a refined sub-grain structure and high dislocation density. AlSi10Mg have lower strength compared to the other materials. Low variations between wrought and AM are observed in terms of strength for the Al-alloys.

2.3 Fatigue behaviour

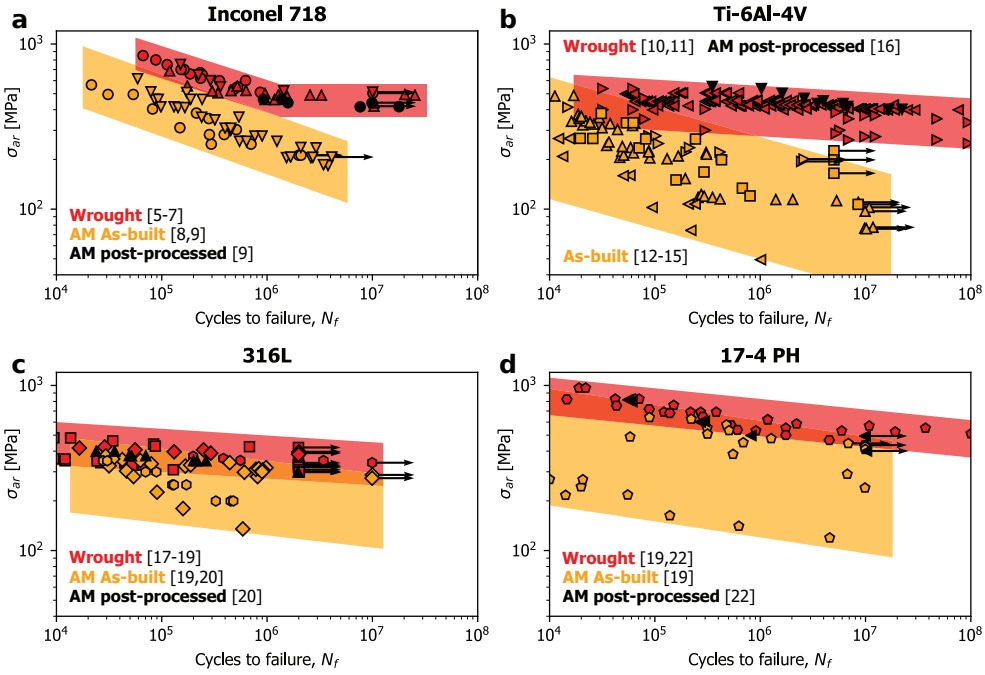

Figure 2.8: Collection of experimental fatigue data of some common engineering materials; Inconel 718 [48, 49, 50, 51, 52], Ti-6Al-4V [53, 54, 55, 56, 57, 58, 59], 316L [60, 61, 62, 63] and 17-4PH [62, 64, 40].

In this section, a comparison of fatigue data from the literature is presented. Similar to the previous section, the performance of AB and PP AM metals are compared with the same materials in the wrought condition. The fatigue data in the literature were tested using different methodologies in terms of mean stress levels. Due to this, a mean stress correction was done to the data from the literature. For this, the Smith-Watson-Topper (SWT) mean stress correction was used [65]. The fatigue data are presented in Fig. 2.8, where the number of cycles to failure is compared to the equivalent applied stress for R=0. Results from Inconel 718, Ti-6Al-4V, 316L and 17-4PH are shown. The general result is that in the AB condition, the fatigue performance is low for all the materials. However, after post-processing, the performance of the materials can be enhanced to the same level as their wrought counterparts.

High strength alloys are popular in AM. One of the challenges when dealing with high strength

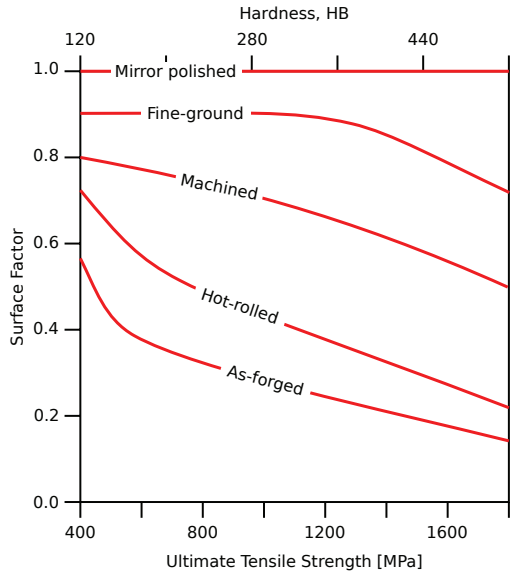

Figure 2.9: Surface finish effects in conventionally manufactured metals. Surface factor versus UTS and Brinell hardness (HB). Adapted from Ref. [66]

metals is that they are often sensitive to defects in fatigue loading. Fig. 2.9 shows a diagram presented in many engineering and fatigue textbooks. The diagram compares the surface factor (i.e. the fatigue limit correction factor) versus the UTS and Hardness of the material. A surface factor of 1.0 means that the fatigue limit is not influenced by the surface, while a factor of 0.5 means that the fatigue limit is halved. The diagram shows that for a given surface finish, e.g. machined, the surface factor is higher for a high strength material than for a low strength material.

The fatigue behaviour of AM metals is influenced by the defects and features deriving from the AM process. Fatigue is usually initiating from geometric defects such as surface defects or internal porosity. Fig. 2.10 shows two examples of fracture surfaces of AM 18Ni300 specimens. Fatigue initiation from AB surface is shown in Fig. 2.10a and fatigue initiation from an internal defect located at a machined surface is shown in Fig. 2.10b. Further, the microstructural anisotropy and the residual stresses can also influence the fatigue behaviour.

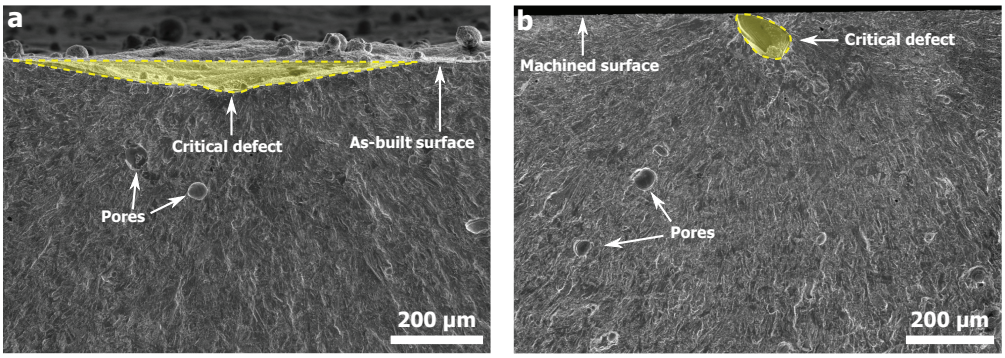

Figure 2.10: Examples of two fracture surfaces of 18Ni300 specimens failing from fatigue. (a) As-built surface (b) machined surface

2.4 Fatigue of notch geometries

In Article II-V the fatigue behaviour of notched specimens produced by PBF-LB/Inconel 718 was studied. The specimen geometries are shown in Fig. 1.8 and Table 1.1. The fatigue data are shown in Fig. 2.11. From the SN-curves, it can be observed that as the notch acuity increases, the fatigue strength decreases, this effect is typically seen as a result of the increasing stress concentration [67]. The scatter of the fatigue data, $T_{\Delta\sigma}$, also decreases as the notch acuity increases.[1]

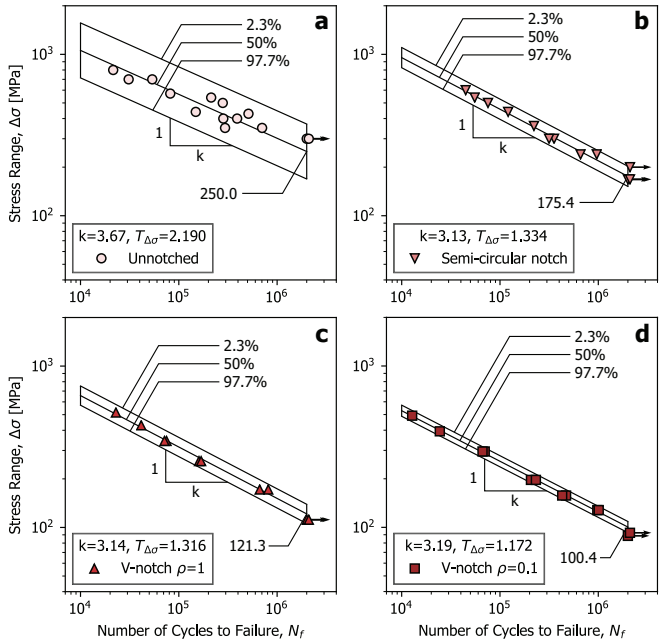

Figure 2.11: Fatigue data of the different notch geometries in as-built Inconel 718. (a) unnotched (b) semi-circular (c) v-notch $\rho = 1$ (d) v-notch $\rho = 0.1$

In Fig. 2.12 selected fracture surfaces are shown. Fig. 2.12a-d shows a full view of the fracture surfaces of unnotched, semi-circular, v-notch 1mm and v-notch 0.1mm. In the case of unnotched and semi-circular, fatigue initiates from one side, while for the v-notch geometries fatigue initiates from two sides. Fig. 2.12e and f show details from the defects initiating fatigue. The micrographs reveal large variations in the size and morphology of the defects at the fatigue initiation site.

Fig. 2.13 shows the different surface morphologies in the up- and down-skin regions in the notch. Similar trends to what was described in Sec. 2.1.1 is observed; a wavy up-skin surface and a down-skin surface with higher surface roughness.

2.5 The effect of heat treatment on the notched fatigue behaviour

Heat treatment (HT) is an effective method of improving the mechanical performance of many engineering alloys. The superalloy Inconel 718 is a good example of an alloy where the fatigue behaviour can be increased by HT. In this section, the influence of HT on notched AB Inconel 718 specimens are presented. One set of "unnotched" and "v-notch 1mm" specimens (referring to Fig. 1.8) were heat-treated and tested under fatigue loading. There are several ways of heat treating Inconel 718, the most common method of heat treating Inconel 718 to have increased fatigue behaviour is to do homogenization and/or solution

[1] The scatter index, $T_{\Delta\sigma}$ is given by the ratio of the stress from the confidence bands at the upper and lower boundary, *i.e.* $T_{\Delta\sigma} = \Delta\sigma_{10}/\Delta\sigma_{90}$.

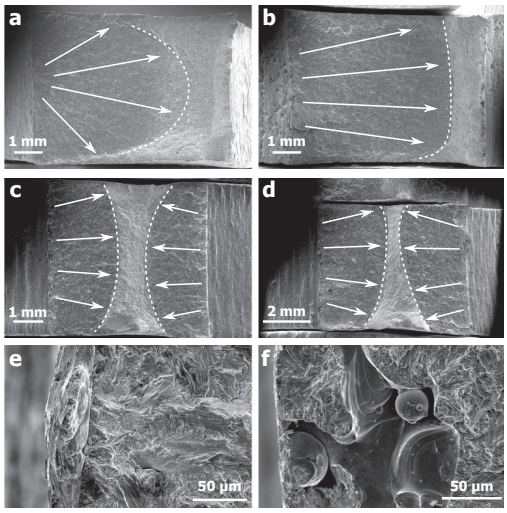

Figure 2.12: Different fracture surfaces and defects for fatigue of AM Inconel 718. (a) unnotched (b) semi-circular (c) v-notch 1mm (d) v-notch 0.1mm (e) and (f) defects from fatigue initiation sites.

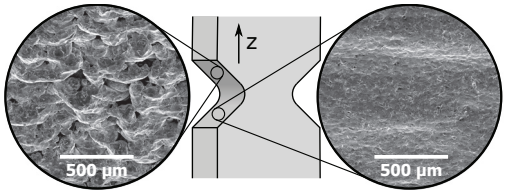

Figure 2.13: Surface morphology of up- and down-skin surfaces.

treatment followed by ageing [68]. The homogenization/solution treatment is done at between 980°C and 1200°C for dissolving hardening constituents into the matrix. Afterwards, ageing is done between 650°C and 900°C, usually in two stages. The ageing process is done for forming γ' and γ'' precipitates. Here, the following heat treatment was done; first 1 h at 1,095°C followed by air cooling to room temperature, then double ageing, first 8 h at 720°C followed by furnace cooling at 50 C/h until 620°C and aged for 8 h. Finally, the specimens were air-cooled to room temperature.

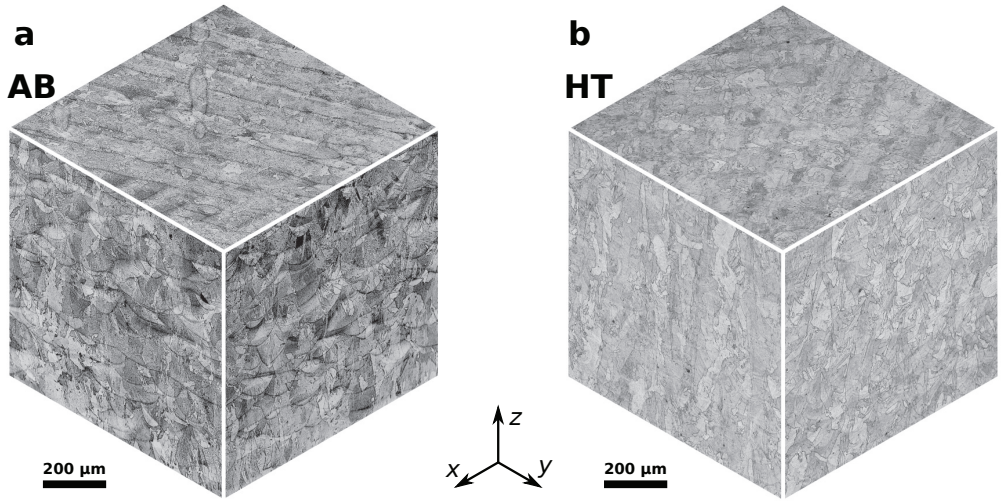

Figure 2.14: General microstucture of AB and HT Inconel 718 obtained by optical microscope.

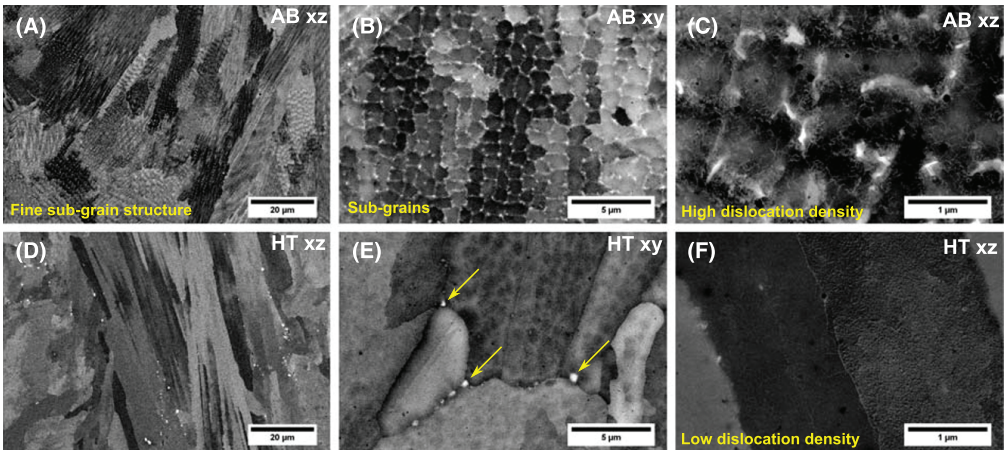

Figure 2.15: BSE analysis with different magnification and orientation of the microstructure of AM Inconel 718. (a-c) AB condition, (d-f) HT condition.

Fig. 2.14 shows a comparison of the general microstructure of AB and HT Inconel 718. In both cases, elongated grains were found in the build direction (z) and traces of the hatching strategy are visible in the xy-plane, these features are common in AM Inconel 718 [68]. Higher magnified images of the microstructure are shown in Fig. 2.15. Here, some more distinct differences in the microstructure can be observed. Comparing Fig. 2.15a and d, a fine sub-grain structure is observed in the AB state, while this is erased in the HT state. In Fig. 2.15b and e, the same difference is observed when comparing the subgrain structure. In addition to this, precipitates are visible along the grain boundaries in Fig. 2.15e, these are indicated by the arrows. In Fig. 2.15c and f differences in the dislocation density (white lines) can be observed; high dislocation density is observed in AB condition while lower density is observed in the HT state. Similar results were observed by Zhang et al. [69].

Vickers hardness (HV1) was measured for both AB and HT, the measurements showed that the hardness of the material increased from ∼300 to ∼500. Further, the tensile strength was measured. In the AB state, a tensile strength of 948 MPa and an elongation 13.0% was obtained, while in the HT state a tensile strength of 1,374 MPa and an elongation 7.7% was obtained. The low elongation was attributed to the fact that the specimens were tested in their AB (surface) state and not machined.

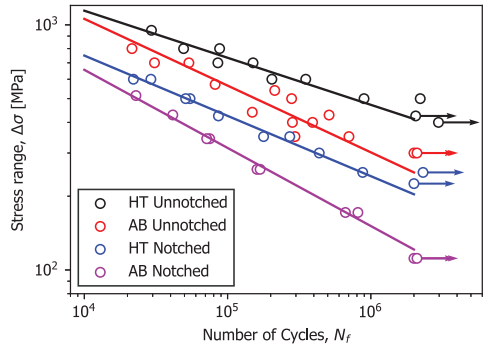

Figure 2.16: SN diagram of AB and HT Inconel 718. Notched and unnotched specimens.

The fatigue life curves from the AB and HT state are shown in Fig. 2.16. The experimental data shows that for both notched and unnotched specimens the fatigue life is substantially improved after heat treating the specimens.

2.6 Defect sizes and fatigue life

It is well established that the size and shape of geometric defects/notched/cracks are detrimental to the fatigue behaviour of metals [70]. With the defects that are common for metals produced by AM, it is no surprise that correlations can be found between the defects and the fatigue life [71].

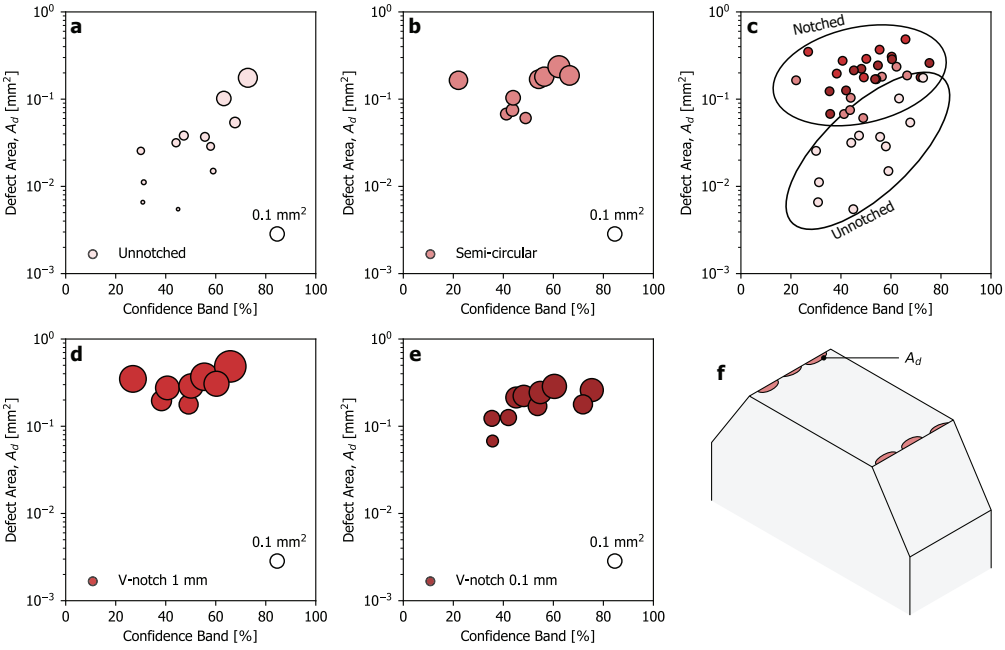

Figure 2.17: Correlations between defect size and fatigue life for notched AM Inconel 718 specimens produced by AM.

The fracture surfaces of all the AB Inconel specimens (in Article II) were captured by SEM, and the size of the defect found at the fatigue initiation site was measured. Fig. 2.17 shows the defects areas and their position within the confidence bands from the fatigue life curves in Fig. 2.11 (Taken as % chance of survival). For all the different geometries, there is a correlation between the defects size and fatigue life; large defects cause short fatigue life and small defects cause long fatigue life. Similar results have been observed in AM alloys by several researchers[71, 72]. This result shows the in the AB state, the surface defects are the critical feature for determining the scatter in the fatigue behaviour.

2.7 Failure locations

In the study of the notched Inconel 718 specimens, two geometric features are influencing the fatigue behaviour; The notches and the defects in the surface region. When investigating the specimens it was found that failure did not occur from the notch roots. Fig. 2.18 shows the polished cross-section of a specimen discontinued after 2×10^6 fatigue loading cycles. From the micrograph, a defect can be observed in the down-skin region above the notch root from which a fatigue crack has initiated (Fig. 2.18b and c). Fig. 2.18d shows an example of LoF and pores close to the surface.

Fig. 2.19 shows a collection of the failure locations for all the AB specimens correlated with the position within the confidence bands from Fig. 2.11. Here, no correlations were observed between the location and the fatigue life. However, correlations were found between the locations and the notch

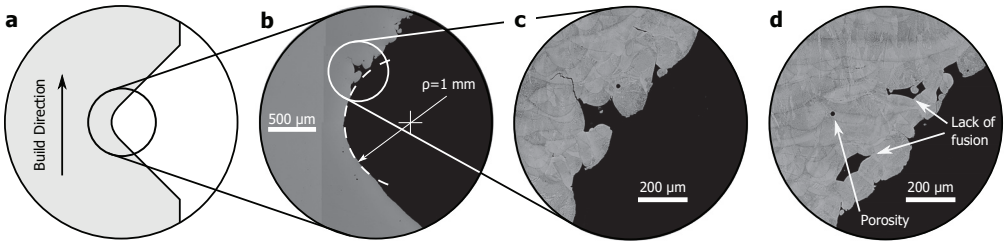

Figure 2.18: Polished cross section of a v-notched specimen fatigue loaded until 2×10^6 cycles.

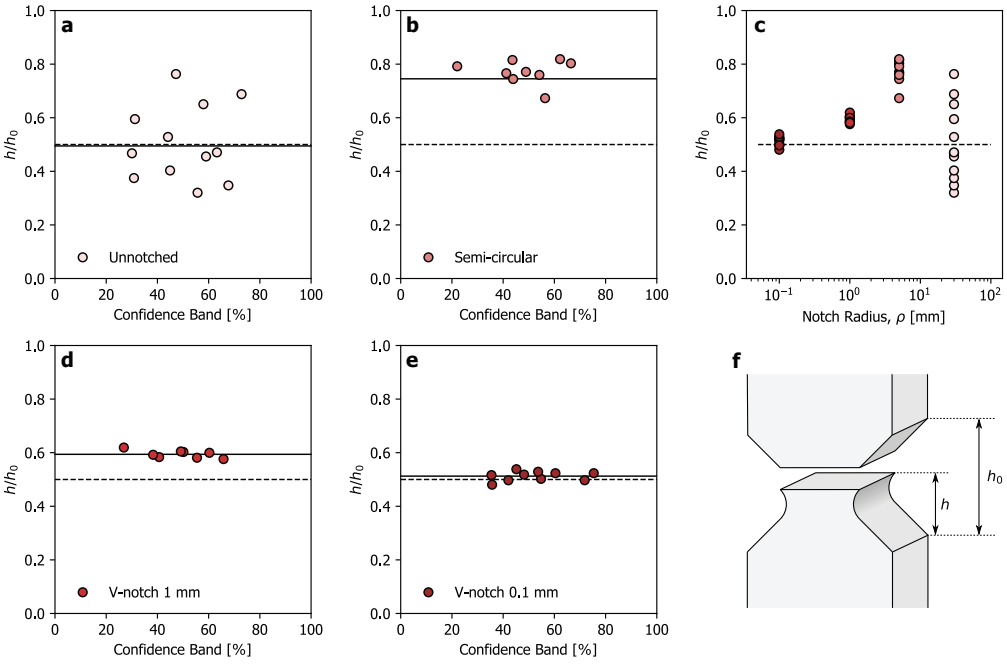

Figure 2.19: Correlations between failure location and fatigue life for notched AM Inconel 718 specimens produced by AM.

geometries. The trend can be divided into three categories:

- For sharp notches, the specimens were failing close to the notch root - here, the notch stress concentration is assumed to be the determining factor.
- For unnotched specimens, the specimens were failing with a large scatter in the failure locations: as it is a clear correlation between the defect sizes and the fatigue life, the location of the critical defect is assumed to determine the failure location.
- In the intermediate case of a blunt notch, the specimens were failing as a combination of the notch stress concentration and the local stress from the defects.

The failure locations were also captured in Article V where the AB and HT specimens were compared. When comparing failure location data for AB and HT specimens some variations were observed. Less scatter in the failure locations were observed for the unnotched specimens, i.e. the HT specimens failed closer to the smallest cross-section. In the case of the notched specimens, the failure locations were also

closer to the notch root, and fatigue initiated both from one and two sides, whereas the AB specimens failed from both notches. The results from the comparison are shown in Fig. 2.20e.

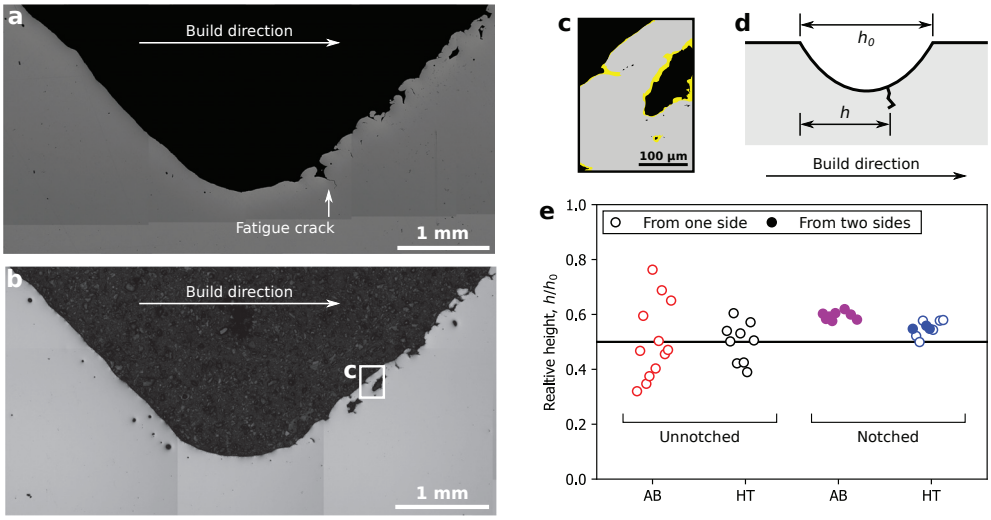

Figure 2.20: Comparison of failure locations in AB and HT Inconel 718. (a) AB notch, (b) HT notch, (c) Detail of oxide film in HT specimen, (d) definition of failure location and (e) captured failure locations.

The cross-sections of AB and HT notches subjected to 2×10^6 cycles are compared in Fig. 2.20a and b, in the AB specimen a fatigue crack is observed while in the HT specimen this is not the case. After HT, the specimens displayed an oxide film, this is highlighted in Fig. 2.20c. Several explanations can be given for the different failure locations in the two different states; the HT increase the fatigue resistance and could therefore also have ha different sensitivity to defects, the oxide film could delay the initiation of fatigue cracks by suppressing slipping [48, 49, 73, 74, 75] or there could be local variations in the specimens tested. A more thorough explanation of the different possible reasons is given in Article V.

As geometric considerations are usually not considered in test specimens, few studies report the failure locations. However, there are some cases where the failure locations are reported dealing with the fatigue of AM; In studies of machined specimens, the location of the internal defects (e.g. distance from surface) are frequently reported [71]; in lattice structures [76, 77, 78] or in directional fatigue of AB specimens, where the down-skin surface has higher roughness the up-skin surface [79].

2.8 From quasi-static to cyclic loading

In Sec. 2.2 and 2.3 the tensile and fatigue properties of AM metals were presented, in this section, the focus is set on the transition from quasi-static to fatigue loading. Two cases are considered; the behaviour of notched Inconel 718 specimens and the behaviour of 316L specimens.

2.8.1 Notched Inconel 718

In the previous sections regarding the fatigue behaviour, one of the main findings was that the defects are acting as fatigue crack initiation sites and reducing the fatigue life. In static loading, however, the defects are reducing the elongation at failure, but not necessarily decreasing the strength. In notched members, the notches are similarly influencing the fatigue behaviour as the defects; it acts as stress risers and reduces the fatigue behaviour. Along with the stress concentration produced by the notch follows

a more complex stress state, this can be referred to as stress triaxiality. The stress triaxiality is defined as the relative degree of hydrostatic stress and it can be calculated by taking the ratio between the hydrostatic stress and the von mises stress. According to the Von Mises failure criteria, a hydrostatic stress state cannot cause failure in a material (only deviatoric stresses can). This would mean that introducing a notch would increase the strength (of a material obeying the Von Mises failure criteria). This phenomenon is referred to as *notch strengthening* and is common for some ductile engineering alloys and materials failing for shear mechanisms [80, 81]. A more thorough explanation of this phenomena can be found in Article IV (Section II) and in Ref. [80].

Inconel 718 is one of the materials that exhibit the notch strengthening effect. The results for static loading of several specimen geometries are shown in Fig. 2.21. When increasing the notch acuity, the strength is increased while the elongation is decreased. In terms of elongation, the same effects is seen for notches and defects; it is decreased. Fig. 2.22 shows the fatigue life curve for the same geometries. As expected, the fatigue life is reduced when comparing the notched specimens to unnotched specimens. A transition between notch strengthening and notch weakening is found around 10^3 cycles.

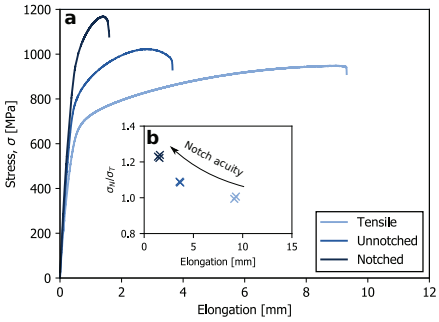

Figure 2.21: Quasi static behaviour of different notch geometries of Inconel 718.

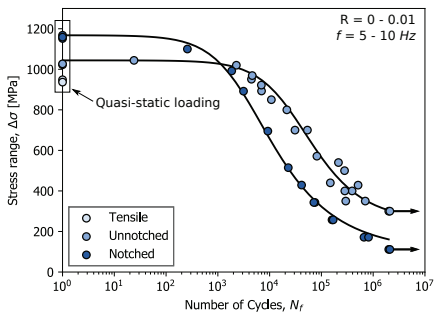

Figure 2.22: Fatigue life curves ranging from quasi static loading to fatigue loading.

Examples of two fractured specimens are shown in Fig. 2.23; one from quasi-static loading and one from HCF-loading. The fracture surface of the specimen subjected to quasi-static loading is shown in Fig. 2.23a with the corresponding side view in Fig. 2.23c. The fracture surface of the specimen subjected to fatigue loading is shown in Fig. 2.23b with the corresponding side view in Fig 2.23d. Fig. 2.23e and f shows defects from fracture surfaces corresponding to fatigue loading. In fatigue loading (Fig. 2.23b) cracks are propagating from both notches towards the centre of the specimen. In the case of the specimen subjected to quasi-static loading(Fig. 2.23a), the fracture surface is different, crack growth is not observed, and the cross-section is deformed due to necking.

Comparing the front view of the specimens in Fig. 2.23c and d, there are some differences. The specimen subjected to fatigue loading has failure initiating from the down-skin region above the notch root, while for the specimen subjected to quasi-static loading, the peaks and valleys of the fracture surface are ranging across the centre of the notch. In both cases, the dashed lines indicate the notch bisector line and the solid lines indicates the peaks and valleys of the fracture surface. Both in the case of quasi-static and cyclic loading, defects were found in the fracture surface. The fatigue cracks were found to initiate directly from the defects, as shown in Fig. 2.23f.

The failure locations in the specimens were captured and are shown in Fig. 2.24. The locations are represented as the relative height within the notch versus the load level. The plot is showing the peaks and valleys of the fracture surface and the fatigue initiation site. The general trend observed for both specimen geometries is that in cyclic loading, the defects are determining the failure location while moving towards quasi-static loading, failure is shifted towards and ranging across the minimum cross-

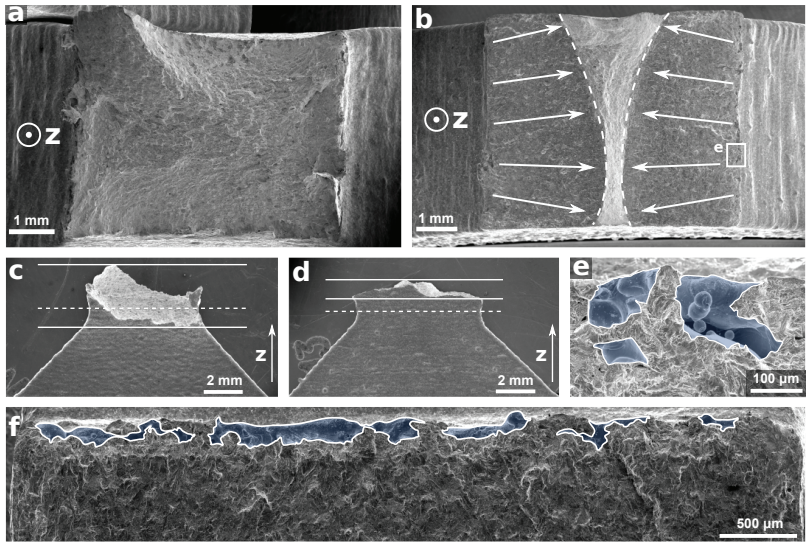

Figure 2.23: Fracture surfaces of notched Inconel 718 specimens failing under static (a,c) and fatigue loading (b,d,e,f).

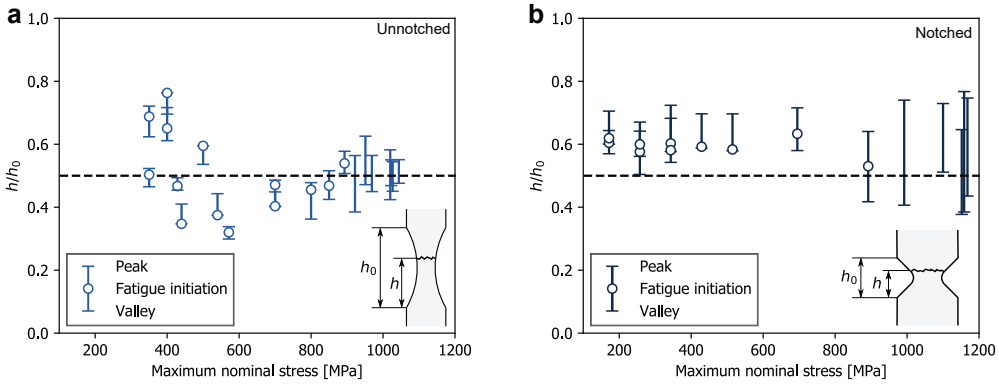

Figure 2.24: Summary of the failure locations (a) unnotched and (b) notched specimens

section. In the unnotched specimens, a large scatter is observed in the HCF regime and the specimens are failing from both the up- and down-skin region. For the notched specimens, the failure locations are located in the down-skin region in the HCF regime, while the fracture surfaces range across the notch region at higher loads. However, the mean value is still in the down-skin region. This indicates that the defects are influencing the failure location also under quasi-static loading.

2.8.2 Internal defects and surface roughness in 316L

Another example of transitions when moving in the fatigue regime was found in the study of 316L specimens (Article VI). Here, AB dogbone specimens with a high amount of porosity were studied. Fracture surfaces from different load levels are shown in Fig. 2.25 with the critical defects highlighted. The fracture surfaces show that at high loads and QS loading, the internal defects are critical, while in the HCF regime, the surface defects are critical. The corresponding fatigue data are shown in Fig. 2.26a.

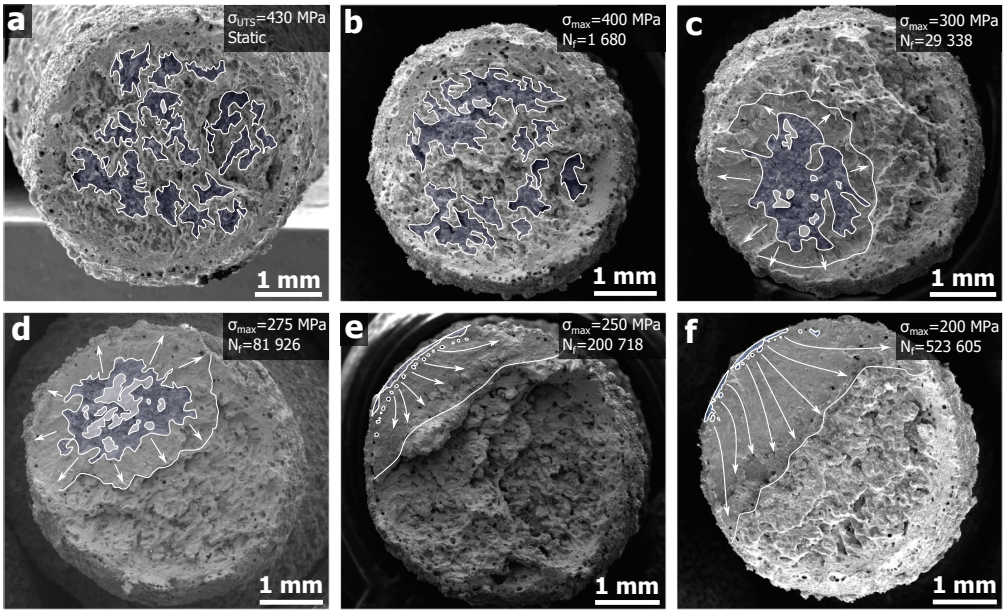

Figure 2.25: Fracture surfaces for AM 316L steel ranging from QS (a) to HCF loading (f).

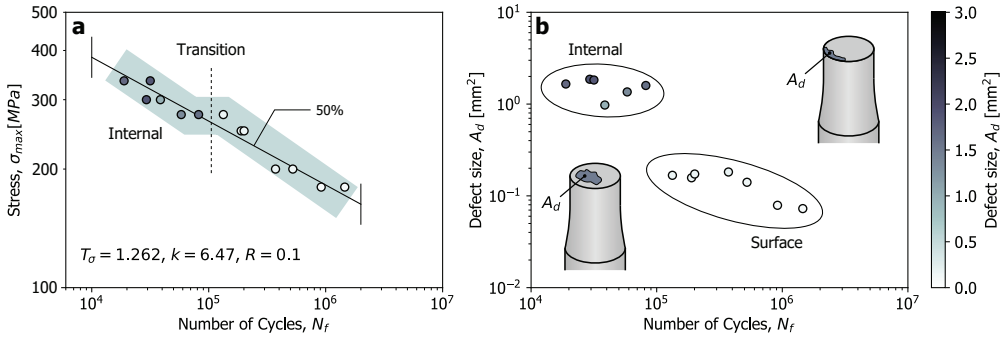

Figure 2.26: Fatigue data and critical defect size for AM 316L steel. (a) fatigue life curve and (b) defect size versus number of cycles to failure.

The fatigue life data shows a transition between internal defects being critical to surface defects being critical at about 10^5 cycles. Similar results were obtained by Andreau et al. [82]. The defect sizes and fatigue life are further compared in Fig. 2.26b.

2.9 Directional fatigue behaviour

As discussed in Sec. 2.3, the direction of fatigue loading, with respect to the build direction, influences the fatigue behaviour. However, it is not as simple as stating the one orientation is favourable to another, different materials and process parameters result in different trends in the directional fatigue behaviour. Three of the main effects used to explain the differences in the directional fatigue behaviour are shown in Fig. 2.27 and can be summarized as:

- The orientation of the internal defects

- The orientation of the microstructure
- The surface roughness variations

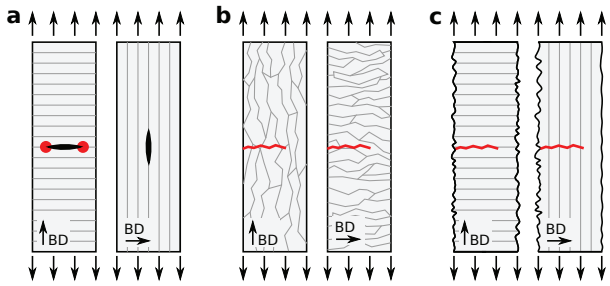

Figure 2.27: Different build orientation effects. (a) Orientation of the internal defects (b) orientation of the microstructure and (c) Surface roughness variations due to the build direction.

As described in Sec. 2.1, LoF defects are planar regions which have not been properly fused. As LoFs are crack-like defects, they are most critical when loading is occurring parallel to the build direction [83]. The microstructure in AM metals is in many cases anisotropic due to columnar grain growth parallel to the build direction[84]. When loading occurs parallel to the build direction, the fatigue crack needs to propagate through several grain boundaries than when crack growth occurs normal to the build direction, this is illustrated in Fig. 2.27b. Riemer et al. found that the threshold SIF was higher for 316L built in the vertical orientation than in the horizontal orientation, and reasoned this by stating that the fatigue crack needed to propagate through several grain boundaries [85]. Dealing with uniaxial fatigue behaviour, the research usually finds that the fatigue life is higher for specimens built in the horizontal orientation than for the specimens built in the vertical orientation[62, 86, 56]. The surface roughness and morphology are also dependent on the build orientations. Typically, down-skin surfaces display higher surface roughness than up-skin surfaces. The valleys in the surface roughness profile act as stress risers, making them prone to fatigue initiation. Due to this, the main trend is that when the directional fatigue behaviour is assessed with an as-built surface, fatigue initiates from the down-skin region and not the up-skin region.

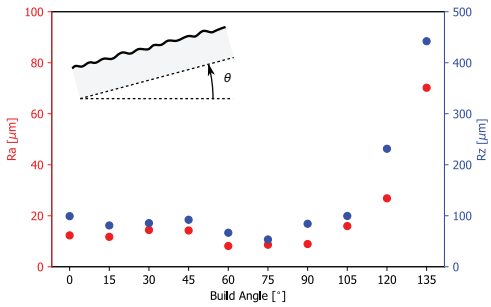

Figure 2.28: Surface roughness Ra and Rz compared for each of the investigated build orientations.

In article VII, the directional fatigue behaviour of PBF-LB/18Ni300 was studied. To evaluate the fatigue behaviour from up-skin surfaces, a new test methodology was proposed where all sides were machined expect one. In that way, fatigue was guided to initiate from the only present AB surface. Specimens of 18Ni300 were built in 10 different orientations. The surface roughness conditions are shows in Fig. 2.28, and shows that the surface roughness is constant from 0 to 90 and increases as the surface is progressively facing downward. The majority of the specimens were tested at the same load, which corresponded to 500 MPa, the data results are shown in Fig. 2.29, where Fig. 2.29a shows the fatigue data presented in a S-N diagram compared to data from the literature. The directional fatigue behaviour of 18Ni300 was also studied by Meneghetti et al. [86] and Damon et al. [87], finding that specimens built

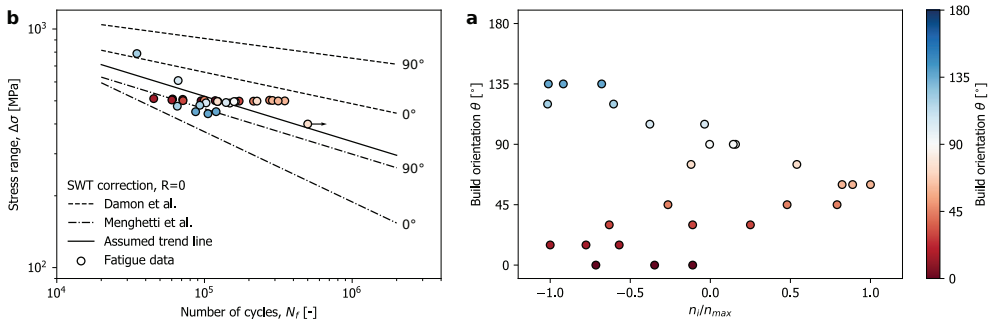

Figure 2.29: Directional fatigue behaviour of AM 18Ni300. (a) The fatigue data compared to experimental data from the literature Meneghetti et al.[86] and Damon et al.[87] (b) Fatigue life parameter n_i/n_{max} compared to the build angle.

vertically had higher fatigue life than specimens built horizontally. The fatigue results presented here coincides with the data from the literature. As the specimens were machined and one surface was left in the AB condition, some variations in the cross-sectional area were observed, this resulted in variations in the nominal stress level of the specimens (which was supposed to be constant for the comparison). To take this into account, an assumed trend line of the fatigue data was created based on the trend lines of the fatigue data from the literature, further, the deviation from this new trend line to each data point was evaluated. Fig. 2.29b shows a comparison of the build angle and the normalized deviation from the assumed trend line n_i/n_{max}. Fig. 2.29b shows that similar to the results by Meneghetti et al. [86] and Damon et al. [87], the specimens close to the horizontal orientation (0°) have the lowest fatigue life, while it is decreasing as it is approaching the vertical state. The highest fatigue life is found for the specimens in the 60°-orientation, which also displayed the lowest surface roughness. After 60°, the fatigue decreases until the 135° orientation. Based on these observations it seems like that the microstructure favours the vertical orientation, but that the surface roughness decreases the fatigue life. The effect of the surface roughness can be observed by comparing the corresponding build orientations, e.g. 135° and 45°, 120° and 60°, and 75° and 105°. In all these cases, the down-skin specimens display lower fatigue life than the up-skin.

Chapter 3

Fatigue assessment

In this chapter, different approaches for making fatigue predictions of AM metals are presented. First, some general considerations are given, then different methods and models are presented and applied to the experimental data obtained in the project.

3.1 Some general considerations

Fig. 3.1 highlights some of the main challenges regarding fatigue assessment of AM parts. First, the part is printed with a given orientation. Based on the geometry and the AM method, the thermal history of the part is determined and defects based on the process will be present. During the use of the part (Fig. 3.1b) boundary conditions and loads are applied resulting in a global stress state. This global stress state is accompanied by local effects (Fig. 3.1c and d). Two extremes can be identified; the as-built state and the fully post-processed state. In the AB state, features such as pores, LoFs and surface defects can be present. In the PP state, the defects in the AB state have been removed, and a lower amount of local effects are present.

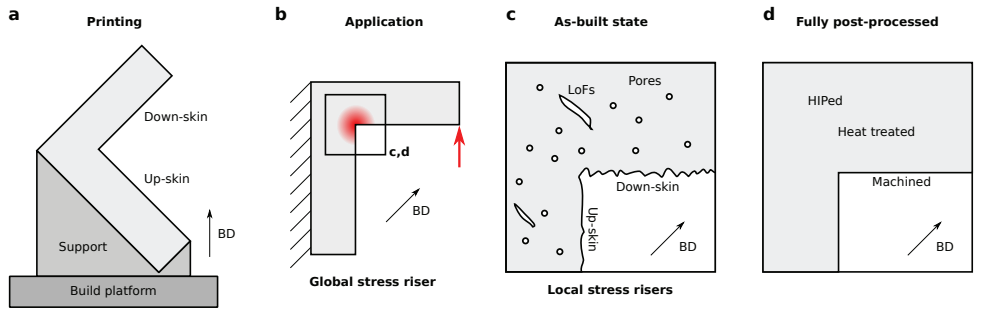

Figure 3.1: Illustration of factors to take into account when making fatigue assessment of AM parts. (a) Printing and orientation, (b) Loading and boundary conditions result in a global stress state, (c) Local effects in the as-built state, (d) (lack of) local effects in the fully post-processed state. BD indicates the build direction.

When making fatigue assessment of AM metals it is clear that many factors are at interest, some of these are:

- Complex stress states (in e.g. topology optimized, internal or other complex structures)
- Surface roughness effects

- Pores
- Lack of Fusion defects (LoF)
- Microstructural factors (such as anisotropy or weak phases)

There are many factors that *may* influence the fatigue behaviour, however, fatigue is a weakest link mechanism and to be pragmatic when making assessments only the main influencing factors should be taken into account.

Dealing with fatigue assessments, several approaches can be done. The selected fatigue assessment method needs to be chosen based a what features that are likely to influence the fatigue behaviour. As mentioned above, different factors can be taken into account by using different approaches. Many of the factors influencing the fatigue act local and can be tackled by a local fatigue assessment approach, in such case, it might also be beneficial to assist it with a global approach. Many local approaches for the fatigue assessment of AM metals are based on LEFM, where defects and cracks are taken into account on a local level. Here one of the challenges is to determined which degree of accuracy the geometric factors needs to be taken into account at. Some models are developed for analytical calculations but can be implemented in Finite Element (FE) codes.

3.2 Theory of Critical Distances

The Theory of Critical Distances (TCD) is a local approach for evaluating fatigue failure. Local approaches are based on the idea that the stresses surrounding a geometric discontinuity (i.e. notch, pore or crack) are locally higher than the nominal stress that results in failure. The first proposal of a local approach for evaluating failure was Neuber's concept of elementary structural volume and microstructural support length [88, 89]. TCD states that failure occurs when the stress at a certain distance or averaged over a certain distance/area/volume reaches a critical value failure initiates [90]. Fig. 3.2 shows graphical interpretations of the line and point method formulations of TCD. The line method can be expressed as

$$\Delta\sigma_{eff} = \frac{1}{L}\int_0^L \Delta\sigma_I(\theta = 0, r)dr = \Delta\sigma_0. \tag{3.1}$$

Where $\Delta\sigma_{eff}$ is the range of the effective stress calculated by TCD, $L/2$ is the critical distance of the material, $\Delta\sigma_I$ is the principal stress component, θ is the angular deviation from the notch bi-sector line, r is the distance and $\Delta\sigma_0$ is the fatigue limit. The stress ahead of the notch root is averaged over a certain length, L, so that the effective stress is equal to the fatigue limit. The point method is similar, but here the stress is evaluated in one point at $L/2$.

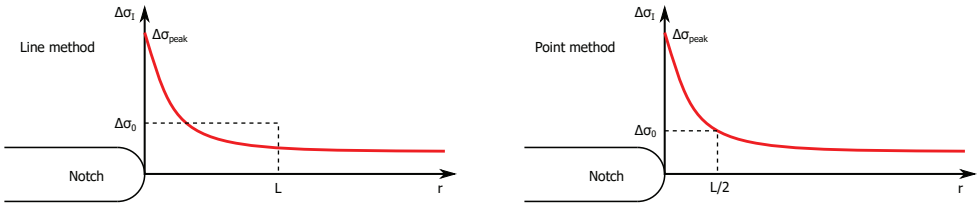

Figure 3.2: Definition of TCD; line method and point method

In Article IV a trial was done to check if TCD could be applied to a cross-section, obtained by OM, for predicting the failure location. The set-up of the FEA is shown in Fig. 3.3. The geometry from the OM in Fig 2.18 and 2.20 was imported to the FEA software and the boundary conditions were set on

the global dimensions of the specimens. From the contour plots, the maximum stress is located at the defect from which fatigue is initiating. The stress fields from the FEA are showed in Fig. 3.4. From the defect, mode I and mode II stress singularities were found (3.4a), while from the notch root, a stress concentration was found (3.4b). Fig 3.4c shows a comparison of the tangential stress components from both the notch and the defect. The stress components are shown along with the critical distance ($L/2$) of Inconel 718 has previously been reported to be 77μm by Louks and Susmel [91]. The results showed that the stress from the defect was higher than from the notch at a distance of about 10μ from the tip. At the critical distance, the stress from the notch was higher than the stress from the defect. To confirm that this was that case also for other orientations around the notch/defect root, the tangential stress component was plotted along circular a path located at $r = L/2$. Also in this case, the stress from the notch was found to be of higher magnitude than the stress from the defects.

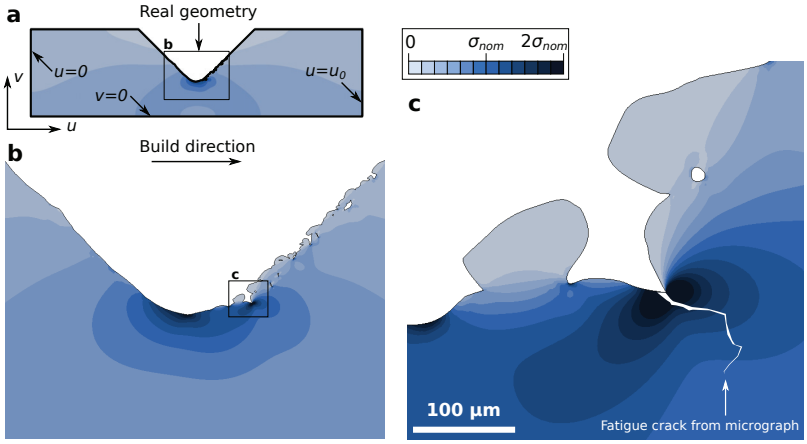

Figure 3.3: FEA of local defect within the "real" notch geometry. (a) Set-up in Abaqus, (b) Stress distribution and (c) stress field at the defect root with the fatigue crack overlayed.

Based on the result from the FEA, the fatigue crack should have initiated from the notch root and not from the defect. There could be several reasons for this. It is possible that the value of critical distance used is not representative for the AM material. The selected cross-section might not be representative for the full specimen. This could be the case if sharper or larger defects were present close by. Another possibility could be the 3D-effects (resulting in stress triaxiality), which were not taken into account. In study by Vayssette et al. [92] 3D-effects were taken into account when using TCD for fatigue life predictions of AM Ti-6Al-4V.

One of the main advantages of using TCD in FEA is that it tackles the challenges regarding the evaluation of stress singularities. Fatigue usually initiates at stress risers, stress concentrations with a finite value can easily be evaluated. However, in the case of sharp notches producing stress singularities (in linear elastic material models), it might be difficult to evaluate what is critical and what is not critical. With TCD these problems can be avoided. Some of the challenges with TCD is that the designer needs to use the correct $L/2$ value and a geometry that is representative of the component evaluated.

3.3 Strain Energy Density

The strain energy density (SED) is a similar approach to TCD. Rather than evaluating the stress, the average strain energy density is evaluated over a fixed distance/area/volume [93]. The first proposal of strain energy as a failure criterion was by Beltrami in 1885 [94]. Further, Sih proposed, for cracks,

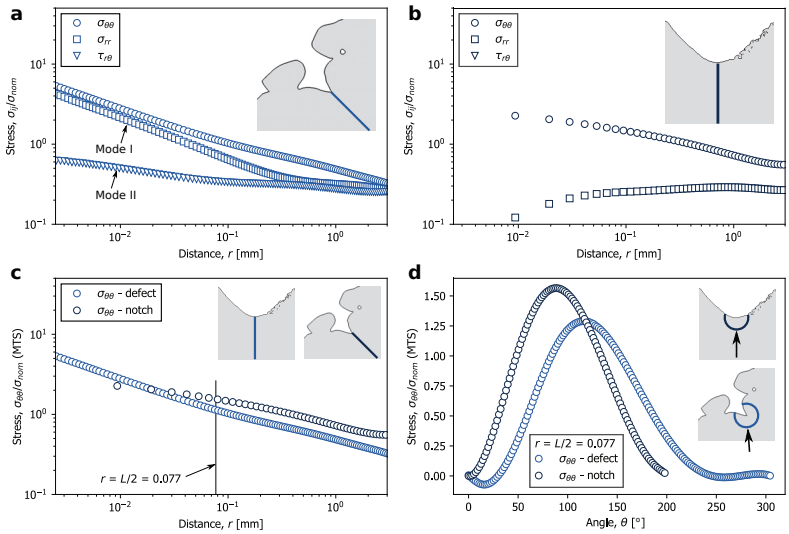

Figure 3.4: Stress fields from FEA. (a) Stress components ahead of the defect, (b) Stress components ahead of the notch, (c) comparison of the tangential stress components of the notch and the defect and (d) Tangential stress component around the notch and defect roots.

to evaluate a parameter dependent on the strain energy density and a critical distance from the crack tip singularity [95], where crack propagation would occur if the value of SED were equal to the critical value for the material. The theory was further extended to notches, using a reference point at the notch surface, where the tangential stress component has the maximum value. The SED failure criterion was refined and formulated in [96].

SED proposed by Lazzarin and Zambardi [93] evaluate SED in a defined control volume surrounding the notch tip. The criterion states that failure occurs when the mean value of SED, $\bar{W}$, in the control volume is equal to the critical value of energy for the material, W_c. In the case of static loading for a plain specimen, failure is evaluated by use of the ultimate tensile strength, σ_{uts}, and Young's modulus, E, of the material

$$W_c = \frac{\sigma_{uts}^2}{2E}. \tag{3.2}$$

One of the main advantages with SED is that when it is applied in an FEA, it does not have a sensitivity to the mesh size, contrary to stress-based approaches [97]. However, it is required that the mesh can represent the geometry it is supposed to represent. The definition of the control volume is shown in Fig. 3.5, where R_0 is the radius of the control volume (similar to L in TCD) and r_0 is determining the centre of the circle defining the control volume for blunt notches. r_0 is defined by Lazzarin and Tovo in Ref. [98].

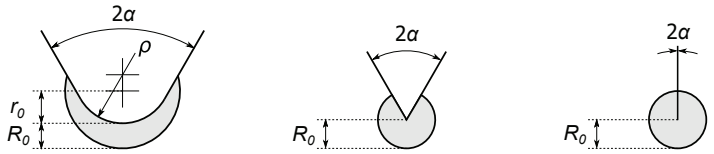

Figure 3.5: Definition of SED control volume for blunt notch, sharp notch and crack.

In Article II, SED was employed to collect the fatigue life curves of the different notch geometries

into one unified fatigue life curve. The SED was calculated based on FEA analysis of the different input specimen geometries, i.e. the defects and particularities of the AM process were not taken into account (like was done in the previous section on TCD). After the FEA of each specimen geometry using a unit load, the stress levels from the fatigue data in Fig. 2.11 was scaled with the corresponding SED value. Fig. 3.6 shows the unified fatigue life curve of the data.

From Fig. 2.17 it was shown that the defects and the fatigue life were correlated. In addition to this it was shown that the failure locations were not in the notch roots, but determined by a combination of the defects and the notch acuities (Sec. 2.7). In particular, the semi-circular specimens failed far away for the notch root. From the SED results, the semi-circular data does not completely coincide with the others, this could be caused by the fact that the failure locations were away from the notch roots. The SED method captures the main trends but does not take into account the variations in the defect sizes.

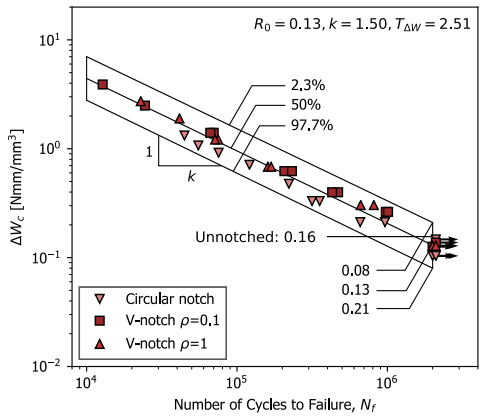

Figure 3.6: Unified SED curve for different notch geometries by AM Inconel 718.

One of the main advantages with SED when dealing with AM could be that it is insensitive to the mesh size. When performing FEA on complex geometries (e.g. designed by topology optimization) where the stresses are evaluated refined mesh is required and large computational effort would be required. By using SED, courser mesh can be used and these models would require less computational efforts. One of the shortcomings of the SED method is that the current definition of the control volume is only valid for notches with a constant radius. In addition to this, if the method were to be used locally on the real defects, a fine mesh would be needed in order to capture the geometric features, and the method would no longer be mesh independent.

3.4 Murakami-method

As AM metallic materials usually contain defects at some scale, the $\sqrt{area}$-model proposed by Murakami, has been proven useful for fatigue life correlations [99, 100, 101, 102]. The method is based on the assumption that the SIF produced by a defect can be estimated by taking the square root of the effective defect size projected onto the plane normal to the loading direction. The SIF can be expressed as

$$K = Y\sigma\sqrt{\pi\sqrt{area}}, \tag{3.3}$$

further, the fatigue limit σ_w can be estimated by using the Vicker's Hardness of the material

$$\sigma_w = Y\frac{(HV + 120)}{\sqrt{area}^{1/6}}. \tag{3.4}$$

In Article V, the $\sqrt{area}$-method was applied to AB AM Inconel 718 specimens with different heat treatments and notch geometries. One set of specimens were tested in the AB state and the other

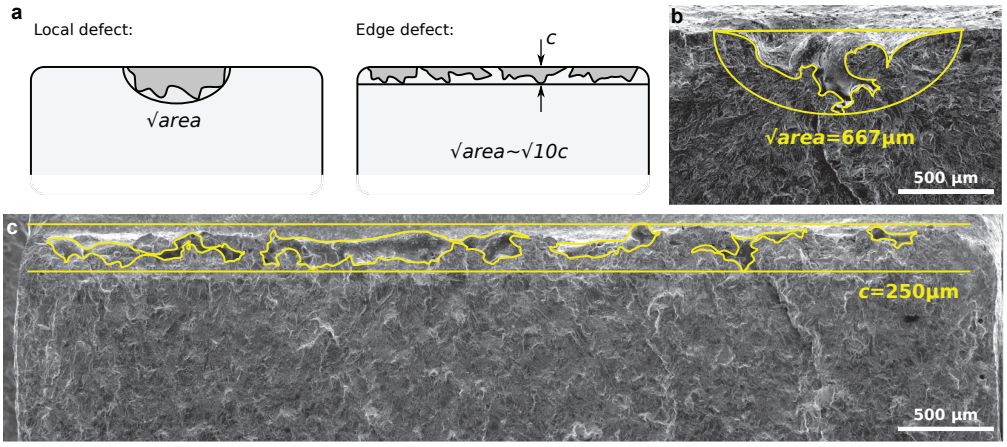

Figure 3.7: Defects captured by SEM from fracture surfaces used to predict the fatigue behaviour by the Murakami method

was tested in the HT state. In the AB state, the hardness was HV 300 while after HT the hardness increased to HV 500, correspondingly, the HT specimens displayed higher fatigue strength. Fig. 3.7b and c shows examples of fracture surfaces used for predicting the fatigue life. Fig. 3.7b and c, shows a typical defect and the effective defect area for the unnotched and notched specimens respectively. In the unnotched specimens, local defects were found, while in the notched specimens, defects were found along the thickness of the specimens.

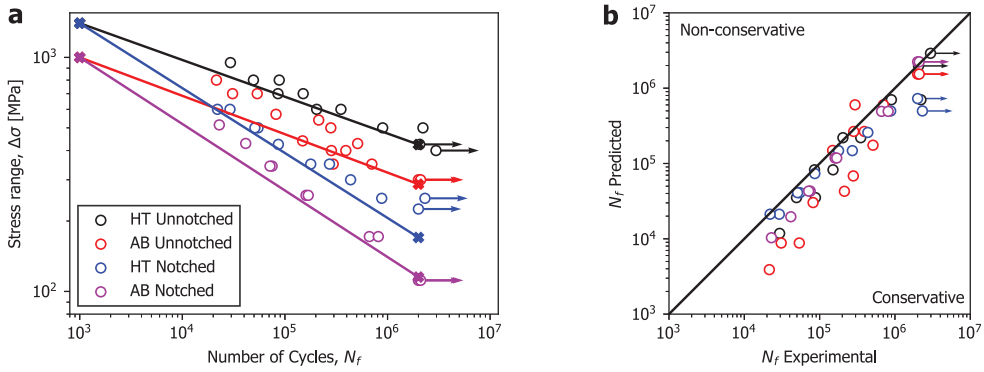

Figure 3.8: Fatigue life predictions using the Murakami method using hardness, defects size and tensile strength.

Since two different defect types were found, different geometry factors, Y, had to be applied in the predictions. The stress concentrations of the two different specimen geometries were included in the predictions, along with the mean stress effect. In addition to predicting the fatigue limit, the tensile strengths of the two different materials were used for predicting the full fatigue life curves. In Sec. 2.8.1, it was shown that the tensile strength was equal to the QS strength at $\sim 10^3$ cycles for both unnotched and notched specimens. The fatigue data and the predicted fatigue behaviour are shown in Fig. 3.8a. Further, a comparison of the experimental number of cycles and the predicted number of cycles are shown in Fig. 3.8b. The general conclusion is that the predictions are conservative when comparing with the

experimental data. It should be noted that the defect size for each specimen was not taken into account, but only one specimen for each case. It is expected that the scatter in the data would be decreased if the defect sizes for all the specimens were taken into account as a clear correlation was found between the defect sizes and the fatigue life in the AB specimens in Fig. 3.4.

3.5 Kitagawa-Takahashi diagram

The Kitagawa-Takahashi diagram [103] introduced in 1976 has recently gained popularity in the literature dealing with the fatigue of AM alloys [99, 100, 101, 102]. The diagram evaluates the influence of small defects on the fatigue limit of a material. In the diagram, the defect size is plotted versus the fatigue limit/strength of a material. Naturally, there is a correlation between the defect size and the fatigue life; larger defects gives shorter fatigue life and vice verse. The diagram also shows an effect from the fatigue crack growth behaviour of metals; as discussed in Sec. 2.3: a certain value of SIF needs to be reached for fatigue cracks to initiate. This means that for defects below the threshold defect/crack size, the fatigue strength/limit is not influenced.

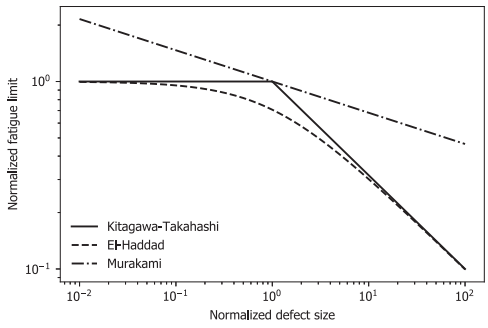

Figure 3.9: Comparison of the Kitagawa-Takahasi, El-Haddad and Murakami models for fatigue strength predictions.

Fig. 3.9 shows the Kitagawa-Takahashi diagram with different trend lines; Kitagawa-Takahashi, El-Haddad and Murakami. The Kitagawa-Takahashi solution (to the diagram) predicts that the fatigue life is unaffected by defects smaller than a critical size. The El-Haddad solution is based on the idea of a critical defect size, very similar to what Kitagawa and Takahasi proposed. The El-Haddad method predicts the fatigue strength, $\Delta\sigma_w$, as a correction to the fatigue strength free of defects, $\Delta\sigma_e$, by comparing the defect size, l, to the critical defect size, l_0. The fatigue strength is then given by:

$$\Delta\sigma_w = \Delta\sigma_e \sqrt{\frac{l_0}{l + l_0}}. \tag{3.5}$$

Further, the critical defect size can be estimated by

$$l_0 = \left(\frac{\Delta K_{th}}{Y \Delta\sigma_e}\right)^2 \frac{1}{\pi}. \tag{3.6}$$

Where Y is a geometry factor and ΔK_{th} is the threshold value for fatigue crack growth.

In Fig. 3.9, The three different models are shown and the defect/crack size and the fatigue strength is taken as a normalized value. From the comparison, El-Haddad and Kitagawa-Takahasi coincide, while the Murakami approach does not include a threshold defect size.

3.6 A simple method for obtaining Kitagawa-Takahasi diagrams

To demonstrate the use of the Kitagawa-Takahashi diagram, the fatigue data from the AB unnotched Inconel 718 was used. In Fig. 2.19 this set of fatigue data showed a correlation between the positions in

the confidence bands and the defect sizes. This is the same as the Kitagawa-Takahashi diagram if the position within the confidence bands is considered as the stress. To make this more in line with the general use of the diagram, the fatigue data points were interpolated onto the run-out limit $N_f = 2 \times 10^6$. The fatigue data and the interpolation is demonstrated in Fig. 3.10a. The interpolation is done by calculating the intersecting Basquin curve (using the same slope of the regression curve) for all the data points by first finding

$$A_i = \frac{\Delta\sigma_i}{N_i^B}, \tag{3.7}$$

where A_i is the vertical shift of the curve, fitted to each data point σ_i and N_i. Further, the interpolated fatigue limit is calculated by

$$\Delta\sigma_{wi} = A_i N_w^B = \Delta\sigma_i \left(\frac{N_w}{N_i}\right)^B \tag{3.8}$$

where N_w is the run-out limit. The results are shown in Fig. 3.10b plotted along with the El-Haddad solution modified by Beretta and Romano [101] which is defined as

$$\Delta\sigma_w = \Delta\sigma_e \sqrt{\frac{\sqrt{area}_0}{\sqrt{area} + \sqrt{area}_0}}. \tag{3.9}$$

Where $\sqrt{area}_0$ is the critical defect size. Here $\sqrt{area}_0$ was taken as 80μm, as this is similar to the values obtained by Sheridan et al. [99], who also obtained Kitagawa-Takahashi diagrams for AM Inconel 718.

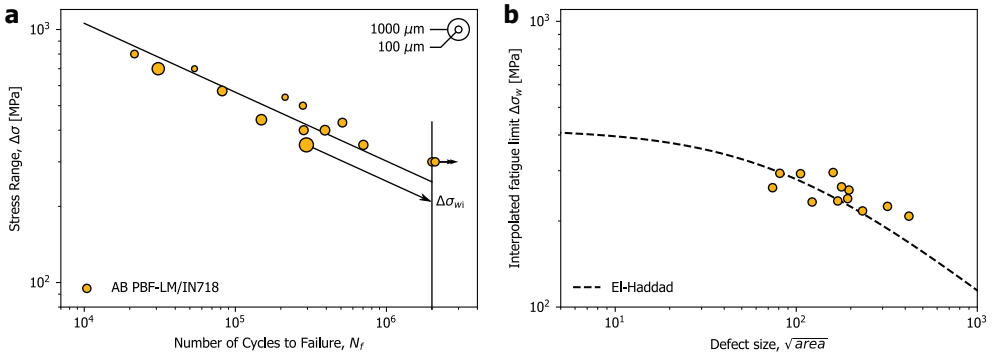

Figure 3.10: Application of Kitagawa-Takahashi diagram. (a) interpolation of AB unnotched Inconel 718 fatigue data (b) experimental data in the Kitagawa-Takahashi diagram

This method of generating Kitagawa-Takahashi diagrams allows to simply use the standard fatigue life data in combination with fractographic analyses. This is less time consuming than searching for the fatigue limit and then finding the critical defects in these specimens. One of the main challenges with this method was highlighted by Sheridan et al. and also discussed in Article III and Article VI: The defect sizes might be correlated with the load level. Why? because at higher loads there is a tendency that neighbouring defects act together, and appear as one on the fracture surface. This can be the case if two LoFs are in planes above each other, and both are overlapping in the fractography (This might be the case for the 316L specimens in Fig. 2.25b-d).

3.7 A diagram for capturing and predicting failure locations

Based on the observations made regarding the failure locations in the AB Inconel 718 specimens in Fig. 2.19, a diagram for correlating the failure locations to the notch geometries was proposed. The proposal of the diagram is shown in Fig. 3.11. The diagram correlates the notch acuity to the failure locations

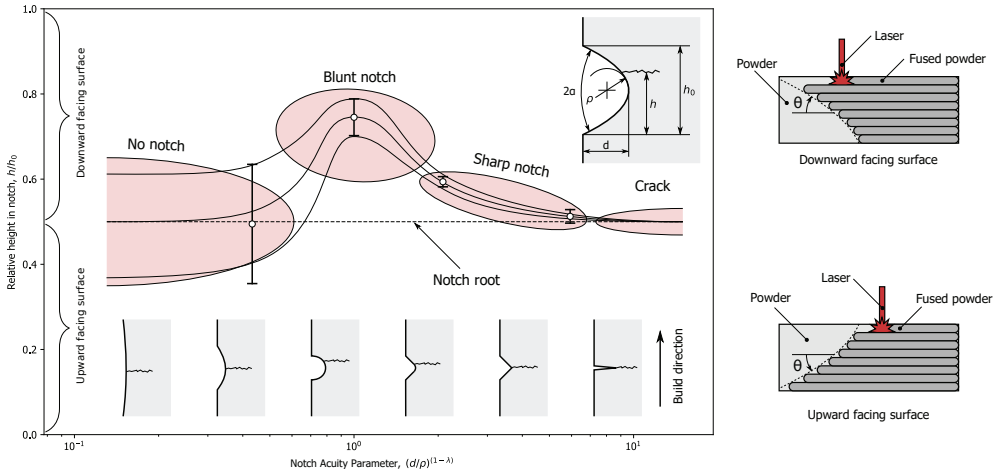

Figure 3.11: Proposal of diagram for capturing and predicting the failure locations within notch geometries

according to the trends described in the previous section. The diagram shows that for an unnotched geometry the failure location is on average occurring at the centre of the specimen (i.e. the smallest cross-section) with a large scatter. The failure locations are determined by the location of the critical defects, and the scatter in the locations of the defects are causing the scatter. For a blunt notch, the down-skin surface displays a high surface roughness and surface defects, due to this, the failure locations are located in this region. As the notch acuity is increased, the failure locations are shifted towards the notch roots and the scatter is decreased. Here, the notch and the surface roughens/defects are competing in initiating the fatigue cracks. For a sharp notch or a crack, the failure occurs at the notch root, and the surface roughness is no longer influencing the failure location.

The diagram evaluates the notch acuity versus the failure locations. The notch acuity is defined as

$$\xi = \frac{d}{\rho}^{1-\lambda} . \tag{3.10}$$

Where d is the notch depth, ρ is the notch radius and λ is a parameter given by the notch opening angle. λ is one of the parameters used in the analytical models describing elastic stress fields adjacent to notches proposed by Tovo and Lazzarin [98].

Based on the proposed diagram in Fig. 3.11, an analytical framework was proposed for capturing and predicting the trends in the failure locations in various notches. The proposal of the analytical framework is shown in Fig. 3.12a and b and displays three trend lines: H_a, H_l and H_u, describing the average location and the lower and upper locations based on the statistics. The formulation reads:

$$H_a = H_0 + Ae^{-B(\xi+C)^2} \tag{3.11}$$

$$H_u = H_0 + Ae^{-B(\xi+C)^2} + De^{-E\xi} \tag{3.12}$$

$$H_l = H_0 + Ae^{-B(\xi+C)^2} - De^{-E\xi} \tag{3.13}$$

Where, ξ is the notch acuity, H_0 is the notch root location and A, B, C, D and E are fitting parameters. The model is fitted with the experimental data in Fig. 3.13.

The diagram can be used for displaying experimental data or as a tool for understanding which are the dominating factors influencing the failure locations. In the case of AM, the diagram could also be used for specimens with different orientations, this is shown in Fig. 3.14a and b. In the case of vertically built specimens, the failure locations would be as above, while for horizontally built specimens (Fig.

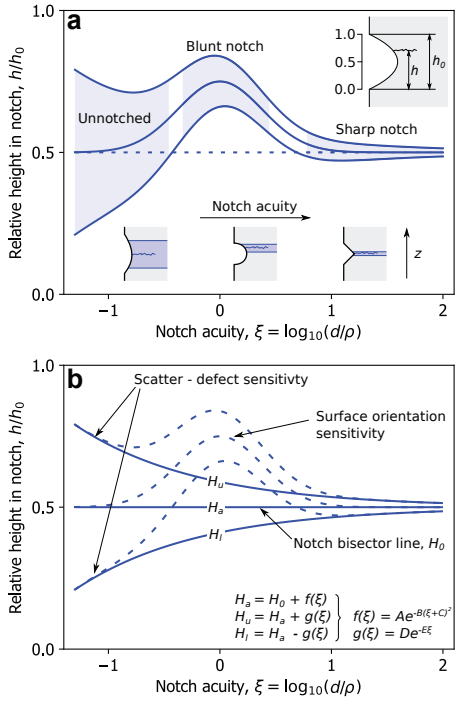

Figure 3.12: A diagram for capturing and predicting the failure locations in AM compoents

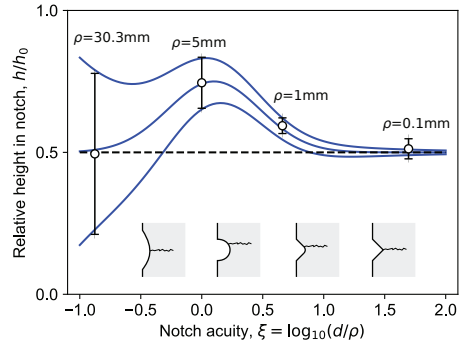

Figure 3.13: Proposed analytical framework for the diagram fitted with experimental data.

3.14b), the maximum surface roughness would coincide with the notch root and probably the failure locations would always have the average value in the notch roots. The diagram could also be used to compare fatigue failure to static failure (a similar approach was done in sec. 2.8.1), this is shown in Fig. 3.14c and d. Failure from static loading occurs with less scatter than fatigue failure as it is less sensitive to defects and more sensitive to the main dimensions of the specimens. Another application of the diagram can be mixed-mode loading. Fig. 3.14e and f shows the location of the maximum stress, σ_{max}, in mode I (in-plane tension) and mode II (in-plane shear) loading of a notch. For mode I loading, the maximum stress is always located at the notch root, while in mode II loading the maximum stress is not located in to notch root. However, as the notch radius tends to zero, the peak stress approaches the centre of the notch.

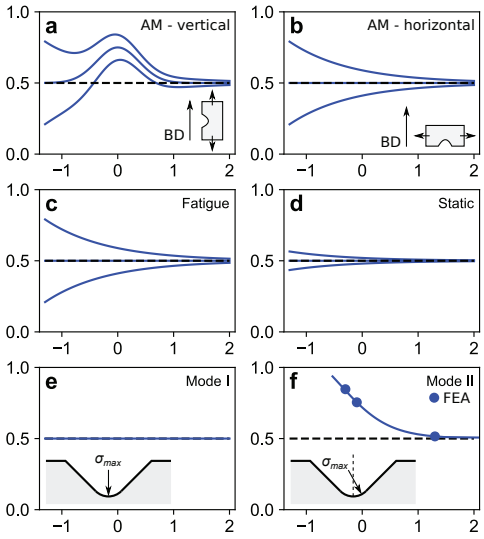

Figure 3.14: Different applications of the diagram for capturing failure locations.

3.8 Other approaches

There are of course many other approaches to fatigue assessment and predictions than those shown in the previous sections. Some of the approaches to fatigue predictions of AM metals that are different to those presented here are probabilistic approaches [104], multiscale approaches [105, 106] and cyclic plasticity models approaches [107].

Chapter 4

Design

In the previous chapters we saw how the AM metals are performing under fatigue loading and how to correlate the properties to the features responsible for the variations in the fatigue life. The next question to be answered is how parts should be designed, and more importantly; why should a part be produced by AM?

4.1 Advantages with AM

The wide variety of advantages in AM are usually stated in research articles dealing with AM. For companies, the transfer to AM is likely connected to getting increased value and/or reducing costs. This section aims to review some of the main advantages and business models in AM. Extensive research is not only done dealing with the technical aspects of AM but also the business models have been studied[108, 109, 110, 111, 2]. Table 4.1 gives an overview of the advantages and their applications in AM, according to Attaran [111]. Attaran proposes five key benefits with AM; quality, cost, speed, innovation and impact [111].

Savolainen et al. [110] states that there are three main business areas in additive manufacturing; rapid prototyping, rapid tooling and rapid manufacturing. Dealing with metals, AM enables a cost-efficient way to produce parts that are usually expensive to produce by conventional methods. It is difficult to replace high volume production lines, however, it can support high volume production by replacing less frequently demanded parts. In addition to this, they state that the adaption to AM is slower where it cannibalizes other business area and it can compete with the conventional manufacturing methods only if it is overall cost-efficient.

Holzman et al. propose two main business models for the players in the AM industry: "Low-cost online" and "technology expert" [108]. The low-cost online player mainly aims toward low-cost production using extrusion-based polymer printers for prototyping and similar applications. Most of the players in this category are "born digitally" and does not have a past from other manufacturing methods. The technology expert player has a different approach to AM. These players usually print a wider range of materials, including metals and are working more closely with research institutions such as universities. They aim for high quality in the printed parts and the most frequent revenue is selling printing systems.

Bourell [2] gives a comparison of the cost related to producing AM parts and injection moulded parts; an adapted figure is shown in Fig. 4.1. The predictions show that the cost of producing AM parts are constant for both low and high volumes, for injection moulded parts the cost per part is high for low volumes but decreases until a stable level for high volume production. This indicates that AM is favourable compared to injection moulding for low production series. The influence of increasing the part complexity of the part was also predicted, indicated by the horizontal arrow. The predictions state that part with higher complexity are more expensive in low volumes, but the same stable cost can be achieved

Application	Advantages
Rapid Prototyping	○ Reduce time to market by accelerating prototyping ○ Reduce the cost involved in product development ○ Making companies more efficient and competitive at innovation
Production of Spare Parts	○ Reduce repair times ○ Reduce labor cost ○ Avoid costly warehousing
Small Volume Manufacturing	○ Small batches can be produced cost-efficiently ○ Eliminate the investment in tooling
Customized Unique Items	○ Enable mass customization at low cost ○ Quick production of exact and customized replacement parts on site ○ Eliminate penalty for redesign
Very Complex Work Pieces	○ Produce very complex work pieces at low cost
Machine Tool Manufacturing	○ Reduce labor cost ○ Avoid costly warehousing ○ Enables mass customization at low cost
Rapid Manufacturing	○ Directly manufacturing finished components ○ Relatively inexpensive production of small numbers of parts
Component Manufacturing	○ Enable mass customization at low cost ○ Improve quality ○ Shorten supply chain ○ Reduce the cost involved in development ○ Help eliminate excess parts
On Site and On-Demand Manufacturing of Customized Replacement Parts	○ Eliminate storage and transportation costs ○ Save money by preventing downtimes ○ Reduces repair costs considerably ○ Shorten supply chain ○ The need for large inventory is reduced ○ Allow product lifecycle leverage
Rapid Repair	○ Significant reduction in repair time ○ Opportunity to modify repaired components to the latest design

Table 4.1: Advantages and applications in AM, as stated by Attran [111]

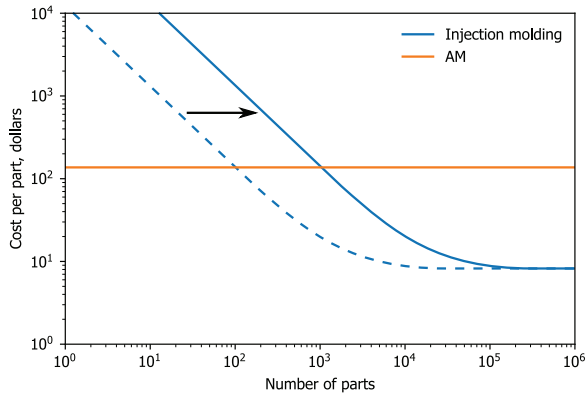

Figure 4.1: Predicted cost difference between AM and injection moulded parts by Mourell. The arrow indicate the shift in the cost when increasing the part complexity.

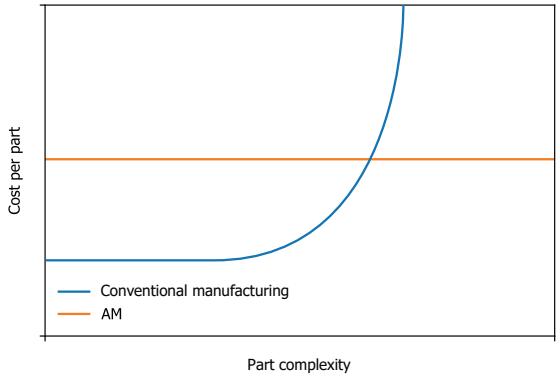

Figure 4.2: Correlation between the cost and part complexity when comparing conventional to AM.

for high volume production. One of the advantages with AM is that there are almost no limitations in terms of part complexity, the same is not the case for conventional manufacturing methods.

Fig. 4.2 shows a comparison of the part complexity and cost per part for AM and conventional manufacturing. Based on the predictions of Bourell [2] a constant cost per part can be achieved for injection moulding when reaching high production series. In AM, the cost per part can be assumed to be constant regardless of the part complexity. However, when increasing the complexity beyond a certain level, the cost is expected to increase for conventional manufacturing method until reaching an asymptote. Beyond this asymptote, it is not only more cost-efficient to produce by AM, but it is also the only possible manufacturing method.

Figs. 4.1 and 4.2 shows that in terms of cost, AM would be beneficial for low production volumes and high geometric complexity in the parts.

4.2 Conventional fatigue design

There are several established methods for fatigue design. The most common approaches are [112]:

- Infinite-life design
- Safe-life design
- Fail-safe design
- Damage-tolerant design

The infinite fatigue design approach is the most conservative approach. Here the aim is to design parts that will never fail due to fatigue, in this case, the service loads of the part should be below the fatigue/endurance limit of the material. This approach may not be economical. In safe-life design, the parts are designed for finite fatigue life. This can be done based on stress-life, strain-life of crack growth models, here a margin for scatter in the fatigue data should be considered. The fail-safe approach is based on the idea that the system does not fail if the part fails. This approach accepts that failure occurs, and benefit from having it occur in a controlled manner. The damage-tolerant design approach accepts that damage is accumulating in parts during fatigue loading. Here, the parts are monitored during service and stresses in the plastic regime can be accepted.

In order to improve the fatigue life of parts, some simple design principles can be applied [113, 114]. Some of the most common recommendations are to avoid stress concentrations, as these act as fatigue initiation sites. Know the material properties and the sensitivity to fatigue (e.g. materials of higher

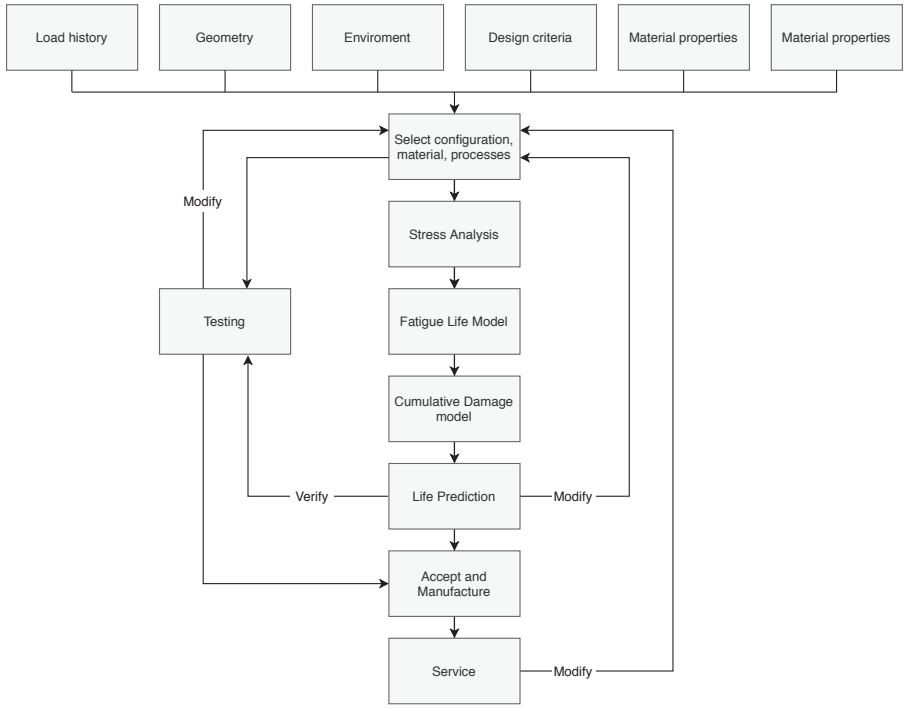

Figure 4.3: Fatigue design procedure proposed by Fatemi [112]

strength and hardness are more sensitive to stress concentrations see Fig. 2.9). Design according to established design codes and have unambiguous constructions to be certain of the load cases.

A methodology for fatigue design is shown in Fig. 4.3. In the methodology, properties such as load history, geometry (i.e. part design), design criteria and so on are first considered. Then follows an analysis part where the different input properties are considered, a fatigue life models are chosen and the fatigue life is predicted. Further, testing is done to verify the predictions and based on the test results, the design is updated. This process is repeated until the design is accepted, manufactured and put in service. Based on the performance of the part during service, the processes can be revised again.

4.3 Design tools and current methodologies for AM

Wiberg et al. [115] has categorized the design for AM in three main categories:

- System design
- Part design
- Process design

System design deals with what and why something should be manufactured. Here the focus is set on the components boundaries. The main focus is set on defining whether a part is suitable for AM or not. Part design is the actual design of the parts. In part design, the geometrical aspects and determining if the geometric features of a parts are suitable for AM. Process design is about optimizing the AM process. Here, the process parameters and post processing steps and sequence is in focus for optimizing the process. Based on these observations, Wiberg et al. proposed a methodology for designing for AM, the methodology is reproduced in Fig. 4.4.

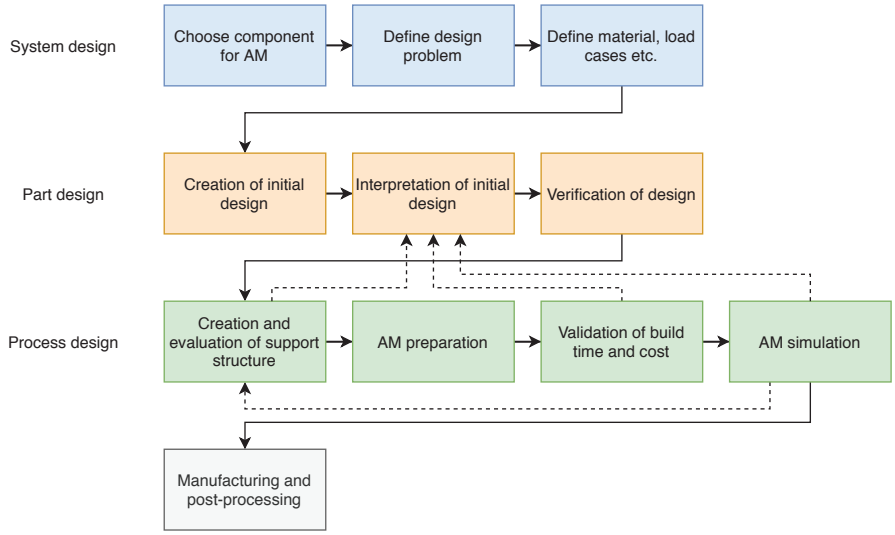

Figure 4.4: Design for AM process proposed by Wiberg et al.

System design is further divided into three processes. First, a component must be chosen for AM, in order to do this, manufacturing methods should be reviewed. Guidance of good part candidates for AM is described in Refs. [116, 117, 118]. Further, the design problem should be defined, this can be done by challenging the initial product boundaries [119, 120] by e.g. combining several parts into one [121]. The last step in system design is to determine the material and load cases of the component. The load cases can be determined by traditional approaches for the design of mechanical components [122, 123] or by tailored schemes for AM [124]. Also when it comes to the material selection, traditional approaches can be done [125], however, as made clear previous in this thesis, the behaviour of AM materials can deviate from their conventionally manufactured counterparts, and material selection methodologies created for AM can be used [126].

The part design is also divided into three steps. First, the initial design is created. Here Wiberg et al. propose that "To take full advantage of the manufacturing technology it is important to think outside the box and not get stuck on conventional design thoughts. For structural components, topology optimization is recommended.". Based on the advantages coupled with the different applications in table 4.1, it is clear that topology optimization might not always be the best choice, this will be further discussed in Sec. 4.4. In some cases, topology optimization of structures is a good way to reduce the material usage and optimize the stiffness of a part [18, 19]. Topology optimization is usually done by inputting the component boundary conditions in a software, further, the software removes all material that does not contribute to supporting the boundary conditions. Parts can be optimized for different criteria such as stiffness, maximum allowed stresses, mass and so on. After the design is created it should be interpreted and evaluated, this can be done according to different design recommendations, where e.g. part orientation, down-skin sections and placement of support structures can be evaluated [127, 128, 129]. Then, the design can be verified by different software. The software and the verifications criteria should be defined based on the expected use of the component. Typical approaches would be FEA or computational fluid dynamics.

The process design is divided into four steps. After the part design is done and verified, support structures can be generated [130, 131], along with part orientation and print strategy. Further, the build file can be prepared and validated, this can be done by simulations in an appropriate software. The simulations can be done at different levels, in some cases, rough estimates of the time and cost are

needed [132] while in other cases, more thorough investigations of the specifics of the manufacturing process are needed [133]. Based on the findings of the process design steps, the part design can be updated. After these steps, the part can be produced.

4.4 Proposal of three main design categories for structural applications

There are many advantages and new possibilities with AM. However, it is clear that several of the advantages can not be combined. E.g. it is not possible to do near-to-net shape manufacturing (where machining is intended) while also manufacturing complex geometries with internal structures while also operating with short lead time. Dealing with structural components, three main approaches to AM are proposed here; cost reduction (high end), cost reduction (low end) and geometric complex parts.

(i) **Cost reduction (High-end):** By producing components near-to-net shape, the material-usage can be optimized. In this approach, AM is used for *e.g.* reducing the amount of machining required in a conventionally manufactured part. Here, the goal is to remove all critical defects and features from the AM process, so that designers do not have to deal with the fact that AM materials have reduced mechanical performance. This means that parts can be produced by high strength materials such as Ti6Al4V or Inconel 718 without wearing out the tools and minimizing material usage. In this category, very high quality is the goal. Hence quality control is key in all stages of the manufacturing process, and process monitoring methods are very relevant. Due to the high quality in these parts, they aim to replace components of high criticality.

(ii) **Cost reduction (Low-end):** Standard components are produced by AM for optimizing, e.g. the supply chain process. Here standard CAD models can be used for printing, and the parts are expected to have a short life. The amounts of post-processing are reduced to the minimum for saving both time and money. The components are usually designed for temporally replacing components; defects can be allowed due to the low fatigue life expected. However, these components cannot be of very high criticality for the system they are placed into.

(iii) **Geometric complexity:** A very high degree of geometric complexity can be achieved by the AM processes. Topology optimization can be utilized for optimizing stiffness-weight ratios, including internal structures. In this approach, post-processing such as machining the surface for removing defects is restricted, and the designers will have to deal with the defects. In these components, there are likely to be several notched regions, resulting in components where it is hard to define the critical regions.

To get a visual interpretation of different approaches in the three different part categories, a diagram was created with two axes: Part complexity and quality improvement by post-processing, the diagram is shown in Fig. 4.5. The maximum "component quality" curve defines the manufacturing space one can operate in AM. Here it should be noted that the term "component quality" can be interpreted many different ways, dealing with fatigue, it would e.g. be natural to link this term to a combination of the largest defect present in the part and some other material parameters influencing the fatigue behaviour (such as the hardness). For low part complexity, it is possible to fully machine the whole component and apply any desired post-processing method for increasing the performance of the part. Contrary, when dealing with parts of high geometric complexity machining and other post-processing routines might be impossible to apply. In addition to this, when approaching the resolution of the printer, the dimensional tolerances have larger deviations (in per cent) than for large sections. This means that designers could be forced to accept lower mechanical performance for highly geometric parts.

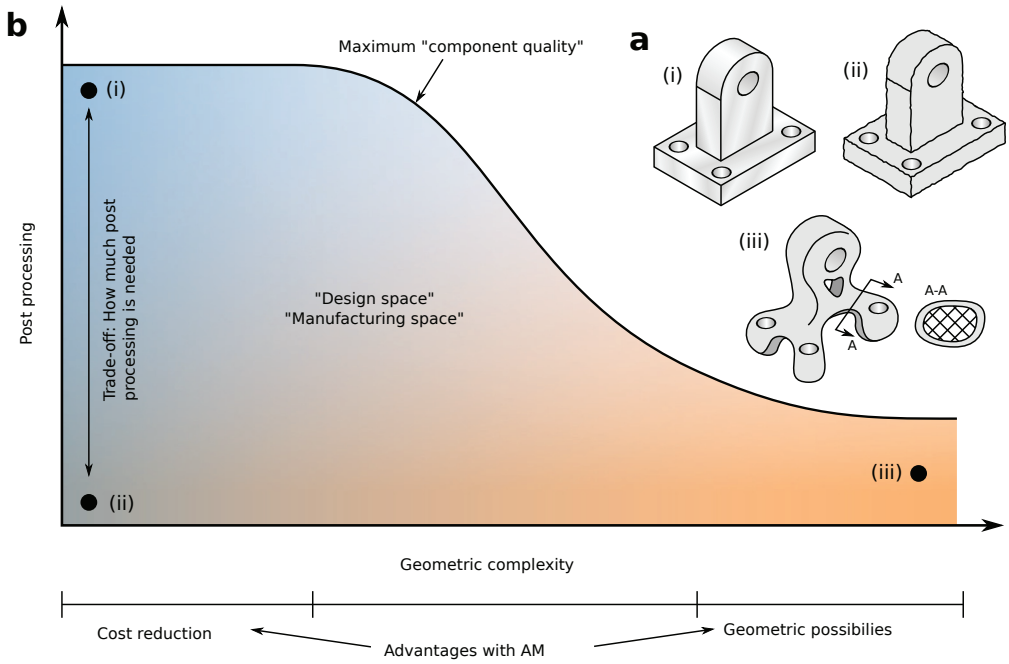

Figure 4.5: Identifying three main design categories in AM

4.5 Part categories and fatigue considerations

Several different approaches to fatigue assessment have been described in Sec. 3. Based on the different design philosophies from Fig. 4.5, different fatigue assessment methods can be employed.

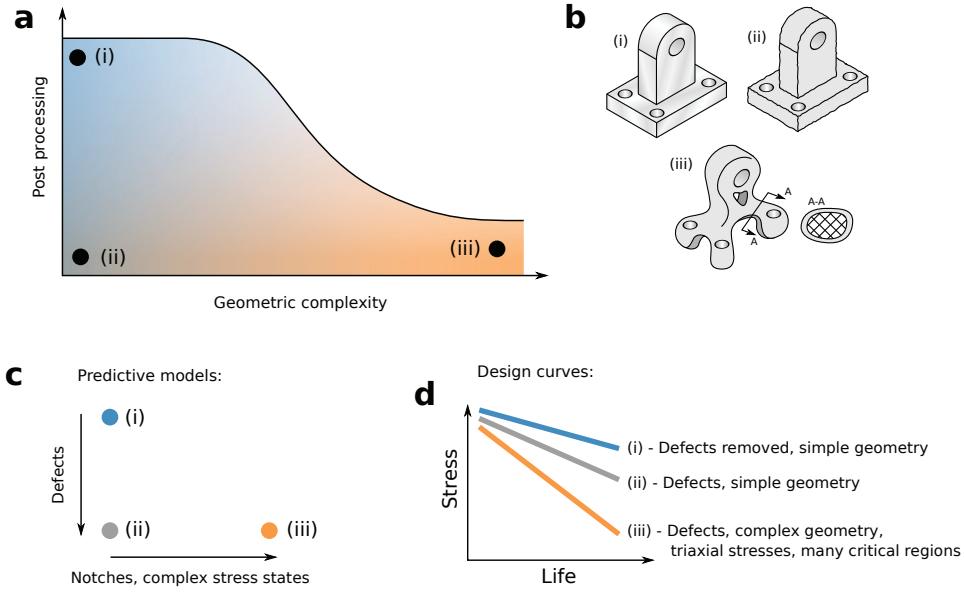

Figure 4.6: Fatigue assessment of the three different part categories

Fig. 4.6 shows some perspectives on fatigue assessment and the part categories. In (i), the aim is to have no defects, here there is, of course, a change of the presence of defects, but models based on microstructural features will likely be important for predictions. In addition to this, the part geometry needs to be considered. For these components, it is likely easy to determine the critical section. In the case of (ii), the defects will play a more dominant role. Here it is likely that the defects acting locally will influence the results. In the case of (iii), defects and complex geometries (resulting in complex or triaxial stress states) needs to be taken into account. If these parts are designed by topology optimization, the material utilization can be expected to be at a similar degree over large parts of the components. This would mean that it can be difficult to determine the critical sections.

It is clear that (i) has superior fatigue performance when comparing to (ii) or (iii), but there are also other factors to be taken into account when designing against fatigue. One of these factors is the confidence in the properties. In general, what is desired when designing a structure against fatigue is:

- High performance e.g. high strength and long life
- High confidence in the performance e.g what is the certainty that the part will endure a given load for a given time

This means that not only do we desire good properties, but we also properties we can count on (or monitor). Dealing with components of category (iii), the AB surface will be present, in addition to geometric configurations. The AB surface is likely to have a (high) roughness and probably defects. If the manufacturing conditions are consistent, defects may be present, but the variations in them might be small. This would result in low scatter in the fatigue behaviour. Contrary, when dealing with category (i), the aim is to remove all defects to have the highest possible material quality. Here, it is crucial to remove all the defects, as one large defect may cause the same damage in a category (i) part as a category (iii) part.

A similar effect to what would be the difference due to post-processing can be observed when increasing the geometric complexity. Going from (ii) to (iii), parts are likely to contain notched and down-skin regions. By comparing the fatigue data from Article II (Fig. 2.11), where the unnotched specimens displayed larger variations in defect sizes and failure locations had high scatter in the fatigue life compared to the notched specimens which had low variations in the defects sizes and failure locations. The fatigue data and the scatter is compared in Fig. 4.7. From the fatigue life curves, it would be easier to accurately predict the fatigue life of the notched specimens (representing (ii)) than the unnotched specimens (representing (iii)).

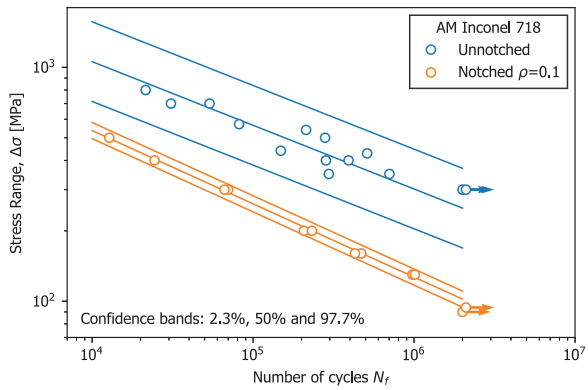

Figure 4.7: Difference in scatter of AB unnotched and notched Inconel 718 specimens.

At first glance, (iii) seems hopeless; defects, low fatigue resistance, complex geometry and so on. However, it might not be hopeless if it is possible to achieve high confidence in the quality. Contrary,

(i) seems like the only possible way of producing an AM part at first, however, it is not sure that the material can be utilized to its full potential due to the probability large scatter in the fatigue data.

Based on the observations above, it is tempting to propose an implementation of "weak-spots" in the part designs. Such spots could make both predictions and inspections of the parts more simple. The implementation of weak-spot or design for failure is already implemented in many industries and can be the idea behind fail-safe designs. In AM it would be the opposite approach to topology optimization, where the aim, in many cases, is to have the same degree of material utilization all over a component.

When it comes to using experimental data from testing for designing there are several approaches. Some of them could be:

- Using experimental data from the literature
- Testing coupons from a build with the same process parameters
- Testing coupons from the same build as the produced part
- Sacrificially testing coupons from the parts
- Testing the actual part

The amount of testing desired for having the right confidence level in the final part can be determined by the criticality level of the part. The criticality level of the can be determined by e.g. the consequence of failure and can be divided in to e.g. low, medium and high criticality.

A similar effect to what would be the difference due to post-processing can be observed when increasing the geometric complexity. Going from (ii) to (iii), parts are likely to contain notched and down-skin regions. By comparing the fatigue data from Article II (Fig. 2.11), where the unnotched specimens displayed larger variations in defect sizes and failure locations had high scatter in the fatigue life compared to the notched specimens which had low variations in the defects sizes and failure locations. The fatigue data and the scatter is compared in Fig. 4.7. From the fatigue life curves, it would be easier to accurately predict the fatigue life of the notched specimens (representing (ii)) than the unnotched specimens (representing (iii)).

4.6 Fatigue design framework

In Sec. 4.3 a framework for designing AM parts were presented. In this section, the framework proposed by Wiberg et al. for design of AM parts is modified to also including necessary steps for designing parts for fatigue applications [134]. This include the generating and use of experimental data. The updated framework is shown in Fig. 4.8.

The modified methodology in Fig. 4.8 includes testing for generating experimental data and fatigue assessment. The idea is to follow the procedure of Wiberg et al. and then input fatigue predictions in the design stage, initially this can be done based on e.g. experimental data from the literature. Further, the experimental data can also be used as input in the process design. After the part is designed, and ready for production, testing can be done; either by test coupons or by sacrificial testing. These results can further be used for fatigue life predictions for updates of the design until satisfactory results are achieved. This is of course only a simplified rout of sketching the process, and for the fatigue assessment, the steps described in Fig. 4.3 can be used.

For different design part categories and criticality levels, different approaches to fatigue design can be done. The different criticality levels can be dealt with by defining a required amount of testing and predictions. For a part with low criticality, the use of experimental data from literature or testing test coupons from the same build parameter might be sufficient coupled with some fatigue life predictions. For parts of medium criticality, more thoroughly testing might be desired, coupled with predictions.

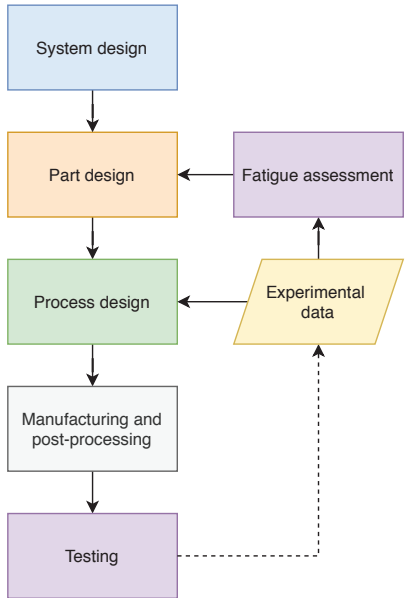

Figure 4.8: Design AM process proposed by Wiberg et al. modified for fatigue considerations

For parts of high criticality sacrificial or full-scale testing might be desired. In that case, simulations might be excessive. It should also be noted that since AM is a new production method, low amount of confidence is put in the components and the predictive models, due to this extensive testing might be required from the end-user. It is important to keep in mind that the aim of including the testing steps is to gain high confidence in the behaviour of the materials. The higher criticality level a component has, the higher confidence is required in the properties and perhaps also "higher properties".

4.7 Recommendations for fatigue design of AM components

Some general guidance points when designing for AM:

- Determine the reason and which advantages to be utilized when moving to AM.
- Determined the fatigue design approach: infinite-life, safe-life, fail-safe or damage-tolerant design.
- Determine the criticality level of the component. This can be decided based on e.g. the application and consequence of failure.
- Determine the required testing scope. This can be decided on e.g. the required confidence level.
- Determined the critical section(s) of the part. Here, both global and local considerations should be taken into account and the critical defect size in the critical section can be determined.
- Decide on fatigue prediction model and approach. This can be done based on the part category; AB parts should be dealt with differently than machined parts.

Chapter 5

Conclusion and outlook

In this thesis, aspects of the fatigue behaviour, assessment and design of AM metallic components have been investigated. In the experimental part, three different alloys were investigated; Inconel 718, 316L and 18Ni300 by using different specimens with different post-processing methods.

5.1 Conclusions

The conclusions can be dived into three main categories following the structure of the thesis, experimental, assessment and design.

The following conclusions are given regarding the experimental results:

- The fatigue behaviour of Inconel 718, 316L and 18Ni300 has been investigated. All the materials were found to have inferior fatigue strengths when comparing to their wrought counterparts.
- Defects deriving from the manufacturing process were found to decrease the fatigue performance. In all fracture surfaces investigated, geometric defects were found at the fatigue initiation site. The fatigue life was found to be correlated with the defect sizes and morphologies, meaning that removing the defects will enhance the fatigue strength.
- The surface roughness of surfaces built down-skin were found to be higher than the surface built up-skin. This resulted in decreased performance of specimens which had down-skin surface in their critical sections. Further, for the notch geometries, fatigue did not initiate from designed notch roots, but from defects in the down-skin region close to the notch roots.
- A method of testing the fatigue behaviour of both up- and down-skin surfaces has been proposed. By machining all sides of test specimens except one, the effect of the surface roughness of different surfaces was evaluated.

The following conclusions are given regarding fatigue models and predictions:

- Fatigue life predictive models based on LEFM and small cracks are popular in AM and can be used for correlating fatigue life and the defects deriving from the manufacturing process. In this thesis, concepts such as TCD, SED, $\sqrt{area}$ have been used for fatigue assessment.
- The concept of SED was used for creating unified fatigue life curves for various notch geometries based on the nominal geometries. The local effects were not considered.
- A local approach to fatigue assessment was done by using TCD. Here the stress fields from a notch region with the real geometry from micrographs were analysed. A refined mesh was required for the analysis and it was determined that a 2D-model is not sufficient for fully describing the local stress fields.

- A modified version of the Murakami method was proposed for giving simple estimates of the fatigue life curves of notched and unnotched specimens.
- The Kitagawa-Takahashi diagram is popular in AM and can be used to determine the critical defect size in a material. In this work, fatigue data for Inconel 718 were transferred into the form of a Kitagawa-Takahasi diagram by a simple interpolation procedure.
- An analytical model for capturing and predicting failure locations was proposed. The failure locations are presented in a diagram based on experimental data of Inconel 718 where specimens did not fail from the notch roots.

The following conclusions are given regarding fatigue design:

- Three main AM part categories for structural applications have been identified. The different part categories utilize different advantages in AM; complex geometries and intricate designs, near-net-shape parts for cost reductions and high material quality and low-lead-time parts where parts of lower quality can be accepted if they are delivered fast.
- In order to design parts to endure fatigue applications it is important to know the purpose of the AM part and have a clear strategy in the fatigue design.
- The design and manufacturing process can be optimized for increasing the resistance to fatigue, experimental testing should be done to gain confidence in the performance of the materials.
- The fatigue life predictive models used for the part design should be decided based on the design strategy of the part. Making fatigue life predictions of a complex part with AB surface is different from a machined part with a simple geometry which is fully post-processed.

5.2 Recommendations for future works

Since this study has limitations in both the time frame and the scope, some recommendations for further works are given:

- In this work, mainly the effects of the AB surface have been investigated, in further studies, the effect of machined surfaces should be investigated. Both with and without internal defects present. When the internal defects are present, the interaction between the global and local geometric effects might play an important role.
- If no defects are present the global geometry and the microstructure will be key to understanding and giving good predictions of the fatigue behaviour. Here, the directional fatigue behaviour and the residual stresses are some of the topics that deserve further investigations.
- Fatigue life prediction methods should be based on the design approach and it should be differentiated between different defect types and morphologies. It is likely that the same models will not be used for machined and AB surfaces. Further understanding of which models that should be used for different applications should be investigated.
- To understand the role and different approaches to fatigue design, real applications and case studies should be carried out. The final aim is of course real and reliable fatigue-resistant components, and different knowledge will derive for a case study than from specimens in a controlled lab.

Bibliography

[1] J. J. Beaman, D. L. Bourell, C. C. Seepersad, D. Kovar, Additive Manufacturing Review: Early Past to Current Practice, Journal of Manufacturing Science and Engineering 142 (11), 110812.

[2] D. L. Bourell, Perspectives on additive manufacturing, Annual Review of Materials Research 46 (1) (2016) 1–18.

[3] C. B. Williams, F. Mistree, D. Rosen, A Functional Classification Framework for the Conceptual Design of Layered Manufacturing Technologies, International Design Engineering Technical Conferences and Computers and Information in Engineering Conference (2008) 35–48.

[4] S. Mirzababaei, S. Pasebani, A review on binder jet additive manufacturing of 316l stainless steel, Journal of Manufacturing and Materials Processing 3 (2019) 82.

[5] ASTM, Standard terminology for additive manufacturing—general principles. part 1: Terminology.

[6] N. A. Chartrain, C. B. Williams, A. R. Whittington, A review on fabricating tissue scaffolds using vat photopolymerization, Acta Biomaterialia 74 (2018) 90–111.

[7] Z. Liu, Y. Wang, B. Wu, C. Cui, G. Yu, C. Yan, A critical review of fused deposition modeling 3d printing technology in manufacturing polylactic acid parts, The International Journal of Advanced Manufacturing Technology 102.

[8] Y. L. Yap, C. Wang, S. L. Sing, V. Dikshit, W. Y. Yeong, J. Wei, Material jetting additive manufacturing: An experimental study using designed metrological benchmarks, Precision Engineering 50 (2017) 275–285.

[9] W. E. King, A. T. Anderson, R. M. Ferencz, N. E. Hodge, C. Kamath, S. A. Khairallah, A. M. Rubenchik, Laser powder bed fusion additive manufacturing of metals; physics, computational, and materials challenges, Applied Physics Reviews 2 (4) (2015) 041304.

[10] M. Ziaee, N. B. Crane, Binder jetting: A review of process, materials, and methods, Additive Manufacturing 28 (2019) 781–801.

[11] A. Singh, S. Kapil, M. Das, A comprehensive review of the methods and mechanisms for powder feedstock handling in directed energy deposition, Additive Manufacturing 35 (2020) 101388.

[12] B. G. Mekonnen, G. Bright, A. Walker, A study on state of the art technology of laminated object manufacturing (lom), in: D. K. Mandal, C. S. Syan (Eds.), CAD/CAM, Robotics and Factories of the Future, Springer India, New Delhi, 2016, pp. 207–216.

[13] K. G. Prashanth, S. Scudino, T. Maity, J. Das, J. Eckert, Is the energy density a reliable parameter for materials synthesis by selective laser melting?, Materials Research Letters 5 (6) (2017) 386–390.

[14] J. Robinson, I. Ashton, P. Fox, E. Jones, C. Sutcliffe, Determination of the effect of scan strategy on residual stress in laser powder bed fusion additive manufacturing, Additive Manufacturing 23 (2018) 13 – 24.

[15] D. Ramos, F. Belblidia, J. Sienz, New scanning strategy to reduce warpage in additive manufacturing, Additive Manufacturing 28 (2019) 554 – 564.

[16] R. Mertens, S. Clijsters, K. Kempen, J.-P. Kruth, Optimization of scan strategies in selective laser melting of aluminum parts with downfacing areas, Journal of Manufacturing Science and Engineering 136.

[17] H. Ali, H. Ghadbeigi, K. Mumtaz, Effect of scanning strategies on residual stress and mechanical properties of selective laser melted ti6al4v, Materials Science and Engineering: A 712 (2018) 175 – 187.

[18] Y. Saadlaoui, J.-L. Milan, J.-M. Rossi, P. Chabrand, Topology optimization and additive manufacturing: Comparison of conception methods using industrial codes, Journal of Manufacturing Systems 43 (2017) 178 – 186.

[19] J. ZHU, H. ZHOU, C. WANG, L. ZHOU, S. YUAN, W. ZHANG, A review of topology optimization for additive manufacturing: Status and challenges, Chinese Journal of Aeronautics.

[20] T. Childerhouse, M. Jackson, Near net shape manufacture of titanium alloy components from powder and wire: A review of state-of-the-art process routes, Metals 9 (2019) 689.

[21] R. P. REED, The economic effects of fracture in the united states, Washington, D.C., U.S. Dept. of Commerce, National Bureau of Standards.

[22] United states (usa) gdp - gross domestic product.
URL `https://countryeconomy.com/gdp/usa?year=1982`

[23] Wikimedia commons, norsk oljemuseum, alexander l kielland and edda.
URL `https://https://upload.wikimedia.org/wikipedia/commons/4/4b/Alexander_L_Kielland_and_Edda_2-7C_NOMF-02663-1-650.jpg`

[24] W. Schutz, A history of fatigue, Engineering Fracture Mechanics 54 (2) (1996) 263 – 300.

[25] M. Matsuichi, T. Endo, Fatigue of metals subjected to varying stress, Japan Society of Mechanical Engineers.

[26] P. Paris, F. Erdogan, A critical analysis of crack propagation laws, Journal of Basic Engineering 85 (1963) 528–533.

[27] C. Haskins, Systems engineering analyzed, synthesized, and applied to sustainable industrial park development, Doctoral Thesis NTNU.

[28] D. Greitemeier, C. D. Donne, F. Syassen, J. Eufinger, T. Melz, Effect of surface roughness on fatigue performance of additive manufactured ti–6al–4v, Materials Science and Technology 32 (7) (2016) 629–634.

[29] A. Triantaphyllou, C. L. Giusca, G. D. Macaulay, F. Roerig, M. Hoebel, R. K. Leach, B. Tomita, K. A. Milne, Surface texture measurement for additive manufacturing, Surface Topography: Metrology and Properties 3 (2) (2015) 024002.

[30] A. Sola, A. Nouri, Microstructural porosity in additive manufacturing: The formation and detection of pores in metal parts fabricated by powder bed fusion, Journal of Advanced Manufacturing and Processing 1 (3) (2019) e10021.

[31] T. Mukherjee, T. DebRoy, Mitigation of lack of fusion defects in powder bed fusion additive manufacturing, Journal of Manufacturing Processes 36 (2018) 442 – 449.

[32] C. Zhao, N. D. Parab, X. Li, K. Fezzaa, W. Tan, A. D. Rollett, T. Sun, Critical instability at moving keyhole tip generates porosity in laser melting, Science 370 (6520) (2020) 1080–1086.

[33] M. Saunders, X marks the spot - find ideal process parameters for your metal am parts, www.reinshaw.com.

[34] D. Herzog, V. Seyda, E. Wycisk, C. Emmelmann, Additive manufacturing of metals, Acta Materialia 117 (2016) 371 – 392.

[35] T. Hamre, Exploring the modeling and strength prediction of additively manufactured materials; numerical and analytical approaches, NTNU Mater Thesis.

[36] J. J. Lewandowski, M. Seifi, Metal additive manufacturing: A review of mechanical properties, Annual Review of Materials Research 46 (1) (2016) 151–186.

[37] S. Gorsse, C. Hutchinson, M. Gouné, R. Banerjee, Additive manufacturing of metals: a brief review of the characteristic microstructures and properties of steels, ti-6al-4v and high-entropy alloys, Science and Technology of Advanced Materials 18 (1) (2017) 584–610.

[38] J. Luo, X. Jia, R. Gu, P. Zhou, J. Sun, M. Yan, 316l stainless steel manufactured by selective laser melting and its biocompatibility with or without hydroxyapatite coating, Metals 8 (2018) 548.

[39] N. Haghdadi, M. Laleh, M. Moyle, S. Primig, Additive manufacturing of steels: a review of achievements and challenges, Journal of Materials Science 56 (2021) 548.

[40] P. Nezhadfar, R. Shrestha, N. Phan, N. Shamsaei, Fatigue behavior of additively manufactured 17-4 ph stainless steel: Synergistic effects of surface roughness and heat treatment, International Journal of Fatigue 124 (2019) 188 – 204.

[41] D. F. C. S. T. S. Sean Dobson, Swathi Vunnam, Powder variation and mechanical properties for slm 17-4 ph stainless steel, Solid Freeform Fabrication 2019: Proceedings of the 30th Annual International (2019) 478– 493.

[42] T. LEBRUN, K. TANIGAKI, K. HORIKAWA, H. KOBAYASHI, Strain rate sensitivity and mechanical anisotropy of selective laser melted 17-4 ph stainless steel, Mechanical Engineering Journal 1 (5) (2014) SMM0049–SMM0049.

[43] Asm arerospace spesification materials inc, special metals inconel® alloy 718.

[44] Asm arerospace spesification materials inc, titanium ti-6al-4v (grade 5), annealed.

[45] Asm arerospace spesification materials inc, aisi type 316l stainless steel, annealed bar.

[46] K. Kempen, L. Thijs, J. Humbeeck, J.-P. Kruth, Mechanical properties of alsi10mg produced by selective laser melting, Physics Procedia 39 (2012) 439–446.

[47] Z. Li, P. K G, Y. Deng, D. Raabe, C. Tasan, Metastable high-entropy dual-phase alloys overcome the strength-ductility trade-off, Nature.

[48] N. Kawagoishi, Q. Chen, H. Nisitani, Fatigue strength of inconel 718 at elevated temperatures, Fatigue & Fracture of Engineering Materials & Structures 23 (3) 209–216.

[49] Q. Chen, N. Kawagoishi, H. Nisitani, Evaluation of notched fatigue strength at elevated temperature by linear notch mechanics, International Journal of Fatigue 21 (9) (1999) 925 – 931.

[50] A. Yadollahi, N. Shamsaei, Additive manufacturing of fatigue resistant materials: Challenges and opportunities, International Journal of Fatigue 98 (2017) 14 – 31.

[51] K. Solberg, F. Berto, Notch-defect interaction in additively manufactured inconel 718, International Journal of Fatigue 122 (2019) 35 – 45.

[52] D. Wells, Overview of fatigue and damage tolerance performance of powder bed fusion alloy n07718, Tech. rep., NASA (2016).

[53] P. J. Golden, R. John, W. J. Porter, Investigation of variability in fatigue crack nucleation and propagation in alpha+beta ti-6al-4v, Procedia Engineering 2 (1) (2010) 1839 – 1847, fatigue 2010.

[54] R. K. Nalla, R. O. Ritchie, B. L. Boyce, J. P. Campbell, J. O. Peters, Influence of microstructure on high-cycle fatigue of ti-6al-4v: Bimodal vs. lamellar structures, Metallurgical and Materials Transactions A 33 (3) (2002) 899–918.

[55] J. Pegues, M. Roach, R. S. Williamson, N. Shamsaei, Surface roughness effects on the fatigue strength of additively manufactured ti-6al-4v, International Journal of Fatigue 116 (2018) 543 – 552.

[56] P. Edwards, M. Ramulu, Fatigue performance evaluation of selective laser melted ti–6al–4v, Materials Science and Engineering: A 598 (2014) 327 – 337.

[57] S. Razavi, P. Ferro, F. Berto, J. Torgersen, Fatigue strength of blunt v-notched specimens produced by selective laser melting of ti-6al-4v, Theoretical and Applied Fracture Mechanics 97 (2018) 376 – 384.

[58] M. Kahlin, H. Ansell, J. Moverare, Fatigue behaviour of notched additive manufactured ti6al4v with as-built surfaces, International Journal of Fatigue 101 (2017) 51 – 60.

[59] E. Brandl, C. Leyens, F. Palm, Mechanical properties of additive manufactured ti-6al-4v using wire and powder based processes, IOP Conference Series: Materials Science and Engineering 26 (2011) 012004.

[60] H. Huang, Z. Wang, J. Lu, K. Lu, Fatigue behaviors of aisi 316l stainless steel with a gradient nanostructured surface layer, Acta Materialia 87 (2015) 150 – 160.

[61] T. Roland, D. Retraint, K. Lu, J. Lu, Fatigue life improvement through surface nanostructuring of stainless steel by means of surface mechanical attrition treatment, Scripta Materialia 54 (11) (2006) 1949 – 1954.

[62] T. M. Mower, M. J. Long, Mechanical behavior of additive manufactured, powder-bed laser-fused materials, Materials Science and Engineering: A 651 (2016) 198 – 213.

[63] C. Elangeswaran, A. Cutolo, G. K. Muralidharan, C. de Formanoir, F. Berto, K. Vanmeensel, B. V. Hooreweder, Effect of post-treatments on the fatigue behaviour of 316l stainless steel manufactured by laser powder bed fusion, International Journal of Fatigue 123 (2019) 31 – 39.

[64] H. A. Leybold, Axial-load fatigue tests on 17-7 ph stainless steel under constant-amplitude loading.

[65] A stressstrain function for the fatigue of metals, Journal of Materials 5 (4).

[66] S. McKelvey, A. Fatemi, Surface finish effect on fatigue behavior of forged steel, International Journal of Fatigue 36 (1) (2012) 130 – 145.

[67] E. Hearn, Chapter 10 - contact stress, residual stress and stress concentrations, in: E. Hearn (Ed.), Mechanics of Materials 2 (Third Edition), third edition Edition, Butterworth-Heinemann, Oxford, 1997, pp. 381 – 442.

[68] E. Chlebus, K. Gruber, B. Kuźnicka, J. Kurzac, T. Kurzynowski, Effect of heat treatment on the microstructure and mechanical properties of inconel 718 processed by selective laser melting, Materials Science and Engineering: A 639 (2015) 647 – 655.

[69] D. Zhang, W. Niu, X. Cao, Z. Liu, Effect of standard heat treatment on the microstructure and mechanical properties of selective laser melting manufactured inconel 718 superalloy, Materials Science and Engineering: A 644 (2015) 32 – 40.

[70] Y. Murakami, 4 - effect of size and geometry of small defects on the fatigue limit, in: Y. Murakami (Ed.), Metal Fatigue (Second Edition), second edition Edition, Academic Press, 2019, pp. 39 – 59.

[71] Y. Hu, S. Wu, P. Withers, J. Zhang, H. Bao, Y. Fu, G. Kang, The effect of manufacturing defects on the fatigue life of selective laser melted ti-6al-4v structures, Materials & Design 192 (2020) 108708.

[72] S. Tammas-Williams, P. Withers, I. Todd, P. Prangnell, The influence of porosity on fatigue crack initiation in additively manufactured titanium components, Scientific Reports 7 (2017) 7308.

[73] P. Nezhadfar, A. S. Johnson, N. Shamsaei, Fatigue behavior and microstructural evolution of additively manufactured inconel 718 under cyclic loading at elevated temperature, International Journal of Fatigue 136 (2020) 105598.

[74] D. L. Prakash], M. Walsh, D. Maclachlan, A. Korsunsky, Crack growth micro-mechanisms in the in718 alloy under the combined influence of fatigue, creep and oxidation, International Journal of Fatigue 31 (11) (2009) 1966 – 1977, fatigue Damage of Structural Materials VII.

[75] D. Zheng, A. Rosenberger, H. Ghonem, Influence of prestraining on high temperature, low frequency fatigue crack growth in superalloys, Materials Science and Engineering: A 161 (1) (1993) 13 – 21.

[76] M. Leary, M. Mazur, H. Williams, E. Yang, A. Alghamdi, B. Lozanovski, X. Zhang, D. Shidid, L. Farahbod-Sternahl, G. Witt, I. Kelbassa, P. Choong, M. Qian, M. Brandt, Inconel 625 lattice structures manufactured by selective laser melting (slm): Mechanical properties, deformation and failure modes, Materials & Design 157 (2018) 179 – 199.

[77] T. Persenot, A. Burr, R. Dendievel, J.-Y. Buffière, E. Maire, J. Lachambre, G. Martin, Fatigue performances of chemically etched thin struts built by selective electron beam melting: Experiments and predictions, Materialia 9 (2020) 100589.

[78] A. Burr, T. Persenot, P.-T. Doutre, J.-Y. Buffiere, P. Lhuissier, G. Martin, R. Dendievel, A numerical framework to predict the fatigue life of lattice structures built by additive manufacturing, International Journal of Fatigue 139 (2020) 105769.

[79] N. Sanaei, A. Fatemi, Analysis of the effect of surface roughness on fatigue performance of powder bed fusion additive manufactured metals, Theoretical and Applied Fracture Mechanics 108 (2020) 102638.

[80] X. Lei, C. Li, X. Shi, X. Xu, Y. Wei, Notch strengthening or weakening governed by transition of shear failure to normal mode fracture, Scientific Reports 5 10537.

[81] R. L. Narayan, L. Tian, D. Zhang, M. Dao, Z.-W. Shan, K. J. Hsia, Effects of notches on the deformation behavior of submicron sized metallic glasses: Insights from in situ experiments, Acta Materialia 154 (2018) 172 – 181.

[82] O. Andreau, E. Pessard, I. Koutiri, J.-D. Penot, C. Dupuy, N. Saintier, P. Peyre, A competition between the contour and hatching zones on the high cycle fatigue behaviour of a 316l stainless steel: Analyzed using x-ray computed tomography, Materials Science and Engineering: A 757 (2019) 146 – 159.

[83] A. Yadollahi, N. Shamsaei, S. M. Thompson, A. Elwany, L. Bian, Effects of building orientation and heat treatment on fatigue behavior of selective laser melted 17-4 ph stainless steel, International Journal of Fatigue 94 (2017) 218 – 235, fatigue and Fracture Behavior of Additive Manufactured Parts.

[84] D. Herzog, V. Seyda, E. Wycisk, C. Emmelmann, Additive manufacturing of metals, Acta Materialia 117.

[85] A. Riemer, S. Leuders, M. Thöne, H. Richard, T. Tröster, T. Niendorf, On the fatigue crack growth behavior in 316l stainless steel manufactured by selective laser melting, Engineering Fracture Mechanics 120 (2014) 15 – 25.

[86] G. Meneghetti, D. Rigon, C. Gennari, An analysis of defects influence on axial fatigue strength of maraging steel specimens produced by additive manufacturing, International Journal of Fatigue 118 (2019) 54 – 64.

[87] J. Damon, T. Hanemann, S. Dietrich, G. Graf, K.-H. Lang, V. Schulze, Orientation dependent fatigue performance and mechanisms of selective laser melted maraging steel x3nicomoti18-9-5, International Journal of Fatigue 127 (2019) 395 – 402.

[88] H. Neuber, Kerbspannungslehre, Springer-Verlag, 1958.

[89] H. Neuber, Über die berücksichtigung der spannungskonzentration bei festigkeitsberechnungen, Konstruktion 20 (7) (1968) 245–251, cited By 246.

[90] L. Susmel, The theory of critical distances: a review of its applications in fatigue, Engineering Fracture Mechanics 75 (7) (2008) 1706 – 1724, critical Distance Theories of Fracture.

[91] R. Louks, L. Susmel, The linear-elastic theory of critical distances to estimate high-cycle fatigue strength of notched metallic materials at elevated temperatures, Fatigue & Fracture of Engineering Materials & Structures 38 (6) (2014) 629–640.

[92] B. Vayssette, N. Saintier, C. Brugger, M. E. May, E. Pessard, Numerical modelling of surface roughness effect on the fatigue behavior of ti-6al-4v obtained by additive manufacturing, International Journal of Fatigue 123 (2019) 180 – 195.

[93] P. Lazzarin, R. Zambardi, A finite-volume-energy based approach to predict the static and fatigue behavior of components with sharp v-shaped notches, International Journal of Fracture 112 (3) (2001) 275–298.

[94] E. Beltrami, Sulle condizioni di resistenza dei corpi elastici, rend. r. ist. lombardo di scienze, Lettere e Arti 18 (1885) 704, cited By 1.

[95] G. Sih, B. Cha, A fracture criterion for three-dimensional crack problems, Engineering Fracture Mechanics 6 (4) (1974) 699 – 723.

[96] Mechanics of Fracture Initiation and Propagation, Kluwer, 1991.

[97] P. Lazzarin, F. Berto, M. Zappalorto, Rapid calculations of notch stress intensity factors based on averaged strain energy density from coarse meshes: Theoretical bases and applications, International Journal of Fatigue 32 (10) (2010) 1559 – 1567.

[98] P. Lazzarin, R. Tovo, A unified approach to the evaluation of linear elastic stress fields in the neighborhood of cracks and notches, International Journal of Fracture 78 (1996) 3–19.

[99] L. Sheridan, J. E. Gockel, O. E. Scott-Emuakpor, Stress-defect-life interactions of fatigued additively manufactured alloy 718, International Journal of Fatigue 143 (2021) 106033.

[100] R. Biswal, X. Zhang, A. K. Syed, M. Awd, J. Ding, F. Walther, S. Williams, Criticality of porosity defects on the fatigue performance of wire + arc additive manufactured titanium alloy, International Journal of Fatigue 122 (2019) 208 – 217.

[101] S. Beretta, S. Romano, A comparison of fatigue strength sensitivity to defects for materials manufactured by am or traditional processes, International Journal of Fatigue 94 (2017) 178 – 191, fatigue and Fracture Behavior of Additive Manufactured Parts.

[102] E. Wycisk, A. Solbach, S. Siddique, D. Herzog, F. Walther, C. Emmelmann, Effects of defects in laser additive manufactured ti-6al-4v on fatigue properties, Physics Procedia 56 (2014) 371 – 378, 8th International Conference on Laser Assisted Net Shape Engineering LANE 2014.

[103] H. Kitagawa, S. Takahashi, Applicability of fracture mechanics to very small cracks in the early stage, in: Procs. Second International Conference on Mechanical Behaviour of Materials.

[104] S. Romano, S. Miccoli, S. Beretta, A new fe post-processor for probabilistic fatigue assessment in the presence of defects and its application to am parts, International Journal of Fatigue 125 (2019) 324 – 341.

[105] H. Wan, Q. Wang, C. Jia, Z. Zhang, Multi-scale damage mechanics method for fatigue life prediction of additive manufacture structures of ti-6al-4v, Materials Science and Engineering: A 669 (2016) 269 – 278.

[106] R. Hedayati, H. Hosseini-Toudeshky, M. Sadighi, M. Mohammadi-Aghdam, A. Zadpoor, Multi-scale modeling of fatigue crack propagation in additively manufactured porous biomaterials, International Journal of Fatigue 113 (2018) 416 – 427.

[107] T. Lindström, D. Ewest, K. Simonsson, R. Eriksson, J.-E. Lundgren, D. Leidermark, Constitutive model of an additively manufactured ductile nickel-based superalloy undergoing cyclic plasticity, International Journal of Plasticity 132 (2020) 102752.

[108] P. Holzmann, R. Breitenecker, E. Schwarz, Business model patterns for 3d printer manufacturers, Journal of Manufacturing Technology Management 31 (2019) 1281–1300.

[109] F. Piller, C. Weller, R. Kleer, Business Models with Additive Manufacturing—Opportunities and Challenges from the Perspective of Economics and Management, 2015, pp. 39–48.

[110] J. Savolainen, M. Collan, Industrial Additive Manufacturing Business Models—What Do We Know from the Literature?, Springer International Publishing, Cham, 2020, pp. 115–130.

[111] M. Attaran, The rise of 3-d printing: The advantages of additive manufacturing over traditional manufacturing, Business Horizons 60 (5) (2017) 677 – 688.

[112] A. Fatemi, Chapter 2 fatigue design, University of Toledo.

[113] D. R. Jones, M. F. Ashby, Chapter 19 - fatigue design, in: D. R. Jones, M. F. Ashby (Eds.), Engineering Materials 1 (Fifth Edition), fifth edition Edition, Butterworth-Heinemann, 2019, pp. 301 – 324.

[114] J.-T. Harris, D., Classical fatigue design techniques as a failure analysis tool, Journal of Failure Analysis and Prevention 9 (2009) 81–87.

[115] A. Wiberg, J. Persson, J. Ölvander, Design for additive manufacturing – a review of available design methods and software, Rapid Prototyping Journal ahead-of-print.

[116] M.-C. Chiu, Y.-H. Lin, Simulation based method considering design for additive manufacturing and supply chain, Industrial Management & Data Systems 116 (2016) 322–348.

[117] C. Klahn, B. Leutenecker, M. Meboldt, Design strategies for the process of additive manufacturing, Procedia CIRP 36 (2015) 230 – 235, cIRP 25th Design Conference Innovative Product Creation.

[118] R. Campbell, H. Jee, Y. Kim, Adding product value through additive manufacturing, Proceedings of the International Conference on Engineering Design, ICED 4 (2013) 259–268.

[119] M. Orquéra, S. Campocasso, D. Millet, Design for additive manufacturing method for a mechanical system downsizing, Procedia CIRP 60 (2017) 223 – 228, complex Systems Engineering and Development Proceedings of the 27th CIRP Design Conference Cranfield University, UK 10th – 12th May 2017.

[120] C. Emmelmann, M. Petersen, J. Kranz, E. Wycisk, Bionic lightweight design by laser additive manufacturing (LAM) for aircraft industry, in: P. Ambs, D. Curticapean, C. Emmelmann, W. Knapp, Z. T. Kuznicki, P. P. Meyrueis (Eds.), SPIE Eco-Photonics 2011: Sustainable Design, Manufacturing, and Engineering Workforce Education for a Green Future, Vol. 8065, International Society for Optics and Photonics, SPIE, 2011, pp. 181 – 192.

[121] H. Rodrigue, M. Rivette, An assembly-level design for additive manufacturing methodology.

[122] D. G. Ullman, The mechanical design process. boston, mau. :mcgraw-hill, 2003.

[123] K. Ulrich, S. Eppinger, Product design and development, mcgraw-hill/irwin, new york,ny.

[124] W. Gao, Y. Zhang, D. Ramanujan, K. Ramani, Y. Chen, C. B. Williams, C. C. Wang, Y. C. Shin, S. Zhang, P. D. Zavattieri, The status, challenges, and future of additive manufacturing in engineering, Computer-Aided Design 69 (2015) 65 – 89.

[125] A. A. Rahim, S. N. Musa, S. Ramesh, M. K. Lim, A systematic review on material selection methods, Proceedings of the Institution of Mechanical Engineers, Part L: Journal of Materials: Design and Applications 234 (7) (2020) 1032–1059.

[126] M. Alghamdy, R. Ahmad, B. Alsayyed, Material selection methodology for additive manufacturing applications, Procedia CIRP 84 (2019) 486 – 490, 29th CIRP Design Conference 2019, 08-10 May 2019, Póvoa de Varzim, Portgal.

[127] D. Thomas, The development of design rules for selective laser melting, phd thesis, university of wales.

[128] G. A. Adam, D. Zimmer, Design for additive manufacturing—element transitions and aggregated structures, CIRP Journal of Manufacturing Science and Technology 7 (1) (2014) 20 – 28.

[129] J. Kranz, D. Herzog, C. Emmelmann, Design guidelines for laser additive manufacturing of lightweight structures in tial6v4, Journal of Laser Applications 27 (S1) (2015) S14001.

[130] B. Leutenecker-Twelsiek, C. Klahn, M. Meboldt, Considering part orientation in design for additive manufacturing, Procedia CIRP 50 (2016) 408 – 413, 26th CIRP Design Conference.

[131] G. Strano, L. Hao, R. Everson, K. Evans, A new approach to the design and optimisation of support structures in additive manufacturing, The International Journal of Advanced Manufacturing Technology 66.

[132] S. Yim, D. Rosen, Build time and cost models for additive manufacturing process selection, Vol. 2, 2012.

[133] P. Stavropoulos, P. Foteinopoulos, Modelling of additive manufacturing processes: A review and classification, Manufacturing Review 5 (2018) 2.

[134] R. Molaei, A. Fatemi, Fatigue design with additive manufactured metals: Issues to consider and perspective for future research, Procedia Engineering 213 (2018) 5 – 16, 7th International Conference on Fatigue Design, Fatigue Design 2017, 29-30 November 2017, Senlis, France.

Part II

Articles

Article I

What is going on with fatigue of additively manufactured metals?

Klas Solberg, Filippo Berto

Materials Design & Processing Communications, Letter

This brief communication gives an overview of fatigue behaviour and assessment of additively manufactured metals. The high cycle fatigue behaviour of as-built and post-processed additively manufactured superalloy 718, stainless steel (316L and 17-4PH), and Ti-6Al-4 V is compared with their wrought counterparts. Further, different approaches used for assessment of the fatigue behaviour are presented.

https://doi.org/10.1002/mdp2.84

What is going on with fatigue of additively manufactured metals?

Klas Solberg*, Filippo Berto

Institutt for maskinteknikk og produksjon, NTNU, Trondheim, Norway

Abstract

This brief communication gives an overview of fatigue behaviour and assessment of additively manufactured metals. The high cycle fatigue behaviour of as-built and post processed additively manufactured superalloy 718, stainless steel (316L and 17-4PH) and Ti6Al4V are compared with their wrought counterparts. Further, different approaches used for assessment of the fatigue behaviour are presented.

Keywords: Fatigue, Additive Manufacturing, Defects, Post-treatments, Inconel 718, Ti6Al4V, 316L, 17-4 PH

Recently, an increasing effort is put into developing understanding and confidence of additively manufactured (AM) metals for load-bearing applications [1–4].AM is based on adding material, by, *e.g.* fusing powder particles, as shown in Fig. 1a, where powder particles are fused to a solid, layer-by-layer using a laser beam. Materials can be manufactured in a new way, opening up possibilities in terms of geometrical complexity never possible before. However, materials produced by AM exhibit unfavourable properties in their as-built state, such as reduction in fatigue life, reduced strength, reduced elongation at failure, high surface roughness, defects, anisotropic microstructure, residual stresses [1–4].By various post treatments, the fatigue strength of AM materials can be increased to the level of wrought materials. This is because post-processing can alleviate the defects that influence the fatigue life of AM material but typically cannot neutralise those completely [4]. The idea of producing components made by high strength materials such as superalloys, titanium alloys or steel alloys by AM is tempting, because it may reduce the need for machining, *i.e.* saving cost. However, the fatigue strength is reduced by defects and high surface roughness, especially for high strength materials [2]. Fig. 1b shows the typical test specimens for fatigue, Fig. 1cshows a fracture surface with a rough surface, surface defect and sub-surface defects and Fig. 1d shows the as-built microstructure with visible melt pools and elongated grains in build direction, deriving from the temperature gradient from the cooling during manufacturing. The main two results seen in almost all cases when AM (as-built) specimens are compared to conventional materials are that (1) for static loading elongation at failure and strength is reduced (2) fatigue life is reduced [1–4]. The reason for the reduction in strength and fatigue life in the as-built state is typically due to defects as shown in Fig. 1c.

In order to compare the fatigue performance of AM metals to their wrought counterparts fatigue data reported in the literature are compared in S-N diagrams. High cycle fatigue data for Superalloy Inconel 718 [5–9] , Ti6Al4V [10–16], stainless steel 316L [17–20] and 17-4PH [19, 21, 22] are shown in Fig. 2a-c respectively. All data are corrected for mean stress employing the Smith-Watson-Topper (SWT) correction [23]

$$\sigma_{ar} = \sigma_{max}\sqrt{\frac{1-R}{2}}. \tag{1}$$

From Fig. 2a-c the general trend is that the fatigue life is reduced when comparing AM as-built with wrought. These two cases are the two extremes in terms of fatigue life. The fatigue performance of AM materials can be improved by various post processing methods, typically involving machning and/or heat treatments. Machining removes rough surface and defects in the surface region (defects and rough surface can be seen in Fig. 1c). Heat treatments can remove residual stresses, alter the microstructure of the material; make the microstructure isotropic and introduce *e.g.* precipitation hardening or hot isostatic pressing (HIP) can close internal pores by applying a combination of pressure and heat [3]. For each material presented in Fig. 2 one set of AM materials subjected to post processing is shown

*Corresponding author: E-mail: klas.solberg@ntnu.no

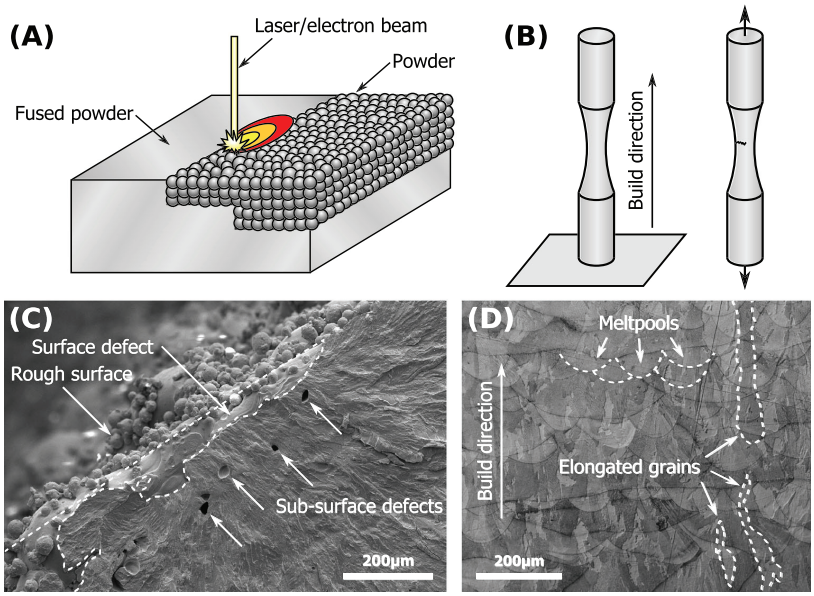

Figure 1: (a) Schematic illustration of powder bed fusion process. (b) Schematic illustration of as-built specimen and fatigue loading. (c) Example of SEM image of a fatigue initiation site in AM 316L (d) Example of microstructure in AM Inconel 718 obtained by means of optical microscope.

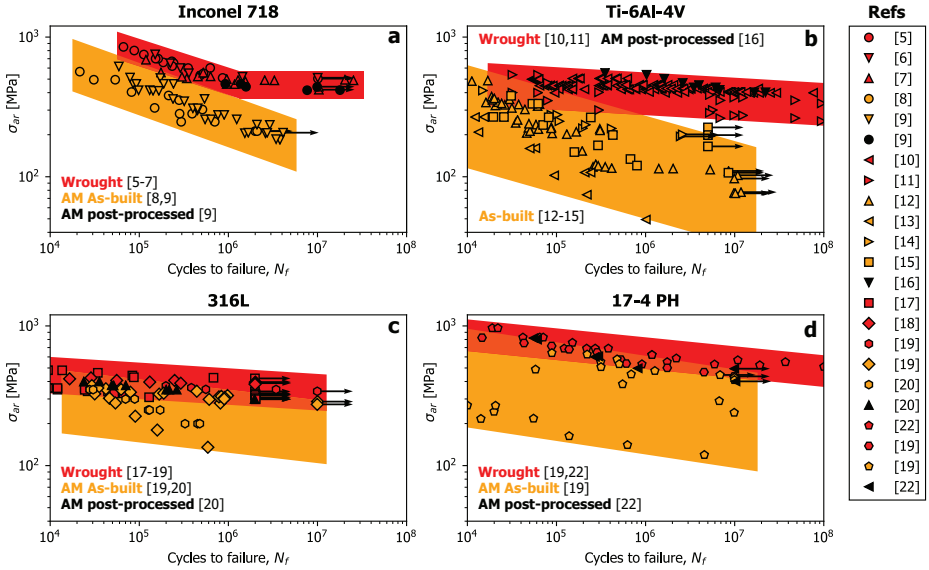

Figure 2: Comparison of fatigue data for wrought and AM materials. The data is presented in S-N curves given in stress amplitude (corrected by SWT) versus number of cycles to failure: (a) Inconel 718; (b) Ti-6Al-4V; (c) 316L SS and (d) 17-4PH SS. (Arrows indicate discontinued tests.)

[9, 16, 20, 22]. These materials are post-processed by combinations of the methods mentioned above and achieve the same fatigue strength as wrought materials.

Assessment of the fatigue behaviour of materials containing residual stresses, geometrical defects and anisotropic microstructure is a complicated task. As the geometrical defects

are usually reported as the main mechanism for fatigue and fracture, most works dealing with fatigue assessment are aiming to take the critical defects into account. There are three main approaches when dealing with fatigue assessment of AM metals: (1) Considering the effects of defects as statistical scatter. This is done by only designing according to the statistics of the fatigue life curve without taking into account the various defects. (2) Taking into account the defects by means of analytically approaches *e.g.* employing fracture mechanics. Here several works are considering the defect as a crack by assuming the crack size is equal to the $\sqrt{\text{area}}$ of the defect and further correlates this value to the hardness in order to predict the fatigue limit [24–26]. (3) Modelling the material with the geometrical defects, usually by means of finite element software. This method can be done based on, *e.g.* computed tomography 3D image or surface profile from a confocal microscope, obtaining the geometry, then importing it as a 3D model into a finite element software and applying loads [27].

The fatigue strength is reduced when comparing as-built AM metals to their wrought counterparts. Post processing AM metals can give similar fatigue life as wrought materials. Fatigue of AM metals usually initiates from defects deriving for the AM process. When assessing the fatigue behaviour, these defects are taken into account by different methods.

References

[1] J. J. Lewandowski, M. Seifi, Metal additive manufacturing: A review of mechanical properties, Annual Review of Materials Research 46 (2016) 151–186.

[2] P. Li, D. Warner, A. Fatemi, N. Phan, Critical assessment of the fatigue performance of additively manufactured ti6al4v and perspective for future research, International Journal of Fatigue 85 (2016) 130 – 143.

[3] T. DebRoy, H. Wei, J. Zuback, T. Mukherjee, J. Elmer, J. Milewski, A. Beese, A. Wilson-Heid, A. De, W. Zhang, Additive manufacturing of metallic components process, structure and properties, Progress in Materials Science 92 (2018) 112 – 224.

[4] D. Herzog, V. Seyda, E. Wycisk, C. Emmelmann, Additive manufacturing of metals, Acta Materialia 117 (2016) 371 – 392.

[5] N. Kawagoishi, Q. Chen, H. Nisitani, Fatigue strength of inconel 718 at elevated temperatures, Fatigue & Fracture of Engineering Materials & Structures 23 (????) 209–216.

[6] Q. Chen, N. Kawagoishi, H. Nisitani, Evaluation of notched fatigue strength at elevated temperature by linear notch mechanics, International Journal of Fatigue 21 (1999) 925 – 931.

[7] A. Yadollahi, N. Shamsaei, Additive manufacturing of fatigue resistant materials: Challenges and opportunities, International Journal of Fatigue 98 (2017) 14 – 31.

[8] K. Solberg, F. Berto, Notch-defect interaction in additively manufactured inconel 718, International Journal of Fatigue 122 (2019) 35 – 45.

[9] D. Wells, Overview of Fatigue and Damage Tolerance Performance of Powder Bed Fusion Alloy N07718, Technical Report, NASA, 2016.

[10] P. J. Golden, R. John, W. J. Porter, Investigation of variability in fatigue crack nucleation and propagation in alpha+beta ti-6al-4v, Procedia Engineering 2 (2010) 1839 – 1847. Fatigue 2010.

[11] R. K. Nalla, R. O. Ritchie, B. L. Boyce, J. P. Campbell, J. O. Peters, Influence of microstructure on high-cycle fatigue of ti-6al-4v: Bimodal vs. lamellar structures, Metallurgical and Materials Transactions A 33 (2002) 899–918.

[12] J. Pegues, M. Roach, R. S. Williamson, N. Shamsaei, Surface roughness effects on the fatigue strength of additively manufactured ti-6al-4v, International Journal of Fatigue 116 (2018) 543 – 552.

[13] P. Edwards, M. Ramulu, Fatigue performance evaluation of selective laser melted ti6al4v, Materials Science and Engineering: A 598 (2014) 327 – 337.

[14] S. Razavi, P. Ferro, F. Berto, J. Torgersen, Fatigue strength of blunt v-notched specimens produced by selective laser melting of ti-6al-4v, Theoretical and Applied Fracture Mechanics 97 (2018) 376 – 384.

[15] M. Kahlin, H. Ansell, J. Moverare, Fatigue behaviour of notched additive manufactured ti6al4v with as-built surfaces, International Journal of Fatigue 101 (2017) 51 – 60.

[16] E. Brandl, C. Leyens, F. Palm, Mechanical properties of additive manufactured ti-6al-4v using wire and powder based processes, IOP Conference Series: Materials Science and Engineering 26 (2011) 012004.

[17] H. Huang, Z. Wang, J. Lu, K. Lu, Fatigue behaviors of aisi 316l stainless steel with a gradient nanostructured surface layer, Acta Materialia 87 (2015) 150 – 160.

[18] T. Roland, D. Retraint, K. Lu, J. Lu, Fatigue life improvement through surface nanostructuring of stainless steel by means of surface mechanical attrition treatment, Scripta Materialia 54 (2006) 1949 – 1954.

[19] T. M. Mower, M. J. Long, Mechanical behavior of additive manufactured, powder-bed laser-fused materials, Materials Science and Engineering: A 651 (2016) 198 – 213.

[20] C. Elangeswaran, A. Cutolo, G. K. Muralidharan, C. de Formanoir, F. Berto, K. Vanmeensel, B. V. Hooreweder, Effect of post-treatments on the fatigue behaviour of 316l stainless steel manufactured by laser powder bed fusion, International Journal of Fatigue 123 (2019) 31 – 39.

[21] H. A. Leybold, Axial-load fatigue tests on 17-7 ph stainless steel under constant-amplitude loading (1960).

[22] P. Nezhadfar, R. Shrestha, N. Phan, N. Shamsaei, Fatigue behavior of additively manufactured 17-4 ph stainless steel: Synergistic effects of surface roughness and heat treatment, International Journal of Fatigue 124 (2019) 188 – 204.

[23] K. Smith, T. Topper, P. Watson, A stressstrain function for the fatigue of metals (stress-strain function for metal fatigue including mean stress effect), J Materials 5 (1970) 767–778.

[24] J. Gunther, D. Krewerth, T. Lippmann, S. Leuders, T. Troster, A. Weidner, H. Biermann, T. Niendorf, Fatigue life of additively manufactured ti6al4v in the very high cycle fatigue regime, International Journal of Fatigue 94 (2017) 236 – 245. Fatigue and Fracture Behavior of Additive Manufactured Parts.

[25] Y. Yamashita, T. Murakami, R. Mihara, M. Okada, Y. Murakami, Defect analysis and fatigue design basis for ni-based superalloy 718 manu-

factured by selective laser melting, International Journal of Fatigue 117 (2018) 485 – 495.

[26] H. Masuo, Y. Tanaka, S. Morokoshi, H. Yagura, T. Uchida, Y. Yamamoto, Y. Murakami, Influence of defects, surface roughness and hip on the fatigue strength of ti-6al-4v manufactured by additive manufacturing, International Journal of Fatigue 117 (2018) 163 – 179.

[27] B. Vayssette, N. Saintier, C. Brugger, M. E. May, E. Pessard, Numerical modelling of surface roughness effect on the fatigue behavior of ti-6al-4v obtained by additive manufacturing, International Journal of Fatigue 123 (2019) 180 – 195.

Article II

Notch-defect interaction in additively manufactured Inconel 718

Klas Solberg, Filippo Berto

International Journal of Fatigue, Article

Powder bed fusion based additively manufactured components are known to have poor surface quality, especially when building downward facing surfaces. These surfaces can contain defects, from which fatigue cracks can be initiated. In this work the notched fatigue behaviour of Inconel 718 specimens produced by selective laser melting is investigated. The main focus is set on the interaction between notch geometries and local defects due to the amount of overhang in the notch region. Four different geometries are considered, with different amount of notch acuities and degree of downward facing surfaces. A variation in failure sites, with respect to the notch bisector line, was fond in the specimens, and the position was found to be dependent on the amount of overhang and notch acuity. The fatigue life was found to be dependent on the size of surface defects measured in fracture surfaces. Further, the use of average strain energy density as a failure criteria in additively manufactured metals is discussed.

https://doi.org/10.1016/j.ijfatigue.2018.12.021

Notch-Defect Interaction in Additively Manufactured Inconel 718

K. Solberg[a,*], F. Berto[a]

[a]*Department of Mechanical and Industrial Engineering, Norwegian University of Science and Technology, 7034 Trondheim, Norway*

Abstract

Powder bed fusion based additively manufactured components are known to have poor surface quality, especially when building downward facing surfaces. These surfaces can contain defects, from which fatigue cracks can be initiated. In this work the notched fatigue behaviour of Inconel 718 specimens produced by selective laser melting is investigated. The main focus is set on the interaction between notch geometries and local defects due to the amount of overhang in the notch region. Four different geometries are considered, with different amount of notch acuities and degree of downward facing surfaces. A variation in failure sites, with respect to the notch bisector line, was fond in the specimens, and the position was found to be dependent on the amount of overhang and notch acuity. The fatigue life was found to be dependent on the size of surface defects measured in fracture surfaces. Further, the use of average strain energy density as a failure criteria in additively manufactured metals is discussed.

Keywords: Fatigue, Additive Manufacturing, Fracture, Defect, Surface

1. Introduction

Additive Manufacturing (AM) is a manufacturing method, producing components by adding material in a layer-by-layer manner. Components of high complexity can be produced, based on computer-aided designs. However, for Powder Bed Fusion (PBF) based AM methods, components are displaying poor surface quality, especially when building downward facing surfaces [1–7]. With increasing interest in using AM components in engineering applications, it is necessary to evaluate the structural integrity of the respective components [8]. A schematic illustration of manufacturing process and as-built part is shown in Fig. 1.

The structural integrity for a wide range of AM metals has previously been studied [2, 3], the general trend is that as-built specimens are showing the lowest strength and mechanical properties. Different post-processing methods can increase the mechanical properties [4]. Typical post-processing employed to increase the mechanical properties are heat treatment, Hot Isostatic Pressing (HIPing), and machining [2, 9]. Heat treatment can remove residual stresses and alter the microstructure. HIPing can close internal voids, such as lack of fusion and gas pores; however, defects open to the surface will not be closed [10]. Machining the surface will remove the outer layer of the material, generally found to have high surface roughness and defects [2, 3, 11]. In the case of fatigue, especially for high strength metals, geometrical defects and surface roughness is a major factor determining the fatigue life [4, 12, 13]. Relating geometrical defects to the fatigue behaviour, several papers [13–17] are recently employing the $\sqrt{\text{area}}$-method developed by Murakami [18]. The method is based on measuring the effective size of the defect found in the fracture surface, then relating this effective size to the fatigue life of the component.

With the new allowed degree of complexity in components by use of AM, engineers are looking into combining components, topology optimisation and grid structures [8]. This increase in geometrical complexity makes it more challenging to evaluate stresses in a Finite Element (FE) model, as refine meshes are needed. Because of this, failure criteria independent of the mesh are desirable. Average Strain Energy Density (ASED) is a failure assessment method used for brittle fracture in static and cyclic loading for the assesment of fracture and fatigue failures, evaluating the average value of Strain Energy Density (SED) within a fixed control volume surrounding the notch tip [19]. When applied in FE models it has low sensitivity to the mesh size [19–22]. The possibility of employing ASED

*Corresponding author
Email address: klas.solberg@ntnu.no (K. Solberg)

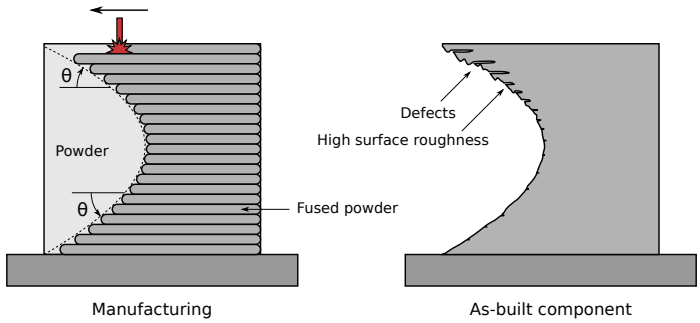

Figure 1: Schematic illustration of Manufacturing and as-built additive manufactured component. The as-built component has defects and poor surface quality in regions built with downward facing surfaces.

for AM metals has previously been investigated by Razavi et al. [23]. ASED has previously been employed on welded joints, which similar to AM metals contain residual stresses and defects [19].

Inconel 718 is a Ni-based superalloy, with high strength and fatigue properties at a wide range of temperatures [24, 25]. The material is commonly used for turbine blades, pipeline components, aerospace components and other applications requiring high mechanical properties at extreme temperatures. Inconel 718 is a high strength material and with AM it can be manufactured to near-net shaped components, reducing the need of machining. Reported results of AM Inconel 718 shows poor resistance to crack growth in the threshold region and fatigue cracks are initiating from defects such as lack of fusion [4, 17, 26, 27].

In this work notched fatigue behaviour of as-built Inconel 718 specimens produced by SLM is investigated. Four different specimen geometries with different notch radii and amounts of overhang is considered. The paper is aiming to (1) Describe the relationship between fatigue life and surface defects for notched and unnotched specimens. (2) Propose a model relating the position of crack initiation site, in terms of height with respect to the notch bisector line, to the degree of overhang in a notch geometry. (3) Investigating the challenges and opportunities of applying ASED as a failure criterion in AM components.

2. Theoretical background

The first proposal of local approach for evaluating failure was Neuber's concept of elementary structural volume and microstructural support length [28, 29]. The main idea is from these concepts is that static or fatigue failure is governed not by the theoretical maximum stress in the notch, but rather the stress in the vicinity of the notch averaged over a volume or a length close to the notch root. The first proposal of strain energy as a failure criterion was by Beltrami in 1885 [30], stating that failure occurs when the level of strain energy reaches a critical value. Further, Sih proposed, for cracks, to evaluate a parameter dependent on SED and a critical distance from the crack tip singularity [31]. Where crack propagation would occur if the value of SED were equal to the critical value for the material. The theory was further extended to notches, using a reference point at the notch surface, where the tangential stress component has the maximum value. The SED failure criterion was refined and formulated in [32].

ASED proposed by Lazzarin and Zambardi [33] evaluates SED in a defined control volume surrounding the notch tip. The criterion states that failure occurs when the mean value of SED, $\bar{W}$, over the control volume is equal to the critical value of energy for the material, W_c:

$$\bar{W} = W_c. \tag{1}$$

Based on the coordinate system of Lazzarin and Tovo [34], the control volume is defined for cracks, sharp notches and blunt notches. The generalised definition of the control volume is shown in Fig. 2, for sharp and blunt notches. ρ is the notch root radius, 2α is the opening angle of the notch, R_0 is the critical radius defining the size of the control volume, this parameter is dependent on the material and r_0 defines the centroid of control volume.

In the case of static loading for a plain specimen, failure is evaluated by use of the ultimate tensile strength, σ_t, and Young's modulus, E, of the material.

$$W_c = \frac{\sigma_t^2}{2E}. \tag{2}$$

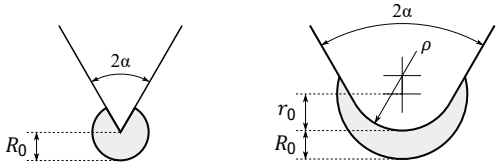

Figure 2: Generalized notch geometry and control volume used for average strain energy density.

In the case of sharp notches, ASED can be evaluated analytically for mode I loading by referring to the generalised notch stress intensity factor, K_I^V

$$\bar{W}_I = \frac{I_1}{4E\lambda_1(\pi-\alpha)}\left(\frac{K_I^V}{R_0^{1-\lambda_I}}\right)^2, \tag{3}$$

where I_1 is a parameter dependent on the opening angle of the notch and λ_1 is the Williams' series eigenvalue [35]. In the case of blunt notches, ASED can be calculated analytically for mode I loading by referring to the maximum stress at the notch tip σ_{max}

$$\bar{W}_I = F(2\alpha) \times H\left(2\alpha, \frac{R_0}{\rho}\right) \times \frac{\sigma_{max}^2}{E}, \tag{4}$$

where F is a function dependent on 2α and H is a function dependent on 2α and the ratio between R_0/ρ [19]. ASED has previously been employed on a wide range of materials and loading conditions, including multi-axial fatigue of Ti6Al4V [19, 36–38].

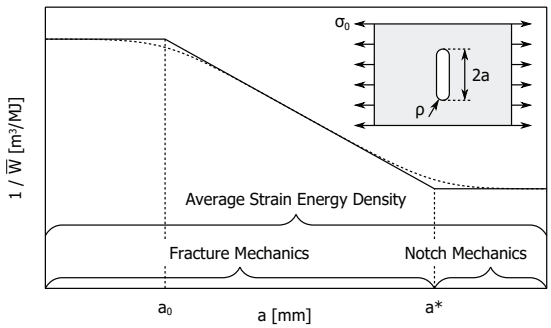

Figure 3: Schematic illustration of Atzori-Lazzarin diagram [39, 40], inverse of average strain energy density versus defect size.

The Atzori-Lazzarin diagram [39, 40], an extension of Kitagawa-Takahashi diagram [41] has interesting applications for AM materials. The diagram is evaluating ASED at the fatigue limit for different notch/crack sizes, a. A schematic illustration of the diagram is shown in Fig. 3. The diagram consists of two plateaus of $1/\bar{W}$ and a transition between them. The diagram can easily be understood by considering an arbitrary defect in a material, with constant notch acuity a/ρ, where a is the size (depth) of the defect and ρ is the notch radius of the defect. For a defect with size less than a_0, the defect will not influence the fatigue limit. For a defect size larger than a^*, the defect is acting as a notch, and linear notch mechanics can be applied. In the transition region between these two plateaus, the defect is affecting fatigue behaviour and should be taken into account locally, by applying linear elastic fracture mechanics.

AM components and specimens can contain global defects, such as notches, and at the same time local defects, such as lack of fusion or pores. Looking to models such as the Atzori-Lazzarin diagram, taking into account the whole range of defects in the fatigue assessment, combining notch mechanics and fracture mechanics can be useful in future applications when developing tools determining the fatigue life of AM components.

3. Experimental procedure, testing and material

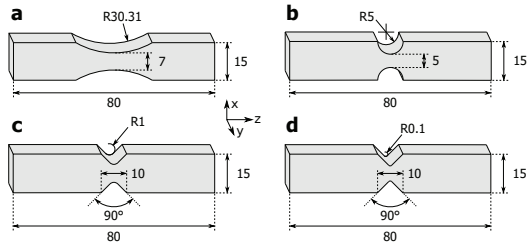

Figure 4: Specimen geometries: (a) Unnotched; (b) semi-circular notch; (c) v-shaped notch with notch radius equal to 1 mm; (d) v-shaped notch with notch radius equal to radius 0.1 mm. Notch depth of specimens: 4 mm, 5 mm, 4.59 mm and 4.96 mm for (a), (b), (c) and (d) respectively.

The fatigue behaviour of four different specimen geometries of AM Inconel 718 produced by SLM was investigated. The geometry of the different specimens is shown in Fig. 4. An unnotched specimen geometry was compared to three double notch specimen geometries; semi-circular, v-shaped notch with a radius equal to 1 mm and v-shaped notch with a radius equal to 0.1 mm. All specimens were of 5 mm thickness. The specimen geometries investigated was based on notch geometries proposed by Pilkey et al. [42]. The specimens were produced by SLM, by use of standardised processing parameters on an SLM Solution system. The specimens were build to a solid

layer by layer in the z-direction, referring to coordinate system in Fig. 4, with a layer height of 50 μm and energy density of 60 J/mm^3. No distortion was found in the specimens potentially causing misalignments in the fatigue testing, like what has been reported previously in literature for additively manufactured cylindrical maraging steel specimens of comparable dimensions [15].

Specimens were tested for high cycle fatigue under uniaxial loading on an MTS Landmark Servohydraulic test system, with a loading ratio $R = 0$ and a frequency of 10 Hz. The tests were performed at room temperature. Specimens that did not fail after 2×10^6 cycles were considered as run out, and the fatigue strength was evaluated at this number of cycles. The fatigue data obtained was presented in S-N diagrams, with scatter bands at 2.3 %, 50 % and 97.7% probability of failure.

The surface roughness of surfaces build in different orientations was measured in terms of R_a on an Alicona Infinite Focus Microscope. Surface roughness was evaluated for v-notch specimens, on surfaces built vertical, upward facing (45°) and downward facing (45°). The surface roughness was evaluated along lines of 4 mm. The microstructure of the material was obtained by polishing and etching according to ASTM E407-07, with etchant 94 [43]. Fractography was performed by the means of SEM. Fracture surfaces were analysed, and the area of the defects found to initiate fatigue was measured. In the cases that the edge of the specimens were hard to define, regions displaying clear signs of lack of fusion close to or in contact with the surface, were measured. The position of failure in the notch region, with respect to the notch bisector line, was measured for all specimens. As uniaxial loading was applied, the fracture surfaces were flat for the crack growth region, according to mode I loading.

The elastic stress concentration factor, K_t, was determined for the different geometries by use of the Finite Element (FE) software Abaqus. Two-dimensional models were made, assuming plane strain conditions and utilising symmetry in the specimens. The stress concentration factor was obtained by evaluating ratio of the maximum stress at the notch root and the nominal stress in the net cross-sectional area of the notch. The material was considered to obey a linear elastic behaviour, with Young's modulus and the Poisson ratio equal to 200 GPa and 0.29, respectively [44]. The fatigue reduction factor, K_f, was obtained for the different geometries by evaluating $K_f = \Delta\sigma^S/\Delta\sigma^N$, where $\Delta\sigma^S$ and $\Delta\sigma^N$ is the unnotched and notched fatigue strength at 2×10^6 cycles, respectively. The notch sensitivity, q, was evaluated by $q = (K_f - 1)/(K_t - 1)$.

ASED of the different geometries was done using the same FE model as used for evaluating the stresses. The volume for evaluating the ASED was created according to Fig. 2. In order to give an estimation of the control volume for the material, ASED of the unnotched specimen was evaluated at the fatigue limit by means of Eq. (2). Referring to this value, the control volume giving the corresponding value of ASED for v-notch specimens with 0.1 mm radius was determined.A similar approach for determining critical distance in critical distance theory and critical radius ASED previously reported in literature [45, 46]. ASED-analysis was performed for a unit load, and then the result obtained for each geometry was scaled to the correct load level, for each fatigue data, by means of Eq. (2).

4. Results

4.1. Fatigue data

The fatigue data for all specimen geometries are presented by means of S-N diagrams in Fig. 5, with confidence bands at 2.3 %, 50 % and 97.7 % probability of failure. The fatigue strength of unnotched specimens was 250 MPa, the fatigue strength was then reduced with decreasing notch radius; 175 MPa for the semi-circular notch, 121 MPa for v-notch with 1 mm radius and 100 MPa for v-notch with 0.1 mm radius. The inverse slope of the confidence bands, k, and scatter parameter, $T_{\Delta\sigma}$, are shown in the plots. The scatter parameter is decreasing as the notch radius decreases. The inverse slope of the confidence bands is 3.67, 3.13, 3.14 and 3.19 for unnotched, semi-circular, v-shaped notch with 1 mm radius and v-shaped notch with 0.1 mm radius, respectively. The slope is similar for the different notch geometries, while it is lower for the unnotched specimens. Fatigue strength at 2×10^6 cycles for the different confidence bands are shown in Table 1, for all geometries.

4.2. Notch Sensitivity

The elastic stress concentration factor, the fatigue notch factor and the notch sensitivity are compared and shown in Table 1. The fatigue strength was reduced as the stress concentration factor was increased. V-notch with a radius of 0.1 mm showed the highest fatigue notch factor, then the v-shaped notch with 1 mm radius and then the semi-circular notch. For v-notch geometries the fatigue notch factor were smaller than the stress

	$\Delta\sigma$ - 97.7%	$\Delta\sigma$ - 50%	$\Delta\sigma$ - 2.3%	K_t	K_f	q
Unnotched	168.93	250.00	369.99	1.07	-	-
Semicircular	151.88	175.40	202.58	1.31	1.42	1.35
V-notch ρ=1	105.77	121.33	139.17	2.43	2.06	0.74
V-notch ρ=0.1	92.76	100.44	108.74	6.28	2.49	0.24

Table 1: Values for confidence bands at 2×10^6 cycles, elastic stress concentration factor, K_t (referring to net cross sectional area), fatigue notch factor, K_f, and fatigue notch sensitivity, q.

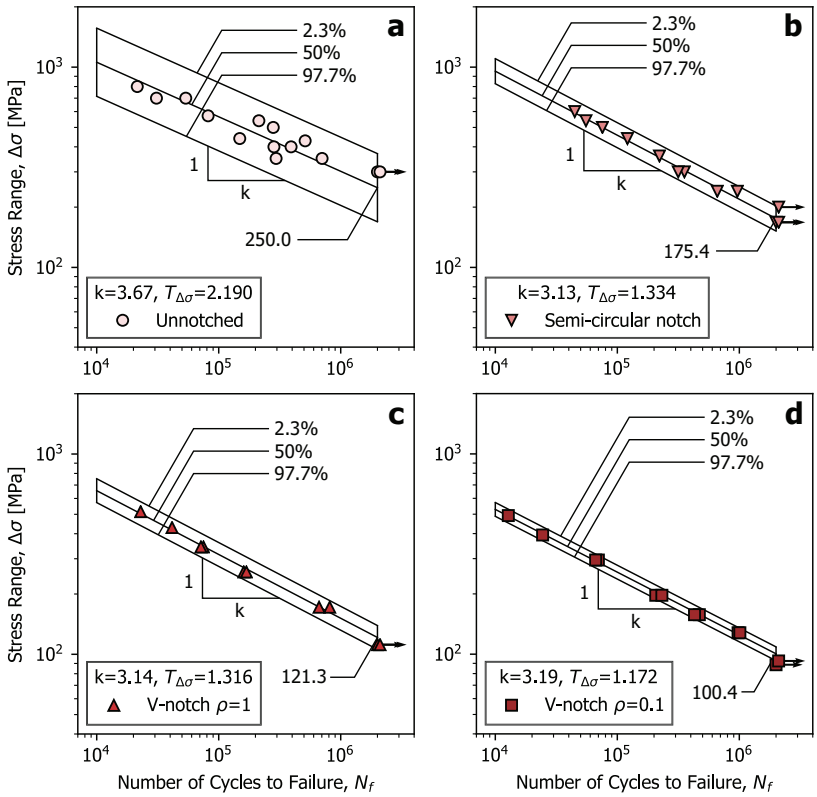

Figure 5: Fatigue data obtained for different specimen geometries tested with loading ratio R=0: (a) Unnotched; (b) Semi-circular notch; (c) v-notch 1 mm radius; (d) v-notch 0.1 mm radius.

concentration factor, while for the semi-circular notch, the fatigue notch factor was higher than the stress concentration factor, i.e. a notch sensitivity above 1, taking the unnotched specimen as a reference.

4.3. Surface Roughness and Microstructure

The surface roughness of different regions was measured. For v-notch specimens, the vertical built surface and upward facing surface of the notch was measured to be 3.08 μm and 3.20 μm respectively. The downward facing surface of the notch was measured to have a surface roughness of 20.95 μm. Fig. 6 shows SEMs of upward and downward facing surfaces.

The notched region of a v-notch specimen loaded until 2×10^6 cycles is shown in Fig. 7. From Fig. 7b the geometry in the notch root is shown, in the overhanging region the surface is rougher, and defects are present. From one of the defects in the overhanging region a fatigue crack can be seen. This fatigue crack and the microstructure of the material is shown with a

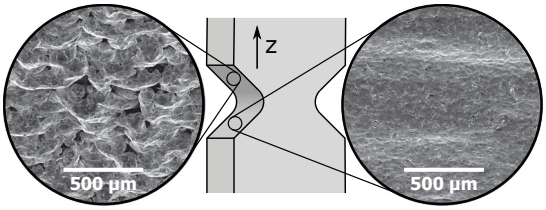

Figure 6: SEM of surface build facing downwards and upwards.

higher magnification in Fig. 7c. The defect from which the fatigue crack is growing is of depth ~200 μm. Fig. 7d shows a porosity and lack of fusion defects in the downward facing surface. In Fig. 7c and d the microstructure of the material is shown, cross sections of the melt pools and elongated grains growing across the melt pools are visible.

4.4. Fractography

Fractography was conducted by means of SEM of all fracture surfaces. One fracture surface of each geometry is shown in Fig. 8a-d. Arrows indicates the crack growth and dashed lines indicates the transition from fatigue crack growth to final rupture. The general trends in the fracture surfaces are: (1) Unnotched specimens have crack initiation on one side of the specimen. In the fracture surfaces small defects were found, as seen in Fig. 8e. (2) Semi-circular notch specimens failed from one side, and lack of fusion defects were found at crack initiation site. (3) V-shaped notch specimens with notch radii of 1 and 0.1 mm failed from both sides of the specimen, and lack of fusion defects was found at crack initiation site, as seen in Fig. 8f.

All specimens were found to have crack initiation from surface defects, none of the specimens had crack inidistotiating from internal defects. The surface defects of all the specimens were captured by SEM, and the area of each defect initiating crack growth was measured. The total area of defects in the surface region of each specimen was measured, giving a simple representation of the measurable defect size. Fig. 9 shows the fatigue data for all specimens, where the marker is plotted as the size of the surface defect. In Fig. 10, the measured defect area is shown for one specimen of each geometry, the defects are marked in red.

In order to further investigate the relation between the fatigue life and the defect size, the position of each fatigue data with respect to the confidence band was plotted versus the defect size, this is shown in Fig. 11a, b, d and e. Here the marker size is indicating the size of the defects, A_d, measured. A comparison of the defect size in the different specimens is shown in Fig. 11c.

4.5. Failure Site

Generally, for notched components, the crack initiation site is at the position of the maximum stress, i.e. the notch root for mode I loading. The specimens investigated here did not show this typical behaviour. The failure was often occurring from the downward facing surface region, and as seen in the previous section, the specimens failed from surface defects such as lack of fusion. The position of the failure site was measured in the build direction for all specimens. The relative height in the notch was considered by h/h_0, where h is the height of failure initiation in build direction, and h_0 is the total height of the notch, as defined in Fig. 12f. The failure site, measured as relative height in the notch, was further compared with the position of the specimen in the confidence bands. The result is shown in Fig. 12a, b, d and e. In the plots, the dashed lines are indicating the notch bisector line.

In the unnotched specimens failure is occurring with a large scatter in h/h_0. The semi-circular specimens are failing from the overhang region, with less scatter than the unnotched. For the v-notches, the failure is approaching the notch root as the notch radius decreases. The failure site was plotted versus the radius of the notch in Fig. 12c. The following observations were made: (1) The general trend is that as the notch radius decreases, the scatter decreases. (2) There is no dependency between confidence bands and failure site, unlike what was seen when evaluating defect size. (3) With a blunt notch and high amount of overhang the specimens are failing from the overhang region.

4.6. Strain Energy Density

ASED analysis were performed in Abaqus. The results for ASED analysis are shown in Fig. 13a and b, with $R_0 = 0.13$ mm. In Fig. 13a, ASED are shown for the fatigue data of both v-notches, while in b, the fatigue data for semi-circular specimens are added. Confidence bands at 2.3 %, 50 % and 97.7 % are shown in the plots. ASED of the fatigue data are presented in a scatter bands with scatter parameter $T_{\Delta W} = 1.45$ and inverse slope $k = 1.45$ for the first case and $T_{\Delta W} = 2.51$ and $k = 1.50$ for the second case.

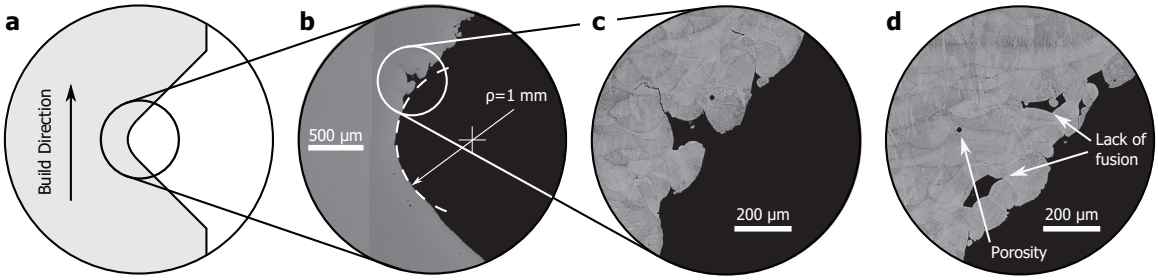

Figure 7: V-notch specimen with 1 mm radius tested until 2×10^6 cycles; (a) Schematic illustration of notch and build direction; (b) Optical micrograph of centre plane of specimen, polished; (c) Microstructure and defect initiating fatigue crack growth; (d) Microstructure and defects in downward facing region.

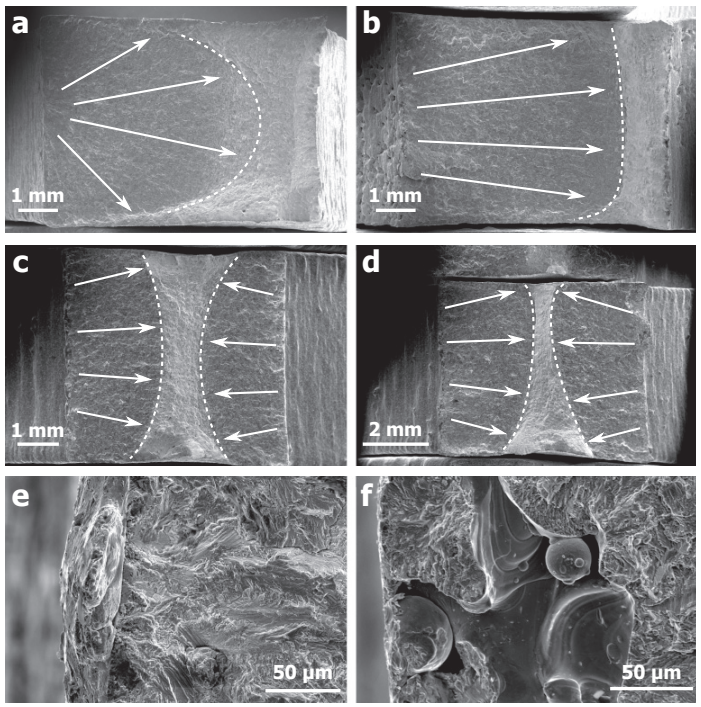

Figure 8: Fracture surface for different specimen: (a) Unnotched speicmen, crack growth from one side; (b) Semi-circular notch, crack growth from one side; (c) v-notch 1 mm radius, crack growth from both sides; (d) v-notch 0.1 mm radius, crack growth from both sides; (e) Defect from unnotched specimen; (f) Defect from v-notch specimen with 1 mm radius, lack of fusion defect, unfused powder particle visible.

5. Discussion

Fatigue behaviour for different notch geometries of AM Inconel 718 has been studied. Fractography was conducted by SEM, and all specimens were found to fail from defects in the surface region. Failure initiation site, as relative height in the notch, was obtained for all specimens. For decreasing notch radius, decreasing scatter in failure initiation site was obtained. Based on the defects found in fracture surfaces, and the failure initiation sites, it is believed that there are two main competing factors for crack initiation in the specimens; local and global notches. The global notches being the notch geometries studied, and local notches being notches/defects caused by the poor surface quality distributed all over the surface of the specimens, and the size of the defects being dependent on the amount of overhang.

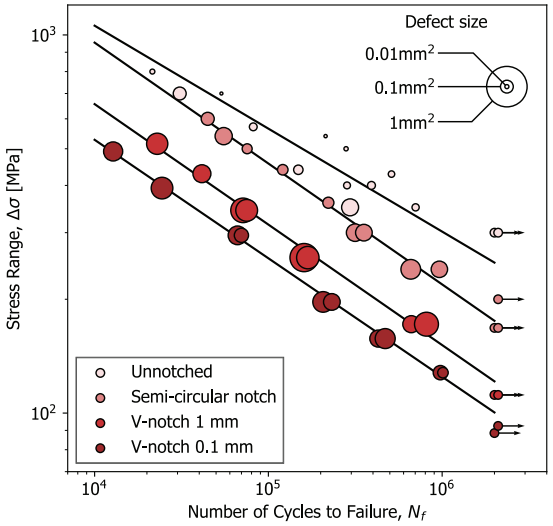

Figure 9: Fatigue data for all specimen geometries, with marker size as measured defect area from crack initiation. Loading ratio R=0.

5.1. Notch sensitivity

From the fatigue data obtained, the fatigue notch factor and notch sensitivity were evaluated and compared to the elastic stress concentration factor. According to the formulation of notch sensitivity [47], the notch sensitivity decreases, as the notch radius decreases. That is also the case for the AM Inconel 718 specimens investigated here; the notch sensitivity is decreased as the radius of the notch is decreased. The formulation of notch sensitivity states that if the notch has no effect, the notch sensitivity is equal to zero, while if the notch has a full effect, notch sensitivity is equal to one. For both v-notches, the notch sensitivity is between zero and one, as expected. The semi-circular notch, however, showed a notch sensitivity above one, which should not be possible.

The unnaturally high notch sensitivity obtained for semi-circular specimen can be explained by the specimens failing from lack of fusion defects, far away from the notch root, as seen in Fig. 12. The combination of notch sensitivity above one and specimens failing from defects in the downward facing region of the notch indicates that for this geometry the local defects are stronger mechanisms for fatigue than the global notch geometry. Further, it can be argued that the values obtained for notch sensitivity does not describe the material properties, but rather a combination of material and ”component” properties, including geometrical effects from the build. Another possible factor influencing the unnaturally high notch sensitivity seen in the semi-circular specimens can be that the unnotched specimens have $K_t = 1.07$ and not $K_t = 1.00$. However, this should account for a small change in the value of notch sensitivity.

5.2. Scatter bands

In the case of the S-N data presented in Fig. 5, the size of the scatter bands for the different specimen geometries is decreasing as the notch radius is decreasing. The variation of defect size is decreasing as the notch radius is decreasing, so is the variation of the failure initiation site. These observations can be connected to the idea that fatigue is a weakest link mechanism. In the notched specimens the global notch is competing with the local defects, as blunt notch specimens show large defects and are not failing from the notch root, while when the notch radius is decreasing, the failure site is localising at the notch root again. For the unnotched specimens, it seems more arbitrary if there is a defect present and where it is located, as the surface region close to the gauge section has a low degree of overhang and the stress concentration is low and equal to $K_t = 1.07$.

5.3. Fractography

The fracture surfaces were investigated for all specimens, and it was found that all specimens had crack initiation from defects in the surface region. It was also found that unnotched specimens failed from one local defect, with no particular sign of lack of fusion, while the notched specimens failed from larger defects, caused by lack of fusion, distributed along the whole edge of the specimen.

In this work the defect size is related to the fatigue life by the scatterbands, this is similar to the approach of Tammas-Williams et al. for machined Ti6Al4V specimens [13]. For the unnotched specimens, a strong dependence between the confidence band and the defect size was found, this was also seen in the specimens of Tammas-Williams et al. For the notch specimens less dependence between defect size and scatter bands was found, also the scatter bands were smaller.

5.4. Failure initiation site

The position of failure initiation site measured as relative height in notch, was obtained for all specimens. Results showed that the unnotched specimens had a large scatter in failure initiation sites, but on average the specimens failed from the centre.

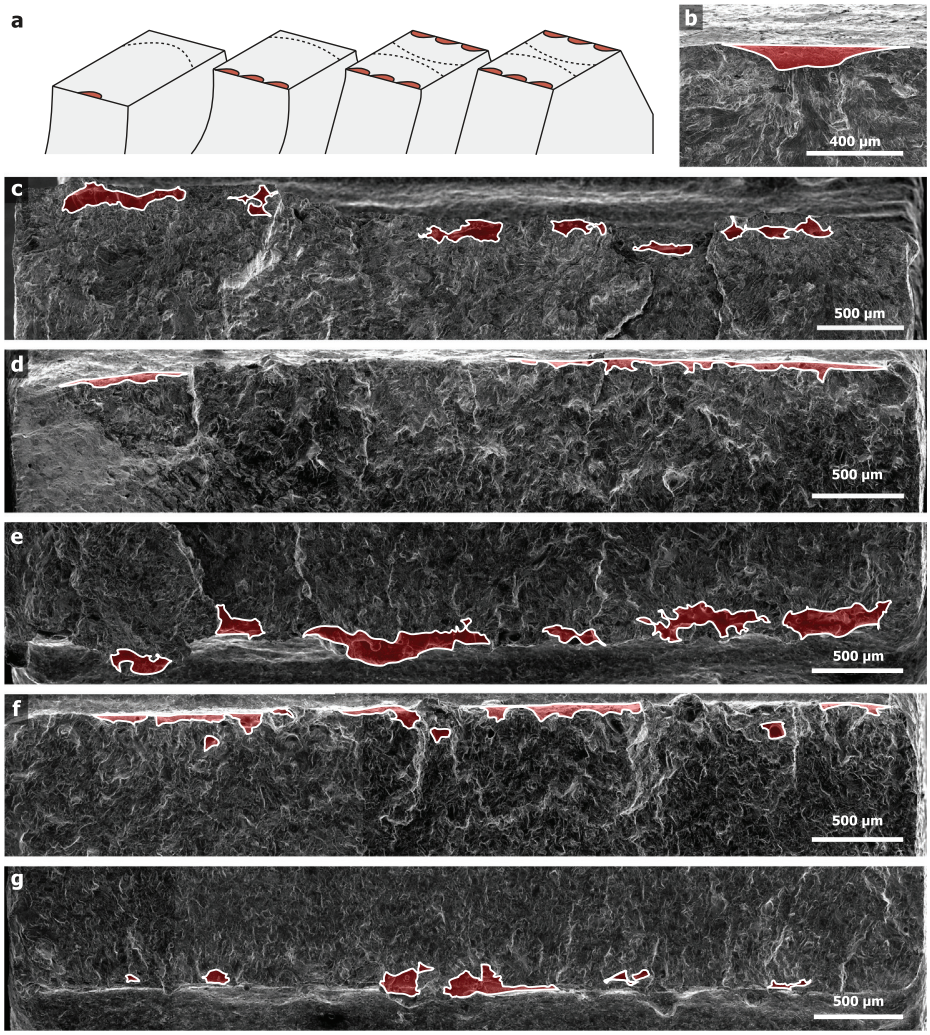

Figure 10: (a) Schematic illustration of fracture surface of unnotched, semi-circular, and v-notch specimens. Fractography of defects in specimens: (b) unnotched; (c) semi-circular; (d, e) v-notch radius 1 mm; (f, g) v-notch radius 0.1 mm.

The semi-circular notch specimens have a weak stress concentration factor (K_t=1.31), and the failure was governed by the lack of fusion defects in the overhang region of the notch. With a decreasing notch radius and an increased stress concentration factor, the scatter was decreased, and the position of the failure site was moved closer to the notch root.

Based on these observations a diagram relating the position of failure to the acuity of the notch was created. The diagram is shown in Fig. 14, and is considering the average failure initiating position and standard deviation for each geometry, in terms of relative height in the notch, h/h_0. The acuity of the notch is described by a geometrical based parameter

$$\left(\frac{d}{\rho}\right)^{(1-\lambda)}, \tag{5}$$

where d is the depth of the notch, ρ is the notch radius and λ is the Williams' series eigenvalue [35], a parameter dependent on the notch opening angle. AM metal parts will always have a finite resolution based on the accuracy of the manufacturing method, the notch radius will therefore never be zero, and the notch acuity parameter will always be defined. The dashed line

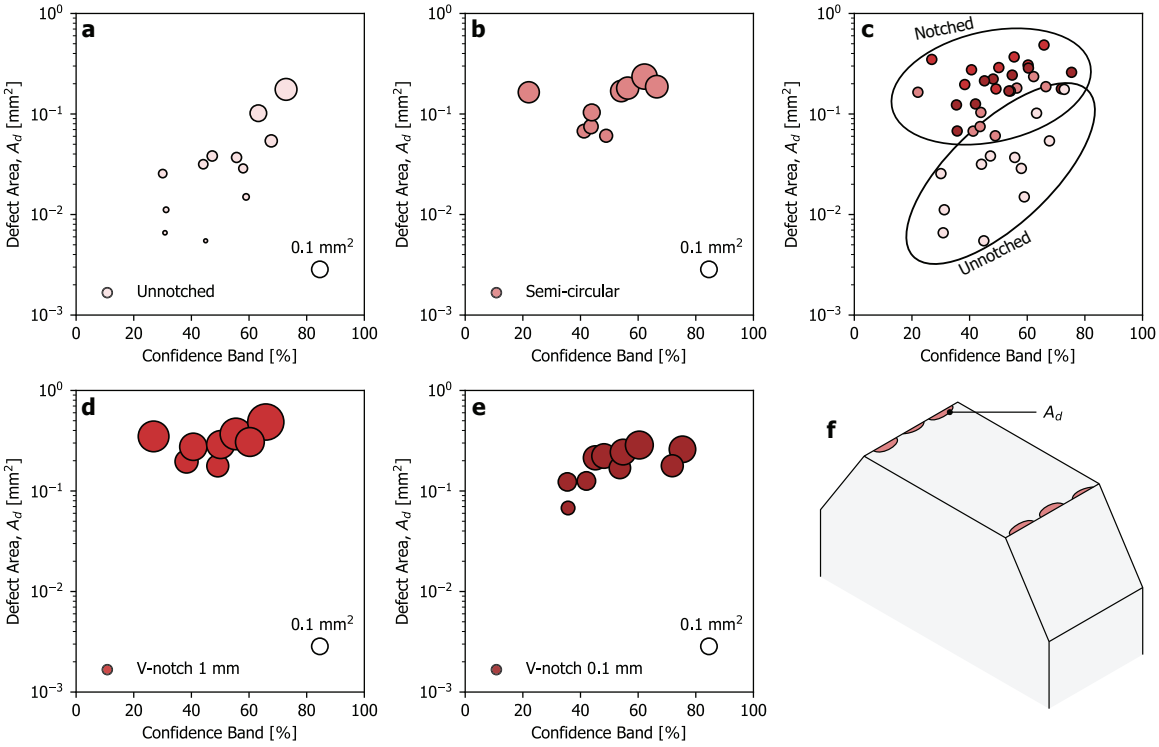

Figure 11: Dependency between defect size initiating fatigue and placement in scatter band: (a,b,d,e) Unnotched specimen, semi-circular specimen, v-notch 1 mm radius and v-notch 0.1 mm radius respectively; (c) All specimens; (f) Schematic illustration of cross section and defect size, A_d.

in the diagram is representing the centre of the notch, e.i. the position of maximum stress.

The diagram shows that: (1) For a decreasing notch acuity, the scatter in failure initiation site is decreased. (2) At some combination of stress concentration due to the notch and amount of overhanging surface, the failure is occurring from the overhang region. (3) Gives some indication of whether the local defects or the notch geometry is controlling the failure initiation site. The diagram can easily be extended to other build orientations and altered based on the particularities of the AM method.

5.5. Strain Energy Density

When evaluating the structural integrity of AM metallic components it is evident that parameters such as residual stresses, geometrical defects, surface roughness, distortions and microstructure deriving from the manufacturing process are influencing factors. However, taking into account all of these parameters is a task too complex from a practical point of view. The process parameters used for additive materials are continuously being improved; hence, the aim of this work is not reporting the fatigue data from some specific process and material, but rather addressing a general problem related to the interaction between defects and component geometry, which to some degree will always be present in as-built AM components, e.g. machining of surfaces will not always be possible due to the geometrical complexity of the component. Energy based approaches such as ASED, not sensitive to mesh size, could be a way to deal with these kinds of problems; however, there are some challenges.

Few data exist of what should be used as the critical radius of Inconel 718. Notched fatigue data of Inconel 718 by Chen et al. [24], was analysed by use of critical distance by Louks and Susmel [46], using a critical distance of 0.15 mm. In the case of the AM specimens investigated here, a critical radius of 0.13 mm was used, which is close to the value proposed for critical distance. It should be noted that the material of Chen et al. was heat treated and machined, in contrast to the material considered here, which was produced by SLM and tested as-built.

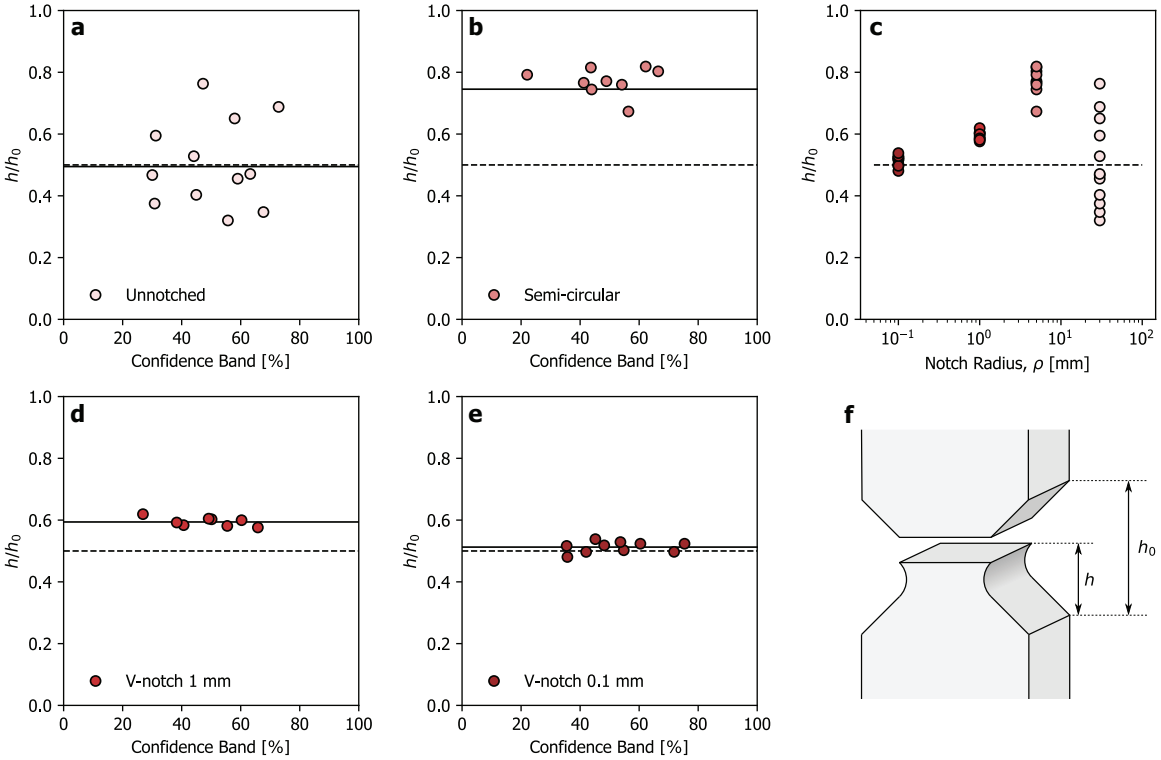

Figure 12: Failure initiation site for different specimens: (a,b,d,e) Height of failure for the different geometries; (c) Failure site versus notch radius; (f) Schematic illustration of relative height in notch.

Also, the theory of critical distances and ASED are different, but the reported result of distance proposed by Louks and Susmel for critical distance can be taken as a reference value.

From the Atzori-Lazzarin diagram re-interpreted in terms of ASED it is evident that if either fracture mechanics or notch mechanics apply, ASED can be applied. However, in the case of the specimens investigated here, there is an interaction between local and global defects. Global defects can be considered by linear notch mechanics, and local defects can be considered by fracture mechanics, by for example the $\sqrt{\text{area}}$-method, as previously seen in literature for AM metals [13–17]. It should be noted that the $\sqrt{\text{area}}$-method only considers the defect area initiating fatigue and not the interaction of several defects.

Here, ASED of the specimens was evaluated to see if it was possible to present fatigue data for AM specimens in unified scatter bands, and to uncover challenges related to it. The diagram proposed in Fig. 14 shows that based on a combination of notch acuity and amount of overhang, failure is controlled by local or global geometrical effects.

The results for ASED of the v-notch geometries in Fig. 13a, shows that both the v-notch geometries are coinciding with the unnotched fatigue strength at 2×10^6 cycles, with a scatter of $T_{\Delta W} = 1.45$. When also taking into account the value from the semi-circular notch, in Fig. 13b, the scatter is increased, and the data is not coinciding with the rest of the data. From the results, it seems that when the failure is initiating at notch tip or close to it, and the notch is a stronger and/or comparable strength as the local defects, it is possible to apply it. But in the case of the semi-circular specimens, the failure is governed by the local defects, and linear notch mechanics can not be applied. The threshold of which is the stronger factor for initiating fatigue, of the local and global defects, should be further studied in order develop understanding of which of them should be evaluated, and which could be taken as statistical scatter.

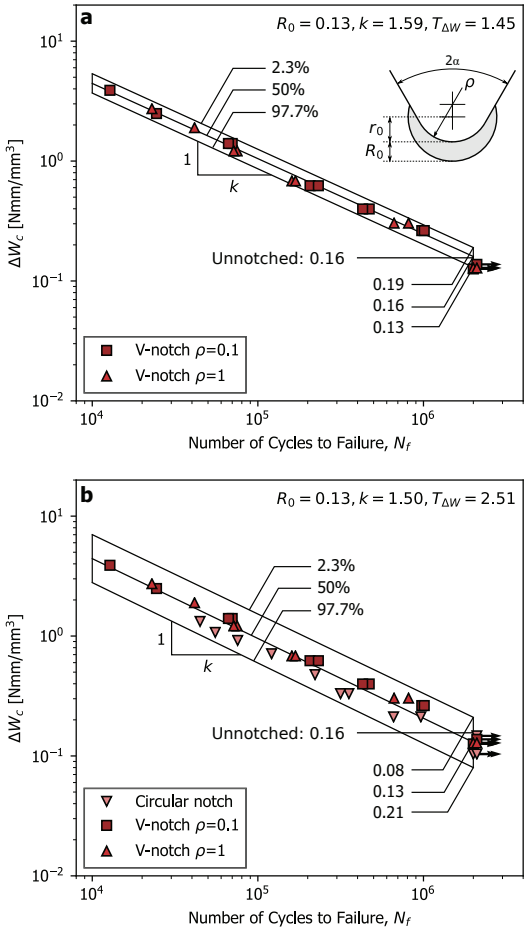

Figure 13: ASED versus number of cycles to failure for: (a) V-notch specimens;(b) All notch specimens

6. Conclusion

Fatigue assessment of different notched as-built AM Inconel 718 specimens produced by SLM has been conducted. The main findings can be summarised as:

1. Stress concentration factor, fatigue notch factor and notch sensitivity were obtained for the different geometries. The fatigue notch factor was increasing with deceasing notch radius. For the v-notched specimens, a notch sensitivity between zero and one was obtained, while for the semi-circular specimens, a notch sensitivity above one was obtained. This effect was assigned to the poor surface quality obtained building downward facing surfaces. It is also suggesting that the values obtained, when evaluating notch sensitivity of AM as-built specimens, are not valid as a material parameter, but rather as a material-component parameter.
2. The scatter in fatigue life and the scatter in the position of failure, with respect to the notch bisector line, in specimens was reduced with deceasing notch radius. This effect was assigned to the interaction between global and local stress risers, i.e. notch geometry and local defects from overhanging region. For low stress concentration from the notch geometry, the local defects are the stronger mechanism, and a large scatter is seen, while for stronger stress concentration from the notch geometry the failure is localising at the notch root.
3. All specimens were found to fail from defects in the surface region. The unnotched specimens failed from localised defects, while the notched specimens failed from larger defects, caused by lack of fusion, distributed along the whole edge of the notch. A strong dependency between the area of the defect and placement in confidence bands was found for unnotched specimens; a weaker dependency was obtained for notched specimens.
4. A diagram relating the scatter in failure position, with respect to the notch bisector line, to the notch acuity was proposed. The diagram gives an indication whether the notch geometry or the local defects is the driving mechanism for fatigue, and where failure can be expected in a notch geometry.
5. The fatigue data was analysed by means of ASED. The analysis showed that it was possible to present specimens failing from the notch root, or in the region close to it, in unified scatter bands.

Acknowledgement

Funding: This work was supported by the Norwegian Centre for International Cooperation in Education [PNA-2017/10077]; and Norwegian University of Science and Technology.

References

[1] J. Pegues, M. Roach, R. S. Williamson, N. Shamsaei, Surface roughness effects on the fatigue strength of additively manufactured ti-6al-4v, International Journal of Fatigue 116 (2018) 543 – 552.

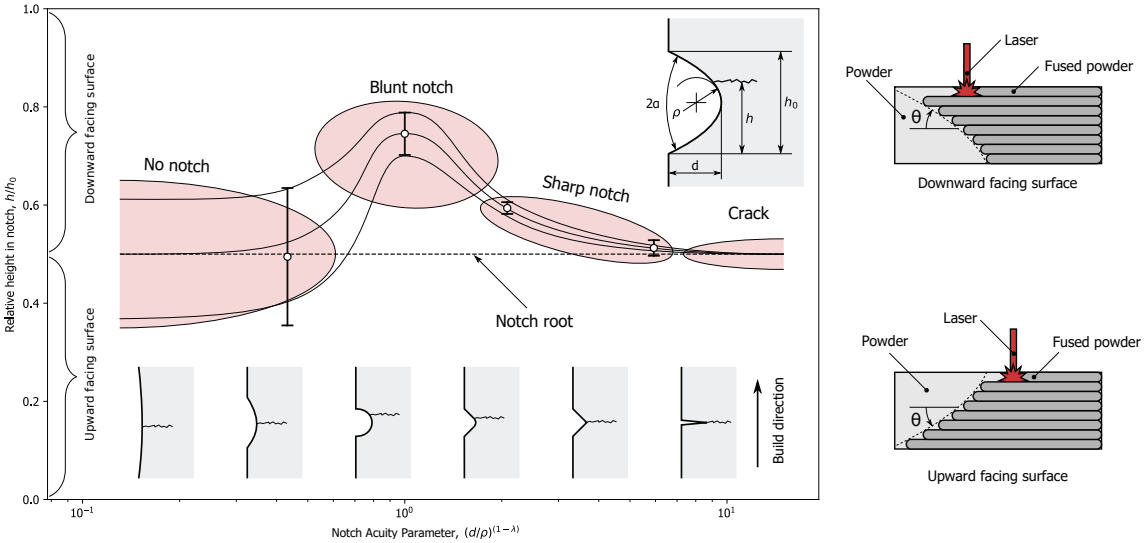

Figure 14: Diagram relating failure initiation site in a notched region to the notch acuity.

[2] J. J. Lewandowski, M. Seifi, Metal additive manufacturing: A review of mechanical properties, Annual Review of Materials Research 46 (1) (2016) 151–186.

[3] T. DebRoy, H. Wei, J. Zuback, T. Mukherjee, J. Elmer, J. Milewski, A. Beese, A. Wilson-Heid, A. De, W. Zhang, Additive manufacturing of metallic components process, structure and properties, Progress in Materials Science 92 (2018) 112 – 224.

[4] A. Yadollahi, N. Shamsaei, Additive manufacturing of fatigue resistant materials: Challenges and opportunities, International Journal of Fatigue 98 (2017) 14 – 31.

[5] G. Nicoletto, Directional and notch effects on the fatigue behavior of as-built dmls ti6al4v, International Journal of Fatigue 106 (2018) 124 – 131.

[6] R. Mertens, S. Clijsters, K. Kempen, J.-P. Kruth, Optimization of scan strategies in selective laser melting of aluminum parts with downfacing areas, Journal of Manufacturing Science and Engineering 136.

[7] D. Wang, Y. Yang, Z. Yi, X. Su, Research on the fabricating quality optimization of the overhanging surface in slm process, The International Journal of Advanced Manufacturing Technology 65 (9) (2013) 1471–1484.

[8] M. Seifi, A. Salem, J. Beuth, O. Harrysson, J. J. Lewandowski, Overview of materials qualification needs for metal additive manufacturing, JOM 68 (3) (2016) 747–764.

[9] R. Molaei, A. Fatemi, N. Phan, Significance of hot isostatic pressing (hip) on multiaxial deformation and fatigue behaviors of additive manufactured ti-6al-4v including build orientation and surface roughness effects, International Journal of Fatigue 7 (2018) 352 – 370.

[10] S. Tammas-Williams, P. J. Withers, I. Todd, P. B. Prangnell, The effectiveness of hot isostatic pressing for closing porosity in titanium parts manufactured by selective electron beam melting, Metallurgical and Materials Transactions A 47 (5) (2016) 1939–1946.

[11] S. Tammas-Williams, H. Zhao, F. Lonard, F. Derguti, I. Todd, P. Prangnell, Xct analysis of the influence of melt strategies on defect population in ti6al4v components manufactured by selective electron beam melting, Materials Characterization 102 (2015) 47 – 61.

[12] S. M. J. Razavi, G. G. Bordonaro, P. Ferro, J. Torgersen, F. Berto, Fatigue behavior of porous ti-6al-4v made by laser-engineered net shaping, Materials 11 (2).

[13] S. Tammas-Williams, P. Withers, I. Todd, P. Prangnell, The influence of porosity on fatigue crack initiation in additively manufactured titanium components, Scientific Reports 7 (2017) 7308.

[14] H. Masuo, Y. Tanaka, S. Morokoshi, H. Yagura, T. Uchida, Y. Yamamoto, Y. Murakami, Influence of defects, surface roughness and hip on the fatigue strength of ti-6al-4v manufactured by additive manufacturing, International Journal of Fatigue 117 (2018) 163 – 179.

[15] G. Meneghetti, D. Rigon, C. Gennari, An analysis of defects influence on axial fatigue strength of maraging steel specimens produced by additive manufacturing, International Journal of Fatigue 118 (2019) 54 – 64.

[16] J. Gunther, D. Krewerth, T. Lippmann, S. Leuders, T. Troster, A. Weidner, H. Biermann, T. Niendorf, Fatigue life of additively manufactured ti6al4v in the very high cycle fatigue regime, International Journal of Fatigue 94 (2017) 236 – 245, fatigue and Fracture Behavior of Additive Manufactured Parts.

[17] Y. Yamashita, T. Murakami, R. Mihara, M. Okada, Y. Murakami, Defect analysis and fatigue design basis for ni-based superalloy 718 manufactured by selective laser melting, International Journal of Fatigue 117 (2018) 485 – 495.

[18] Y. Murakami, Chapter 2 - stress concentration, in: Y. Murakami (Ed.), Metal Fatigue, Elsevier Science Ltd, Oxford, 2002, pp. 11 – 24.

[19] F. Berto, P. Lazzarin, Recent developments in brittle and quasi-brittle failure assessment of engineering materials by means of local approaches, Materials Science and Engineering: R: Reports 75 (2014) 1 – 48.

[20] Averaged strain energy density evaluated rapidly from the singular peak stresses by fem: cracked components under mixed-mode (i+ii) loading, Theoretical and Applied Fracture Mechanics 79 (2015) 113 – 124, recent

development of Energy density methods: Mechanics of solids (EDMS).

[21] A. Campagnolo, G. Meneghetti, F. Berto, Rapid finite element evaluation of the averaged strain energy density of mixed-mode (i+ii) crack tip fields including the t-stress contribution, Fatigue & Fracture of Engineering Materials & Structures 39 (8) 982–998.

[22] G. Meneghetti, A. Campagnolo, F. Berto, Averaged strain energy density estimated rapidly from the singular peak stresses by fem: Cracked bars under mixed-mode (i+iii) loading, Engineering Fracture Mechanics 167 (2016) 20 – 33, sI:CRACK PATHS 2015.

[23] S. Razavi, P. Ferro, F. Berto, J. Torgersen, Fatigue strength of blunt v-notched specimens produced by selective laser melting of ti-6al-4v, Theoretical and Applied Fracture Mechanics 97 (2018) 376 – 384.

[24] Evaluation of notched fatigue strength at elevated temperature by linear notch mechanics, International Journal of Fatigue 21 (9) (1999) 925 – 931.

[25] N. Kawagoishi, Q. Chen, H. Nisitani, Fatigue strength of inconel 718 at elevated temperatures, Fatigue & Fracture of Engineering Materials & Structures 23 (3) 209–216.

[26] D. Witkin, D. Patel, G. Bean, Notched fatigue testing of inconel 718 prepared by selective laser melting, Fatigue & Fracture of Engineering Materials & Structures 0 (0).

[27] R. Konen, L. Kunz, G. Nicoletto, A. Baa, Long fatigue crack growth in inconel 718 produced by selective laser melting, International Journal of Fatigue 92 (2016) 499 – 506, fatigue crack paths 2015.

[28] H. Neuber, Kerbspannungslehre, Springer-Verlag, 1958.

[29] H. Neuber, ber die bercksichtigung der spannungskonzentration bei festigkeitsberechnungen, Konstruktion 20 (7) (1968) 245–251, cited By 246.

[30] E. Beltrami, Sulle condizioni di resistenza dei corpi elastici, rend. r. ist. lombardo di scienze, Lettere e Arti 18 (1885) 704, cited By 1.

[31] G. Sih, B. Cha, A fracture criterion for three-dimensional crack problems, Engineering Fracture Mechanics 6 (4) (1974) 699 – 723.

[32] Mechanics of Fracture Initiation and Propagation, Kluwer, 1991.

[33] P. Lazzarin, R. Zambardi, A finite-volume-energy based approach to predict the static and fatigue behavior of components with sharp v-shaped notches, International Journal of Fracture 112 (3) (2001) 275–298.

[34] P. Lazzarin, R. Tovo, A unified approach to the evaluation of linear elastic stress fields in the neighborhood of cracks and notches, International Journal of Fracture 78 (1996) 3–19.

[35] M. L. Williams, On the stress distribution at the base of a stationary crack, Journal of Applied Mechanics 24(1) (1956) 109–114.

[36] F. Berto, A. Campagnolo, P. Lazzarin, Fatigue strength of severely notched specimens made of ti6al4v under multiaxial loading, Fatigue & Fracture of Engineering Materials & Structures 38 (5) (2014) 503–517.

[37] G. Meneghetti, A. Campagnolo, F. Berto, K. Tanaka, Notched ti-6al-4v titanium bars under multiaxial fatigue: Synthesis of crack initiation life based on the averaged strain energy density, Theoretical and Applied Fracture Mechanics 96 (2018) 509 – 533.

[38] A. Campagnolo, G. Meneghetti, F. Berto, K. Tanaka, Crack initiation life in notched steel bars under torsional fatigue: Synthesis based on the averaged strain energy density approach, International Journal of Fatigue 100 (2017) 563 – 574, multiaxial Fatigue 2016: Experiments and Modeling.

[39] B. Atzori, P. Lazzarin, Notch sensitivity and defect sensitivity under fatigue loading: Two sides of the same medal, International Journal of Fracture 107 (1) (2001) 1–8.

[40] P. Lazzarin, F. Berto, From neuber's elementary volume to kitagawa and atzori's diagrams: An interpretation based on local energy, International Journal of Fracture 135 (1) (2005) L33–L38.

[41] H. Kitagawa, S. Takahashi, Applicability of fracture mechanics to very small cracks in the early stage, in: Procs. Second International Conference on Mechanical Behaviour of Materials.

[42] W. D. Pilkey, D. F. Pilkey, Peterson's Stress Concentration Factors, Wiley, New Yersey, 2008.

[43] ASTM E407-07(2015)e1, Standard Practice for Microetching Metals and Alloys, ASTM International, West Conshohocken, PA, 2015, www.astm.org.

[44] Inconel alloy 718, Tech. rep., Special Metals (2018).

[45] R. Branco, J. D. M. Costa, F. Berto, S. M. J. Razavi, J. A. M. Ferreira, C. Capela, L. Santos, F. Antunes, Low-cycle fatigue behaviour of aisi 18ni300 maraging steel produced by selective laser melting, Metals 8 (1).

[46] R. Louks, L. Susmel, The linear-elastic theory of critical distances to estimate high-cycle fatigue strength of notched metallic materials at elevated temperatures, Fatigue & Fracture of Engineering Materials & Structures 38 (6) (2014) 629–640.

[47] H. Neuber, Theory of Notch Stresses, 2nd Edition, Springer, Berlin, 1958.

Nomenclature

AM	Additive Manufacturing
ASED	Average Strain Energy Density
CT	Computed Tomography
FE	Finite Element
HIP	Hot Isostatic Pressing
PBF	Powder Bed Fusion
SED	Strain Energy Density
SEM	Scanning Electron Microscopy
SLM	Selective Laser Melting
2α	Notch opening angle
a, d	Crack/Notch depth
a_0	Lower threshold value of notch depth
a^*	Short crack/notch
A_d	Total defect area
ΔK_I	Notch Stress Intensity Range
$\Delta\sigma$	Stress range
$\Delta\sigma^S$	Stress range unnotched specimen
$\Delta\sigma^N$	Stress range notched specimen
E	Young's Modulus
h	Failure site in notch
h_0	Height of notch opening in build direction
K_I^V	Generalised stress intensity factor
k	Inverse slope of scatter bands
K_f	Fatigue notch factor
K_t	Stress concentration factor
λ_I	Eigenvalue of Willams' series
N_f	Number of cycles to failure
q	Notch sensitivity
R	Loading ratio
R_0	Critical radius
r_0	Centroid of critical radius
ρ	Notch radius
σ_t	Tensile strength
σ_{max}	Maximum stress
$T_{\Delta\sigma}$	Scatter parameter
$\bar{W}$	Average Strain Energy Density
W_c	Critical Average Strain Energy Density

Article III

A diagram for capturing and predicting failure locations in notch geometries produced by additive manufacturing

Klas Solberg, Filippo Berto

International Journal of Fatigue, Technical note

In a recent work by the authors Solberg and Berto (2019), as-built notch geometries of Inconel 718 produced by selective laser melting was investigated under fatigue loading. One of the findings was that fatigue did not initiate from the notch roots, but from defects adjacent. A diagram was developed for capturing the failure locations. Here, a generalized formulation of the diagram is proposed. The model can be useful for developing understanding of which is the dominant feature determining the failure locations; local or global notch geometries.

https://doi.org/10.1016/j.ijfatigue.2019.105428

A diagram for capturing and predicting failure locations in notch geometries produced by additive manufacturing

Klas Solberg[a,*], Filippo Berto[a]

[a]*Department of Mechanical and Industrial Engineering, Norwegian University of Science and Technology, 7034 Trondheim, Norway*

Abstract

In a recent work by the authors [1], as-built notch geometries of Inconel 718 produced by selective laser melting was investigated under fatigue loading. One of the findings was that fatigue did not initiate from the notch roots, but from defects adjacent. A diagram was developed for capturing the failure locations. Here, a generalized formulation of the diagram is proposed. The model can be useful for developing understanding of which is the dominant feature determining the failure locations; local or global notch geometries. The diagram can be applied in various loading cases, ranging from fatigue to static loading.

Keywords: Failure Location, Fatigue, Additive Manufacturing, Defects

1. A diagram for predicting failure location

When dealing with fatigue and fracture of materials and structures, three main questions arise, namely: (1) How much load does it carry? (2) How long does it carry it? And (3) Where does the failure occur? The first two questions are usually emphasized, while the third question remains as a "matter of course". Failure is, of course, occurring in the critical region. So where is this critical region located? At the sharpest notch? At the highest peak stress? At the highest critical distance stress?

There are many useful criteria capable of predicting failure locations, ranging between brittle and ductile, uniaxial and multiaxial, static and fatigue, local and global. In some cases it is common to report the failure location or the failure mode, this is usually done when dealing with weldments [2], Lattice structures [3], buckling [4] and in general for failure investigations of real structures. One of the reasons for the failure location not being a matter of interest could be the test set-ups (and standardisations of mechanical testing), which are designed for having damage localized in one specific region [5, 6]. Another reason could be that it requires effort dealing with the statistics and the variations in the observations, especially if the findings do not support the conclusions of the work.

In the case of additive manufacturing (AM), reporting the failure location can be very useful for understanding the mechanical performance. There are two main reasons:

1. The freedom of design made possible with AM increases the probability of designing complex structures containing notches of different scales, orientations and acuities [3, 7–9]
2. The material properties and the manufacturing defects are dependent on the build history, including the geometry of the build [10–14].

Some of the common manufacturing defects in AM are anisotropic microstructure [15, 16], residual stresses [17, 18], porosity [19], lack-of-fusion [20, 21], and high surface roughness [22, 23]. In particular, the surface roughness and the amount of defects in the surface region are dependent on the orientation of the surface [12, 24]. This means that the combination of complex geometries and manufacturing defects from the process can result in failure initiating from unexpected locations.

Fatigue assessment of AM components is usually done based on manufacturing defects, employing the $\sqrt{area}$-method of Murakami [25]. The defects can be captured either by fractography [26, 27] or by computed tomography[28]. In the $\sqrt{area}$-method, the location of the defects within the cross-section has to be taken into account. Probabilistic approaches for fatigue assessment has also been developed [29, 30]. In particular, the method proposed by Romano *et al.* is interesting, analysing the

*Corresponding author
Email address: klas.solberg@ntnu.no (Klas Solberg)

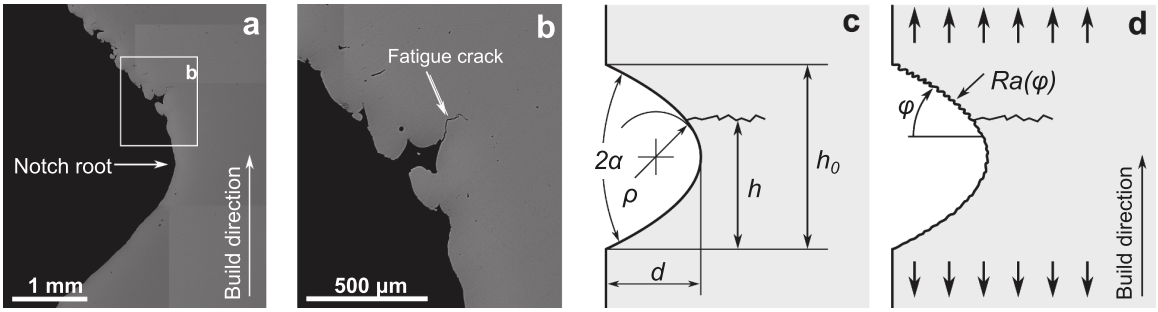

Figure 1: **a** Cross section of a notch geometry built by AM and subjected to fatigue loading. **b** Detail of a fatigue crack initiating from a defect. **c** Generalized notch geometry with dimensions. **d** Schemtic illustration of a notch geometry built by AM, with higher surface roughness in the down-skin surface.

location, distribution and size of internal porosity in the presence of notches [29].

In a recent study by the authors [1], it was shown that in as-build AM Inconel 718, fatigue did not initiate from the notch roots in various notch geometries. In Fig. 1a, a polished cross-section of a notched specimen subjected to 2×10^6 cycles is shown. The down-skin surface displays higher surface roughness than the up-skin surface. Fig. 1b shows a fatigue crack initiating from a defect in the down-skin region. A generalized notch geometry is shown in Fig. 1c, and the surface effect generally observed in AM is illustrated in Fig. 1d.

In the work mentioned above, different symmetric double-notched specimen geometries were tested, and the failure locations in the specimens were captured. A brief description of the specimens and some key data are presented in Appendix A; further information can be found in ref. [1]. Based on the results, a diagram was proposed for capturing the failure location in AM Inconel 718 notch geometries. A schematic illustration of the diagram is shown in Fig. 2a. The vertical axis describes the relative height in the notch, h/h_0, and the horizontal axis is the notch acuity, ξ.

The diagram can be separated into three sections: unnotched, blunt notch and sharp notch. The regions are shaded in Fig. 2a. For a low notch acuity (unnotched) a large scatter in the failure locations were observed; however, on average, the specimens failed from the notch bisector line. Here, the position of the critical defect is controlling the failure location. For a high notch acuity (sharp notch), failure was occurring at the notch root, with a small scatter. In this case, the notch is controlling the failure location. In the intermediate case between unnotched and sharp notch, we have a blunt notch, here the specimen is not failing from the notch root, but from the down-skin region adjacent. This is due to the defects, as shown in Fig. 1a and b.

Based on the design of the specimens in ref. [1], three competing features controlling the failure location can be identified: (1) Variation in cross-section width (2), macroscopic stress from the notch and (3) the local stress from the defects. In Appendix B, two parametric studies are included; One showing the effect of the macroscopic stresses by varying the notch acuity and one showing the effect of the cross-sectional width for a constant notch acuity.

In this work, an analytical framework for the trend lines in the diagram (Fig. 2a) is proposed, along with some possible applications.

2. Analytical formulation

The diagram compares the notch acuity and location of failure initiation. The notch acuity, ξ, is defined as

$$\xi = \log_{10}(d/\rho). \tag{1}$$

Where ρ is the notch radius and d is the notch depth. The notch acuity corresponds to the exponent of the ratio d/ρ *e.g.* $1/1 = 10^0 \Rightarrow \xi = 0$. The location of failure is defined as the relative height in the notch h/h_0, as shown in Fig. 1c.

The diagram and the model are shown in Fig. 2b and consists of three functions; H_a, H_u and H_l, where H_a is the average/mean position of failure, H_u and H_l is the upper and lower predicted positions of the scatter bands based on *e.g.* two standard deviations in failure location. The three functions are de-

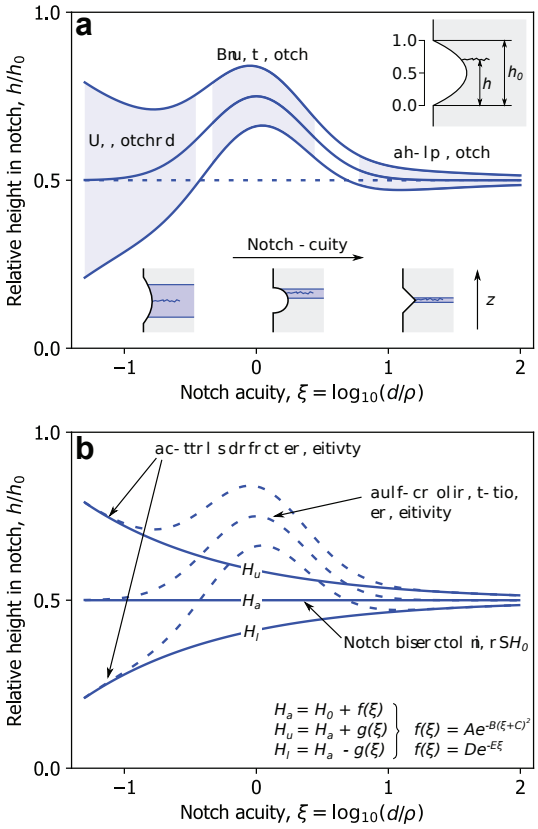

Figure 2: **a** Schematics of initial diagram developed for AM Inconel 718 from [1] **b** Generalised diagram and model

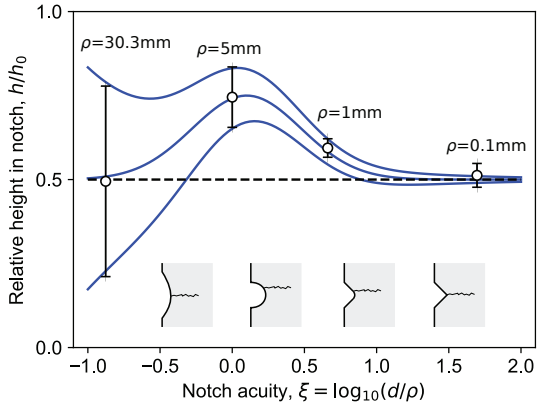

Figure 3: Model fitted to data from additively manufactured as-built specimens of Inconel 718 [1]

fined as

$$H_a = H_0 + f(\xi) \tag{2}$$

$$H_u = H_a + g(\xi) \tag{3}$$

$$H_l = H_a - g(\xi) \tag{4}$$

where

$$f(\xi) = Ae^{-B(\xi+C)^2} \tag{5}$$

$$g(\xi) = De^{-E\xi}. \tag{6}$$

H_0 is the location of the notch bi-sector line, *i.e.* 0.5 for a symmetric notch. $f(\xi)$ describes the roughness-dependence of the surface orientation, *i.e.* $f(\xi)$ is non-zero if the surface roughness is dependent on the build orientation of the surface (which is common in AM metals [23, 31, 32]). However, if the surface roughness is not dependent on the build orientation $f(\xi)$ is equal to zero. $g(\xi)$ is describing the scatter in failure locations. It reflects the trend in failure locations occurring with a small scatter for high notch acuity and larger scatter for low notch acuity.

The functions $f(\xi)$ and $g(\xi)$ consists of the parameters: A, B, C, D and E. First considering $f(\xi)$, A is a parameter describing the sensitivity of the build orientation, the height of the perturbation, it should be in in the range of 1 and -1. For $A = 0$, there is no sensitivity to the surface orientation, B is describing the width of the perturbation, and C is shifting the location of the peak of the perturbation.

Then $g(\xi)$ is a function describing the scatter of the data or the sensitivity to local defects. D describes the amount of scatter, while E describes the sensitivity to local defects at low notch acuity compared to high notch acuity.

Combining Eq. (2), (3) and (4) with Eq. (5) and (6), the formulations yields

$$H_a = H_0 + Ae^{-B(\xi+C)^2} \tag{7}$$

$$H_u = H_0 + Ae^{-B(\xi+C)^2} + De^{-E\xi} \tag{8}$$

$$H_l = H_0 + Ae^{-B(\xi+C)^2} - De^{-E\xi} \tag{9}$$

And gives the diagram as shown in Fig. 2b.

The notch acuity parameter has been altered from the proposed diagram [1]. The eigenvalue exponent based on the notch opening angle of the Lazzarin-Tovo stress field [33] has been removed in order to simplify the model.

Fig. 3 shows the model fitted to the above-mentioned data for AM Inconel 718. The error bars are indicating two standard deviations.

3. Some special cases and applications of the diagram

The diagram and the analytical framework developed here is possible to apply to both empirical data and theoretical values. It can be applied to empirical data from either static of fatigue loading, seeing the scatter and the trends of failure location. Or it can be applied to loading cases where the notch root is not the critical location, *e.g.* the peak stress location under mixed-mode loading. In this section, some of the possible applications of the diagram and the model are shown.

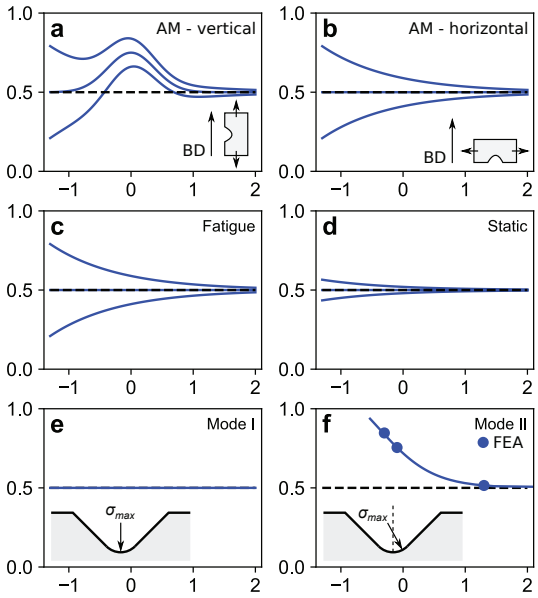

Figure 4: Possible applications of the diagram. **a** AM built in z-direction, **b** AM built in x-direction, **c** Fatigue loading with surface roughness, **d** static loading with surface roughness, **e** Mode I loading, **f** Mode II loading, verified by FEA.

3.1. Surface roughness dependence of surface orientation - additive manufacturing

In the case of AM, the roughness of a surface is dependent on its orientation [31]. *e.g.* down-skin surfaces typically display higher surface roughness than up-skin surfaces. Analytical formulations for connecting the surface roughness to the build orientation has been developed for selective laser melting [31] and fused deposition modelling [32].

Following this, it is possible to make predictions of how the diagram would look for differently orientated specimens subjected to fatigue loading. In Fig. 4a and b, two cases are compared; vertically and horizontally built specimens. The vertically built specimens have highest surface roughness in the down-skin surfaces, and failure is expected to occur from this region in some range of notch geometry. The horizontally built specimens have the highest surface roughness in the notch root. Hence, failure is likely to initiate from this location for all notch acuities. In both cases, the high surface roughness will contribute to generating scatter in the location of failure initiation when dealing with a low notch acuity.

3.2. Static and fatigue loading

In general (not referring to AM), when comparing static and fatigue loading, it should be evident that since fatigue is controlled by localized defects, and are sensitive to sharp notches [34] we expect a high scatter in the failure locations. In the case of static loading, especially for (ductile) engineering materials, the global dimensions are more dominating than the local defects. Hence, less scatter in failure location is expected in the case of static loading than in fatigue.

For a specimen with uniform surface roughness, the general trend for static and fatigue loading is shown in Fig. 4c and d. In static loading, failure will occur close to the minimal cross-section (and notch root), while for fatigue, higher scatter is expected.

3.3. Mixed mode loading

The diagram and the model can be applied to different loading cases, *e.g.* mode I, mode II or mixed-mode loading. In mode I loading the peak stress is located at the notch root. In combinations of mode I and mode II loading, the point of the maximum stress along the edge of the notch does not coincide with the notch root. The location of the peak stress is shifted along the notch edge, according to the ratio between the generalized notch stress intensity factors[35].

The diagram can be employed to compare the different locations of the peak stresses in mode I and mode II loading. For mode I loading, the peak stress is located at the notch root; this is shown in Fig. 4e. For mode II loading a finite element analysis was carried out, capturing the location of the maximum prin-

cipal stress. A square plate with an opening angle of $2\alpha = 90°$, a constant notch depth and a variable notch radius was considered. Unit displacements were applied according to Lazzarin *et al.* [36] in order to obtain shear loading. The peak stress was located with an angle of 38°, and the results are plotted in the diagram in Fig. 4f.

4. Conclusions

The work can be summarized by the following points:

- An analytical framework for a diagram connecting failure location to notch acuity has been proposed. The model can fit data on failure initiation site for as-built AM notch geometries subjected to fatigue loading.
- The diagram can increase the understanding of how defects and geometrical features are interacting when dealing with fatigue and fracture behaviour of materials.
- Some applications of the diagram has been demonstrated, both for predictions and for capturing empirical data.

5. Appendix A. Specimen geometries and fatigue data

Fig. A.1a shows the specimen geometries from ref. [1]. Four different double notched geometries were considered: unnotched, semi-circular, two v-notch with 1 mm radius and v-notch with 0.1 mm radius. The specimens were produced by selective laser melting with a layer height of 50μm. Fatigue testing was done between 10^4 and 2×10^6 cycles, with a loading ratio of $R = 0$. The fatigue data is shown in Fig. A.1b. Further information about the specimens and the results are available in ref. [1].

6. Appendix B. Parametric study of geometric features

In order to understand the influence of the different features of the notch geometries, two parametric studies of the geometric effects were done. In this appendix, we show the geometric effect of the cross-section width and the effect of the notch radius.

Two-dimensional Finite Element Analyses (FEA) were done in Abaqus, using symmetry and applying tension loading. A linear elastic material and CPS8 plane stress elements were used. The maximum principal stress was recorded along the notch edge and normalized with respect to the maximum value for each analysis.

The effect of the cross-sectional width was analysed by considering a semi-circular notch with ρ = 5mm and changing the width from 0.06 mm to 200 mm. This was done in order to see the variations in the stress gradient along the notch edge for different widths. Examples of both narrow and wide cross-section are shown in Fig. B.1a. The normalized stress fields are shown in Fig. B.1b, displaying steep stress gradients for small ligaments and less steep gradients for wide ligaments. Assuming that a defect is present at a certain distance from the notch root, the defects will be more critical if the section is wide, due to the different stress gradients.

Following this logic, a contour plot of the stresses along the free surface was created. The contour plot is shown in Fig. B.1c, with the failure locations from the semi-circular specimens inserted. The contour plot shows that for wide cross-sections, the stress fields are stable and not influenced by the width. From the contour plot, it seems that for wide sections the defects will be critical, while for narrow cross sections the cross-section will be the dominant feature.

The effect of the notch radius was investigated based on the v-notched and unnotched specimen geometries. In the FEA-model, a constant width (w = 5 mm), notch depth (ρ = 5 mm) and opening angle ($2\alpha = 90°$) was used. The geometry is shown in Fig. B.2a. The normalized stress fields are shown in Fig. B.2b. For small notch radiuses, the stress fields are steep, while for large notch radiuses, the stress fields are less steep. *i.e.* a similar result as in the previous case. A contour plot was generated for the stresses as a function of the notch radius; this is shown in Fig. B.2c. The plot in Fig. B.2c shows a similar trend as in Fig. B.1c. A small notch radius gives a steep stress field, indicating failure from the notch tip. For a large notch radius (*i.e.* unnotched) the stress gradient is less steep, and it is expected that the defects are likely to be the dominant feature in failure initiation.

References

[1] K. Solberg, F. Berto, Notch-defect interaction in additively manufactured inconel 718, International Journal of Fatigue 122 (2019) 35 – 45.

[2] B. R. Somers, A. W. Pense, Welding failure analysis, Materials Characterization 33 (3) (1994) 295 – 309.

[3] S. Y. Choy, C.-N. Sun, K. F. Leong, J. Wei, Compressive properties of ti-6al-4v lattice structures fabricated by selective laser melting: Design, orientation and density, Additive Manufacturing 16 (2017) 213 – 224.

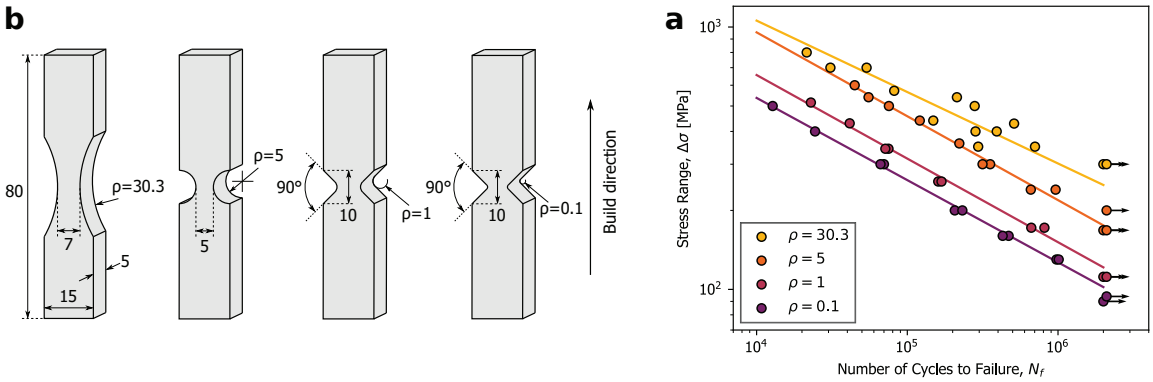

Figure A.1: **a** Specimen geometries of selective laser melted Inconel 718 and **b** Fatigue data from ref. [1]

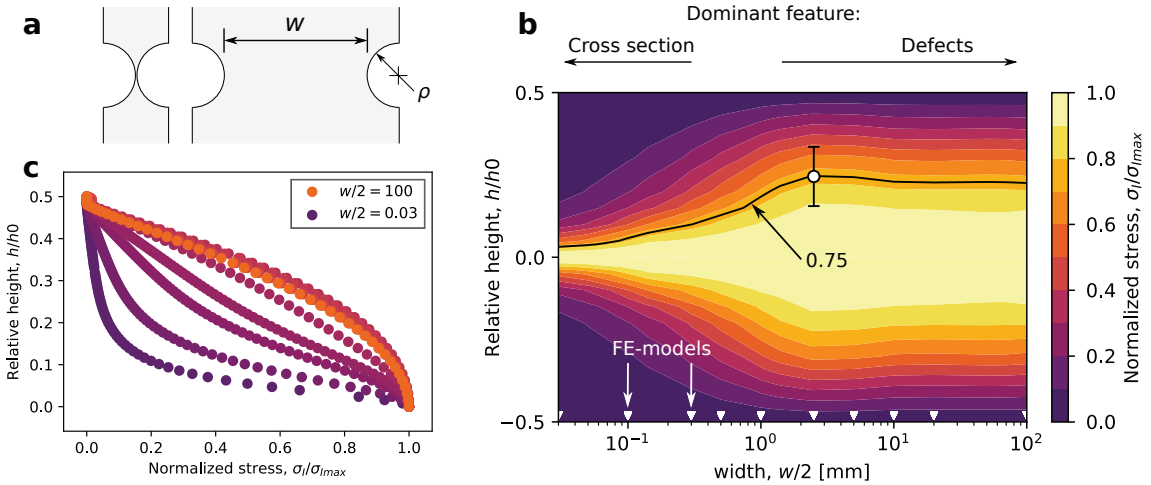

Figure B.1: Parametric study of specimen width. **a** Example of narrow and wide ligament. **b** Normalized maximum principal stress along the edges of the notches. **c** Contour plot of the stresses along the notch edge for different widths.

[4] H. Debski, P. Rozylo, A. Gliszczynski, T. Kubiak, Numerical models for buckling, postbuckling and failure analysis of pre-damaged thin-walled composite struts subjected to uniform compression, Thin-Walled Structures 139 (2019) 53 – 65.

[5] ASTM, E1820-09 standard test method for measurement of fracture toughness, Standard E1820-09, ASTM International, West Conshohocken, PA (2009).

[6] ASTM, E399-19 standard test method for linear-elastic plane-strain fracture toughness kic of metallic materials, Standard E399-19, ASTM International, West Conshohocken, PA (2019).

[7] A. Vyatskikh, S. Delalande, A. Kudo, X. Zhang, C. Portela, J. Greer, Additive manufacturing of 3d nano-architected metals, Nature Communications 9 (2018) 593.

[8] R. Wauthle, B. Vrancken, B. Beynaerts, K. Jorissen, J. Schrooten, J.-P. Kruth, J. V. Humbeeck, Effects of build orientation and heat treatment on the microstructure and mechanical properties of selective laser melted ti6al4v lattice structures, Additive Manufacturing 5 (2015) 77 – 84.

[9] A. Hussein, L. Hao, C. Yan, R. Everson, P. Young, Advanced lattice support structures for metal additive manufacturing, Journal of Materials Processing Technology 213 (7) (2013) 1019 – 1026.

[10] M. Seifi, M. Gorelik, J. Waller, N. Hrabe, N. Shamsaei, S. Daniewicz, J. J. Lewandowski, Progress towards metal additive manufacturing standardization to support qualification and certification, JOM 69 (3) (2017) 439–455.

[11] M. Seifi, A. Salem, D. Satko, J. Shaffer, J. J. Lewandowski, Defect distribution and microstructure heterogeneity effects on fracture resistance and fatigue behavior of ebm ti6al4v, International Journal of Fatigue 94 (2017) 263 – 287, fatigue and Fracture Behavior of Additive Manufactured Parts.

[12] A. Yadollahi, N. Shamsaei, Additive manufacturing of fatigue resistant materials: Challenges and opportunities, International Journal of Fatigue 98 (2017) 14 – 31.

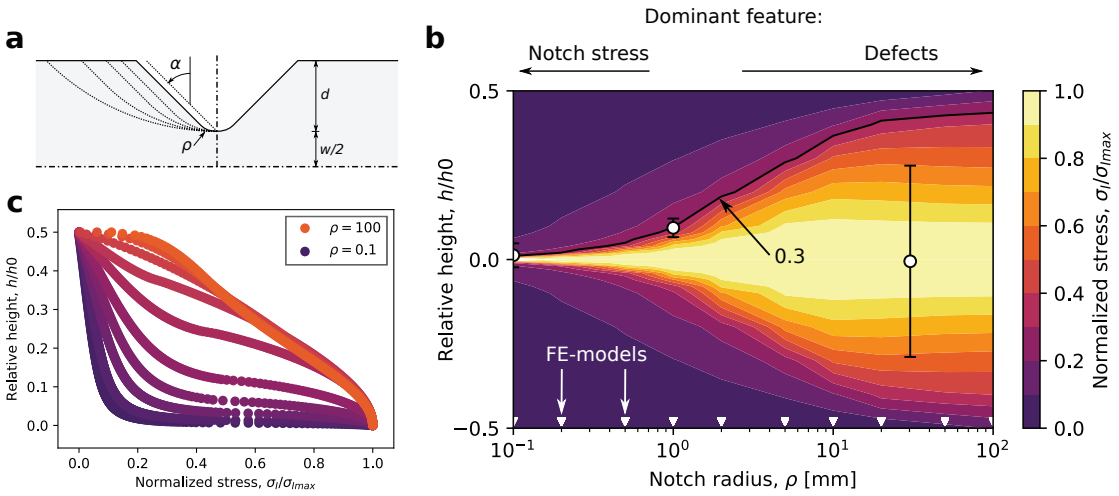

Figure B.2: Parametric study of notch radius. **a** Different notch radius **b** Normalized maximum principal stress along the edges of the notches. **c** Contour plot of the stresses along the notch edge for different widths.

[13] E. Hosseini, V. Popovich, A review of mechanical properties of additively manufactured inconel 718, Additive Manufacturing 30 (2019) 100877.

[14] S. Tammas-Williams, I. Todd, Design for additive manufacturing with site-specific properties in metals and alloys, Scripta Materialia 135 (2017) 105 – 110.

[15] Y. Kok, X. Tan, P. Wang, M. Nai, N. Loh, E. Liu, S. Tor, Anisotropy and heterogeneity of microstructure and mechanical properties in metal additive manufacturing: A critical review, Materials & Design 139 (2018) 565 – 586.

[16] J. J. Lewandowski, M. Seifi, Metal additive manufacturing: A review of mechanical properties, Annual Review of Materials Research 46 (1) (2016) 151–186.

[17] T. Mukherjee, W. Zhang, T. DebRoy, An improved prediction of residual stresses and distortion in additive manufacturing, Computational Materials Science 126 (2017) 360 – 372.

[18] M. Megahed, H.-W. Mindt, N. N'Dri, H. Duan, O. Desmaison, Metal additive-manufacturing process and residual stress modeling, Integrating Materials and Manufacturing Innovation 5 (1) (2016) 61–93.

[19] S. Hojjatzadeh, N. Parab, W. Yan, Q. Guo, L. Xiong, C. Zhao, M. Qu, L. Escano, X. Xiao, K. Fezzaa, W. Everhart, T. Sun, L. Chen, Pore elimination mechanisms during 3d printing of metals, Nature Communications 10 (2019) 3088.

[20] T. Mukherjee, T. DebRoy, Mitigation of lack of fusion defects in powder bed fusion additive manufacturing, Journal of Manufacturing Processes 36 (2018) 442 – 449.

[21] S. Coeck, M. Bisht, J. Plas, F. Verbist, Prediction of lack of fusion porosity in selective laser melting based on melt pool monitoring data, Additive Manufacturing 25 (2019) 347 – 356.

[22] A. R. Balachandramurthi, J. Moverare, N. Dixit, R. Pederson, Influence of defects and as-built surface roughness on fatigue properties of additively manufactured alloy 718, Materials Science and Engineering: A 735 (2018) 463 – 474.

[23] J. Pegues, M. Roach, R. S. Williamson, N. Shamsaei, Surface roughness effects on the fatigue strength of additively manufactured ti-6al-4v, International Journal of Fatigue 116 (2018) 543 – 552.

[24] P. Li, D. Warner, J. Pegues, M. Roach, N. Shamsaei, N. Phan, Towards predicting differences in fatigue performance of laser powder bed fused ti-6al-4v coupons from the same build, International Journal of Fatigue 126 (2019) 284 – 296.

[25] Y. Murakami, Chapter 2 - stress concentration, in: Y. Murakami (Ed.), Metal Fatigue, Elsevier Science Ltd, Oxford, 2002, pp. 11 – 24.

[26] G. Meneghetti, D. Rigon, C. Gennari, An analysis of defects influence on axial fatigue strength of maraging steel specimens produced by additive manufacturing, International Journal of Fatigue 118 (2019) 54 – 64.

[27] J. Gunther, D. Krewerth, T. Lippmann, S. Leuders, T. Troster, A. Weidner, H. Biermann, T. Niendorf, Fatigue life of additively manufactured ti6al4v in the very high cycle fatigue regime, International Journal of Fatigue 94 (2017) 236 – 245.

[28] K. Solberg, S. Guan, S. M. J. Razavi, T. Welo, K. C. Chan, F. Berto, Fatigue of additively manufactured 316l stainless steel: The influence of porosity and surface roughness, Fatigue & Fracture of Engineering Materials & Structures 42 (9) (2019) 2043–2052.

[29] S. Romano, A. Bruckner-Foit, A. Brandao, J. Gumpinger, T. Ghidini, S. Beretta, Fatigue properties of alsi10mg obtained by additive manufacturing: Defect-based modelling and prediction of fatigue strength, Engineering Fracture Mechanics 187 (2018) 165 – 189.

[30] J. R. Yates, P. Efthymiadis, A. A. Antonysamy, C. Pinna, J. Tong, Do additive manufactured parts deserve better?, Fatigue & Fracture of Engineering Materials & Structures 42 (9) (2019) 2146–2154.

[31] G. Strano, L. Hao, R. M. Everson, K. E. Evans, Surface roughness analysis, modelling and prediction in selective laser melting, Journal of Materials Processing Technology 213 (4) (2013) 589 – 597.

[32] S. Rahmati, E. Vahabli, Evaluation of analytical modeling for improvement of surface roughness of fdm test part using measurement results, The International Journal of Advanced Manufacturing Technology 79 (5) (2015) 823–829.

[33] P. Lazzarin, R. Tovo, A unified approach to the evaluation of linear elastic stress fields in the neighborhood of cracks and notches, International Journal of Fracture 78 (1996) 3–19.

[34] B. Atzori, P. Lazzarin, Notch sensitivity and defect sensitivity under fatigue loading: Two sides of the same medal, International Journal of Fracture 107 (1) (2001) 1–8.

[35] F. Berto, P. Lazzarin, Recent developments in brittle and quasi-brittle failure assessment of engineering materials by means of local approaches, Materials Science and Engineering: R: Reports 75 (2014) 1 – 48.

[36] P. Lazzarin, M. Zappalorto, F. Berto, Generalised stress intensity factors for rounded notches in plates under in-plane shear loading, International Journal of Fracture 170 (2) (2011) 123.

Article IV

The effect of defects and notches in quasi-static and fatigue loading of Inconel 718 specimens produced by selective laser melting

Klas Solberg, Filippo Berto

International Journal of Fatigue, Article

Additively manufactured components are likely to contain defects deriving from the manufacturing process. They are also likely to be designed with high geometric complexity (including notches), due to very few design-limitations. In order to understand the influence of these two types of geometric features, we here investigate as-built Inconel 718 specimens produced by selective laser melting under quasi-static and cyclic loading. Notched and unnotched specimens are considered, and the main emphasis is set on the influence of the defects and on how they influence the failure locations at different load levels.

https://doi.org/10.1016/j.ijfatigue.2020.105637

The effect of defects and notches in quasi-static and fatigue loading of Inconel 718 specimens produced by selective laser melting

Klas Solberg[a,*], Filippo Berto[a]

[a]*Department of Mechanical and Industrial Engineering, Norwegian University of Science and Technology, 7034 Trondheim, Norway*

Abstract

Additively manufactured components are likely to contain defects deriving from the manufacturing process. They are also likely to be designed with high geometric complexity (including notches), due to very few design-limitations. In order to understand the influence of these two types of geometric features, we here investigate as-built Inconel 718 specimens produced by selective laser melting under quasi-static and cyclic loading. Notched and unnotched specimens are considered, and the main emphasis is set on the influence of the defects and on how they influence the failure locations at different load levels.

Keywords: Fatigue, Notch, Defect, Additive manufacturing, Inconel 718

1. Introduction

Additive manufacturing (AM) has opened up a new dimension of what is possible in design complexity of mechanical components. Parts are manufactured by adding material in a layer-by-layer manner, assisted by computed generated designs. AM can produce intricate geometric configurations previously not possible. One of the main challenges when dealing with AM components is that the material properties are dependent on the manufacturing process, and the parts are likely to contain defects [1–3].

Defects deriving from the AM process of metals play a crucial role in the mechanical behaviour of the materials [4–6]. Metals produced from powder bed fusion-based AM process typically exhibits high surface roughness [7], geometrical discontinuities [8, 9], residual stresses [10] and anisotropic microstructure [3] in its as-built condition. Under cyclic loading, the geometric defects are detrimental for the mechanical performance, and recently extensive research has been done to correlate the defects to the fatigue behaviour[11–14]. In the case of static loading of AM metals, the low elongation is often attributed to geometrical discontinuities[15]. The mechanical behaviour of AM metals can be increased by various post-processing schemes [16–18]. However, when dealing with *e.g.* internal structures, the post-processing possibilities are limited.

Geometrical features in AM components are not only present as defects deriving from the manufacturing process, but they can also be a part of the designs. Complex geometric configurations introduce notches and complex stress states. The effect of notches and complex loading conditions is a well-established field in fatigue and fracture. So is fatigue in the presence of defects, *e.g* by methods such as $\sqrt{area}$ by Murakami [19]. In fatigue assessment of AM metals, we meet challenges from both these fields. And in particular localized defects within larger geometric configurations.

Dealing with the notched fatigue behaviour of AM metallic components, two main approaches are made: testing machined specimens and testing as-built specimens. In the first approach, the notch geometries might interact with internal defects [20]. In the second approach, the surfaces of the notches are populated with smaller notches/defects, deriving from the AM process. The defects in the surface region act as notches within the actual notch geometry [21, 22], and fatigue initiate from these [22–24]. It should also be noted that the microstructural features are dependent on the notch geometries and that this might influence the results [23]. The quasi-static behaviour of as-built AM notches have also been studied [23, 25], showing notch strengthening behaviour and that the influence of defects are reduced as the notch acuity increases [25].

In this work, the quasi-static and fatigue behaviour of as-built Inconel 718 specimens are investigated. Notched and un-

*Corresponding author
Email address: klas.solberg@ntnu.no (Klas Solberg)

notched specimens are considered, and the main emphasis is set on the interaction between the notches and the geometric defects within them. In order to understand which are the detrimental geometrical feature for failure, the fracture surfaces and failure locations were captured and analyzed.

2. Methods and experimental procedure

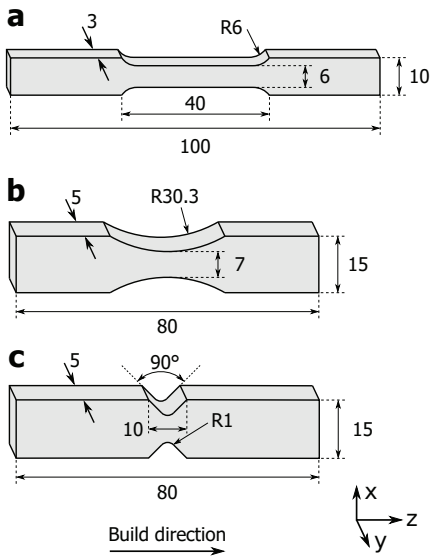

Figure 1: Dimensions of the specimens: **(a)** Tensile specimen; **(b)** Unnotched fatigue specimen; **(c)** Notched fatigue specimen.

Three different specimen geometries were considered; one for tensile loading and two for fatigue loading, where one is characterized as unnotched, and one as notched. The specimen geometries are shown in Fig. 1a-c. The tensile specimen (Fig. 1a) was designed according to ASTM E8, while the two geometries for fatigue loading (Fig. 1b and c) were the same as the ones employed in a recent publication by the authors [22]. All specimens were built to a solid layer-by-layer vertically by selective laser melting(SLM), using Inconel 718 powder. The specimens were produced with an energy density of 60 J/mm^3, and the layer height was 50 μm.

The mechanical testing was done using a servohydraulic MTS uniaxial testing system with a load cell of 50 kN. The static tests were done with displacement control of 0.2 mm/min, and the tensile specimens were tested with strain gauges. The initial distance between the grippers was kept constant for both the notched and unnotched specimens during the testing. Fatigue testing was done with a loading ratio R = 0 - 0.1 and a frequency of 5 - 10 Hz. The fatigue tests were discontinued after 2×10^6 cycles of loading.

The fracture surfaces were investigated by Scanning Electron Microscope (SEM) on a Quanta FEG 650 system. Analysis of the microstructure was done by cutting and polishing cross-sections of the specimens, then Kalling's reagent was used as etchant according to ASTM E407 [26].

Weibull trend lines for the fatigue data were generated based on the method of D'Antuono [27]. The method provides an analytical relation between the Basquin Law

$$S = \bar{b}N^{\bar{a}} \tag{1}$$

and the Weibull curve

$$S = b(N + B)^a + S_e, \tag{2}$$

where N, S and S_e are number of cycles, applied stress and the fatigue limit respectively, further $\bar{a}$, $\bar{b}$, a, b and B are coefficients for curve fitting. The Weibull curve for the data presented here was generated based on the Basquin trend lines of the fatigue data in the high cycle fatigue regime (between 10^4 and 2×10^6 cycles) and the maximum value of stress in the S-N diagram. The relation between the Basquin law and the Weibull curve is further described in Appendix A.

FEA was done in the software Abaqus/CAE. A 2D-analysis based on a cross-section from a micrograph was analyzed. The micrograph was converted to vector graphic in the software Inkscape and further imported into Abaqus. A linear elastic material was assumed.

3. Results and Discussion

3.1. Mechanical behaviour

The results from the quasi-static tests are collected in Fig. 2, showing the applied nominal stress versus the elongation in Fig. 2a and the normalized notch strengthening factor σ_N/σ_T in Fig. 2b. Where σ_N is the tensile strength for the notched specimens and σ_T is the tensile strength for the tensile-specimens. The results show differences in strength and elongation; the lowest strength and the highest elongation was observed in the tensile-specimen (corresponding to 13 % based on the strain gauges), while the tensile stress was increased and the elongation was reduced with an increasing notch acuity. The increased strength for the notched specimens can be attributed to

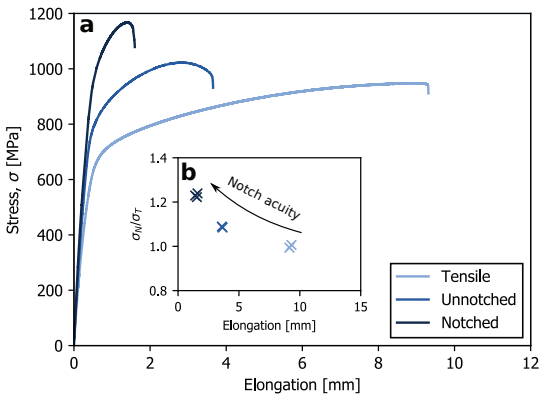

Figure 2: Results from quasi-static loading. (a) Loading curves for the different specimens; stress versus elongation (b) notch strengthening factor, σ_N/σ_T, versus elongation at failure.

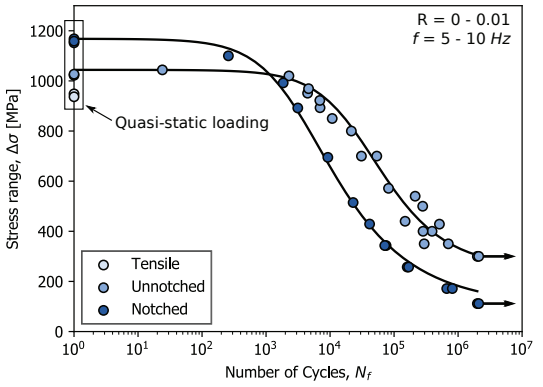

Figure 3: Data from cyclic and quasi-static tests collected in an S-N diagram. Weibull trend lines based on the method of D'Antuono [27].

the notch strengthening effect. The concept of notch strengthening refers to notched components being able to carry higher loads than unnotched components.

Several explanations have been given for notch strengthening [28–30]. Conventionally brittleness/ductileness is used to differentiate between strengthening/weakening in static loading. However, Lei *et al.* [30] argues that the strengthening is caused by forcing a transition from shear-mode failure to normal-mode failure, as a result of the geometrical constraints of the notch geometry. This was demonstrated by showing that a brittle bulk metal glass exhibited notch strengthening by shifting from shear-mode failure to normal-mode failure when introducing notches.

The results from both cyclic and quasi-static loading are shown together in an S-N diagram in Fig. 3. In the HCF-regime, higher scatter is observed in the fatigue data for the unnotched specimens than for the notched specimens. In the HCF regime, notch weakening is observed while in static loading notch strengthening is observed. Comparing the unnotched and notched specimens, a transition between notch weakening and strengthening is observed in the LCF-regime around 10^3 cycles, which corresponds to a stress level of 1000 MPa. From the quasi-static load curve of the notched specimen (Fig. 2), 1000 MPa corresponds to the onset of plasticity and non-linear behaviour.

3.2. Microstructure and surface conditions

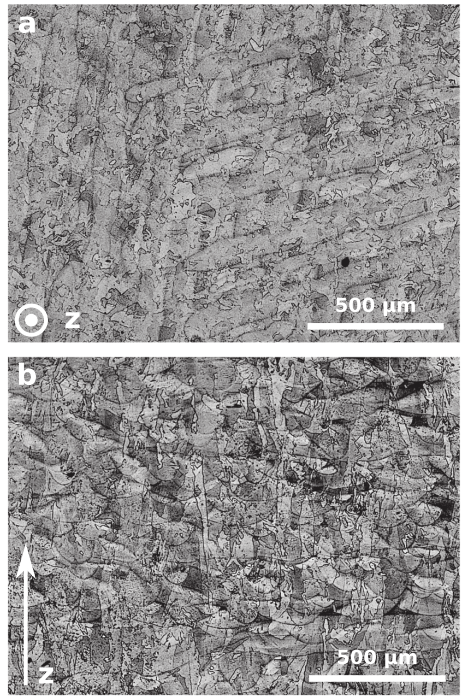

Figure 4: Microstructure of polished and etched sections (a) Perpendicular to build direction, equiaxed grains and hatching pattern visible (b) Parallel to build direction, elongated grains and melt pools visible.

The microstructure of the material is shown in Fig. 4. In the plane perpendicular to the build direction, shown in Fig. 4a, the hatching strategy is visible, and grains in this plane are equiaxed. In the plane parallel to the build direction, shown in Fig. 4b, the cross-section of the hatching lines are visible.

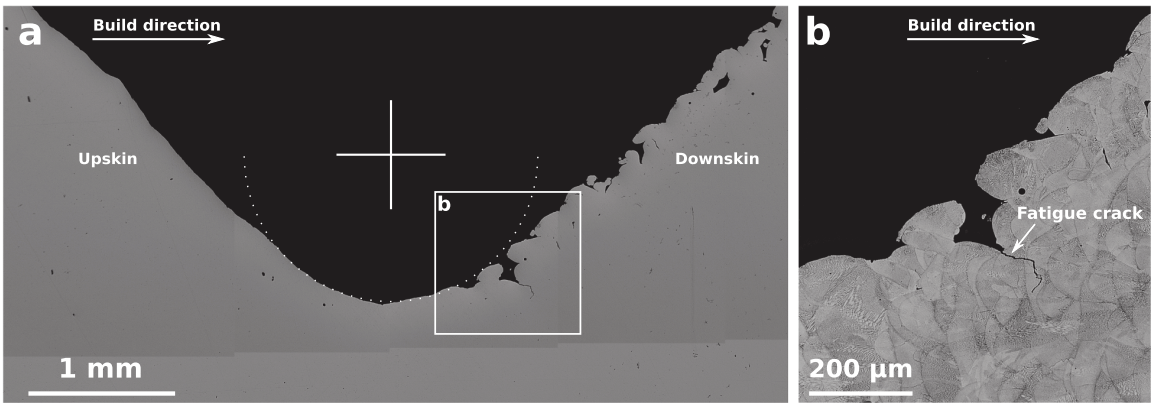

Figure 5: Cross-section of notched specimen fatigue loaded until 2×10^6 cycles. (a) Polised cross-section, (b) etched cross-section, detail of fatigue crack initiation

Here, the grains are elongated and show grains ranging across the build layers. The features of the microstructure are characteristic for Inconel 718 produced by SLM [1].

In order to study the surface conditions, a notched specimen subjected to 2×10^6 cycles of fatigue loading was cut and polished. The cross-section of the specimen is shown in Fig. 5a. A large difference in the surface built down-skin and up-skin was observed. The down-skin surface displays higher roughness, but more importantly: sharp features, including subsurface defects. Fig. 5b shows an etched detail from one of these defects. A fatigue crack can be observed from the root of the defects; this indicates that fatigue initiates from the local defects and not from the designed notch. The melt pool morphologies determine the morphology of the defect. Based on the micrograph in Fig. 5, the Rz value of the up-skin and down-skin surfaces were evaluated showing 77 μm and 259 μm, respectively.

Previously, this kind of defects has been characterized as lack-of-fusion, as they have a similar appearance. However, it can be argued that the defects should be characterized differently, as they are caused by surface effects and not by low laser power. Magnien et al. refer to these defects as ”crust”-defects, which might be a better terminology [31].

3.3. Fractography

Fractography of a tensile-specimen subjected to static loading is shown in Fig. 6a. The side view of the specimen is shown in Fig. 6b, displaying that fracture occurred shear-mode (45°-angle), except from a plateau. This plateau is indicated in Fig. 6a, and shown in more detail in Fig. 6c. In this plateau, the hatching lines from the manufacturing is visible. The morphology of the lines is similar to the hatching lines observed from the microstructural analysis in Fig. 4a.

Fractography of two unnotched specimens is shown in Fig. 7. The fracture surface of the specimen subjected to quasi-static loading is shown in Fig. 7a with the corresponding side view in Fig. 7c. The fracture surface of the specimen subjected to fatigue is shown in Fig. 7b with the corresponding side view in Fig. 7d. In the case of quasi-static loading, failure is occurring in the minimum cross-section, the fracture surface is not dominated by a 45°-angle, as in the tensile specimen, but some local regions have this orientation. In the case of fatigue, the crack is initiating from a defect in the surface (Fig. 7e), then it propagates through the specimen until the final rupture. In this case, fatigue did not initiate in the minimum cross-section.

Fractography of two notched specimens subjected to static and fatigue loading are shown in Fig. 8. The fracture surface and side view of the specimen subjected to quasi-static load is shown in Fig. 8a and c. The same views of the specimen subjected to fatigue are shown in Fig. 8b and d. Fig. 8e and f show defects from fracture surfaces corresponding to fatigue loading.

In fatigue loading (Fig. 8b) cracks are propagating from both notches towards the centre of the specimen. Fig 8e and f show the typical defects from which fatigue initiated. In the case of the specimen subjected to quasi-static loading(Fig. 8a), the fracture surface is different, crack growth is not observed, and the cross-section is deformed due to the necking.

Comparing the front view of the specimens in Fig. 8c and d,

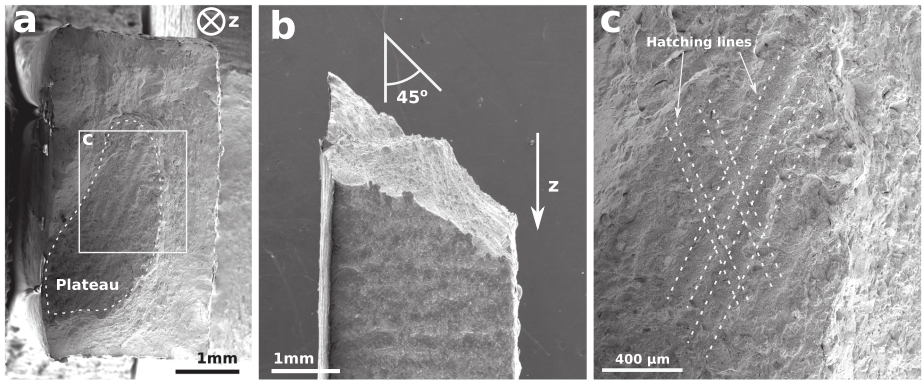

Figure 6: Fractography of plain specimen subjected to quasi-static loading. (a) Fracture surface, (b) side view and (c) detail from the fracture surface. Lines indicating hatch pattern.

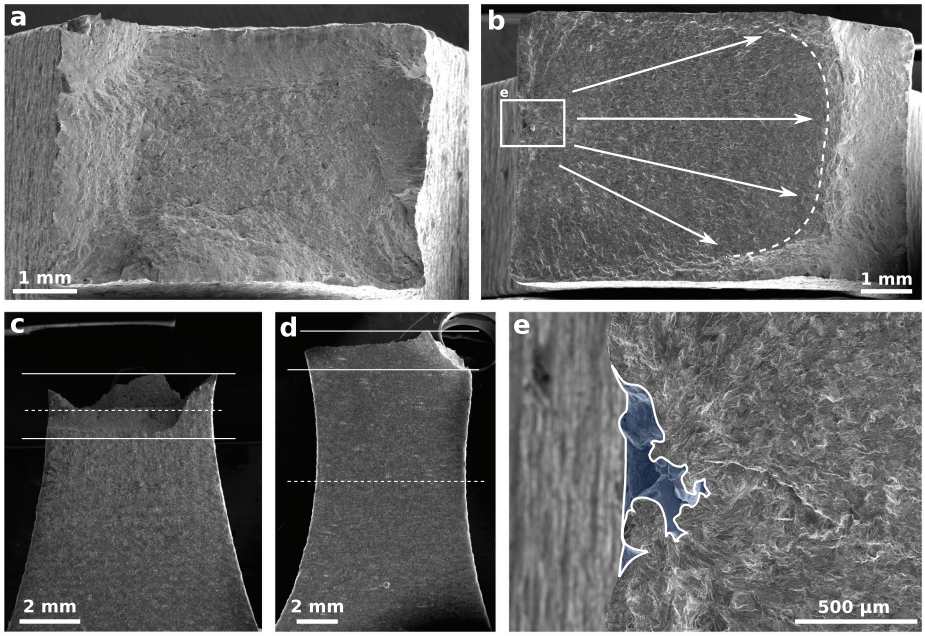

Figure 7: Fractography of unnotched specimens. (a) Fracture surface, static loading (b) Fracture surface, cyclic loading (c) Front view, static loading (d) Front view, cyclic loading (e) Defect from fracture surface in cyclic loading

there are some differences. The specimen subjected to fatigue loading has failure clearly initiating from the down-skin region above the notch root, while for the specimen subjected to quasi-static loading, the peaks and valleys of the fracture surface are ranging across the centre of the notch. In both cases, the dashed lines indicate the notch bisector line and the solid lines indicates the peaks and valleys of the fracture surface.

3.4. Failure locations

The failure locations in the specimens were captured and are shown in Fig. 9. The locations are given as the relative height within the notch h/h_0, defined in Fig. 9, versus the load level. The plot is showing the peaks and valleys of the fracture surface and the fatigue initiation site. The general trend observed for both specimen geometries is that at low load levels, the defects are determining the failure locations while moving

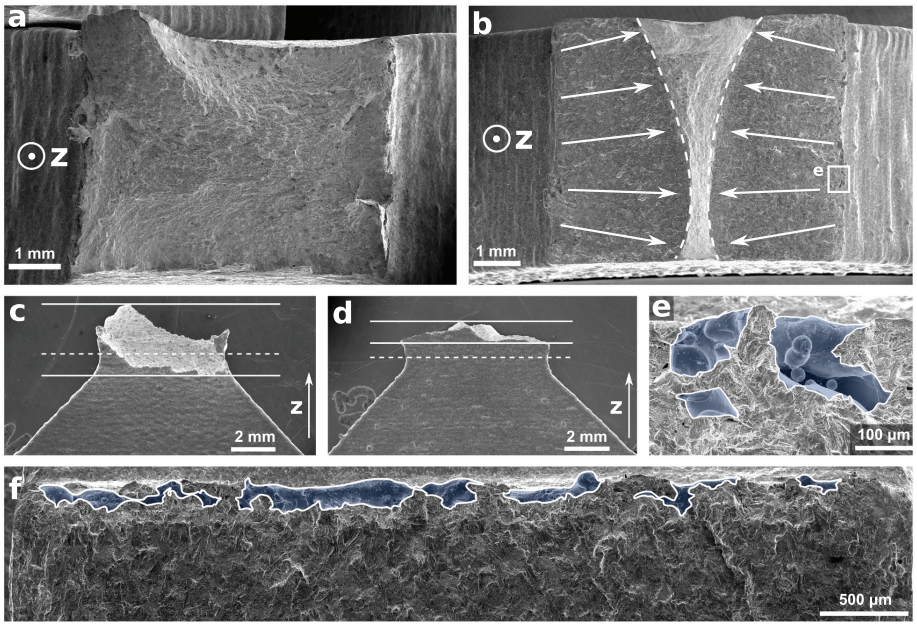

Figure 8: Fractography of notched specimens. (a) Fracture surface, static loading (b) Fracture surface, cyclic loading (c) Front view, static loading (d) Front view, cyclic loading (e) Detail of defect from fatigue initiation (f) Distribution of defects along the edge of a notched specimen failed from fatigue loading.

towards quasi-static loading, failure is shifted towards and ranging across the minimum cross-section.

The failure locations of the unnotched specimens are shown in Fig. 9a. In cyclic loading, there is a large scatter in the failure locations; specimens are failing from both the up-skin and the down-skin region. As the loads are increasing, the failure locations are shifting towards the centre of the specimens. At the same time, the difference between the peaks and valleys are increasing, indicating more shear-mode dominated failure.

From the cyclic loading of the notched specimens (Fig 9b), there is a small amount scatter in the failure locations. All the specimens are failing from the down-skin region and not the notch root. At higher loads, the fracture surfaces are ranging across the notch bisector line. However, the mean value is still in the down-skin region. This could indicate that the defects are influencing the failure location also under quasi-static loading.

3.5. Local stress fields

A two-dimensional FEA was done based on the cross-section in Fig. 5 in order to investigate the stress field in the presence of the defects. The boundary conditions and geometry of the FE-model are shown in Fig. 10a. A unit displacement, u_0, was applied resulting in nominal stress, σ_{nom}, in the gauge section.

The contour plot from the simulation is shown in Fig. 10a-c. From the contour plot, both the notch root and the defect can be identified as critical regions. A peak stress is observed at the notch root, and a stress singularity is observed at the defect close to the notch root. The stress field at the tip of the defect is shown in more detail in Fig. 10c, overlayed by the fatigue crack from the optical microscope in Fig. 5b.

In order to quantitatively analyze the stress fields from the notch and the defect, the different stress components were investigated. This was done by placing a polar coordinate system at the notch/defect roots; the corresponding stress components were captured along the notch bisector lines. The stress fields along the notch bisector lines are shown in Fig. 11a and b for the defect and notch, respectively. In the case of the defect, both mode I and mode II stress singularities are present, indicated by the linear trend in the log-log scale. In the case of the notch root, the shear component is not present.

Comparing the two stress fields can be done by employing the Theory of Critical Distances (TCD) [33, 34]. According to the Maximum Tangential Stress (MTS) criterion applied to TCD by Qian *et al.* [35], failure should occur at the maximum

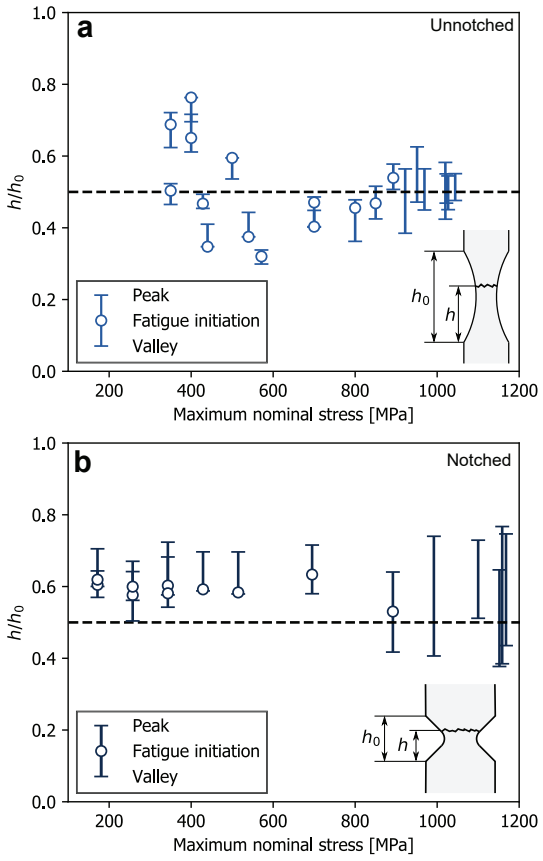

Figure 9: Data summarizing the locations of failure: (a) unnotched specimens (b) notched specimens.

value of tangential stress, $\sigma_{\theta\theta}$. The critical distance, $L/2$, for Inconel 718 has previously been estimated to be L/2 = 0.077 mm by Lokus and Susmel [32]. Fig. 11c shows a comparison of $\sigma_{\theta\theta}$ for the notch and the defect along the notch bisector line. The notch has the highest value of $\sigma_{\theta\theta}$ at L/2, indicating that fatigue should initiate from the notch root and not the defect. As there is a mode II contribution along the notch bisector line for the defect, the $\sigma_{\theta\theta}$-components were evaluated along circumferential paths at $r = L/2$; this is shown in Fig. 11d. Also, in this plot, MTS predicts the notch to be more critical. It should also be noted that the stress from notch still has the highest value at its notch bisector line, while for the defect, the location of the maximum value was shifted.

The FEA is able to capture the two critical regions. However, the TCD and MTS criteria predict that fatigue should initiate from the notch. One possible explanation for this conflicting result could be that the critical distance for AM Inconel 718 could be different from conventional manufactured Inconel 718. The fatigue behaviour can be altered by heat treatments *e.g.* precipitations strengthening [36]. Further, the cross-section might not properly represent the fatigue behaviour of the specimen. This could mean that there might be deeper and sharper regions of the defect close by initiating the fatigue crack. From the fractography in Fig. 8f, variations in the defect depths are observed along the thickness direction. Another explanation is that the three-dimensional effects are not captured in the two-dimensional FEA, excluding the stress triaxiality effects. Further, it should be noted that anisotropy or residual stresses were not taken into account.

In quasi-static loading, the fracture surfaces are ranging across the minimum cross-section. However, the average value is in the down-skin region. From the FEA in Fig. 10, the stress field is also not symmetric. In Fig. 12 the failure locations of the notched specimens are compared to the stress contour at 80% σ_{nom}. The stress contour is also shifted towards the down-skin region. This indicates that the local defects are contributing to the global stress field, and therefore contributing to shifting the failure locations.

3.6. Geometrical effects at different scales and load levels

In the current work, geometric features at two scales have been considered: Macroscopic features *i.e.* designed notches and microscopic features *i.e.* defects deriving from the manufacturing process. Both of these geometric features have been shown to influence the mechanical performance. By analyzing the failure locations in the specimens, it is possible to understand further which of the geometric defects that are detrimental.

In fatigue, the microscopic defects were found to dictate the failure locations. The correlations between fatigue and defects are well established in the fatigue community, and correlations between the defects and fatigue life can be established with, e.g. Kitagawa-Takahashi diagram [37]. The diagram evaluates which defects are influencing the fatigue limit and which are not. In a sense, it defines the scale of fatigue in regular-sized components. Regarding the Kitagawa-Takahashi diagram it can be noted that it is also dependent on the scale, *e.g.* it is evident that structures in the microscale can experience fatigue if large defects comparable to the size of the structure are present.

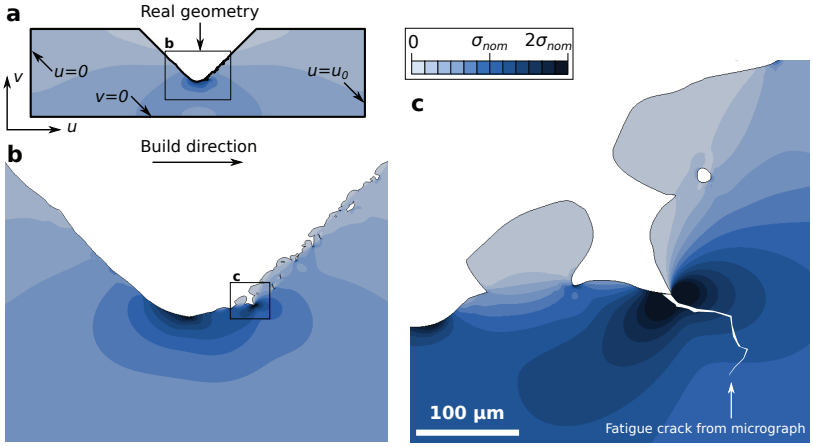

Figure 10: Contour plot of stress field from FEA. (a) FEA model, boundary conditions and load (b) stress field in notch region. (c) stress field ahead of defect, with the crack path from the micrograph in Fig. 5b overlayed.

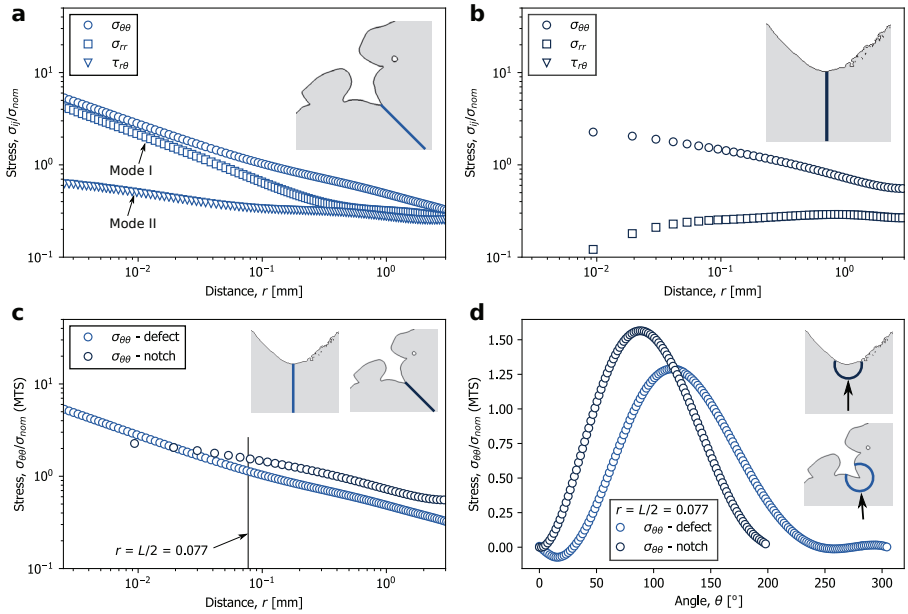

Figure 11: Stress fields surrounding the notch and the defect. (a) Stress components along the notch bisector line for the defects, (b) stress components along the notch bisector line for the notch root, (c) comparison of tangential stress components for the defect and notch, (d) comparison of tangential stress components at r=L/2 [32].

In static loading, the macroscopic features were found to be the dominant feature. When dealing with static loading of AM metals, reduction in elongation is often attributed to a high amount of porosity, while low variations are observed in the tensile strength[15]. One possible explanation for this could be considering the microscopic defects and the notch strengthening effect. Based on Lei *et al.* explanation of notch strengthening [30], it is a phenomenon that occurs if the failure mode is shifted from shear mode to normal mode by geometrical features increasing the stress triaxiality. However, there is an-

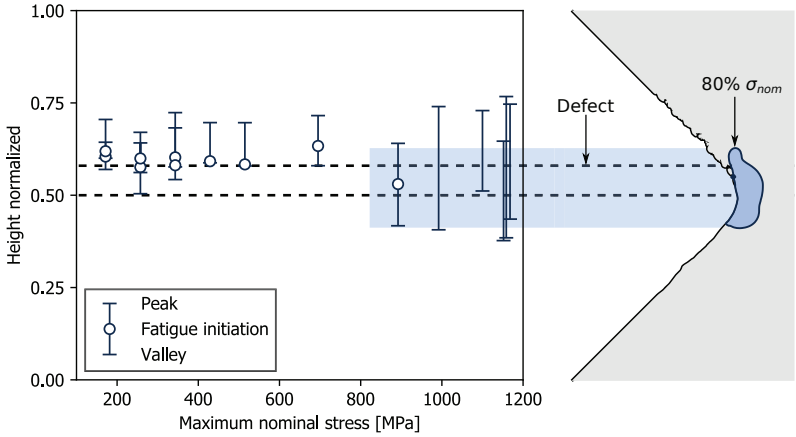

Figure 12: Failure locations of notched specimens compared to (asymmetric) stress field from FEA.

other essential aspect when dealing with notch strengthening: Which cross-section/notches to take into account. *e.g.* there is a large difference between considering the gross and the net cross-section. So, by considering the net section of the designed geometry *i.e.* not considering the defects, we are likely not to capture the notch strengthening effect from the defects. However, we would still observe the reduction in elongation due to the notch strengthening or perhaps "defect strengthening".

4. Conclusions

In this work, SLM AM Inconel 718 was investigated under loading ranging from quasi-static to HCF. The main focus of the work is set on geometrical effects at different load levels. The work can be summarized by the following points:

- Notch strengthening was observed in quasi-static loading, while notch weakening was observed in the HCF regime. A transition between notch strengthening and weakening was observed at $\sim 10^3$ cycles.
- In the HCF regime, the notched specimens failed from defects in the down-skin region and not from the notch roots. In the LCF regime failure occurred in the minimum cross-section.
- For the unnotched specimens failing in the HCF regime, a large scatter were observed in the failure locations. The failure locations were not localized in one region as was observed in the notched specimens. In the LCF regime, the failure locations were shifted towards the minimum cross-section.
- A FEA was done based on a polished cross-section of a notched specimen. The stress field was analyzed by means of TCD. The result showed that FEA of an arbitrary cross-section is not necessarily representable for a three-dimensional component.

Acknowledgement

The authors would like to acknowledge Marius Hornnes and Gard Gabrielsen Moe for experimental work related to their master's theses.

Appendix A - Weibull curve trend lines

In this appendix, the analytical relation between the Weibull curve and the Basquin law for SN-data are described. Only a brief description is given, and the full derivation can be found in Ref. [27]. The Basquin law for SN-diagrams can be written on the form

$$S = \bar{b}N^{\bar{a}}. \tag{3}$$

and the Weibull curve on the form:

$$S = b(N + B)^a + S_e, \tag{4}$$

where N, S and S_e are number of cycles, applied stress and the fatigue limit respectively, further $\bar{a}$, $\bar{b}$, a, b and B are coefficients

Article V

Fatigue assessment of as-built and heat-treated Inconel 718 specimens produced by additive manufacturing including notch effects

Klas Solberg, Di Wan, Filippo Berto

Fatigue & Fracture of Engineering Materials & Structures, Article

The fatigue behaviour of notched and unnotched specimens produced by additively manufactured Inconel 718 were analysed in the as-built and heat-treated conditions. The surfaces display high roughness and defects acting as fatigue initiation sites. In the as-built condition, fine subgrains were found, while in in the heat-treated state, the subgrains were removed and the dislocation density recovered. SN-curves are predicted based on tensile properties, hardness and defects obtained by fractography, using the $\sqrt{area}$-method.

https://doi.org/10.1111/ffe.13300

Fatigue assessment of as-built and heat-treated Inconel 718 specimens produced by additive manufacturing including notch effects

Klas Solberg*,Di Wan, Filippo Berto

Institutt for maskinteknikk og produksjon, NTNU, Trondheim, Norway

Abstract

The fatigue behaviour of notched and unnotched specimens produced by additively manufactured Inconel 718 were analysed in the as-built and heat-treated conditions. The surfaces display high roughness and defects acting as fatigue initiation sites. In the as-built condition, fine sub-grains were found, while in the heat-treated state, the sub-grains were removed and the dislocation density recovered. SN-curves are predicted based on tensile properties, hardness and defects obtained by fractography, using the $\sqrt{\text{area}}$-method.

Keywords: Fatigue, Additive manufacturing, Heat treatment, Inconel 718, Defects, Selective laser melting

1. Introduction

Additive Manufacturing (AM) is a fast-rising production method allowing components to be produced by adding material rather than forming or subtracting, as is characteristic for many established conventional processes. Many design restrictions are avoided with AM and parts can be manufactured with a high degree of design freedom. However, some challenges also arise with the new manufacturing method: high surface roughness, anisotropic microstructure, porosity and residual stresses.[1,2,3,4,5] Due to this, the fatigue behaviour of the materials are often reduced compared to the wrought condition.[6] In particular, the geometric defects such as porosity, surface roughness and lack of fusion reduce the fatigue strengths.[7,8,9,6,10] The defects in the surface region can be removed by machining, and internal pores can be closed by hot isostatic pressing. In many cases, machining is not possible due to the desired complexity of the designed components. However, heat treatments might still be possible to improve the fatigue performance. This is particularly true for alloys such as Inconel 718, whose performance is strongly correlated to the heat treatment schemes.

Inconel 718 is a precipitation hardening alloy which displays high yield, tensile, creep and fatigue strengths at temperatures up to 700°C. In addition to this, the alloy has high weldability, making it a good candidate for AM. The alloy is commonly used in the aerospace, and the oil and gas industry, employing different heat treatment schemes for various applications.[11] There are several possible heat treatment schemes for Inconel 718, and they usually consist of two main stages: (i) homogenization and/or solution treatment at 980-1200°C for dissolving hardening constituents into the matrix and (ii) Ageing treatment at 650-900°C for forming γ' and γ'' precipitates. The ageing process is usually done in two steps.

Due to the high temperature gradients in AM processes such as Selective Laser Melting (SLM), the microstructure usually shows different features than those produced by conventional manufacturing.[12] Typically fine subgrain/dendritic structures are observed in the as-built state.[13] As a result of this, researchers are working on tailoring heat treatments for AM applications.[13,14]

Dealing with fatigue, the general conclusion is that the AM Inconel 718 is sensitive to the defects deriving from the manufacturing process. The material displays its lowest fatigue strength in the as-built (AB) condition, where the surface roughness tends to be high.[15] When machined, the fatigue strength of the material is increased.[15] Here, defects may be present as internal porosity or lack-of-fusion. Their locations and distributions usually cause a higher scatter in the fatigue data.[15] In terms of anisotropy, the specimens manufactured horizontally displays longer fatigue life than those manufactured vertically.[1,16,17] Hot Isostatic Pressing (HIP) can close internal

*Corresponding author: E-mail: klas.solberg@ntnu.no

porosity and has been reported to increase the fatigue strength to the same level as wrought,[18] however, it has also been reported to reduce the strength due to microstructural effects.[19]

Dealing with the influence of notches on the fatigue behaviour of AM Inconel 718 several different approaches has been made. By machining and HIPing the specimens, the designed notch can be taken into account without the influence of defects deriving from the manufacturing process.[20] If the specimens are tested in the AB condition (or if internal defects are present after machining), the surface defects also act as local notches within the notch geometries.[20,21,22,23] Taking advantage of the design freedom in AM, parts are likely to contain notched regions and in addition manufacturing defects. Due to this it is important to address issues related to size effects, both for determining the critical size and location of the defects[24,25] and for determining the appropriate dimensions of testing specimens[23,22]

In this work, the fatigue behaviour of AM Inconel 718 are investigated in the AB and the HT state. This was done for both notched and unnotched specimens. The microstructures of the two different material states were investigated and compared. Defects from the fracture surfaces were captured, and the hardness of the two materials were measured. SN-curves of the different materials and geometries were predicted based on the tensile properties and the $\sqrt{\text{area}}$-method[26] using hardness and defect sizes.

It should be noted that this work is a continuation of a previous work where the fatigue behaviour was studied in the AB condition,[22] the same specimen geometries and process parameters have been used.

2. Materials and methods

In the present work, Inconel 718 specimens produced by SLM are studied. The chemical composition of the material is defined in Table. 1 based on ASTM F3055-14a.[27] Three different specimen geometries were considered: one specimen geometry for static loading and two specimen geometries for fatigue loading. The geometries are shown in Fig. 1. The specimen for quasi-static loading was designed according to ASTM E8. The two geometries for fatigue loading were the same as the ones employed in a previous work by the autors (Solberg & Berto[22]), one unnotched and one double v-notch geometry with stress concentration, K_t, of 1.07 and 2.43 respectively[22]. The specimens were manufactured layer by layer in z-direction referring to the coordinate system in Fig. 1. A layer height of 50 μm and an energy density of 60 J/mm^3 was employed in the SLM process.

The specimens were tested in two different conditions: AB and HT. The specimens were heat-treated at 1095 °C for 1 h then air-cooled to room temperature and double aged 720 °C for 8 h furnace cooled 50 °C/h and treated at 620 °C for 8 h and air-cooled to room temperature.

Mechanical loading was done using a servohydraulic MTS uniaxial testing system with a load cell of 50 kN. The fatigue testing was done using the same system, a loading ratio $R = 0$ and a frequency of 10 Hz was used. Vickers hardness measurements were done on a Mitutoyo MicroWiZhard system; the reported values were taken as the average and standard deviation of ten measurements in each orientation.

Fractography was done using a Quanta FEG 650 Scanning Electron Microscope (SEM). The microstructure was analysed by different approaches. Analysis done by optical microscope was done by polishing cross-sections and Kalling's reagent according to ASTM E407-07. The final stage of polishing was 1 μm diamond paste. For Electron BackScatter Diffraction (EBSD) and BackScattered-Electron (BSE) analysis, the specimens were not etched but prepared by oxide polishing suspensions, with a particle size of 0.25 μm.

3. Results

3.1. Mechanical behaviour and fatigue data

Based on the tensile tests, the AB specimen showed a tensile strength of 948 MPa and an elongation of 13.0 %. After HT, a tensile strength of 1374 MPa and an elongation of 7.7% was achieved. The increase in strength and reduction in elongation at failure is typical when heat treating AM Inconel 718.[1,28] However, the results obtained here show somewhat lower elongation the other data in the literature.[1] The low elongation in both cases can be attributed to the fact that the specimens were tested with the as-built surface. A strong correlation between the surface roughness and elongation at failure for Ti6Al4V was recently demonstrated by Barba *et al.*[29]

Hardness measurements of the AB and HT materials were done in the xy- and xz-planes, referring to the coordinate system in Fig. 1. The results are shown in Table 2, and shows that

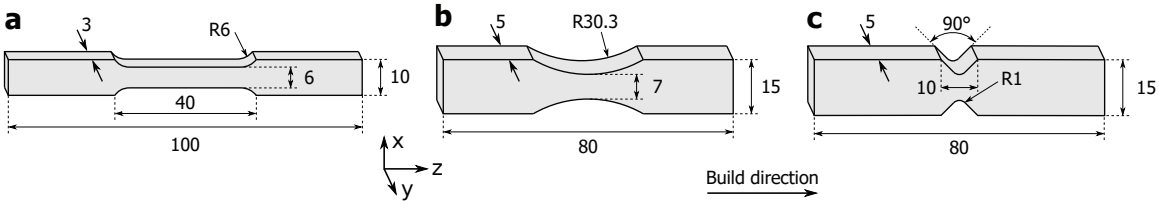

Figure 1: Dimensions of specimens: **(a)** tensile specimen, thickness 3 mm; **(b)** Unnotched fatigue specimen, thickness 5 mm; **(c)** Notched fatigue specimens, thickness 5 mm. All specimens are built in z-direction.

Ni	Fe	Cr	Nb	Mo	Ti	Al	Co	Si	Mn	Cu
50-55	11-22.4	17-21	4.8-5.5	2.8-3.3	0.7-1.2	0.2-0.8	1.0	0.4	0.4	0.3

Table 1: Chemical composition of Inconel 718 as defined by ASTM F3055-14a in wt%.[27]

for AB the hardness was ~300 HV and for HT the hardness was ~500 HV.

AB xy	AB xz	HT xy	HT xz
314.1 ± 16.2	311.1 ± 14.1	494.5 ± 19.0	512.9 ± 19.4

Table 2: Vickers hardness measurements of AB and HT specimens in xy- and xz-planes.

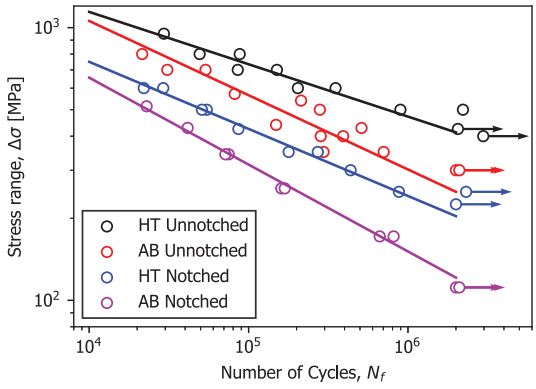

Figure 2: Fatigue data of HT and AB specimens. Tests were performed with a loading ratio R=0 and frequency of 10 Hz.

The fatigue data are collected in the SN-diagram in Fig. 2. Both for unnotched and notched specimens, the fatigue strength is increased when comparing HT to AB. Basquin equation regression lines were added in the range of 10^4 and 2×10^6 cycles, the fatigue strength at 2×10^6 cycles and the inverse slope of the curves are shown in Table 3.

	$\Delta\sigma$ [MPa]	k
HT Unnotched	420.5	5.21
AB Unnotched	250.0	3.67
HT Notched	203.2	4.07
AB Notched	121.2	3.14

Table 3: Summary of the fatigue strength, $\Delta\sigma$, at 2×10^6 cycles and the inverse slope, k, of the regression lines in Fig. 2.

3.2. *Fractographies*

Fracture surfaces of the four different specimen types are shown in Fig. 3a-d. In the unnotched specimens (Fig. 3a and b), the same trend is observed for AB and HT; fatigue initiates from a local defect in the surface and propagates towards the other side of the specimen (indicated by the arrows). For the notched specimens (Fig. 3c and d), two different fracture processes are observed; crack propagation from both notches (Fig. 3c) and crack propagation from one notch(in Fig. 3d). The AB specimens experienced crack propagation from both notches, while for the HT specimens had both cases.

The size and morphology of the defects initiating fatigue are shown in Fig. 3e-h. No distinct difference in the defect morphologies are observed when comparing the AB specimens to the HT specimens; the unnotched specimens fail from local defects, while the notched specimens fail from defects distributed along the thickness direction of the sample.

3.3. *Failure locations and surface defects*

The cross-sections of one AB and one HT notched specimen subjected to 2×10^6 cycles of loading are compared in Fig. 4a and b. The same general trends are observed: defect

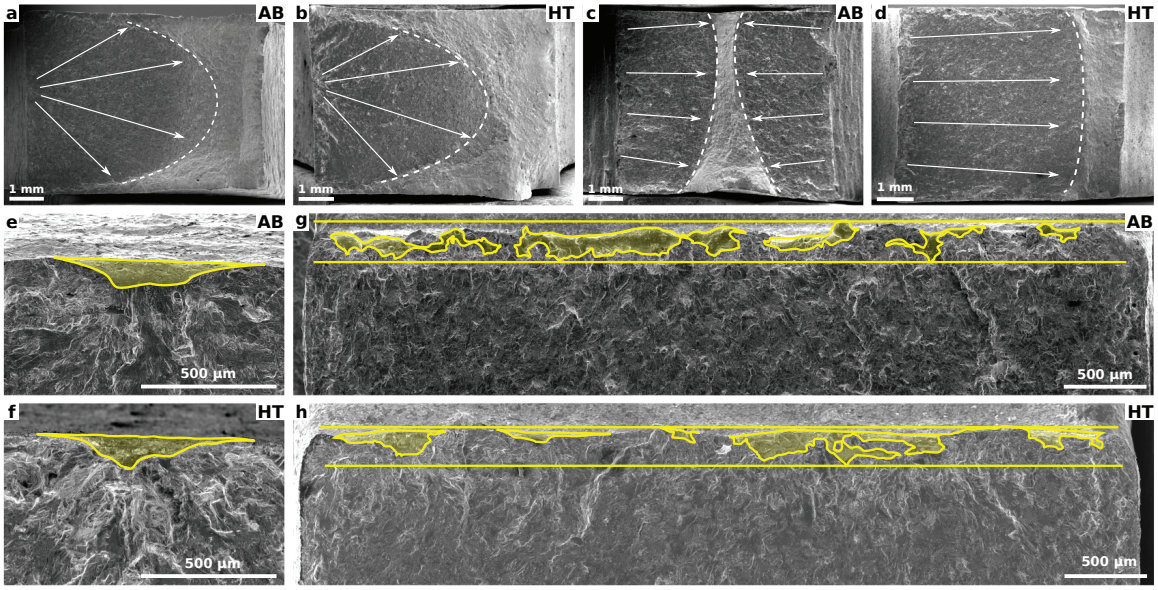

Figure 3: Fracture surface and detail of defects initiating fatigue of the different specimen types: (a-b) unnotched, overview; (c-d) notched, overview; (e-f) unnotched, initiation; (g-h) notched, initiation. The material conditions are indicated in each sub-figure.

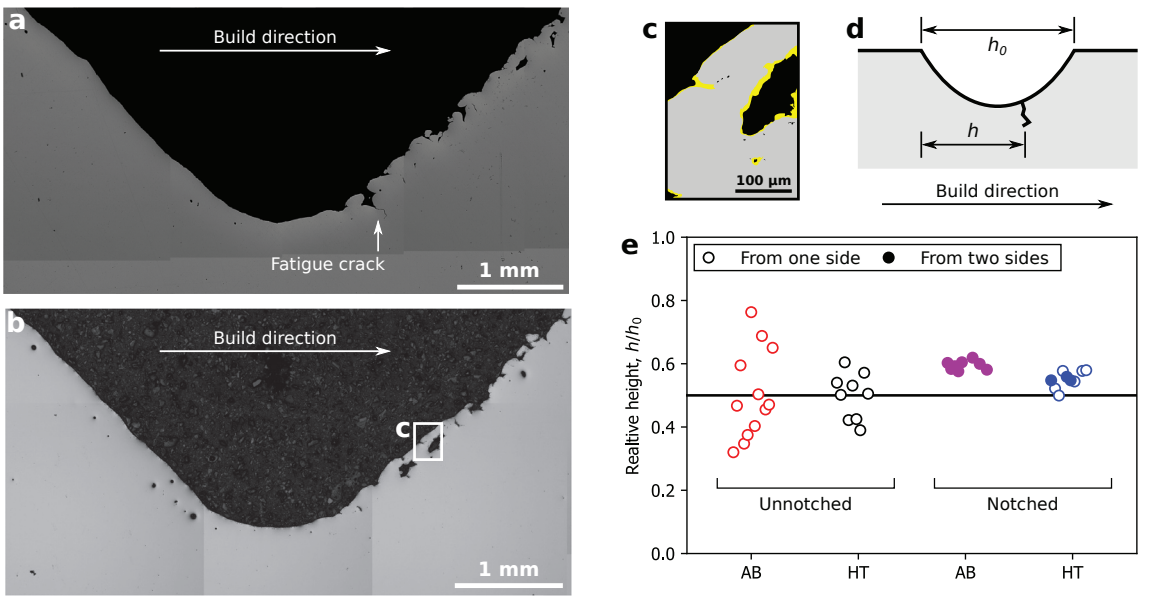

Figure 4: Polished cross sections of notched specimens subjected to 2×10^6 cycles: (a) AB and (b) HT. (c) highlighted oxide layer (yellow). (d) Definition of failure site: relative height, h/h_0 (e) Failure locations for the various tests

populated down-skin region and smoother up-skin surface. The AB specimen displays fatigue crack initiation from the down-skin region; this is not observed within the HT specimen. It should be noted that the morphology of the defects adjacent to the notch root is not the same. Further, Fig. 4 evaluates one plane within the material, which is not necessarily representable

for the whole cross-section.

According to recent research, notch geometries produced by AM subjected to fatigue loading does not necessarily fail from the designed notches, but rather from defects related to the manufacturing process, dependent on the notch acuity and the size of the defects.[22,25] Both the AB and HT specimens display the same general surface morphology and similar values of Rz can be assumed: 77 μm and 259 μm for the up-skin and down-skin respectively.[30] It should be noted that an oxide film was formed on the surface in the HT specimens, as highlighted in Fig. 4c.

The trends in failure locations are shown in Fig. 4e. For the unnotched specimens, AB displays a high scatter in failure locations compared to HT. Based on these differences, it seems like the AB specimens are less sensitive to the nominal stress level, and more sensitive to defects than HT. Further, some differences are observed when comparing the notched specimens. For AB specimens, fatigue initiated from both sides, and always in the down-skin region. For the HT specimens, fatigue shifted between failure from one or two sides. In addition to this, some specimens failed from closer to the notch root.

3.4. Microstructure

The microstructure of the AB and HT condition are shown in Fig. 5a and b, respectively. In AB, the hatch pattern and melt pool morphologies are visible, elongated grains are observed in the build direction (xz- and yz-planes) and equiaxed grains in the xy-plane. In the case of HT, the same general trends are observed. However, the hatching pattern and melt pool morphologies are not as visible. The general microstructure is typical for Inconel 718 produced by SLM.[1] The two materials were further analysed by EBSD and the results are shown in Fig. 6.

The structure of the grains are shown in Fig. 7. Fig. 7a and d show the difference between AB and HT in the xz-plane. In the AB condition, a refined sub-grain structure is observed; in the HT specimen, the boundaries seem erased/smoothed compared to AB. The same trends are observed in the xy-plane, in Fig. 7b and e. In the case of AB, the sub-grains show the same trend as the general microstructure; elongated in the build direction and equiaxed in the xy-plane. Furthermore, precipitates are observed at the grain boundaries in the HT specimen, as indicated by arrows in Fig. 7d. In addition, the dislocation density is compared in Fig. 7c and f. The white lines indicate the dislocations. Compared with AB specimens, a reduced dislocation density is observed for the HT specimens, which is the same to the results reported by Zhang *et al.*[28]

3.5. Fatigue life predictions

When designing against fatigue, SN-diagrams are frequently used to determine the critical load levels. For design purposes, SN-diagrams can either be developed based on experimental data or they can be estimated. In this section, we demonstrate how the Murakami-method[26] and the tensile behaviour can be used for estimating SN-diagrams for AM metals.

The Murakami-model has been frequently employed when analysing AM metals.[31,7,32,33] The model correlates the fatigue limit, σ_w, with the hardness and the critical defect size, $\sqrt{\text{area}}$. The fatigue limit can be estimated (for R=-1 loading) by the following relation:

$$\sigma_{w,R=-1} = \frac{1.43(Hv + 120)}{(\sqrt{area})^{1/6}}. \quad (1)$$

In order to predict the fatigue behaviour the following assumptions were made:

1. The fatigue strength can be predicted to be equal to the tensile strength, σ_{uts}, at $\sim 10^3$ cycles. This is a good estimate for many ductile engineering materials at R=0.[34] This is can also be used for notched specimens due to the notch strengthening effect.[30]
2. The fatigue limit can be predicted based on the critical defect size and the hardness employing the $\sqrt{\text{area}}$-method by Murakami. Note that the fatigue limit should also be corrected for the mean stress and the stress concentration factor.
3. The slope of the SN-diagram can be estimated based on the two above-mentioned estimates by the Basquin equation.

In the case of the fatigue data presented here, the defect-sizes were captured for all the AB specimens. Based on the micrograph in Fig. 4a and b, the surface morphology of AB and HT specimens are similar. In addition , the fracture surfaces in Fig. 3 shows similar defects. This indicates that the defects obtained in the AB specimens can be used to predict the fatigue life of the HT specimens. The loading ratio for the fatigue data in this work is R=0; this means that a mean stress correction should be made of the Murakami-model. The SWT mean stress

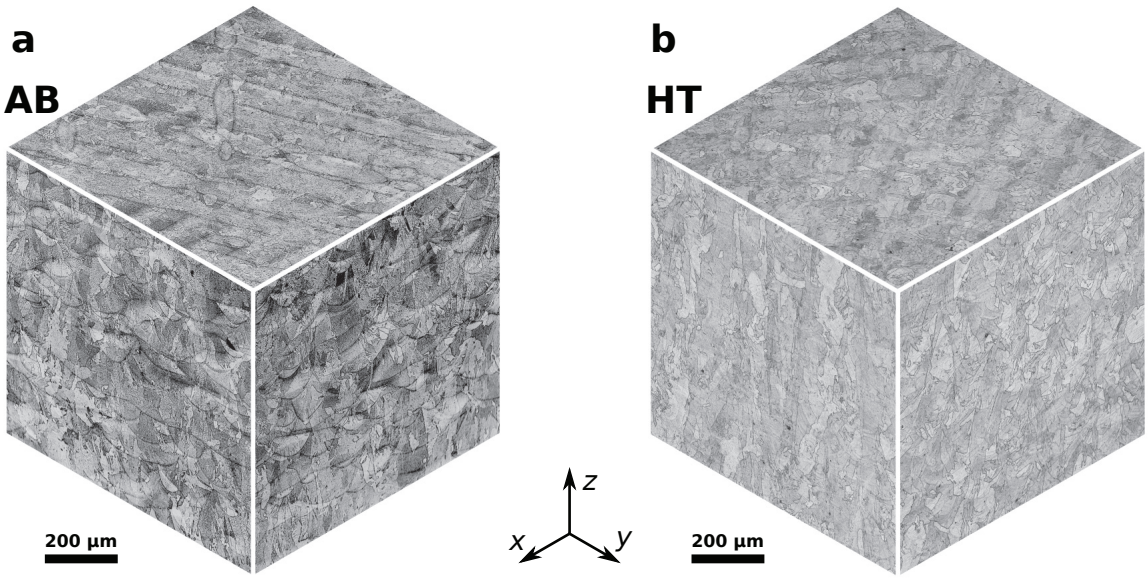

Figure 5: Comparison of the general microstructure and the surface conditions in AB and HT (a) 3 planes of microstructure in AB, (b) 3 planes of microstructure in HT.

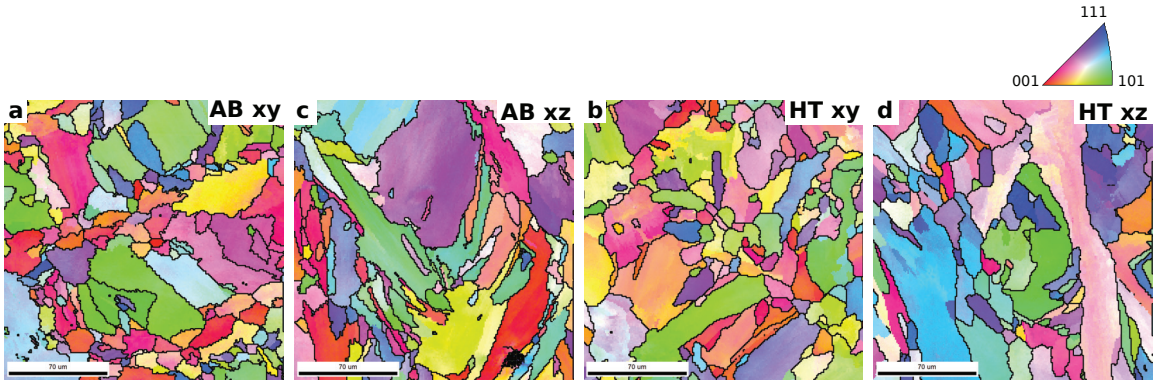

Figure 6: General microstructure obtained by EBSD in terms of normal direction -inverse pole figure (ND-IPF) maps. (a) AB xy-plane, (b) HT xy-plane, (c) AB xz-plane and (d) HT xz-plane. The coloring criterion is the same for all sub-figures, shown by the IPF in the upper right corner.

correction was used.[35] The SWT mean stress correction is given by

$$\sigma_{ar} = \sigma_a \sqrt{\frac{2}{1-R}}, \tag{2}$$

where σ_a is the stress amplitude and σ_{ar} is the equivalent stress amplitude for R=-1. The fatigue limit expressed in terms of the stress range corrected to R=0 loading can then be expressed as

$$\Delta\sigma_{w,R=0} = \sqrt{2} \cdot \frac{1.43(Hv + 120)}{(\sqrt{area})^{1/6}}. \tag{3}$$

The $\sqrt{\text{area}}$ should be taken as the effective defect area projected onto the plane perpendicular to the loading direction. Both in the case of unnotched and notched specimens, the largest defect obtained from fractography was used. The defects and the estimated effective area are shown in Fig. 8. In the case of the unnotched specimen, a semi ellipse was drawn around the defect. In the case of the notched specimens, defects were present along the edge of the notch, and in this case, the effective defect size was taken to be $10c$, where c is the maximum

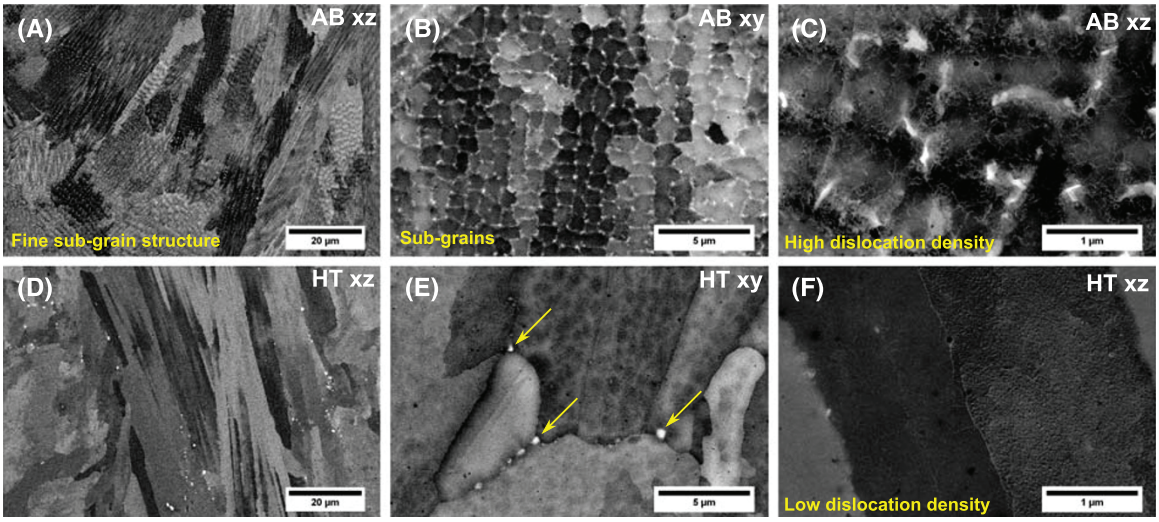

Figure 7: SEM analysis of the microstructure of AB (a,b,c) and HT (d,e,f) material. (a) xz-plane, (b) xy-plane, (c) xz-plane, high dislocation density visible, (d) xz-plane (e) xy-plane (f) xz-plane, low dislocation density visible.

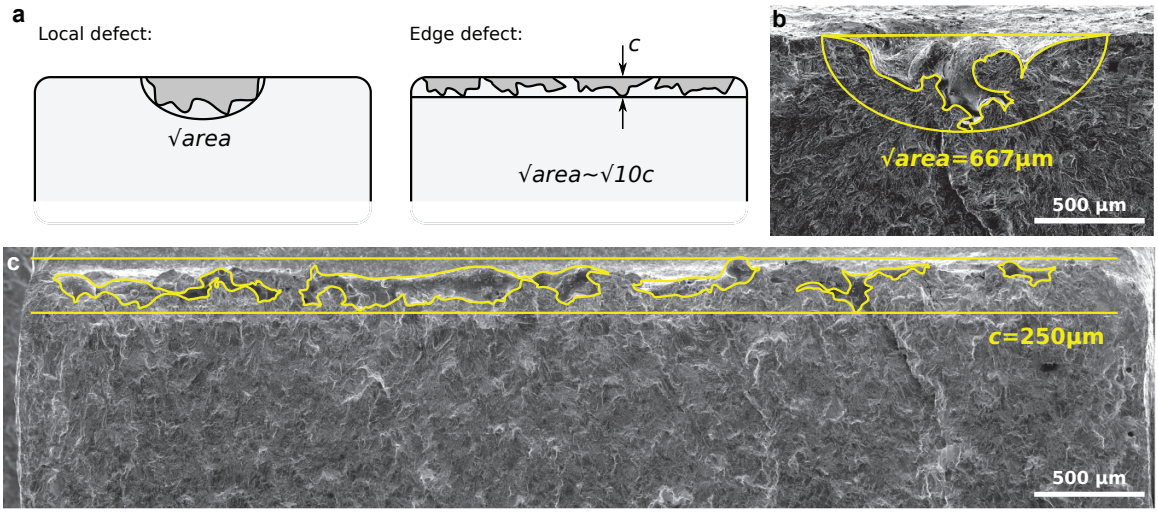

Figure 8: Defects and effective defect area of (a) unnotched specimen and (b) v-notched specimen. (c) Method of estimating the effective defect area of local and edge defects

depth of the defect (as suggested in by Murakami[36]). Based on these assumptions, the predicted fatigue life curves are shown in Fig. 9a, and the accuracy of the predictions are shown in Fig. 9b.

4. Discussion

4.1. Failure locations

In Fig. 4, changes in failure locations are observed when comparing AB and HT. Several explanations can be used for describing the change in failure locations observed when comparing the AB and HT specimens.

The first explanation is based on the ideas of Wan *et al.*,

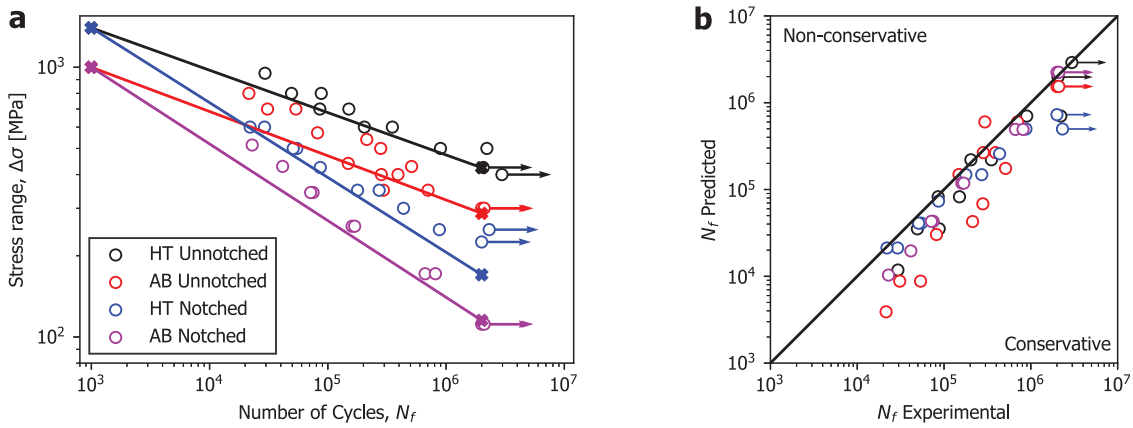

Figure 9: (a) Fatigue life curves predicted based on Murakami-method and tensile properties. (b) Accuracy of SN-curve predictions

where they proposed that heat treatment of AM Inconel 718 could increase the resistance to fatigue initiating from voids.[14] It is widely accepted that the mechanical performance and in particular the fatigue behaviour of Inconel 718 is strongly dependent on the heat treatments. By assuming that voids and defects will always be present in SLM components, Wan *et al.* tailored heat treatments for AM Inconel 718 for making the material less sensitive to the geometric defects. This would be equivalent to altering the *critical distance* of the material.[37] The idea of the critical distance derived from Neuber,[38,39] who proposed that failure is initiating when the stress at a certain distance (or along a structural support length) inside the material reaches a critical value.[40] *I.e.* the stress at a certain distance away from a notch/defect/crack should reach a certain value for failure to occur. Engineering alloys with different mechanical properties have different critical distances.[37,40,41] Usually, specimens for fatigue testing are designed in order to have a fixed failure location. However, in the specimens considered here, there are several possible failure locations, i.e. the local defects and the global geometry. As these two geometrical configurations (appearing at different scales) produce different stress gradients, the failure locations might shift if the critical distance of the material change. This could indicate that the shift in failure locations could be caused a change in the critical distance after the heat treatment, making the stress field from the notch root more critical than the stress from the defects.

Another factor influencing the failure locations could be the effect of the oxide film. The oxide film in HT specimen can be observed in Fig. 4c. Oxidation layers can be used as protection against corrosion.[42] The oxide film forms on free surface and might have a similar effect to what has been observed in high-temperature fatigue of Inconel 718. In high-temperature fatigue of Inconel 718, some researchers are attributing the high fatigue strength and the retardation of short crack growth to the formation of oxide films at the crack tip, which suppresses slipping[43,44,45,46,47]. Assuming that the AB surfaces are "pre-cracked" due to the defects in the surface region, the initiation of crack growth might be suppressed by the oxide film. In addition to this, the oxide films could be "blunting" the defects, so that an oxide layer covers their initial sharp radius. It should be noted that oxides have also been found to decrease the fatigue behaviour of materials, in particular when they take form as imperfections[48,49]. If oxide films can increase the fatigue strength in AM components, it would be a straightforward and cheap way to do post-processing. In conventional components, the oxide film might change the appearance or the tolerances. While in AM AB components, the surfaces are initially rough, and it would not matter if an oxide film is present or not.

A third explanation could be a statistical difference in the defects of the AB and HT specimens. From Fig. 4, it seems that the same morphologies of defects are present in the down-skin region for both specimens. From the fractographies in Fig. 3, defects of similar sizes and morphologies were found in the AB and HT specimens.

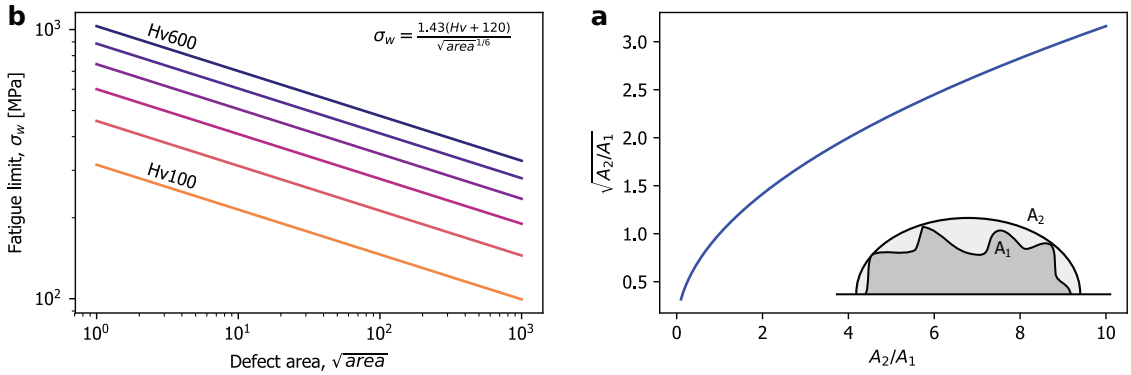

Figure 10: (a) The effect of Hv and $\sqrt{\text{area}}$ on the fatigue limit predicted by Murakami. (b) The influence of the area measured.

4.2. The $\sqrt{area}$-method

The modified approach of the Murakami-method proposed here can give predictions of the fatigue strengths of both notched and unnotched specimens based on tensile properties, hardness and defect-size. The estimates give conservative predictions; however, this result is dependent on what number of cycles one states the fatigue limit to be at. *E.g.* if the fatigue limit is stated to be at 10^7 cycles, then the predictions would be less conservative. It should also be noted that many effects are not taken into account, such as residual stresses and microstructural anisotropy. Despite this, the method can be useful for estimating the fatigue properties when designing components.

One of the main issues dealing with the $\sqrt{\text{area}}$-method is that the effective defect area should be used. In order to obtain this area, specimens usually need to be broken in fatigue loading. But how much does the accuracy of the parameter matter on the fatigue limit predictions? There is a linear relationship between the hardness and the fatigue limit, while there is a power law relation between the defect size and the fatigue limit. In Fig. 10a, the fatigue limit predictions are plotted versus $\sqrt{\text{area}}$ for Hv values ranging from 100 to 600.

The measurement of the effective area in the Murakami model leaves room for deviations. The plot in Fig. 10b shows the effect of deviating measurements. If A_2 is overestimated, *e.g.* by a factor of 10, the resulting error in $\sqrt{}$ is only by a factor of 3. If A_2 is underestimated by a factor 0.1, the resulting error in $\sqrt{}$ is by a factor of 0.3. This means that by taking $\sqrt{\text{area}}$, the errors are corrected to be closer to the real area.

The defect range in AM is typically one order of magnitude, *e.g.* $10^1 - 10^2$ μm. Due to this, making a mistake in calculation, *e.g.* 50% will have a small impact on the result. The Murakami model is mainly concerned with the order of magnitude of the defect.

5. Conclusions

AM Inconel 718 was analysed in the AB and HT state. The tensile and fatigue behaviour of the material were evaluated. Further, the Murakami-model was employed for predicting SN-diagrams. The following conclusions can be drawn:

- Heat treatment of as-built specimens increased the tensile strength, the hardness, and the fatigue strength and decreased the elongation.
- The microstructure showed typical columnar grains in the build direction for both AB and HT. In the AB state, fine subgrain structures were observed; these were erased after HT and precipitates were observed at the grain boundaries. The dislocation density was reduced after heat treatment.
- SN-curves were predicted based on the Murakami-model and the tensile strengths, for both unnotched and notched specimens. The predictions indicated that the method is suitable design purposes in engineering applications.

Acknowledgement

The authors would like to acknowledge Marius Hornnes for experimental works associated with his master's thesis.

CRediT authorship contribution statement

Klas Solberg: Conceptualization, Formal analysis, Investigation, Visualization, Writing - Original Draft **Di Wan**: Investigation, Writing - Review & Editing **Filippo Berto**: Conceptualization, Writing - Review & Editing, Supervision

References

[1] Hosseini E, Popovich V. A review of mechanical properties of additively manufactured Inconel 718, Addit Manuf. 2019;30: 100877.

[2] Vastola G, Zhang G, Pei Q, Zhang YW, Controlling of residual stress in additive manufacturing of Ti6Al4V by finite element modeling, Addit Manuf. 2016;12: 231-239.

[3] Megahed M, Mindt HW, N'Dri N , Duan H, Desmaison O. Metal additive-manufacturing process 288 and residual stress modeling, Integr Mater Manuf Innov. 2016;5: 6193.

[4] Salvati E, Lunt AJ, Heason CP, Baxter GJ, Korsunsky AM. An analysis of fatigue failure mechanisms in an additively manufactured and shot peened in 718 nickel superalloy. Mater Des. 2020;191:108605.

[5] Barros R, Silva FJG, Gouveia RM, Saboori A, Marchese G, Biamino S, *et al.* Laser powder bed fusion of Inconel 718: Residual stress analysis before and after heat treatment. Metals 2019;12:1290.

[6] Yadollahi A, Shamsaei N. Additive manufacturing of fatigue resistant materials: Challenges and opportunities. Int J Fatigue. 2017;98: 14-31.

[7] Tammas-Williams S, Withers P, Todd I, Prangnell P, The influence of porosity on fatigue crack initiation in additively manufactured titanium components, Sci Rep. 2017;7: 7308.

[8] Li P, Warner D, Fatemi A, Phan N. Critical assessment of the fatigue performance of additively manufactured Ti6Al4V and perspective for future research, International Journal of Fatigue. 2016;85: 130-143

[9] Molaei R, Fatemi A, Phan N. Significance of hot isostatic pressing (hip) on multiaxial deformation and fatigue behaviors of additive manufactured Ti-6Al-4V including build orientation and surface roughness defects. Int J Fatigue 2018;7: 352 - 370.

[10] Hovig EW, Azar AS, Sunding MF, Andreassen E, Srby K, High cycle fatigue life estimation of materials processed by laser powder bed fusion. Fatigue Fract Eng Mater Struct 2019;42(7): 1454-1466.

[11] Donachie MJ, Donachie SJ, Superalloys, a techinal guide, ASM International. 2002

[12] Wang Z, Guan K, Gao M, Li X, Chen X, Zeng X. The microstructure and mechanical properties of deposited IN718 by selective laser melting. J Alloys Compd 2012;513: 518-523.

[13] Tucho WM, Cuvillier P, Sjolyst-Kverneland A, Hansen V, Microstructure and hardness studies of Inconel 718 manufactured by selective laser melting before and after solution heat treatment, Mater Sci Eng A. 2017;687: 220-232.

[14] Wan HY, Zhou ZJ, Li CP, Chen GF, Zhang GP. Enhancing fatigue strength of selective laser melting-fabricated Inconel 718 by tailoring heat treatment route. Adv Eng Mater 2018;20(10): 1800307.

[15] Balachandramurthi AR, Moverare J, Dixit N, Pederson R. Influence of defects and as-built surface roughness on fatigue properties of additively manufactured alloy 718. Mater Sci Eng A 2018;735: 463-474.

[16] Konecna R, Nicoletto G, Kunz L, Baa A, Microstructure and directional fatigue behavior of Inconel 718 produced by selective laser melting, Proc Struct Integ 2016;2: 2381-2388.

[17] Kelley PF, Fatigue behavior of direct metal laser sintered (DMLS) Inconel 718, MSc thesis, Tufts University 2016.

[18] Witkin DB, Patel D, Albright TV, Bean GE, McLouth T, Influence of surface conditions and specimen orientation on high cycle fatigue properties of Inconel 718 prepared by laser powder bed fusion. Int J Fatigue 2020;132: 105392.

[19] Aydinoz M, Brenne F, Schaper M, Schaak C, Tillmann W, Nellesen J, Niendorf T, On the microstructural and mechanical properties of post-treated additively manufactured Inconel 718 superalloy under quasi-static and cyclic loading. Mater Sci Eng A 2016;669: 246-258.

[20] Witkin DB, Patel DN,Bean GE. Notched fatigue testing of Inconel 718 prepared by selective laser melting. Fatigue Fract Eng Mater Struct. 2019;42:166177.

[21] Nicoletto G, Smooth and notch fatigue behavior of selectively laser melted Inconel 718 with as-built surfaces, Int J of Fatigue 2019;128:105211.

[22] Solberg K, Berto F. Notch-defect interaction in additively manufactured Inconel 718. Int J Fatigue. 2019;122: 35-45

[23] Konecna R, Nicoletto G, Riva E, Notch fatigue behavior of inconel 718 produced by selective laser melting, Proc Struct Integr 2019;17:138-145.

[24] Romano S, Nezhadfar P, Shamsaei N, Sei M, Beretta S, High cycle fatigue behavior and life prediction for additively manufactured 17-4PH stainless steel: Effect of sub-surface porosity and surface roughness, Theor Appl Fract Mech 2020;106:102477.

[25] Solberg K, Berto F. A diagram for capturing and predicting failure locations in notch geometries produced by additive manufacturing. Int J Fatigue 2020;134:105428.

[26] Murakami Y. Chapter 5 - effect of hardness HV on fatigue limits of materials containing defects, and fatigue limit prediction equations, Metal Fatigue, Elsevier Science Ltd, Oxford, 2002, pp. 57-74

[27] ASTM, Standard specification for additive manufacturing nickel alloy (uns n07718) with powder bed fusion, Standard ASTM F3055-14a, ASTM International. 2014.

[28] Zhang D, Niu W, Cao X, Liu Z. Effect of standard heat treatment on the microstructure and mechanical properties of selective laser melting manufactured Inconel 718 superalloy, Mater Sci Eng A 2015;644:32-40.

[29] Barba D, Alabort C, Tang Y, Viscasillas M, Reed R, Alabort E. On the size and orientation effect in additive manufactured Ti-6Al-4V. Mater Des 2020;186:108235.

[30] Solberg K, Berto F. The effect of defects and notches in quasi-static and fatigue loading of Inconel 718 specimens produced by selective laser melting, Int J Fatigue 2020;137:105637.

[31] Yamashita Y, Murakami T, Mihara R, Okada M, Murakami Y, Defect analysis and fatigue design basis for Ni-based superalloy 718 manufactured by selective laser melting. Int J Fatigue. 2018;117 485-495

[32] Gunther J *et al*. Fatigue life of additively manufactured Ti6Al4V in the very high cycle fatigue regime. Int J Fatigue. 2017;94: 236-245.

[33] Solberg, K, Guan, S, Razavi, SMJ, Welo, T, Chan, KC, Berto, F. Fatigue of additively manufactured 316L stainless steel: The influence of porosity and surface roughness. Fatigue Fract Eng Mater Struct. 2019; 42: 2043 2052.

[34] N. E. Dowling, Mechanical behavior of materials, 4th edition, Pearson.

[35] Smith K, Topper T, Watson P. A stress-strain function for the fatigue of metals (stress-strain function for metal fatigue including mean stress effect). J Mater. 1970;5: 767-778.

[36] Murakami Y, Chapter 2 - stress concentration. In: Metal Fatigue, Elsevier Science Ltd, Oxford; 2002:11-24.

[37] Taylor D, Geometrical effects in fatigue: a unifying theoretical model, Int J Fatigue 1999;21(5):413-420.

[38] Neuber H, Kerbspannungslehre, Springer-Verlag, 1958.

[39] Neuber H. Uber die berucksichtigung der spannungskonzentration bei festigkeitsberechnungen. Konstruktion 1968;20(7):245-251.

[40] Susmel L. The theory of critical distances: a review of its applications in fatigue, Eng Fract Mech 2018;75(7):1706-1724.

[41] Louks R, Susmel L. The linear-elastic theory of critical distances to estimate high-cycle fatigue strength of notched metallic materials at elevated temperatures. Fatigue Fract Eng Mater Struct 2014;38(6):629-640.

[42] Greene GA, Finfrock CC. OXIDATION OF INCONEL 718 IN AIR AT TEMPERATURES FROM 973 K TO 1620 K. Energy Sciences and Technology Department, Brookhaven National Laboratory. 2000.

[43] Kawagoishi N, Chen Q, Nisitani H. Fatigue strength of Inconel 718 at elevated temperatures. Fatigue Fract Eng Mater Struct 2001;23(3):209-216.

[44] Chen Q, Kawagoishi N, Nisitani H, Evaluation of notched fatigue strength at elevated temperature by linear notch mechanics, Int J Fatigue 1999;21(9):925-931.

[45] Nezhadfar P, Johnson AS, Shamsaei N. Fatigue behavior and microstructural evolution of additively manufactured Inconel 718 under cyclic loading at elevated temperature. Int J Fatigue. 2020;136:105598.

[46] Prakash DGL, Walsh MJ, Maclachlan D, Korsunsky A. Crack growth micro-mechanisms in the IN718 alloy under the combined influence of fatigue, creep and oxidation. Int J Fatigue 2009;31(11):1966-1977.

[47] Zheng D, Rosenberger A, Ghonem H. Influence of prestraining on high temperature, low frequency fatigue crack growth in superalloys, Mater Sci Eng A 1993;161(1):13-21.

[48] Li Z, Luo AA, Wang Q. *et al.* Fatigue Properties of Cast Magnesium Wheels. Metall and Mat Trans A 2016;47:42394257.

[49] Connolley T, Starink MJ, Reed PAS. Effect of oxidation on high temperature fatigue crack initiation and short crack growth in Inconel 718. Proceedings of the 9th International Symposium on Superalloys. The Minerals, Metals & Materials Society (TMS). 2000:435-444 .

Article VI

Fatigue of additively manufactured 316L stainless steel: The influence of porosity and surface roughness

Klas Solberg, Shaui Guan, Seyed Mohammad Javad Razavi, Torgeir Welo, Kang Cheung Chan, Filippo Berto

Fatigue & Fracture of Engineering Materials & Structures, Article

The fatigue behaviour of additively manufactured (AM) 316L stainless steel is investigated with the main emphasis on internal porosity and surface roughness. A transition between two cases of failure are found: failure from defects in the surface region and failure from the internal defects. At low applied load level (and consequently a high number of cycles to failure), fatigue is initiating from defects in the surface region, while for high load levels, fatigue is initiating from internal defects. Porosities captured by X-ray computed tomography (XCT) are compared with the defects initiating fatigue cracks, obtained from fractography. The fatigue data are synthesised using stress intensity factor (SIF) of the internal and surface defects on the fracture surface.

https://doi.org/10.1111/ffe.13077

Fatigue of additively manufactured 316L stainless steel: the influence of porosity and surface roughness

K. Solberg[a,*], S. Guan[b], S.M.J. Razavi[a], T. Welo[a], K.C. Chan[b], F. Berto[a]

[a]*Department of Mechanical and Industrial Engineering, Norwegian University of Science and Technology, 7034 Trondheim, Norway*
[b]*Department of Industrial and Systems Engineering, The Hong Kong Polytechnic University, Hung Hom, Kowloon, Hong Kong.*

Abstract

The fatigue behaviour of additively manufactured (AM) 316L stainless steel is investigated with the main emphasis on internal porosity and surface roughness. A transition between two cases of failure are found; failure from defects in the surface region and failure from the internal defects. At low applied load level (and consequently a high number of cycles to failure) fatigue is initiating from defects in the surface region, while for high load levels, fatigue is initiating from internal defects. Porosities captured by X-ray Computed Tomography (XCT) are compared with the defects initiating fatigue cracks obtained from fractography. The fatigue data is synthesized using Stress Intensity Factor (SIF) of the internal and surface defects on the fracture surface.

Keywords: Fatigue, Surface roughness, Porosity, 316L Stainless steel, Selective Laser Melting

Nomenclature:

A_d, Defect area; A_{eff}, Effective defect area; c, Surface defect depth; E, Energy density; h, Failure site along build orientation; h_0, Length of gauge section; K_{max}, Maximum stress intensity factor; k, Inverse slope; l, Hatch distance; N_f, Number of cycles to failure; P, Laser power ; R, Loading ratio; t, Layer thickness; T_σ, T_K, Scatter index; v, Scanning speed; ΔK, Stress intensity factor range; ΔK_{th}, Threshold of stress intensity factor range; σ_{max}, Maximum stress; σ_{min}, Minimum stress; σ_{nom}, Nominal stress; σ_{UTS}, Ultimate tensile strength

1. Introduction

AM is a processing method capable of producing parts by adding material layer-by-layer, controlled by computer-assisted codes.[1,2,3] AM allows for producing components with high geometric complexity, including internal structures and undercuts in one step without post-processing.[4,5] In recent years, AM is becoming accepted as a manufacturing method for industries like aerospace, medical, energy and automotive.[6,7] However, there are some challenges when dealing with AM. Properties deriving from the processing method such as voids, high surface roughness, residual stresses and anisotropic microstructure can affect the overall mechanical behaviour of these components.[1,2] Especially when dealing with fatigue, the geometrical discontinuities, such as porosities or defects in the surface region, are factors strongly affecting the performance.[8,9,6]

316L is an austenitic chromium-nickel stainless steel. It is one of the most widely used stainless steels due to its good ductility, high strength and high corrosion resistance.[6,7] It is used in engineering applications such as automobile, oil and gas, construction, chemical and petrochemical industries.[6,7] Dealing with AM 316L, it has shown higher strength than its conventionally manufactured counterparts, where a lower ductility has been reported.[7] The higher strength in the as-built condition is attributed to a refined microstructure and a high dislocation density.[7] In the as-built condition, the material display anisotropic mechanical properties, Hot Isostatic Pressing (HIP) and heat treatments can remove anisotropy; it is also leading to a reduction of strength and increased ductility compared to as-built.[10] The fatigue behaviour of as-built AM 316L steel has previously been investigated.[11,12,13,14] The as-built specimens display lower fatigue life than their conventionally manufactured counterparts due to defects deriving from the manufacturing process.[14,15,16] Further, post-processed specimens have been shown to exceed the fatigue life of their conventionally manufactured counterparts.[14]

*Corresponding author
Email address: klas.solberg@ntnu.no (K. Solberg)

In the present work, 316L stainless steel produced by Selective Laser melting (SLM), a Powder Bed Fusion (PBF) method, is investigated. The main objective of this work is to evaluate the effect of internal porosity and surface roughness on the fatigue behaviour, with the main emphasis on the interaction between these two. A series of 316L specimens produced by SLM is tested under static and uniaxial fatigue loading. The specimens were analysed employing XCT, displaying high amounts of porosities. The fracture surfaces were captured in Scanning Electron Microscopy (SEM), and the results were not according to the typical results on AM metals; A transition between failure from surface defects and internal defects were observed. For high stress levels and a low number of cycles, fatigue is initiating from regions of internal defects (voids) while for low stress levels and a high number of cycles to failure, fatigue is initiating from defects in the surface region. Further, the $\sqrt{\text{area}}$-method[17] a popular method when dealing with fatigue assessment of AM metals[15,18,19,20,21,22] was employed in order to express the fatigue life curve in terms of SIF.

2. Materials and Experimental procedure

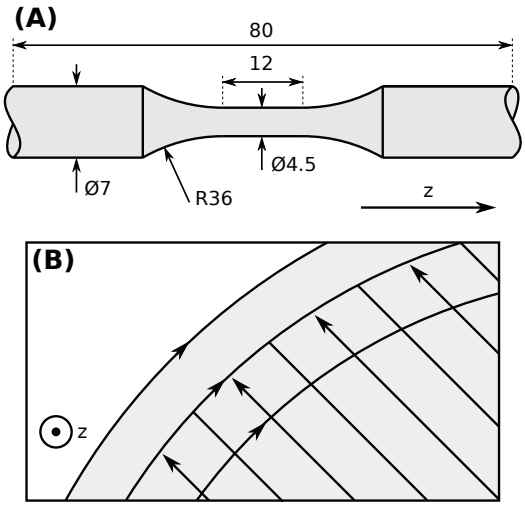

Figure 1: **(a)** Geometry and dimensions of specimen, built layer-by-layer in z-direction. **(b)** Schematic illustration of scanning strategy.

Round hourglass-shaped specimens with a constant gauge section of 4.5 mm diameter according to ASTM E466-15[23] of 316L stainless steel were produced by SLM. The geometry and dimensions of the specimens are shown in Fig. 1a. The process parameters used for manufacturing the specimens are specified in Table 1. The specimens were printed standing in the z-direction so that the layers were perpendicular to the loading direction. The specimens were manufactured with three contours and internal hatching. The scanning strategy is shown in Fig. 1b.

t [μm]	l [μm]	v [mm/s]	P [W]	E [W/mm^3]
50	100	2400	320	26.7

Table 1: Process parameters used for fabrication of the specimens, Layer thickness (t), Hatch distance (l), Scanning speed (v), Laser power (P) and Energy density (E)

The surface roughness, *Ra*, was measured in the gauge section along the z-direction. An Alicona Infinity confocal microscope was used for the measurements. The reported value of *Ra* was taken as the average value of 12 measurements.

X-ray Computed Microtomography (XCT) was conducted on a dual-tube micro-focus x-ray CT System YXLON FF35 CT. A cylindrical control volume with a diameter of 2 mm and a height of 1.65 mm was captured from the gauge section of a specimen. By employing an X-ray tube voltage of 195.0 kV, a current of 100.0 μA, a magnification of 52 and 1800 projections, a resolution of 2.7 μm was obtained. The same method as the one of Lu and Chan[24] was used.

A static tensile test with a loading rate of 0.3mm/min was conducted to obtain the ultimate tensile strength, σ_{UTS}. Fatigue loading was done under load control with a loading ratio $R = \sigma_{min}/\sigma_{max} = 0.1$ and a frequency of 10 Hz. Fatigue data were presented in an S-N diagram, referring to the maximum nominal stress, σ_{max}. Haibach uniform confidence bands[25] at 10, 50 and 90 % probability of failure was calculated according to ISO 12107,[26] ASTM E 739-91,[27] from 10^4 to 2×10^6 cycles. From the confidence bands, the inverse slope, k, and the scatter index, $T_\sigma = \sigma_{90\%}/\sigma_{10\%}$, was obtained. The fatigue tests were discontinued when specimens had withstood 2×10^6 cycles without failure. Both static and fatigue tests were conducted on a servohydraulic MTS system with a load cell of 50 kN.

The fracture surfaces of all specimens were investigated by Scanning Electron Microscopy (SEM). The defects initiating the fatigue cracks were captured and measured. This was done by identifying which regions showed signs of lack of fusion and

unfused particles, and which displayed crack growth. Based on this, a general outline of the defect region was obtained, and internal islands were excluded from the measurement. The effective area of the defects was also measured. The measurement was done according to the method of Murakami,[17] which is further explained in section 3.5. The failure initiation site along the build direction (z-axis in Fig. 1a) was measured for all specimens.

3. Results

3.1. Mechanical properties

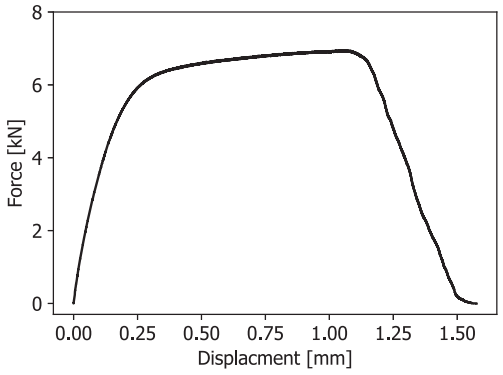

Figure 2: Load-displacement curve from static loading under displacement control.

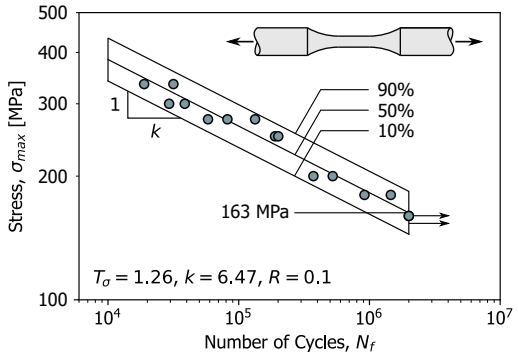

Figure 3: Fatigue data obtained from 316L stainless steel specimens, loading ratio $R = 0.1$.

Load-displacement curve from static loading is shown in Fig. 2. From the static test, an ultimate tensile strength of 437 MPa was obtained. The results from the fatigue loading are shown in Fig. 3. A fatigue strength of 163 MPa at 2×10^6 cycles was obtained, referring to the maximum stress, σ_{max}, applied.

3.2. Fractography

For all the broken specimens, the fracture surfaces were examined. The specimens either showed fatigue initiation from internal defects or surface defects; one example of each case is shown in Fig. 4. Fig. 4a-c shows failure from internal defects while Fig. 4d-e shows failure from the surface defects.

In Fig. 4a, the whole fracture surface of a specimen failing from internal defects, is shown. A detail of the defect initiating fatigue is shown in Fig. 4b, were both the unfused region with powder particles and the crack growth part (indicated by arrows) are visible. The transition from fatigue crack growth (striations) to final rupture (ductile) is shown in Fig. 4c. In Fig. 4d, the whole fracture surface of a specimen failing the surface, is shown, the defect is shown with higher magnification in Fig. 4e, where the arrows are indicating the crack growth. Subsurface defects are present at ~100 μm below the surface. Fig. 4f shows a detail of the final rupture region, where the crack is occurring in steps over different layers. Unfused particles are shown in the different "layers" indicating the final rupture part is dominated by the interaction of defects.

A selection of six specimens ranging from static failure to HCF is shown in Fig. 5. The defects in the fracture surface are shaded and outlined by a white line. In the case of the fatigue loaded specimens, the crack growth is indicated by arrows, and a new line indicates the transition from crack growth to final rupture. Failure from static loading is shown in Fig. 5a, the fracture surface displays a cup-cone morphology, and the core of the specimen displays several regions of defects. Several regions of defects are also seen in Fig. 5b, where the specimen is failing in the low cycle fatigue regime. Two specimens failing from internal defects are shown in Figs. 5c and d (Fig. 5c being the same as Fig. 4a). In Figs 5e and f two specimens with fatigue initiating from the surface are shown (Fig. 5e being the same as Fig. 4e).

The area of defects found in the fracture surfaces was measured and correlated to the fatigue behaviour; this is shown in Figs. 6a and b. A transition between failure from surface defects and internal defects are shown, and the shade of the markers indicates the defect size obtained from the fracture surfaces.

An optical micrograph of a polished cross-section of a specimen that failed from fatigue is shown in Fig. 7. The corre-

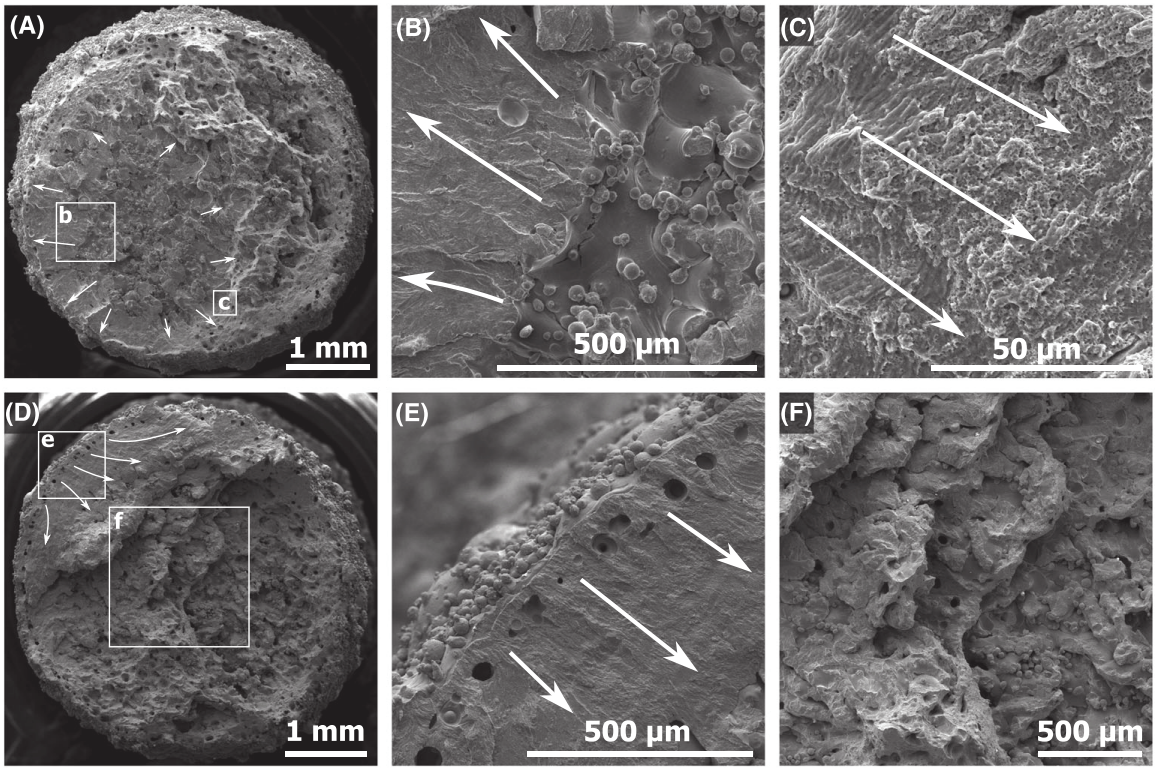

Figure 4: SEM of the two specimens: **(a)** whole fracture surface of specimen failing from internal defect; **(b)** detail from initiation; **(c)** Transition from striations to ductile failure; **(d)** whole fracture surface of specimen failing from surface defect; **(e)** detail of defect at fatigue initiation; **(f)** Detail from final rupture. The arrows are indicating the direction of crack propagation.

sponding fracture surface is shown in Fig. 5f. The crack is propagating from the left side, towards the right. The final rupture part is in different levels and displays large deformation. Like for the fracture surfaces shown in Fig. 5, sub-surface defects are present, followed by a section with a low amount of defects, and then a porous core as can be seen in Fig. 7.

3.3. Failure Initiation Site

Recently a diagram predicting the failure initiation location in AM metals was proposed.[28] The diagram is correlating the failure location, h/h_0 (in Fig. 8), to the notch acuity and the surface roughness. Various notch geometries of as-built SLM Inconel 718 specimens were investigated, and the failure location was found to be dependent on the notch acuity and the amount of surface roughness adjacent to the notch root. Due to higher surface roughness in surfaces built downward-facing, failure did not occur at the notch root for blunt notches, but from the region facing downward adjacent to the notch root. In addition, a large scatter in the failure location site was obtained for plain specimens, where the location of failure was found to be dependent on the location of the critical defects.

The failure location of the specimens investigated here was captured and compared to the plain specimen in the proposed diagram. This is shown in Fig. 8. The specimens investigated here show a similar scatter as the Inconel specimens.

3.4. Porosity and surface roughness

From the control volume examined by XCT-scan, a porosity of 5.4% was obtained. The results from the XCT scan are shown in Fig. 9 compared with the defects found in the fracture surfaces (A_d). Fig. 9a shows the projected area of the defects versus the sphericity of the defects. The main trend is that large defects have a low degree of sphericity, while small defects have a high degree of sphericity. Fig. 9b shows the

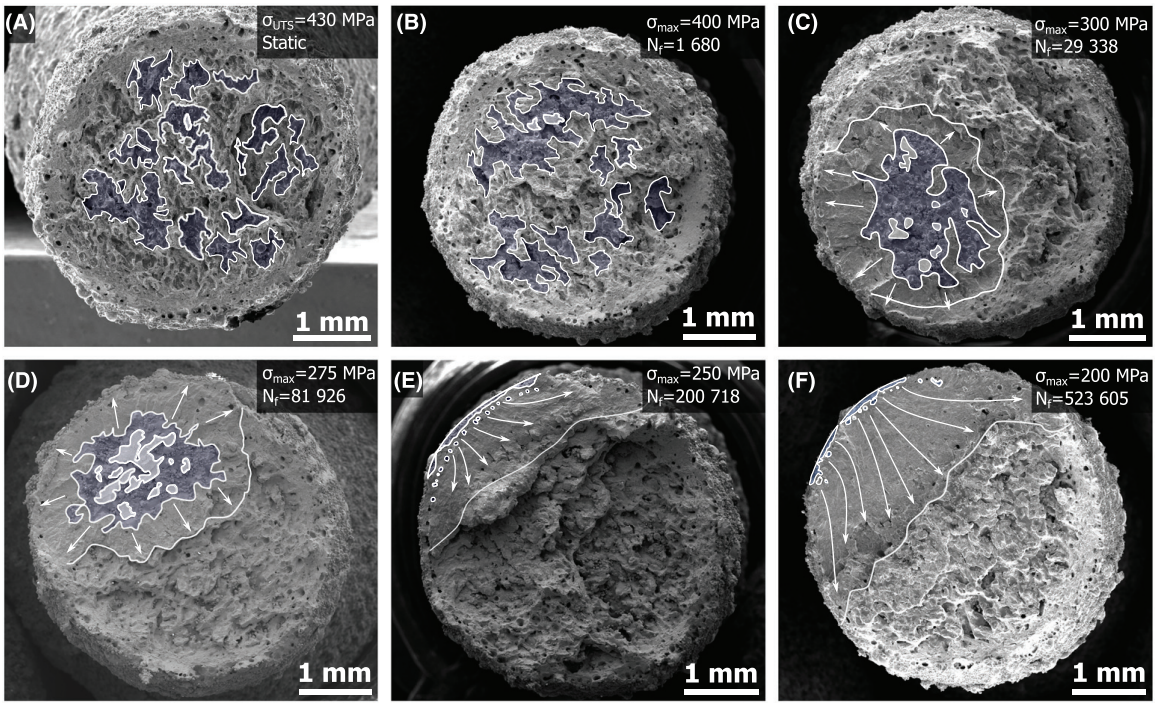

Figure 5: Fracture surfaces at different load levels: **(a)** static; **(b)** below HCF; **(c-d)** internal defects, upper part of HCF; **(e-f)** surface defects, lower part of HCF.

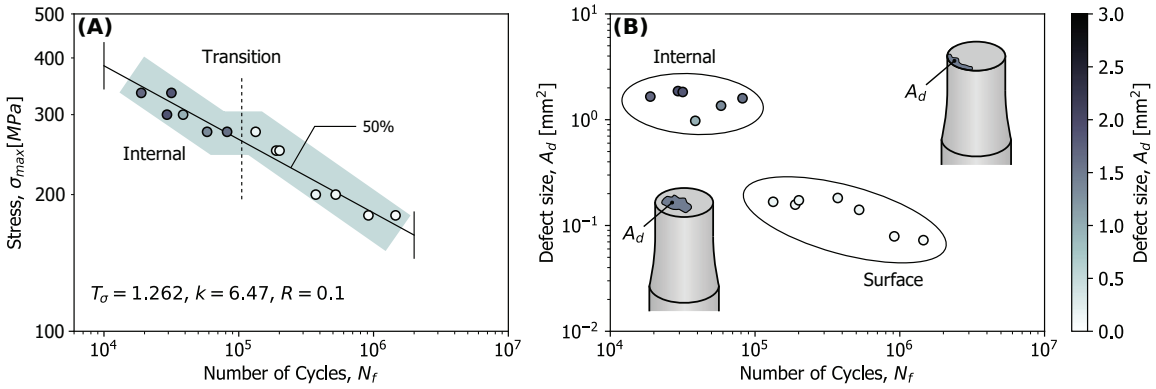

Figure 6: Fatigue behaviour correlated with defect size: **(a)** S-N diagram with marker shade indicating defect size **(b)** Defect size versus number of cycles to failure.

distribution of the defects, displaying two main bulks of defect sizes. Fig. 9c shows the projected area versus the contribution of each defect to the total volume of defects. The most significant defect in the control volume makes a contribution of 23.2% to the total volume of defects.

From Fig. 9a, the smaller defects are shown to have higher sphericity. Fig. 9d shows a comparison of the x, y and z-dimensions of the defects. The z-coordinate is compared to the average of x and y-coordinate in the upper range of defect sizes. For the larger defects, the average of x and y-dimension of the defect is larger than the z-dimension. This means that the smallest dimension of the defects is parallel to the loading direction; the same was observed in Fig. 7 and in recent works dealing with defects in AM metals.[15,20,29]

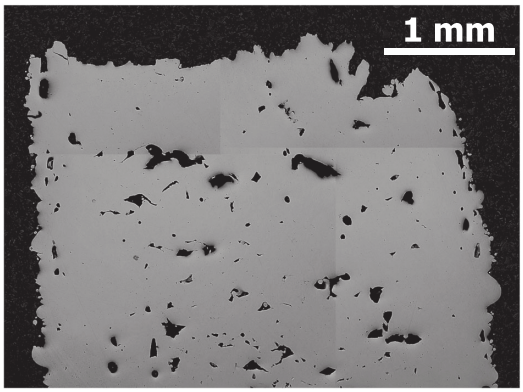

Figure 7: Polished cross section of specimen subjected to fatigue. The corresponding fracture surface is shown in Fig. 5f.

A surface roughness *Ra* of 10.1 was obtained from measurements using a confocal microscope.

3.5. Application of stress intensity factor

The fatigue life curve was expressed in terms of stress intensity factor (SIF) versus the number of cycles to failure. SIF can be applied to a member containing defects by assuming that the crack size is equal to $\sqrt{\text{area}}$ of the defect obtained from the fracture surface so that SIFs can be approximated by[17]

$$K = Y\sigma\sqrt{\pi\sqrt{area}}. \tag{1}$$

Based on this formulation, two calculations were performed, considering the actual area of the defect size measured and considering the effective area (as in the original formulation by Murakami[17]). The geometry factor, Y, is 0.65 for surface defects and 0.5 for internal defects. Using the measured area, Eq. (1) becomes

$$K_{max} = Y\sigma_{max}\sqrt{\pi\sqrt{A_d}} \tag{2}$$

The result of the first calculation is shown in Fig. 10a. The transition between the surface defects and internal defects seen in the S-N curve are no longer present.

For the second calculation, the surface defects and the internal defects are considered based on two different formulations. For internal defects, an effective area, A_{eff}, is drawn around the defect area, while for surface defects, the depth of the defects, c, is captured, as shown in Fig. 10d. Then, Eq. (1) becomes

$$K_{max} = Y\sigma_{max}\sqrt{\pi\sqrt{A_{eff}}} \qquad \text{(Internal defect)} \tag{3}$$

and

$$K_{max} = Y\sigma_{max}\sqrt{\pi\sqrt{10}c} \qquad \text{(Surface defect).} \tag{4}$$

The results are shown in Fig. 10b. When comparing the results from the two calculations, the first method is showing a lower scatter. The size considered as crack length for the two cases is compared in Fig. 10c.

4. Discussion

4.1. Fatigue data and fractography

The fatigue behaviour of 316L specimens prepared by SLM has been investigated. Although the specimens contained high amounts of defects, the fatigue behaviour was found to be comparable to recently reported fatigue data on AM 316L. By employing the SWT means stress correction,[30] the fatigue data reported here gives a fatigue strength of 120 MPa under fully reversed loading (R=-1). The same mean stress correction is employed on fatigue data from the literature, giving a range of 100-300 MPa for AM as-built 316L steels[13,14,31] and 300-420 MPa for wrought 316L steels.[13,11,12] The low fatigue strength obtained here is attributed to the high amount of defects and the high surface roughness in the specimens.

From the investigated specimens, two main categories of fatigue failure were observed: failure initiating from internal defects and failure initiating from surface defects. A transition between these two cases was observed in the number of cycles to failure. This trend indicates that for high loads, the internal defects were critical, while for low loads, the defects in the surface region were critical. For the specimens failing from above 10^5 cycles, fatigue initiates from the surface region. Similar results have been observed by Andreau *et al.*[15] stating that at $\sim 10^6$ cycles, surface defects are initiating fatigue, despite a presence of large internal defects.

The defects measured in the fracture surfaces were comparable to those obtained from XCT as seen in Figs. 9a-c. The largest defects from XCT was in size-range between the surface and internal defects found in the fracture surface. When dealing with the defects from the fracture surface, there is a possibility that the measured defects are larger than the single defects obtained from XCT because there is a possibility of coalescence of defects adjacent to each other. This is illustrated schematically in Fig. 11, where Fig. 11a illustrates fatigue initiating from internal defects while Fig. 11b illustrates fatigue initiating from the surface.

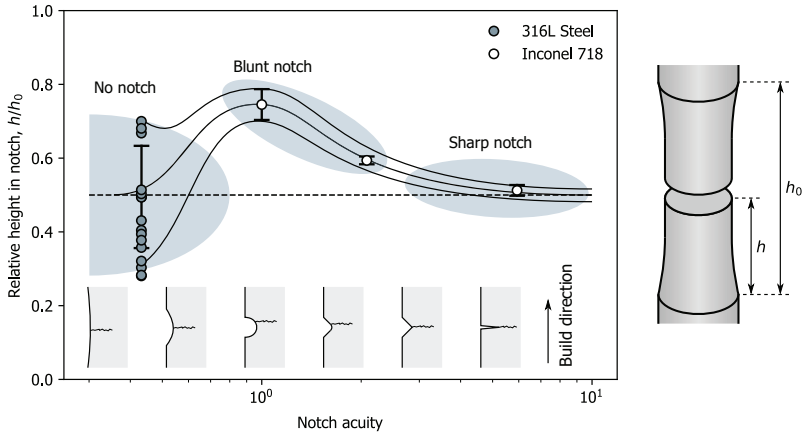

Figure 8: Failure initiation site in AM specimens versus notch acuity. Data from 316L stainless steel combined with AM Inconel 718 fatigue data from literature.[28]

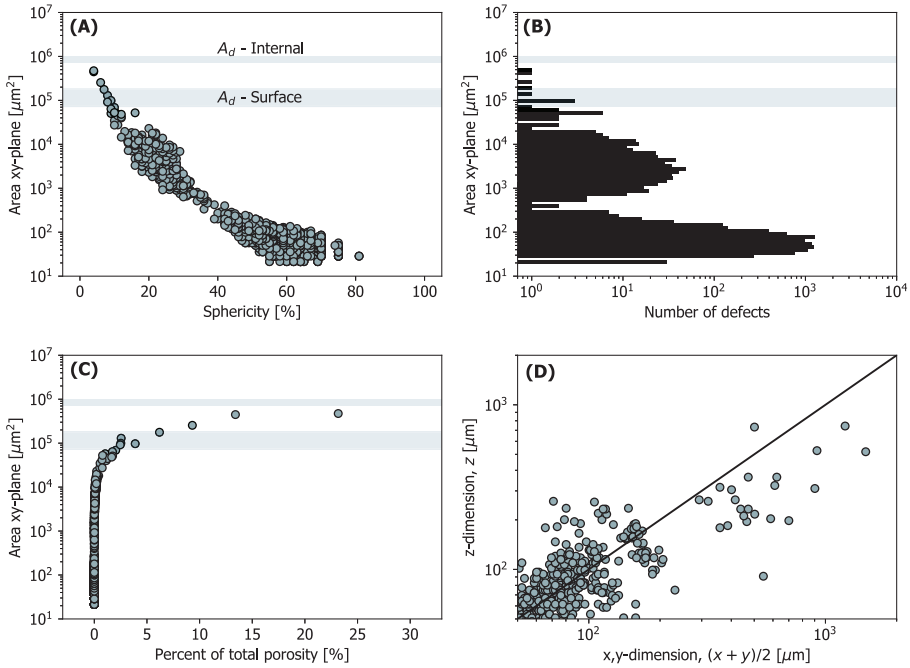

Figure 9: Porosity data from XCT scan: **(a)** Area xy-plane versus sphericity; **(b)** Distribution of defects; **(c)** size of defects as percent of total porosity volume and; **(d)** comparison of the defects x, y and z-dimension. (The range of defect size measured from fracture surface in Fig. 5 is indicated by shade in **(a)**-**(c)**)

It is widely recognised that cracks and defects are decisive when dealing with fatigue. Fatigue usually initiate from defects, acting as local stress risers, if present. Contrary in the case of static failure (especially for ductile materials) failure is not as closely linked to the localised defects as in fatigue. For static failure in ductile materials, failure is usually occurring by coalescence of voids involving plasticity.[32] A transition between the interaction of defects to defects acting alone is expected when moving from static failure to high cycle fatigue. It is possible that the transition observed in the S-N curve is

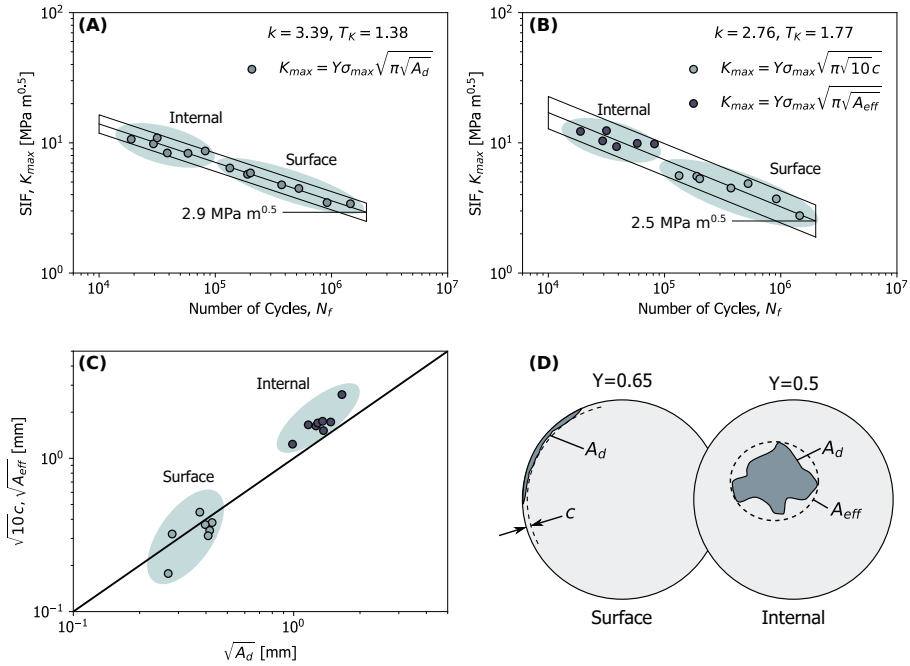

Figure 10: Application of stress intensity factor for initial defect in fracture surface: **(a)** Considering the actual measured area of defect; **(b)** Considering 10c and effective area; **(c)** Comparison between defect size in (a) and (b); **(d)** Schematic illustration of defect and measured size.

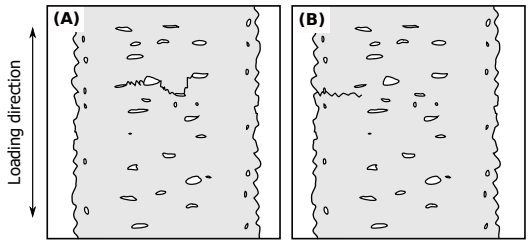

Figure 11: Failure mechanisms in specimens. Schematic illustration of: **(a)** failure from internal defects and **(b)** failure from surface defects.

related to whether the defects are interacting or not.

Interaction between the defects can be observed in the final rupture part of the specimen shown in Fig. 7 and Fig. 5 f, where the fracture is occurring in different height steps. The fatigue crack initiates from the surface and propagates perpendicular to the z-direction, without jumping between layers, indicating that less interaction between the defects is involved.

4.2. Analytical modelling of stress intensity factor

By employing the $\sqrt{\text{area}}$-method, the fatigue life curve was expressed in terms of SIF. This was done both by considering the measured defect area and by considering the effective defect area and the surface defect depth. Comparing the results from the two cases, a lower scatter was obtained in the first method. Further, the step observed in the S-N diagram was removed when considering the measured defect area.

Fatigue crack growth of AM 316L steel in the as-built condition was studied by Riemer *et al.* obtaining a SIF threshold, ΔK_{th}, of 4 MPa m$^{0.5}$ for loading perpendicular to the build direction and 3 MPa m$^{0.5}$ parallel to the build direction.[31] In order to compare the results obtained here to the results of Riemer *et al.* the maximum SIF were converted to SIF range by $\Delta K = 0.9K_{max}$. From this, ΔK is 2.6 and 2.3 at 2×10^6 for the two cases of SIF calculations considered here. This is lower but still comparable to the value of ΔK_{th} reported by Riemer *et al.* The lower value of SIF range reported here can be due to several reasons. The $\sqrt{\text{area}}$-method is an approximate method giving some indication of the equivalent SIF value, so some scatter and error should be expected. The size of the defects is large compared to the cross-sectional area (at least for the internal defects). Further, the microstructure has been reported to affect

the SIF threshold for AM 316L steel.[31]

One advantage of using the effective area is that it can be more efficient than using the real area when measuring the defects manually based on fracture surfaces. A smoothly shaped geometry is drawn around the defect; this is done by various methods. One challenge by this method is that the defect size is not unambiguously defined. By using the real projected area of the defects, it is easier to define the defect size unambiguously. However, it is more time-consuming to define it manually. In the case of obtaining the defect size from XCT data, it is opposite from manual measurements; the real defect size can be extracted directly, while the effective area needs to be calculated.

By employing the $\sqrt{\text{area}}$-method, the theory of linear elastic fracture mechanics is assumed to be valid. Under fatigue loading in the high cycle fatigue regime, cracks are propagating in a brittle manner, and a low amount of plasticity is involved. When the defects are not interacting, and the failure is initiating from localized defects (and not a large region), SIF should be possible to apply. While when the defects are large compared to the cross section, and there is a chance of several defects interacting, it is more uncertain whether it should be applied or not.

4.3. Failure initiation site

The diagram in Fig. 8 shows the failure initiation site in the 316L specimens investigated here compared with AM Inconel 718 specimens. The Inconel specimens were of different notch radii, notch depths and notch opening angles, resulting in different notch acuity and different amount of overhang in the region adjacent to the notch root. The 316L specimens are unnotched and have a constant cross-section in the gauge section, so a scatter in failure location is expected.

The diagram states that if a component contains a sharp notch, fatigue will most likely initiate from the notch root. While if the component contains no notch, the failure location is determined by the location of the critical defect. Because of this, a large scatter in failure location can be expected in plain specimens, but on average failure initiates from the region with the lowest cross-sectional area (Unless there is a problem with a specific layer in the build). For the cases in between these two extremes, failure initiates as a combination of the stress from the notch root and the localised defects from the manufacturing process.

Applying the diagram can give some idea of the quality and the features of a build. Based on the geometrical features of the components and the location of the failure, some idea about the distributions and location of critical defects can be obtained. Also, the interaction between notches and local defects deriving from the manufacturing process can be understood. This is especially interesting when dealing with builds containing downward facing surfaces.

5. Conclusions

From the present work, the following conclusions can be drawn:

- The fatigue behaviour of 316L Stainless steel specimens produced by SLM has been investigated with the main emphasis on the effect of surface roughness and porosity
- Fractography revealed that for the low load levels in the HCF regime, specimens failed from defects in the surface region, while the higher load levels, the specimens failed from internal defects. A transition between these two cases is visible in the fatigue life curve. This result indicates that the porosity and internal defects are controlling fatigue initiation at load levels above 275 MPa, while defects in the surface regime are controlling fatigue initiation at load levels below 275 MPa.
- XCT displayed unfavourable orientation of large defects, and the size of the defects was comparable to the defects found to initiate fatigue from fractography.
- The fatigue life curve has been expressed in terms of SIF based on $\sqrt{\text{area}}$-method, by both considering the measured defect area and the effective defect area.

Acknowledgement

This project was funded by the Norwegian University of Science and Technology and The Hong Kong Polytechnic University.

The authors would like to acknowledge Prof. L.C. Chan and Dr X.Z. Lu for assistance with XCT scan.

References

[1] DebRoy T *et al.* Additive manufacturing of metallic components process, structure and properties, Prog Mat Sci. 2018;92: 112-224.

[2] Herzog D, Seyda V, Wycisk E, Emmelmann C. Additive manufacturing of metals. Acta Mater. 2016;117: 371-392.

[3] Frazier WE. Metal additive manufacturing: A review. Acta Mater. 2016;117: 371-392.

[4] Langelaar M. Topology optimization of 3d self-supporting structures for additive manufacturing. Addit Mauf. 2016;12: 60-70.

[5] Atzeni E, Salmi A, Economics of additive manufacturing for end-usable metal parts. Int J Adv Manuf Tech. 2012;62(9): 1147-1155.

[6] Afkhami A, Dabiri M, Alavi SH, Bjork T, Salminen A, Fatigue characteristics of steels manufactured by selective laser melting, Int J Fatigue. 2019;122: 72-83.

[7] Shamsujjoha M, Agnew SR, Fitz-Gerald JM, Moore WR, Newman TA. High strength and 320 ductility of additively manufactured 316l stainless steel explained. Metall Mater Trans A. 2018;49(7): 3011-3027.

[8] Lewandowski JJ, Sei M. Metal additive manufacturing: A review of mechanical properties, Annu Rev Mater Res. 2016;46(1): 151-186.

[9] Li P, Warner D, Fatemi A, Phan N. Critical assessment of the fatigue performance of additively manufactured Ti6Al4V and perspective for future research, International Journal of Fatigue. 2016;85: 130-143

[10] Zhang M *et al*. High cycle fatigue and ratcheting interaction of laser powder bed fusion stainless steel 316L: Fracture behaviour and stress-based modelling. Int J fatigue. 2019;121: 252-264.

[11] Huang H, Wang Z, Lu J, Lu K, Fatigue behaviors of AISI 316L stainless steel with a gradient nanostructured surface layer. Acta Mater. 2015;87; 150-160.

[12] Roland T, Retraint D, Lu K, Lu J, Fatigue life improvement through surface nanostructuring of stainless steel by means of surface mechanical attrition treatment, Script Mater. 2006;54(11): 1949-1954.

[13] Mower TM, Long MJ. Mechanical behavior of additive manufactured, powder-bed laser-fused materials, Mater Sci Eng A. 2016;651: 198-213.

[14] Elangeswaran C, Cutolo A, Muralidharan GK, Formanoir C, Berto F, Vanmeensel K, Hooreweder BV. Effect of post-treatments on the fatigue behaviour of 316L stainless steel manufactured by laser powder bed fusion. Int J Fatigue. 2019;123; 31-39.

[15] Andreau O *et al*. A competition between the contour and hatching zones on the high cycle fatigue behaviour of a 316L stainless steel: Analyzed using x-ray computed tomography, Mater Sci Eng A. 2019;757: 146-159.

[16] Solberg K, Bero F. What is going on with fatigue of additivley manufactured metals? Mater Des Proc Comm. 2019;1(2): e84.

[17] Murakami Y, Chapter 2 - stress concentration. In: Metal Fatigue, Elsevier Science Ltd, Oxford; 2002:11-24.

[18] Gunther J *et al*. Fatigue life of additively manufactured Ti6Al4V in the very high cycle fatigue regime. Int J Fatigue. 2017;94: 236-245.

[19] Tammas-Williams S, Withers P, Todd I, Prangnell P, The influence of porosity on fatigue crack initiation in additively manufactured titanium components, Sci Rep. 2017;7: 7308.

[20] Romano S *et al*. Fatigue properties of AlSi10Mg obtained by additive manufacturing: Defect-based modelling and prediction of fatigue strength, Eng Fract Mech. 2018;187: 165-189.

[21] Yamashita Y, Murakami T, Mihara R, Okada M, Murakami Y, Defect analysis and fatigue design basis for Ni-based superalloy 718 manufactured by selective laser melting. Int J Fatigue. 2018;117 485-495

[22] Meneghetti G, Rigon D, Gennari C. An analysis of defects influence on axial fatigue strength of maraging steel specimens produced by additive manufacturing. Int J Fatigue. 2019;118: 54-64.

[23] ASTM, Standard practice for conducting force controlled constant amplitude axial fatigue tests of metallic materials, Standard ASTM E466-15, ASTM International. 2015.

[24] Lu X, Chan L, Micromechanics-based damage model for failure prediction in cold forming. Mater Sci Eng A. 2017;690: 120-131.

[25] Haibach CME. The concept of uniform scatter bands for analyzing S-N curves of unnotched and notched specimens in structural steel, ASTM STP 770 1982;770: 549-571.

[26] ISO, Metallic materials - fatigue testing - statistical planning and analysis of data, Standard ISO 12107:2012.

[27] ASTM E73910. Standard Practice for Statistical Analysis of Linear or Linearized Stress-Life (S-N) and Strain-Life (ε-N) Fatigue Data. Standard ASTM E739 - 10, ASTM International. 2015.

[28] Solberg K, Berto F. Notch-defect interaction in additively manufactured Inconel 718. Int J Fatigue. 2019;122: 35-45

[29] Romano S, Brando A, Gumpinger J, Gschweitl M, Beretta S. Qualification of AM parts: Extreme value statistics applied to tomographic measurements, Mater Des. 2017;131: 32-48.

[30] Smith K, Topper T, Watson P. A stress-strain function for the fatigue of metals (stress-strain function for metal fatigue including mean stress effect). J Mater. 1970;5: 767-778.

[31] Riemer A *et al*. On the fatigue crack growth behavior in 316L stainless steel manufactured by selective laser melting. Eng Fract Mech. 2014;120: 15-25.

[32] Tvergaard V, Needleman. Analysis of the cup-cone fracture in a round tensile bar. Act Metall. 1984;32(1): 157-169.

Article VII

Directional fatigue behaviour of maragin steel grade 300 produced by laser powder bed fusion

Klas Solberg, Even Wiberg Hovig, Knut Sørby, Filippo Berto

Under revision, preprinted at:

Surfaces built by additive manufacturing (AM) are known to be rough and populated with defects, this is in particular true for down-skin surfaces. When dealing with the fatigue of as-built surfaces produced by AM, fatigue is typically initiating from surface defects and the down-skin regions if present. In this work, both the up-skin and down-skin fatigue behaviour of maraging steel grade 300 produced by laser powder bed fusion are investigated. This is done by using specimens where all surfaces are machined, except the one at interest. Specimens were built in 10 orientation ranging from 0° (horizontal, up-skin) to 135° (down-skin). The surface roughness was measured for all orientations; high surface roughness was found for down-skin surfaces while wavy surfaces were found for up-skin surfaces. The fatigue behaviour was found to be correlated to the build orientation and the surface roughness.

https://doi.org/10.1016/j.ijfatigue.2021.106229

Directional fatigue behaviour of maraging steel grade 300 produced by laser powder bed fusion

Klas Solberg*, Even Wilberg Hovig, Knut Srby, Filippo Berto

Institutt for maskinteknikk og produksjon, NTNU, Trondheim, Norway

Abstract

Surfaces of metals produced by additive manufacturing (AM) are known to be rough and populated with defects, this is, in particular, true for downward-facing (down-skin) surfaces. When dealing with the fatigue of as-built surfaces produced by AM, fatigue is typically initiating from surface defects. In this work, the fatigue behaviour of maraging steel grade 300 (18Ni300) produced by laser beam powder bed fusion (PBF-LB) is investigated. Fatigue initiation from surfaces built both up- and down-skin are investigated. This is done by using specimens where all surfaces are machined, except the one at interest. Specimens were built in 10 orientation ranging from 0° (horizontal, up-skin) to 135° (down-skin). The surface roughness was measured for all orientations; high surface roughness was found for down-skin surfaces while wavy surfaces were found for up-skin surfaces. The fatigue behaviour was found to be correlated to the build orientation and the surface roughness.

Keywords: Additive manufacturing, Surface roughness, Defects, Directional fatigue, 18Ni300 maraging steel

1. Introduction

Additive manufacturing (AM) offers new possibilities in terms of design freedom, lead time and cost reductions[1, 2, 3]. Nevertheless, the materials often contain defects deriving from the manufacturing process that are reducing the mechanical performance [4, 5]. Typical defects are high surface roughness, lack of fusion, porosity, residual stresses and distortions [5, 6, 7, 8]. In addition to this, the microstructure is often anisotropic, as a result of the steep thermal gradients in the building process [5]. There are several approaches when designing parts for AM, in some cases, parts are produced near-to-net shape and fully post-processed with machining and heat treatment. This is done to remove defects and achieve the highest possible quality while keeping the costs low by reducing material usage and the amount of tooling. In other cases, geometric complexity, only possible to be achieved by the AM process, is desired in the final design. In this case, it might be impossible to perform machining, and designers are forced to accept the presence of the rough and defect populated as-built (AB) surfaces.

The fatigue behaviour is in particularly sensitive to the above-mentioned defects deriving from the AM process. Many of the materials that are popular in metal AM have high strength and hardness, e.g. Inconel 718, Ti6Al4V, 18Ni300 and 17-4PH steel. From conventionally manufactured metals, high tensile strength and hardness are often correlated to a high notch sensitivity in fatigue loading [9]. In the AB state, fatigue usually initiates from the rough surface or defects in the surface region [10]. By machining the surfaces, the surface defects are removed, and fatigue initiates from internal defects such as lack of fusion regions or pores [11]. Machining usually enhances the fatigue life, the same is true for chemical etching and other processes that can be used to remove surface defects [12]. Further enhancement of the fatigue behaviour can be achieved by performing hot isostatic pressing, where defects that are not open to a free surface can be closed [13, 14]. In addition to these "geometry altering" post-processing methods, heat treatments are used to alter the microstructure. The heat treatments are specific to each alloying system [15], and can also be tailored to the specific AM processes [16].

Maraging steel grade 300 (18Ni300) is one of the alloying systems where mechanical performance can be enhanced by heat treatment. Maraging steel is a FeNi-based alloy with a dominating martensitic microstructure strengthened by precipitation hardening. The martensite in maraging steel is not caused

*Corresponding author: E-mail: klas.solberg@ntnu.no

by a high carbon content (like in many other tool steel) but instead by a high Ni-concentration[17]. The lack of carbon leads to good weldability, which makes the material a good candidate for AM[18, 19, 17, 20].

Becker and Dimitrov [21] studied the Fatigue Crack Growth (FCG) of PBF-LB/18Ni300. The study included the effect of crack growth orientation (i.e. parallel and perpendicular to the build layers) and the effect of heat treatment. Faster FCG rates were observed for the AB conditions when comparing them to the HT condition. The HT condition displayed the same FCG behaviour for both directions, which also coincided with the FCG for the wrought material. In the AB condition, faster FCG rate was observed parallel to the build layers than for perpendicular to the build layers. The uniaxial fatigue behaviour of AM 18Ni300 has also been studied; a collection of AM 18Ni300 fatigue data from the literature is shown in Fig. 1, compared to fatigue data of vacuum melted 18Ni300 [22, 23]. The best fatigue performance is obtained in the vacuum melted condition, while the AM studies displayed reduced performance. Concerning the directional fatigue behaviour of the AM materials, conflicting results have been reported. Meneghetti et al.[24] found higher fatigue life for the horizontal orientation than the vertical orientation. Croccolo et al. [25] found similar fatigue performance for both horizontal and vertical orientations for bending fatigue. While Meneghetti et al. [26] and Damon et al. [27] found that vertical specimens outperformed horizontal specimens.

Dealing with the directional fatigue behaviour of AM metals, several explanations are given for differences in the fatigue properties. The three most usual explanations are illustrated in Fig. 2; The orientation of internal defects, the orientation of the microstructure and the surface roughness variations based on the surface orientations. Lack of Fusion (LoF) is one example of build direction-dependent internal defects. LoF defects are planar regions which have not been properly fused. As LoFs are planar-like defects, they are most critical when loading is occurring parallel to the build direction [28]. The microstructure of AM metals are in many cases anisotropic due to columnar grain growth parallel to the build direction[29]. When loading occurs parallel to the build direction, the fatigue crack needs to propagate through several grain boundaries than when loading occurs normal to the build direction, this is illustrated in Fig. 2b. Riemer et al. found that the threshold stress intensity factor (for fatigue crack initiation) was higher for 316L built in the vertical orientation than in the horizontal orientation [30], and reasoned for this by stating that the fatigue crack needed to propagate through several grain boundaries. Dealing with uniaxial fatigue behaviour, the research usually shows that the fatigue life is higher for specimens built in the horizontal orientation [31, 26, 32]. The surface roughness and morphology are also dependent on the build orientations. Typically, down-skin surfaces (i.e. surfaces facing downwards) display higher surface roughness than up-skin surfaces (i.e. surfaces facing upwards). The valleys in the surface roughness profile act as stress risers, making them prone to fatigue initiation. Due to this, the main trend is that when the directional fatigue behaviour is assessed with an as-built surface, fatigue initiates from the down-skin region and not the up-skin region.

The goal of the present work is to evaluate directional fatigue behaviour of PBF-LB/18Ni300 maraging steel and in particular the fatigue behaviour of up- and down-skin surfaces. To do this, a new test specimen is proposed, where all sides of the specimens are machined except one side. Specimens were printed near-to-net shape for different orientations and then machined. To simplify the test scheme, one load level is selected for all the specimens. The fracture surfaces and the surface roughness profiles were investigated. Further, the porosity and microstructure were analyzed. Finally, the fatigue data are discussed in terms of variations in surface conditions and dimensional tolerances.

2. Methods

The specimen geometry is based on ASTM E466-15; Specimens with tangentially blended fillets between a uniform cross-section, the dimensions are shown in Fig. 3. The specimens were built in 10 different orientations relative to the build platform, from 0° to 135° with steps of 15°. Three specimens were built in each orientation. The specimens were built in a Concept Laser system using a quadratic island strategy of 5 mm × 5 mm islands. The islands had an angular shift of 45° for each layer in addition to a 1mm *xy*-shift in the island locations. The perimeter of each layers was scanned with a single contour track. The hatch spacing of the contour track was the same as the volume hatch. The same parameters were used for up-skin and down-skin surfaces A laser power of 180 W, hatch spacing of 105 μm, scan velocity of 650 mm/s and a layer thickness of 30μm was used as process parameters. Support structures were used for all

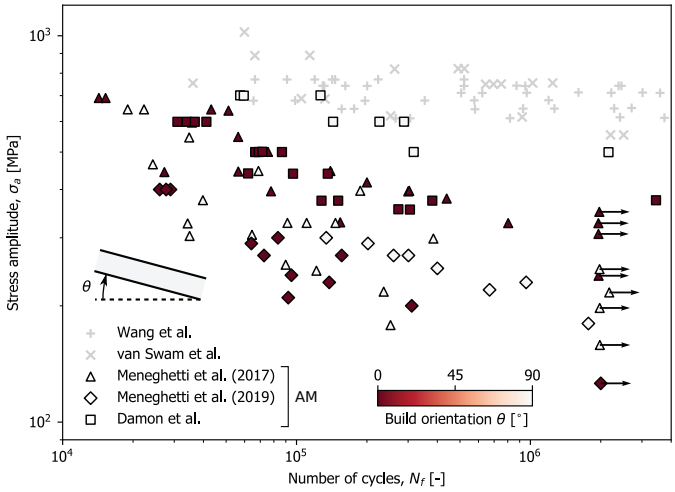

Figure 1: Comparison of fatigue data from the literature. Wang et al.[22] van Swam et al.[23], Meneghetti et al. (2017)[24], Meneghetti et al. (2019)[26] and Damon et al. (PBF-LB) [27]. All fatigue data were tested at R=-1. Build angles are reported using the conventions of the current article: 0° - horizontal, 90° - vertical.

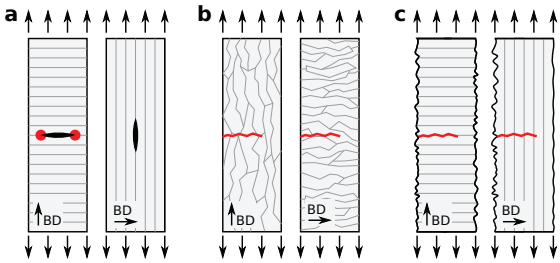

Figure 2: Different features affecting the directional fatigue behaviour of AM metals. a) orientation of defects, b) microstructural anisotropy: orientation of columnar grains and c) surface roughness dependent on surface orientation. Build directions indicated by BD.

down-skin surface except the surfaces left in the AB condition. The support type used was 'block' [33], with a wall thickness of 0.1 mm (one laser line) and a hatching on 1.5 mm between the walls in x- and y-direction. The specimens were heat-treated by direct aging at 500°C for 5 hours prior to removing them from the build platform and machining them.

To be able to observe the fatigue behaviour of the up-skin surfaces, one surface was left in the AB condition, as shown in Fig. 3. First, both sides of the specimens were ground to avoid distortion problems which have been observed for the same material and manufacturing processes [26]. After grinding, the specimens were machined on all sides except one surface.

The fatigue testing was done using a loading ratio R=0 and a frequency of 30 Hz on an MTS servohydraulic system with a 50 kN load cell. To see the influence of the different build orientations and surface conditions without generating full SN-curves for each orientation, one load level was selected for the tests. The load level was based on experimental data on the same alloy from Meneghetti et al. [26] and on some initial trial and error testing of specimens with mistakes in the machining. The load level was determined to correspond to a stress range of 500 MPa, which results in fatigue failures around $\sim 10^5$ cycles. The gauge sections of all the specimens were measured with a caliper before testing.

A Scanning Electron Microscope (SEM) was used for analysing the fracture surfaces and for capturing the morphology of the as-built surfaces. Furthermore, the surface roughness of the as-built surfaces was calculated by extracting the surface profiles as lines in the software InkScape then importing and processing them in python[1]. Two different surface roughness parameters were calculated; the arithmetic mean deviation, *Ra*, and the maximum height of the profile, *Rz*. The arithmetical mean

[1] `https://opencv-python-tutroals.readthedocs.io/en/latest/py_tutorials/py_gui/py_image_display/py_image_display.html`

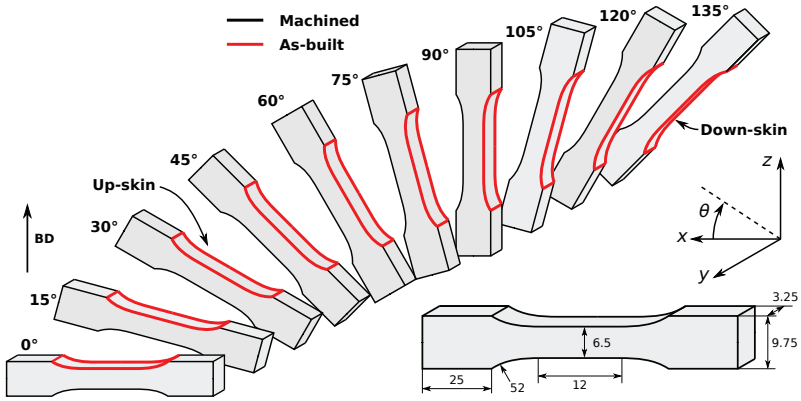

Figure 3: Specimen orientations and dimensions. BD indicates the build direction.

deviation of the assessed profile is given by

$$Ra = \frac{1}{n}\sum_{i=1}^{n}|y_i| \tag{1}$$

and the maximum height of the profile given by

$$Rz = |\max_i y_i| - |\min_i y_i|. \tag{2}$$

Where y_i is the distance from the mean line of n equally spaced points at the i^{th} data point. The mean line was calculated by linear regression using `numpy.polyfit`.

The porosity of the material was determined from optical micrographs of polished cross-sections. The micrographs were analysed by a python script using the `cv2.THRESH_BINARY`[2] threshold filter. The threshold was set so that the porosity was captured and scratches and other irregularities were ignored. The microstructure was investigated in SEM, by Back Scattered Electron (BSE) analysis. Before BSE, oxide suspension polishing was done with a particle size of 0.25 μm. Vickers hardness (1 kg) were measured on a Mitutoyo MicroWiZhard system.

3. Results

3.1. Surface roughness

The AB surfaces were investigated by SEM and are shown in Fig. 4. The side-view of the machined surfaces are shown in Fig. 4a and the view normal to the AB surfaces are shown in Fig. 4b. Fig. 4b shows that for the horizontal specimens (0°), the hatching strategy is visible. For low angles (15°-60°), the different build layers are visible, displaying the staircase effect (see e.g. Fig. 4a 15°) which is characteristic for AM [34]. The surfaces built close to the vertical orientation displays a general roughness, which increases as the surface turns to down-skin. In the down-skin surfaces, the surfaces have increasingly higher roughness and high amounts of particles attached. It should be noted that the sharpness of the valleys of the surface in e.g. 135° are not high compared to what has been observed in other works where the melt pool geometry seems to directly dictate the surface morphology and create sharp corners[10].

Based on the SEMs in Fig. 4a and b, three main surface conditions can be identified:

(i) for angles close to zero the stair-case effect is observed. In 0° the hatching pattern is visible and from 15 – 45° the stair-case effect is observed with an increased amount of attached powder particles as the angle increases.

(ii) For angles between 45° and 90° a general surface roughness is observed, with an increasing amount of attached powder as the angle increases.

(iii) For down-skin surfaces a strongly increasing surface roughness is observed, high amounts of powder particles are attached to the surfaces.

These three categories are illustrated in Fig. 4c.

Based on the captured SEMs of the surface profiles in Fig. 4a the surface roughness parameters Ra and Rz were calculated. An example of a surface profile and the extracted profile is shown in Fig. 5a and the data points and the calculation of

[2] `https://docs.opencv.org/master/d7/d4d/tutorial_py_thresholding.html`

Ra and *Rz* are shown in Fig. 5b. The *Ra* and *Rz* values obtained from all the SEMs are shown in Fig. 6. It should be noted that these data are not taken as the average of several measurements but directly from the SEMs presented in Fig. 4a. The main trend observed in Fig. 6 is that the value of *Ra* and *Rz* is increasing drastically from 105° to 135°. For values between 0° and 90°, the surface roughness values are slightly decreasing. A decrease in surface roughness when going from 0° to 90°, due to the staircase effect, has also been observed in recent literature [35, 36]. The surface roughness for case (i) specimens are dominated by the staircase effect and not equal in different directions. I.e. the surface roughness along the length dimension of the specimens is higher than the surface roughness across the thickness of the specimens (See e.g. 15° in Fig. 4b). In the case of (ii) and (iii), the surface seems to be more uniform in the different directions (See Fig. 4b).

3.2. Porosity

Fig. 7 shows a micrograph of a polished cross-section and the porosity detection. The full micrograph is shown in Fig. 7a and Fig. 7b and c shows a detail of the porosity detection. Note that the black regions with porosity are detected while the grey grinding lines and dirt are neglected. A porosity of 1.68 ± 0.123 % was obtained based on the micrographs.

3.3. Microstructure

The microstructure of the material in the *xz*-plane is shown in Fig. 8 based on BSE analysis. The analysis displays regions of martensite blocks with plates of similar orientations. These regions are indicated by outlining and the direction of the plates are indicated by arrows in Fig. 8. When the material solidifies in the PBF-LB/M process, the high-atomic density vector <110> of the primary α-FCC austenite grains aligns with the direction of the heat flux [37], and the primary austenite grains tend to be elongated in the build direction. As the martensite transformation occurs the martensite plate orientation is dictated by the Kurdjumow-Sachs relationship, meaning that the plates can take any one of 24 orientations. This leads to a weak microstructural texture, much less dominant than what can be observed in other materials such as Inconel 718 [38, 39] and AlSi10Mg [40].

The Vickers hardness (HV1) of the material was measured in the *xz*-plane. The hardness was found to be 634.5 ± 23.4. It should be noted that this is in the same range as what has been reported by Jagle et al. for laser metal deposition and Damon et el. for PBF-LB for similar heat treatment [17, 27]. While Meneghetti et al. reported values of HV 367 for AB PBF-LB/18Ni300 [26].

3.4. Fatigue data

The fatigue data are shown in Fig. 9 and summarized in table 1. In Fig. 9, the number of cycles is plotted versus the build orientation for specimens tested at the same load level (500 MPa). From this plot a clear trend in the fatigue data is visible; the lowest fatigue life is found close to the horizontal orientation, then the fatigue life is increased when approaching the vertical orientation, and decreasing when entering the down-skin region. The highest fatigue life was found for the 60°-specimens. In general, the down-skin specimens displays lower fatigue life than their up-skin counterparts. Although considering the scatter, the difference is striking, e.g. by comparing 45° and 135°, both orientations display a fatigue life in a similar range. The clearest difference is observed between 60° and 120°.

3.5. Fractography

Fracture surfaces analysed by SEM are shown in Fig. 10. All specimens that were investigated were found to have fatigue initiating from defects followed by a region of fatigue crack growth and a final rupture zone. The final rupture zone displayed shear lips along the edges. Concerning the fatigue initiation sites, all specimens did not fail from the as-built surfaces; some specimens failed from internal voids and defects close to the as-built surface. Three different fracture surfaces displaying different fatigue initiations are shown in Fig. 10: failure from internal defect, failure from the centre of the as-built surface and failure from the corner of the as-built surface.

In Fig. 10a and b, a specimen built with 0° angle is shown. The specimen has fatigue initiation from the centre of the AB surface. Fatigue initiates from a defect that is ~70 μm deep, comparable to the *Rz* value from Fig. 6, which was measured to be 99.2 μm. In Fig. 10c and d, a specimen built with 135° angle is shown. This specimen is also failing from the AB surface, but fatigue initiated from the corner of the specimen. In this case, the surface roughness, *Rz*, is higher than the 0° by approximately a factor of 4. In Fig. 10e and f, a specimen built with 60° angle is shown. This specimen does not have fatigue initiation from the AB surface but from a defect close to/at the

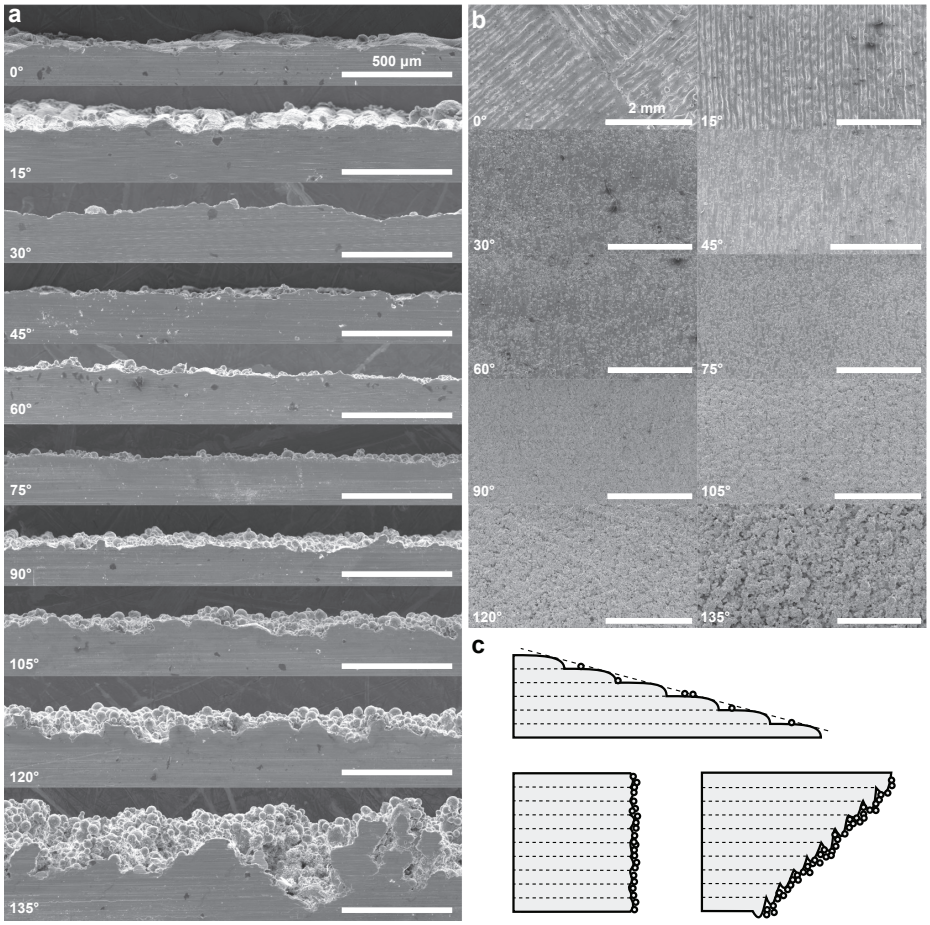

Figure 4: SEM of surface conditions of specimens. (a) machined cross section (b) as-built surface (c) Schematic illustration of the different surface conditions

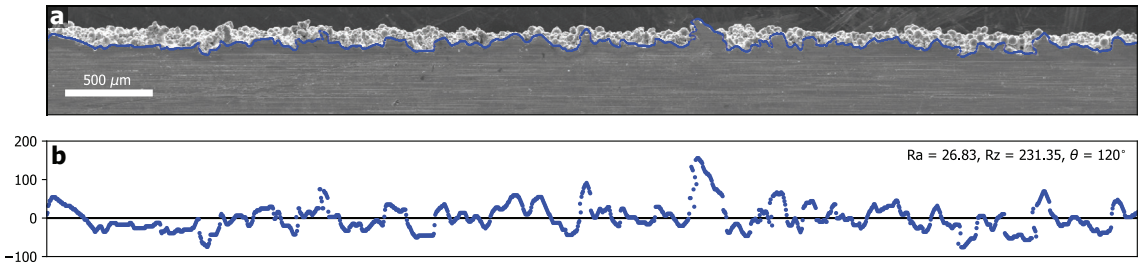

Figure 5: Example of extraction and calculation of surface roughness parameters in python. (a) SEM with surface profile highlighted, (b) detected points used for calculation, note that Eq. (1) uses equally spaced points in the x-direction, which corresponds to the pixels in the SEM image.

machined surface. The specimens in this orientation display the highest fatigue life.

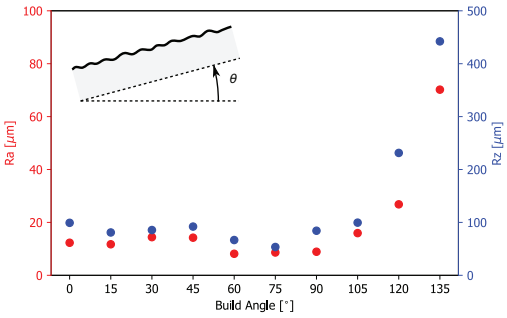

Figure 6: Correlation between surface roughness (from SEM) and build angle

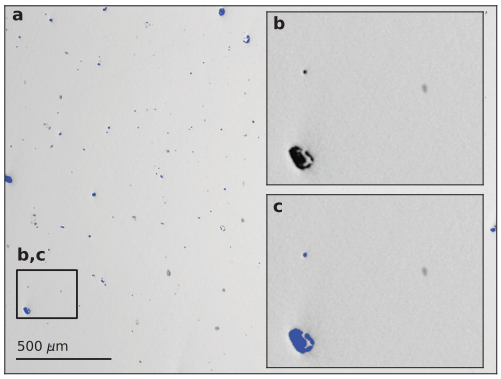

Figure 7: Example of porosity measurement. (a) Optical micrograph of polished cross section with the detected porosity highlighted in blue. (b) detail of micrograph (c) detail of the micrograph with porosity highlighted.

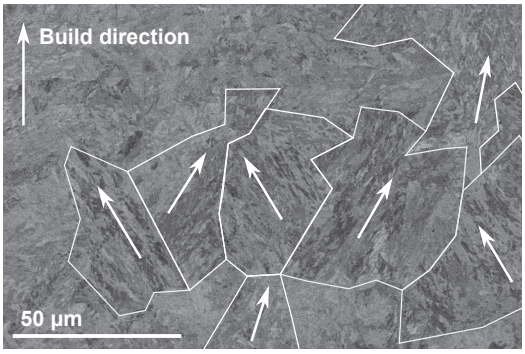

Figure 8: Microstructure of the material in *xz*-plane obtained by BSE. Different regions with a clear orientation of the martensite plates are indicated by outlining and arrows.

4. Discussion

4.1. Comparison to fatigue data from the literature

In Fig. 11 the fatigue data obtained in this study are compared to fatigue data on PBF-LB from the literature, represented as regression lines. The stress values of the fatigue data from the present work is taken as the applied load divided by the measured cross-section, listed in Table 1. It should also be noted that the fatigue data from literature were tested at $R = -1$ and were therefore corrected by the Smith-Watson-Topper (SWT) mean stress correction [41]. The SWT mean stress correction is given by

$$\sigma_{ar} = \sigma_{max}\sqrt{\frac{1-R}{2}}, \tag{3}$$

where σ_{ar} is the stress amplitude at $R = -1$ and σ_{max} is the maximum stress during the loading cycle at the given R value. The comparison in Fig. 11 shows that the fatigue data from the present work is in a similar range as the data from the literature. The data from Meneghetti et al.[26] and Damon et al.[27] displayed higher fatigue life for loading in the vertical orientation than the horizontal orientation. A similar trend was observed for the data presented here, specimens close to the horizontal orientation displayed lower fatigue life than the specimens close to the vertical orientation.

From the data in Fig. 11 it is clear that there are variations in the nominal stress due to the specimen dimensions, although the specimens were tested at the same load level.

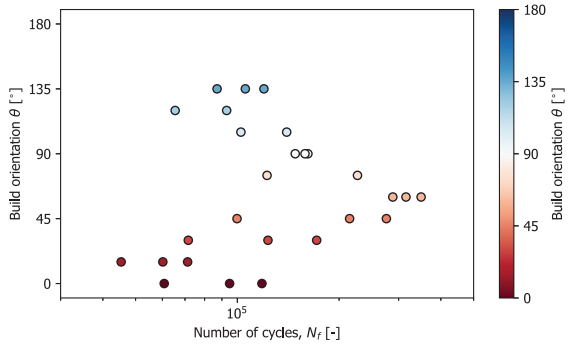

Figure 9: Fatigue data for different orientations.

4.2. Comparison of different build angles

A comparison of the fatigue life, the surface roughness, the nominal stress and the build angle for specimens tested at the same load level is shown in Fig. 12. To compare the up-skin and down-skin surfaces of equal orientation (e.g. 60° and 120°), the build angle is given as

$$\theta^* = \arcsin(\sin(\theta)). \tag{4}$$

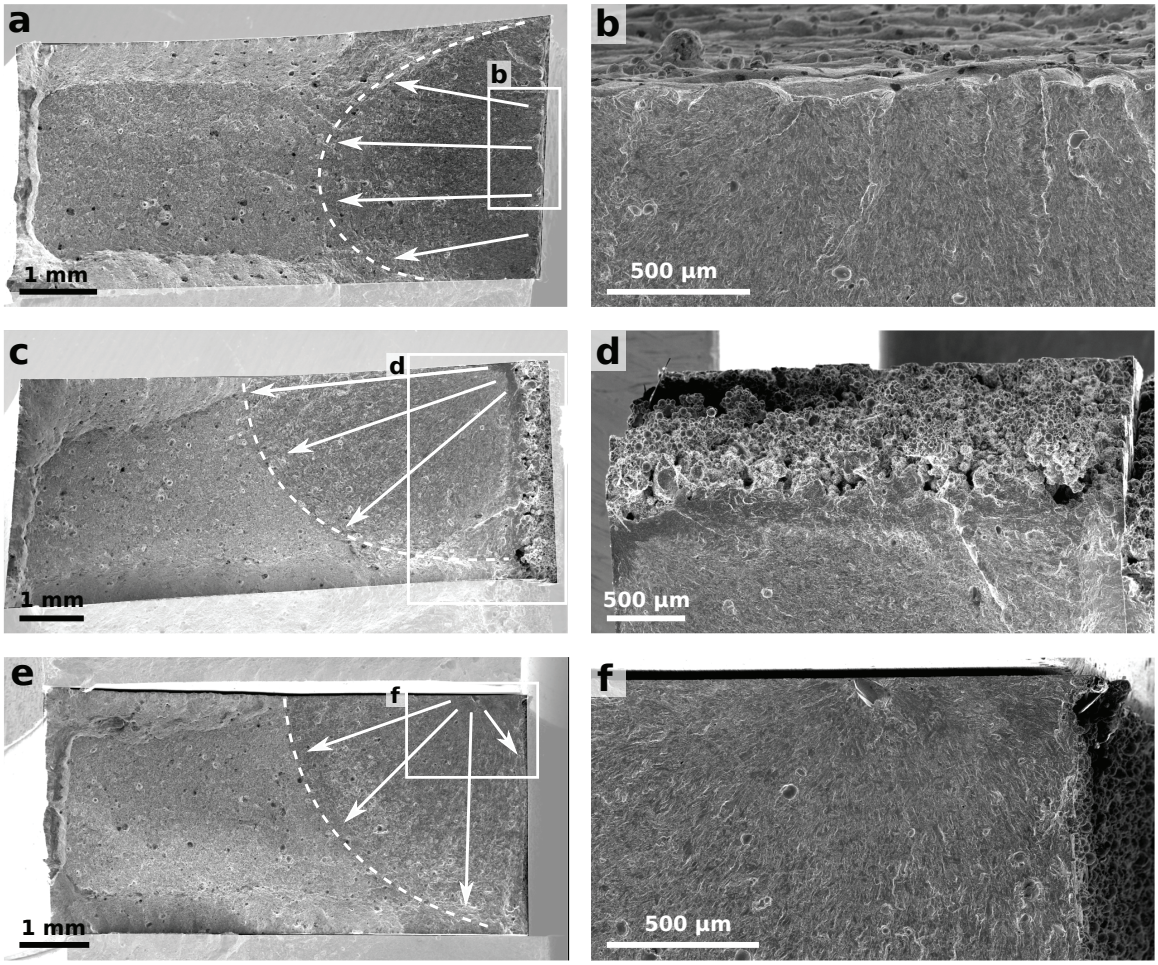

Figure 10: Fracture surfaces of three different fatigue initiations: a and b) 0°, fatigue initiation for centre of the AB surface, c and d) 135°, Fatigue initiation from the corner the AB surface and e and f) 60°, Fatigue initiation from internal defect

Table 1: Specimen dimensions and fatigue data. Build angle θ [°], thickness t [mm], width w [mm], stress range $\Delta\sigma$ [MPa], number of cycles to failure N_f [-].

θ	t	w	$\Delta\sigma$	N_f	Note
0	3.258	6.370	508.9	60760	
0	3.264	6.470	500.1	94862	
0	3.262	6.463	501.0	118234	
15	3.263	6.338	510.7	45314	
15	3.260	6.389	507.1	71265	
15	3.267	6.413	504.1	60186	
30	3.271	6.476	498.6	171628	
30	3.273	6.442	500.9	71586	
30	3.276	6.486	497.1	123178	
45	3.247	6.467	503.0	99761	
45	3.252	6.456	503.1	275975	
45	3.260	6.502	498.3	214804	
60	3.274	6.456	499.7	349644	
60	3.271	6.435	501.8	288333	
60	3.258	6.493	499.3	315357	
75	3.264	6.478	399.6	500000	a
75	3.271	6.500	496.8	122422	
75	3.259	6.498	498.7	226664	
90	3.261	6.620	489.3	148340	
90	3.254	6.547	495.8	161695	
90	3.259	6.529	496.4	158520	
105	3.275	6.557	491.8	139936	
105	3.299	6.531	490.2	102440	
105	3.263	6.388	608.1	66344	b
120	3.252	6.780	479.0	92968	
120	3.245	6.855	474.8	65460	
120	3.248	6.595	789.0	34860	b
135	3.290	7.272	441.5	105578	
135	3.255	7.206	450.3	119832	
135	3.258	7.202	450.1	87085	

[a] Discontinued

[b] Mistake in machining. All sides machined

Fig. 12a shows a comparison of the build angles and the fatigue life, where the average and standard deviation of the fatigue life is calculated for each angle. The lowest number of cycles was observed for the 15°-specimens, while the fatigue life increased as the built angle increased towards 60°, then decreased from 60° to 135°. In general, when comparing the corresponding build angles, the down-skin specimens have lower fatigue life than the up-skin specimens.

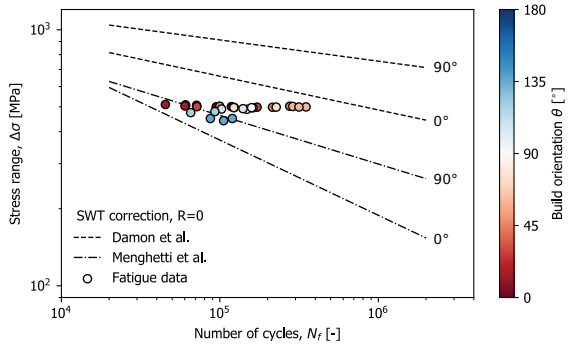

Figure 11: Comparison of fatigue data

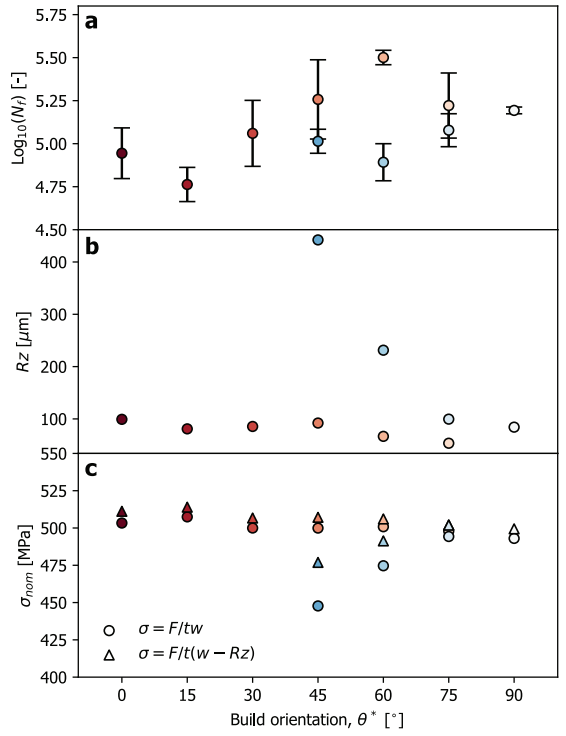

Figure 12: Comparison of a) fatigue life, b) surface roughness and c) nominal stress

Variations were observed in the specimen dimensions in particular due to the unmachined surfaces. To take into account these variations, the average stress for each build angle is

given in Fig. 12c. Based on the dimensions measured by caliper (given values in Table 1), the stress is calculated by $\sigma = F/tw$. The values show that the nominal stress is decreasing for an increasingly down-skin angle. The caliper, however, does not take into account the surface roughness of the specimens and might give a too low value of the nominal stress in the specimens. To take into account the decrease in the cross-sectional area due to the surface roughness, the cross-section was corrected by the Rz values (shown in Fig. 12b), giving a nominal stress calculated by $\sigma = F/t(w - Rz)$. After correction the nominal stress level for the surface roughness, the nominal stress increase slightly for the values between 0° and 105°, while for 120° and 135° the stress increase. It should be noted that correcting by the full value of Rz might be too conservative, but it indicates the possible additional stress level variations. It is also interesting to remark that not only does the surface roughness depend on the build orientation of the surfaces, but also the dimensional tolerances. Deviations in dimensions due to down-skin surfaces has also been observed by other researchers in e.g. Refs. [42, 43].

The fatigue data presented in Fig. 9 and Fig. 12a assumes the load level to be constant. This is, as discussed above, not the case. To correct for the variations in the stress levels, a comparison was made based on the deviation from an assumed fatigue life curve. Fig. 13a shows fatigue data from this study compared with the linear regression of the fatigue data of Meneghetti et al.[26] and Damon et al.[27] (presented previously in Fig. 12). The data from literature are presented in terms of Basquin curves based on power-law fitting of the data. By assuming that the fatigue data presented in this work follows similar trend lines as the data published by Meneghetti et al.[26] and Damon et al.[27], the trend line was described by Basquin's equation. The slope, B, was assumed to have the same value as the Meneghetti et al.[26] 90°-data (as the data are close to this curve). Further, a new "assumed" fatigue life curve was created. The vertical shift, A, of the curve was taken so that the trend line (at 500 MPa) intersects with the mean value of the maximum and the minimum number of cycles at tests done around 500 MPa. The deviation for the assumed fatigue life curve is given by

$$n_i = \log_{10}(N_i) - \log_{10}\left(\left(\frac{\sigma_i}{A}\right)^{\frac{1}{B}}\right). \quad (5)$$

Further, the deviation from the regression line is normalized by the maximum value, n_{max}, and the result is shown in Fig. 13b. This comparison gives, perhaps, a more realistic comparison of the corresponding angles, e.g. 45° and 135° or 60° and 120°. Here, the 135° and 120° angle displays lower fatigue life than the 45 and 60 orientations. This comparison between the fatigue life (n_i/n_{max}) confirms that the fatigue life is lower for the down-skin region than for up-skin region.

4.3. Surface morphology

From the correlation between the build angle and surface roughness in Fig. 12b the main shift in the surface roughness conditions is when the surface turns down-skin. Here, the surface roughness increases by over 4 times when comparing the 135° orientation to the general values for the up-skin surfaces. When investigating the morphology of the surfaces in Fig. 4a, no sharp features (notch roots) are observed, contrary to what has been found in the down-skin surface in other studies [10]. In addition to this, the up-skin surfaces display a waviness morphology (the 15° orientation is the extreme). As discussed in Sec. 3.1, three main surface conditions were identified; high surface roughness for down-skin surface, general surface roughness for vertical orientation and the staircase-like surface for up-skin surfaces. When the surface roughness is governed by the staircase effect, the surface roughness manifests as notches that are defined along the thickness direction of the sample. On the contrary, in the down-skin region, the notches from the surface roughness are not constant along with the thickness direction of the specimens. This could explain why the 15°-specimens, which displays a very distinct staircase surface, has the lowest fatigue life.

5. Conclusions

In the present work, the directional fatigue behaviour of PBF-LB/18Ni300 maraging steel was studied. Specimens with 10 different orientations ranging from 0° to 135° were considered. The following conclusions can be drawn:

- A new test specimen for testing both the up- and down-skin fatigue behaviour of AM metals has been proposed. By machining all sides of a specimen except one, fatigue cracks are guided to initiate from the AB surface.
- The surface roughness was evaluated for surfaces built ranging from 0° (up-skin, horizontal) to 135° (down-skin). The up-skin surfaces displayed the stair-case effect while the down-skin surfaces displayed high surface roughness.

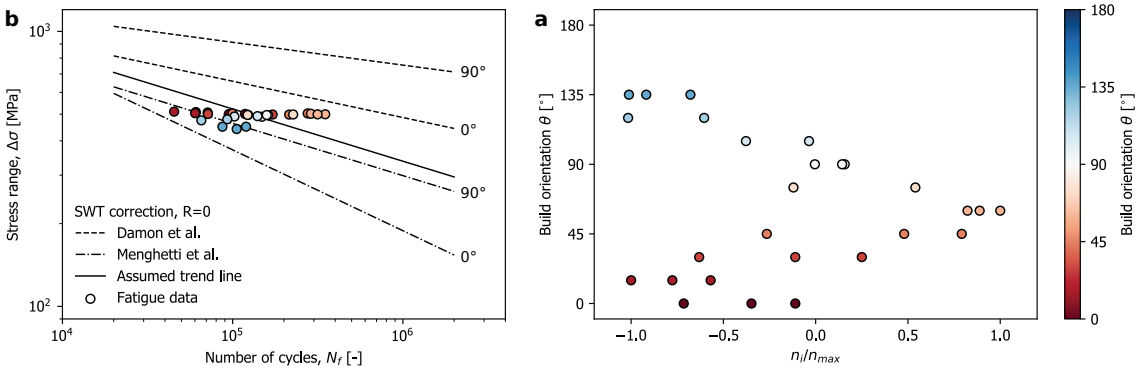

Figure 13: a) Comparison of the fatigue data presented in this study and regression lines of the fatigue data of PBF-LB/18Ni300 by Damon et al. and Meneghetti et al. b) Updated correlation between the build angle and the normalized parameter n_i/n_{max}.

- The fatigue strength was found to be inferior to wrought 18Ni300 but comparable to other works on AM. Specimens built close to the vertical orientation was found to have longer fatigue life compared to specimens built closer to the horizontal orientation. The same and the opposite trend has been found in recent literature on the same material.
- The specimens with AB up-skin surfaces displayed higher fatigue life than the ones with AB down-skin surface due to the higher surface roughness.

Acknowledgement

This work is funded in part by the Norwegian Research Council through grant number 248243, and by the TROJAM project in the INTERREG A/ENI program.

The authors would also like to acknowledge Matija Cuzovic for the work done in his master's thesis.

CRediT author statement

KS: Conceptualization, Methodology, Formal analysis, Writing - Original Draft **EWH:** Conceptualization, Methodology, Formal analysis, Writing - Original Draft **KS:** Supervision, Writing - Review & Editing **FB:** Supervision, Writing - Review & Editing

Declaration of competing interest

The authors declare that they have no competing financial interests or personal relationships that could have appeared to influence the work reported in this paper.

References

[1] D. L. Bourell, Perspectives on additive manufacturing, Annual Review of Materials Research 46 (2016) 1–18.

[2] K. Wong, K. Hernandez, A review of additive manufacturing, ISRN Mechanical Engineering 2012 (2012) 0–10.

[3] A. Wiberg, J. Persson, J. Olvander, Design for additive manufacturing a review of available design methods and software, Rapid Prototyping Journal 25 (2019) 1080–1094.

[4] S. Singh, S. Ramakrishna, R. Singh, Material issues in additive manufacturing: A review, Journal of Manufacturing Processes 25 (2017) 185 – 200.

[5] J. J. Lewandowski, M. Seifi, Metal additive manufacturing: A review of mechanical properties, Annual Review of Materials Research 46 (2016) 151–186.

[6] C. Li, Z. Liu, X. Fang, Y. Guo, Residual stress in metal additive manufacturing, Procedia CIRP 71 (2018) 348 – 353. 4th CIRP Conference on Surface Integrity (CSI 2018).

[7] M. Megahed, H. Mindt, N. NDri, H. Duan, O. Desmaison, Metal additive-manufacturing process and residual stress modeling, Integrating Materials and Manufacturing Innovation 5 (2016) 6193.

[8] T. Mukherjee, W. Zhang, T. DebRoy, An improved prediction of residual stresses and distortion in additive manufacturing, Computational Materials Science 126 (2017) 360 – 372.

[9] S. McKelvey, A. Fatemi, Surface finish effect on fatigue behavior of forged steel, International Journal of Fatigue 36 (2012) 130 – 145.

[10] K. Solberg, F. Berto, Notch-defect interaction in additively manufactured inconel 718, International Journal of Fatigue 122 (2019) 35 – 45.

[11] N. Sanaei, A. Fatemi, Analysis of the effect of internal defects on fatigue performance of additive manufactured metals, Materials Science and Engineering: A 785 (2020) 139385.

[12] P. Jamshidi, M. Aristizabal, W. Kong, V. Villapun, S. C. Cox, L. M. Grover, M. M. Attallah, Selective laser melting of ti-6al-4v: The impact of post-processing on the tensile, fatigue and biological properties for medical implant applications, Materials 13 (2020) 2813.

[13] R. Molaei, A. Fatemi, N. Phan, Significance of hot isostatic pressing (hip) on multiaxial deformation and fatigue behaviors of additive manufactured ti-6al-4v including build orientation and surface roughness effects, International Journal of Fatigue 117 (2018) 352 – 370.

[14] S. Tammas-Williams, P. J. Withers, I. Todd, P. B. Prangnell, The effectiveness of hot isostatic pressing for closing porosity in titanium parts manufactured by selective electron beam melting, Metallurgical and Materials Transactions A 47 (2016) 1939–1946.

[15] D. Croccolo, M. Agostinis, S. Fini, G. Olmi, F. Robusto, S. Kostić, A. Vranić, N. Bogojević, Fatigue response of as-built dmls maraging steel and effects of aging, machining, and peening treatments, metals 8(7) (2018) 505.

[16] H.-Y. Wan, Z.-J. Zhou, C.-P. Li, G.-F. Chen, G.-P. Zhang, Enhancing fatigue strength of selective laser melting-fabricated inconel 718 by tailoring heat treatment route, Advanced Engineering Materials 20 (2018) 1800307.

[17] E. Jgle, Z. Sheng, P. Krnsteiner, S. Ocylok, A. Weisheit, D. Raabe, G. Requena, Comparison of maraging steel micro-and nanostructure produced conventionally and by laser additive manufacturing, Materials 10 (2017).

[18] C. Turk, H. Zunko, C. Aumayr, H. Leitner, M. Kapp, Advances in maraging steels for additive manufacturing, BHM Berg- und Httenmnnische Monatshefte 164 (2019).

[19] P. Bajaj, A. Hariharan, A. Kini, P. Krnsteiner, D. Raabe, E. Jgle, Steels in additive manufacturing: A review of their microstructure and properties, Materials Science and Engineering: A 772 (2020) 138633.

[20] K. Kempen, E. Yasa, L. Thijs, J.-P. Kruth, J. Humbeeck, Microstructure and mechanical properties of selective laser melted 18ni300 steel, Physics Procedia 12 (2011) 255–263.

[21] T. H. Becker, D. Dimitrov, The achievable mechanical properties of slm produced maraging steel 300 components, Rapid Prototyping Journal 22 (2016) 487–494.

[22] B. Wang, P. Zhang, Q. Duan, Z. Zhang, H. Yang, X. Li, Z. Zhang, Optimizing the fatigue strength of 18ni maraging steel through ageing treatment, Materials Science and Engineering: A 707 (2017) 674 – 688.

[23] L. F. Van Swam, R. M. Pelloux, N. J. Grant, Fatigue behavior of maraging steel 300, Metallurgical Transactions A 6 (1975) 45–54.

[24] G. Meneghetti, D. Rigon, D. Cozzi, W. Waldhauser, M. Dabal, Influence of build orientation on static and axial fatigue properties of maraging steel specimens produced by additive manufacturing, Procedia Structural Integrity 7 (2017) 149 – 157.

[25] D. Croccolo, M. De Agostinis, S. Fini, G. Olmi, A. Vranic, S. Ciric-Kostic, Influence of the build orientation on the fatigue strength of eos maraging steel produced by additive metal machine, Fatigue & Fracture of Engineering Materials & Structures 39 (2016) 637–647.

[26] G. Meneghetti, D. Rigon, C. Gennari, An analysis of defects influence on axial fatigue strength of maraging steel specimens produced by additive manufacturing, International Journal of Fatigue 118 (2019) 54 – 64.

[27] J. Damon, T. Hanemann, S. Dietrich, G. Graf, K.-H. Lang, V. Schulze, Orientation dependent fatigue performance and mechanisms of selective laser melted maraging steel x3nicomoti18-9-5, International Journal of Fatigue 127 (2019) 395 – 402.

[28] A. Yadollahi, N. Shamsaei, S. M. Thompson, A. Elwany, L. Bian, Effects of building orientation and heat treatment on fatigue behavior of selective laser melted 17-4 ph stainless steel, International Journal of Fatigue 94 (2017) 218 – 235.

[29] D. Herzog, V. Seyda, E. Wycisk, C. Emmelmann, Additive manufacturing of metals, Acta Materialia 117 (2016).

[30] A. Riemer, S. Leuders, M. Thne, H. Richard, T. Trster, T. Niendorf, On the fatigue crack growth behavior in 316l stainless steel manufactured by selective laser melting, Engineering Fracture Mechanics 120 (2014) 15 – 25.

[31] T. M. Mower, M. J. Long, Mechanical behavior of additive manufactured, powder-bed laser-fused materials, Materials Science and Engineering: A 651 (2016) 198 – 213.

[32] P. Edwards, M. Ramulu, Fatigue performance evaluation of selective laser melted ti6al4v, Materials Science and Engineering: A 598 (2014) 327 – 337.

[33] P. N. Johannes Lindecke, H. Blunk, J.-P. Wenzl, M. Mller, C. Emmelmann, Optimization of support structures for the laser additive manufacturing of tial6v4 parts, Procedia CIRP 74 (2018) 53 – 58. 10th CIRP Conference on Photonic Technologies [LANE 2018].

[34] C. Emmelmann, D. Herzog, J. Kranz, 10 - design for laser additive manufacturing, in: M. Brandt (Ed.), Laser Additive Manufacturing, Woodhead Publishing Series in Electronic and Optical Materials, Woodhead Publishing, 2017, pp. 259 – 279.

[35] G. Strano, L. Hao, R. M. Everson, K. E. Evans, Surface roughness analysis, modelling and prediction in selective laser melting, Journal of Materials Processing Technology 213 (2013) 589 – 597.

[36] E. W. Hovig, A. S. Azar, M. F. Sunding, E. Andreassen, K. Srby, High cycle fatigue life estimation of materials processed by laser powder bed fusion, Fatigue & Fracture of Engineering Materials & Structures 42 (2019) 1454–1466.

[37] A. S. Azar, E. Østby, O. M. Akselsen, Effect of hyperbaric chamber gas on transformation texture of the API-X70 pipeline weld metal, Metallurgical and Materials Transactions A: Physical Metallurgy and Materials Science (2012).

[38] E. Chlebus, K. Gruber, B. Ku??nicka, J. Kurzac, T. Kurzynowski, Effect of heat treatment on the microstructure and mechanical properties of Inconel 718 processed by selective laser melting, Materials Science and Engineering A 639 (2015) 647–655.

[39] W. Hovig, A. S. Azar, F. Grytten, K. Sørby, E. Andreassen, Determination of anisotropic mechanical properties for materials processed by laser powder bed fusion, Advances in Materials Science and Engineering 2018 (2018).

[40] E. Brandl, U. Heckenberger, V. Holzinger, D. Buchbinder, Additive manufactured AlSi10Mg samples using Selective Laser Melting (SLM): Microstructure, high cycle fatigue, and fracture behavior, Materials & Design 34 (2012) 159–169.

[41] K. N. Smith, P. Watson, T. H. Topper, A stress strain function for the fatigue of metals, Journal of Materials 5 (1970) 767 – 778.

[42] O. Andreau, E. Pessard, I. Koutiri, P. Peyre, N. Saintier, Influence of the position and size of various deterministic defects on the high cycle fatigue resistance of a 316l steel manufactured by laser powder bed fusion,

International Journal of Fatigue 143 (2021) 105930.

[43] G. Matache, A. Paraschiv, R. Condruz, Edge and corner effects in selective laser melting of in 625 alloy, Manufacturing Review 7 (2020) 8.

ISBN 978-82-326-6746-8 (printed ver.)
ISBN 978-82-326-6333-0 (electronic ver.)
ISSN 1503-8181 (printed ver.)
ISSN 2703-8084 (online ver.)

NTNU
Norwegian University of
Science and Technology